Validation of a Computer Code for Analysis of Subsonic Aerodynamic Performance of Wings With Flaps in Combination With a Canard or Horizontal Tail and an Application to Optimization

Harry W. Carlson,
Christine M. Darden,
and Michael J. Mann

NASA

Validation of a Computer Code for Analysis of Subsonic Aerodynamic Performance of Wings With Flaps in Combination With a Canard or Horizontal Tail and an Application to Optimization
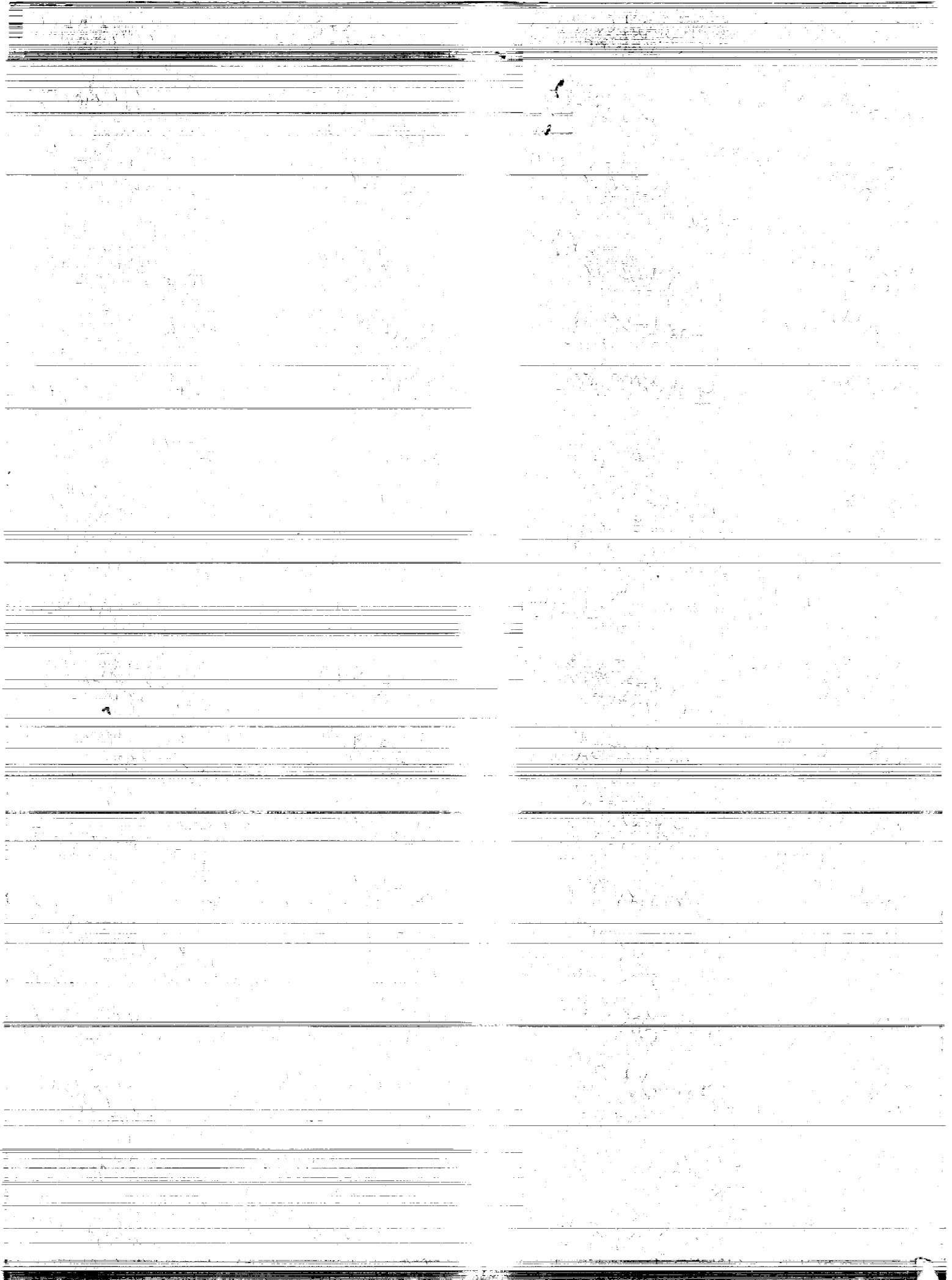
Harry W. Carlson
PRC Kentron, Inc.
Aerospace Technologies Division
Hampton, Virginia

Christine M. Darden
and Michael J. Mann
Langley Research Center
Hampton, Virginia

Summary

Extensive correlations of computer-code results with experimental data are employed to illustrate the use of a linearized-theory, attached-flow method for the estimation and optimization of the longitudinal aerodynamic performance of wing-canard and wing–horizontal-tail configurations that may employ simple hinged-flap systems. Use of an attached-flow method is based on the premise that high levels of aerodynamic efficiency require a flow that is as nearly attached as circumstances permit. The results of this study indicate that linearized-theory, attached-flow, computer-code methods (modified to include estimated attainable leading-edge thrust and an approximate representation of vortex forces) provide a rational basis for the estimation and optimization of aerodynamic performance at subsonic speeds below the drag-rise Mach number. Generally, good prediction of aerodynamic performance, as measured by the suction parameter, can be expected for near-optimum combinations of canard or horizontal-tail incidence and leading- and trailing-edge-flap deflections at a given lift coefficient (conditions which tend to produce a predominantly attached flow).

Introduction

The linearized-theory analysis method of reference 1 provides estimates of the performance of wings at subsonic speeds; these estimates include the effects of attainable leading-edge thrust and separated leading-edge vortex flow. The method, which originally was applicable to flat wings or wings with moderate twist and camber, was modified in reference 2 to cover wings with leading- and trailing-edge flaps. Extensive comparisons of theoretical and experimental wind-tunnel data for a wide variety of wing-body configurations presented in references 3 and 4 provide evidence of the range of application of this method. Generally, good predictions of lift, drag, and pitching moment are achieved. Poor correlations are shown only for undeflected flaps at high lift coefficients and for highly deflected flaps at low lift coefficients; these conditions tend to promote severe flow detachment and poor performance.

This report describes an additional modification of the method of reference 2 to permit the handling of two separate coplanar lifting surfaces, a wing with flaps in combination with either a canard or a horizontal tail. This code differs from other more complete multisurface codes (e.g., refs. 5 to 7) in that it is structured primarily to serve the needs of preliminary-design engineers for a simple-to-use method for the rapid estimation of the longitudinal aerodynamic characteristics, including drag due to lift, of conceptual-airplane lifting-surface arrangements. In this study, as in the previous wing-alone studies, the use of what is basically an attached-flow method is justified by the premise that high levels of aerodynamic performance require a flow as nearly attached as circumstances allow. Thus, if reasonably accurate prediction of aerodynamic performance can be achieved for flap deflections and auxiliary surface incidence that result in high levels of aerodynamic efficiency, poorer correlations can be tolerated for less interesting off-design conditions. This report provides extensive correlations of theory with experimental results to illustrate the applicability and limitations of the computer-code-generated data.

Symbols

AR	aspect ratio, b^2/S
b	span, in.
C_A	axial- or chord-force coefficient
C_D	drag coefficient
ΔC_D	drag coefficient due to lift, $C_D - C_{D,0}$
$C_{D,0}$	drag coefficient at $\alpha = 0°$ for a configuration with no camber or twist, no flap deflections, and no second-surface incidence
C_L	lift coefficient
$C_{L,\alpha}$	lift-curve slope at $\alpha = 0°$, per deg
C_m	pitching-moment coefficient about moment reference center
$C_{m,cg}$	pitching-moment coefficient about assumed center of gravity
C_N	normal-force coefficient
c	local chord, in.
$\bar{c}$	mean aerodynamic chord, in.
c_L	leading-edge-flap chord, in.
c_T	trailing-edge-flap chord, in.
Exp.	experiment
i, j	index of wing-element longitudinal and lateral positions, respectively, within numerical-solution grid system (see fig. 1)
M	Mach number
R	Reynolds number based on mean aerodynamic chord
r	leading-edge radius, in.

S	reference area, in^2
S_s	suction parameter, $$\frac{C_L \tan(C_L/C_{L,\alpha}) - \Delta C_D}{C_L \tan(C_L/C_{L,\alpha} - C_L^2/(\pi \mathrm{AR})}$$
t	section thickness, in.
x, y, z	Cartesian coordinates, positive aft, starboard, and up, respectively, in.
α	angle of attack, deg
β	$= \sqrt{1 - M^2}$
δ_C	incidence of canard reference plane with respect to wing reference plane, positive with leading edge up, deg
δ_H	incidence of horizontal-tail reference plane with respect to wing reference plane, positive with leading edge up, deg
$\delta_{L,n}$	leading-edge-flap deflection angle measured normal to hinge line, positive with leading edge down (segmented flap deflection specified as inboard/outboard), deg
$\delta_{L,s}$	leading-edge-flap streamwise deflection angle, positive with leading edge down (segmented flap deflection specified as inboard/outboard), deg
$\delta_{T,n}$	trailing-edge-flap deflection angle measured normal to hinge line, positive with trailing edge down (segmented flap deflection specified as inboard/outboard), deg
$\delta_{T,s}$	trailing-edge-flap streamwise deflection angle, positive with trailing edge down (segmented flap deflection specified as inboard/outboard), deg
η	location of maximum wing-section thickness as a fraction of chord
$\Lambda_{h,L}$	leading-edge-flap hinge-line sweep angle, deg
$\Lambda_{h,T}$	trailing-edge-flap hinge-line sweep angle, deg

Theoretical Considerations and Description of Computer Code

The computer code used for the analysis of the wing-canard and wing–horizontal-tail configurations treated in this report is the result of a recent modification to a code that has already undergone several stages of development. The description of the code given here is concerned only with an outline of some essential features of the numerical method as previously developed and with a discussion of the changes necessary to accommodate a second lifting surface. For the most part, the reader is directed to specific references for details.

The original computer code described in reference 1 was applicable to a twisted and cambered wing without leading- or trailing-edge flaps. This code offers a unique approach to the theoretical analysis of wings at subsonic speeds. Among the features are linearized-theory solutions by pure iteration and the use of leading-edge singularity parameters to identify separate velocity-distribution components with and without singularities. The latter feature permits more accurate determination of theoretical leading-edge thrust distribution for wings with twist and camber and provides for improved pressure-distribution integration techniques. An empirical determination of attainable leading-edge thrust and detached vortex flow forces is also included in the estimation of overall wing performance. The influence function used, the boundary conditions imposed, and the convergence test for termination of the iteration (which have remained unchanged throughout all stages of code development) are discussed in detail in reference 1.

Extension of the original wing-alone code to permit handling of leading- and trailing-edge-flap systems is described in reference 2. The revised code provides for convenient input of flap-system geometry. This code is arranged so that, with little additional expense, solutions can be found for various combinations of leading- and trailing-edge-flap deflections. Further development of the computer code (ref. 4) provides for an improved accounting of hinge-line singularities in the determination of wing forces and moments.

The present modification of the computer code to handle two separate lifting surfaces requires a substantial increase in computation and storage, but involves no new theoretical concepts. The major changes are geometric and can be represented by lifting-surface arrangements depicted in figure 1. As in the previous applications of the code, the wing lifting surface is used to model both the actual wing and a surface representation of the fuselage. For clarity, fewer elements than usual are shown.

An array of trapezoidal elements employed in an iterative solution of linearized theory for a wing alone is depicted in figure 1(a). Only a very small number of elements are shown for the purpose of

illustration; in practice, several hundred elements would be employed. The elements are superimposed on a rectangular grid; the inboard and outboard element boundaries lie along unit values of the spanwise parameter βy, and the midspan of element leading and trailing edges lie on unit values of the chordwise parameter $x/\Delta x$. The scaling of the wing from model or airplane dimensions to program dimensions is chosen to provide the desired number of elements in the spanwise direction. The distance Δx controls the chordwise spacing of the elements; it is selected by specification of an element aspect ratio that is constant for all but the leading- and trailing-edge elements. Each element is assigned a number (fig. 1(a)), and a record is kept of the number assigned to the leading- and trailing-edge elements in each chordwise row. The indices i and j are used in determining the order of solution; elements are selected first according to advancing values of the i index and then according to advancing values of the j index. The order of solution thus marches front to rear and inboard and outboard. Because of the nonuniform chords of the code leading-edge elements, errors in the numerical solution are introduced. However, a strategy described in reference 1 provided an effective correction.

Figure 1(b) depicts the way in which the present modified code represents a typical wing-canard configuration. The inboard and outboard boundaries of the second surface are made to lie along unit values of the spanwise parameter βy. The code routine that provides for this adjustment also changes the second-surface chords to preserve the surface area (but not the aspect ratio). There may be some overlap of the canard and the wing in the region of the wing-fuselage juncture. This overlap and the change in aspect ratio introduce a small error in the numerical solution. This error and other errors associated with discretization are reduced as the number of spanwise subdivisions is increased. Second-surface elements are numbered in the same manner as those of the wing, and a code index distinguishes between the two surfaces. The order of solution still marches from front to rear and inboard to outboard and either a wing or a second-surface element is taken as its turn comes up.

The computer code has no provision for vertical displacement of the two lifting surfaces. For large vertical-separation distances, this could lead to appreciable errors, but for more moderate separations, the planar representation should be adequate. Experimental-theoretical comparisons presented in this paper help demonstrate the applicability and limitations of the method.

An additional description of the code as now amended to provide for a second lifting surface, with particular emphasis on code input and output data, is given in appendix A.

Analysis of Configuration Performance

The comparisons of theory and experiment used in this paper to explore the applicability of a linearized-theory, attached-flow method to the analysis of wing-canard and wing–horizontal-tail configurations are restricted to force and pitching-moment data. With the proper treatment, however, these data can provide much useful information for a study of the behavior of the lifting systems. The usual lift-drag polars and the data obtained by plotting C_m against C_L are supplemented with plots of axial- and normal-force coefficients versus angle of attack that allow a piece-by-piece study of the factors contributing to aerodynamic performance. Because of the flat or nearly flat wing surfaces (in the absence of flap deflection) of most of the configurations in this study, it is possible to isolate to a large degree the separate contributions of leading- and trailing-edge flaps to the aerodynamic performance. (See ref. 3.)

Data from a variety of experimental programs have been used in this analysis. Wing leading-edge sweep angles vary from $-20°$ to $71°$, Mach numbers from 0.09 to 0.9 are considered, and Reynolds numbers (based on $\bar{c}$) range from 1.35 to 4.19×10^6. The test conditions and sketches of the wing-body planforms are given in each of the correlation figures.

Notes on application of the code to the specific configurations and test conditions included in this study are given in appendix B. Sample code input data for the configurations studied are given in table I. Code representation of the lifting-surface planform for selected configurations is shown in figure 2. To avoid instabilities in the numerical solution, it is necessary to provide an adjustment so that all elements have inboard and outboard boundaries corresponding to unit values of the βy parameter. This adjustment sometimes brings about a change in wing planform that is most evident in figure 2(d). It also generally requires a lateral relocation of the second surface. (See figs. 2(a) and 2(b).) The code routine that provides the necessary relocation also provides an adjustment to preserve the surface area. Leading- and trailing-edge-flap surfaces are also adjusted to meet the boundary condition and preserve the area. This last adjustment is most evident in figure 2(e). The net effect of these adjustments on the numerical solution can be judged only by results. Comparisons of code results with changes in modeling similar to those shown indicate only a small change in computed aerodynamic characteristics. The comparisons of theory with experimental data given in this report also indicate that the errors are not substantial.

3

In the basic aerodynamic data figures, data for an attached-flow computer-code solution that includes no leading-edge thrust forces and no separated leading-edge vortex forces are shown by the short-dash lines. Solutions which include attainable thrust and the effects of a separated vortex whose strength is determined by the Polhamus leading-edge suction analogy (ref. 8) are shown by the long-dash-short-dash line. For reference, drag upper and lower bounds are also shown. The theoretical lower bound $\left[C_{D,0} + C_L^2/(\pi \text{AR})\right]$ is the drag for a wing with an elliptical span-load distribution and a uniform downwash. A theoretical upper bound shown on the figures $\left[C_{D,0} + C_L \tan(C_L/C_{L,\alpha})\right]$ is the drag for a flat wing with no leading-edge thrust and no vortex forces. The zero-lift drag $C_{D,0}$ was obtained from experimental data for a flat configuration (an uncambered wing-body configuration with undeflected flaps at $\alpha = 0°$ in combination with a second surface at zero incidence).

Unswept Wing Canard

As previously mentioned, the computer code used in generating theoretical data for the correlations presented in this paper has no provision for vertical displacement of the two lifting surfaces. Experimental-theoretical comparisons presented in this paper help to assess the effect of vertical separation and to demonstrate the applicability and limitations of the method. The first such comparison (fig. 3) shows data from reference 9 for a wing-canard configuration with three different vertical-separation distances. Both the wing and the canard had rectangular planforms and employed a relatively thick airfoil section (13 percent) with appreciable camber. The canard had an incidence angle of 2° relative to the wing surface. Because data presented in the reference are intended to represent a wing-canard arrangement only, a tare composed of forces measured by the support apparatus with the wing and canard removed was subtracted from all the data. The data presented in reference 9 were not corrected for the wind-tunnel wall effect. The drag data presented here have been corrected to remove that effect by using information from reference 9.

As shown in the three parts of figure 3, canard vertical position has an appreciable effect on the lift-drag relationship only for lift coefficients in excess of 1.4. For lift coefficients in the range of about 0.4 to 1.2, excellent aerodynamic performance (drag values close to the lower bound) is achieved. There is, in general, a very good theoretical prediction of this performance. At higher lift coefficients, there is evidence of flow separation which is influenced by the

canard location and which the theory is incapable of predicting. The theory gives a poor account of the moment characteristics. However, a part of the discrepancy may be caused by a measured moment that is influenced by support-apparatus interference. Reference 9 is not clear on this point.

An interesting characteristic of the code-predicted results is the presence of some amount of attainable thrust at all angles of attack, as indicated by the complete separation of the theoretical axial-force curves with and without thrust. This thrust comes about because of the camber of the two surfaces and the 2° incidence of the canard. Although the thrust of one surface may be nearly zero at some angle of attack, the other surface at this same condition produces thrust.

The theory indicates that the wing and canard camber, in combination with the relatively thick airfoil section, provides a high level of attainable thrust, equal to full theoretical thrust up to an angle of attack of about 6° or a lift coefficient of about 1.1. The experimental data indicate that full theoretical thrust is nearly achieved over an even larger range.

60°-Swept Trapezoidal-Wing Fighter With Canard

Additional data relative to the effect of canard height on aerodynamic performance (fig. 4) for a 60°-swept trapezoidal-wing fighter measured at $M = 0.70$ and $R = 1.35 \times 10^6$ was obtained from reference 10. In contrast with the previous configuration, these lifting surfaces were uncambered and were relatively thin with circular-arc sections; therefore, high levels of performance are not expected.

Data in figure 4(a) for a midfuselage canard location indicate the presence of a small but significant amount of leading-edge thrust (the curvature in the plot of C_A versus α near $\alpha = 0°$) as well as a small separated leading-edge vortex force (the change in curvature in the plot of C_A versus α and the increased slope of the plot of C_N versus α near $\alpha = 6°$). Predicted results that account for an assumed constant leading-edge radius of 0.002 in. for the circular-arc wing sections provide a good estimate of both effects. Reasonably good predictions of the lift-drag polar curve and the pitching moment are also noted. For the low canard position in figure 4(b), there is little change in the experimental data (the theoretical data are, of course, identical), and the correlation remains good. For the high canard position in figure 4(c), there is a greater discrepancy between theory and experiment, but the overall correlation is still reasonable. Thus, data for this and the previous configuration indicate that the

theoretical method can be applicable to two lifting-surface systems with moderate vertical-separation distances.

44°-Swept Trapezoidal-Wing Fighter With Canard

Reference 11 provides data shown in figure 5 for a generic fighter configuration tested in the Langley 7- by 10-Foot High-Speed Tunnel at $M = 0.4$ and $R = 1.9 \times 10^6$. A matrix of canard and flap deflections is covered by the measured data. The matrix is not complete, but there are sufficient data for specified leading- and trailing-edge-flap deflections with specified canard incidence angles to provide a test of code prediction capabilities for reasonably efficient arrangements. In reference 4 it was shown that, in the absence of moment restraints, near-maximum performance for the wing alone was achieved with equal leading- and trailing-edge-flap deflections measured normal to the flap hinge line. Figure 5 presents data for such matched deflection angles ($\delta_{L,n}$ and $\delta_{T,n} = 0°, 12°$, and $20°$) with selected canard-incidence angles.

In this section, comparisons of these data with theoretical results (figs. 5 to 8) provide a test of the ability of the theory to predict performance and identify optimized arrangements within this limited family. A subsequent section of this report (Examples of Configuration Optimization) illustrates an optimization process using theoretical data alone in which leading-edge-flap deflection, trailing-edge-flap deflection, and canard or horizontal-tail incidence may be varied independently.

Figure 5(a) shows data for undeflected flaps and a canard at $\delta_C = 0°$. There is evidence of an appreciable amount of leading-edge thrust and a small vortex force. There is a good theoretical prediction of the measured results. As shown in figures 5(b) and 5(c), a negative incidence of the canard affects axial force in much the same way that leading-edge flap deflection does. The slope of the curve and the negative C_A values can offer performance improvements. The remaining parts of figure 5 treat deflected flaps in combination with canard incidence. Changes in aerodynamic forces and moments due to flap deflection follow much the same pattern as for the wing-alone situation in reference 4. In general, the theory provides a good estimate of the force-and-moment characteristics. Correlation is best for negative incidence angles which offer reduced drag. Correlation is poorest for $\delta_C = 10°$ for which the theory predicts an axial force at high angles of attack much larger than that measured. Canard flow separation is probably responsible for the less-than-anticipated performance penalty.

Suction-parameter data for the flap-deflection and canard incidence combinations of figure 5 are given in figure 6. Experimental and theoretical suction parameters are shown as a function of lift coefficient. Generally, there is good agreement between theory and experiment for deflection and incidence combinations which result in high suction-parameter levels. The primary purpose of these data is their use in the following figures to determine as accurately as possible the maximum aerodynamic efficiency of the flap-canard system and the flap deflection and canard incidence combinations required. This information is helpful in assessing the applicability of linearized-theory, attached-flow methods to the analysis of flap-canard systems operating at or near maximum efficiency.

Suction parameters evaluated from experimental data are shown as functions of the matched leading- and trailing-edge-flap deflection angle for three canard incidence angles and for four lift coefficients at the top of figure 7. At the bottom of the figure, the same data are shown as functions of the canard deflection angles. The data represented by the symbols were obtained from fairings of the experimental data of figure 6. The fairing of the data points in figure 7 is intended to represent as accurately as possible the variation of suction parameter with deflection angles and canard incidence. An attempt was made to have the curves bear a "family" resemblance to each other and to display changes in a progressive manner.

The dashed curves in figure 7 represent an envelope; the maximum suction parameter obtainable with the optimum value of δ_C is shown in the upper plots, and the maximum suction parameter obtainable with the optimum value of $\delta_{L,n}$ and $\delta_{T,n}$ is shown in the bottom plots. The points to generate these curves were obtained by referring to both the top and bottom plots for a given lift coefficient. For example, the maximum value of suction parameter for a given leading- and trailing-edge-flap deflection curve from the bottom plot is entered in the top plot at the designated leading- and trailing-edge-flap deflection angle. This procedure always gives a point equal to or greater than the points representing the faired experimental data from figure 6. An additional check on the generation of the envelope curves is that the maximum suction parameter of each of the pairs of curves must be identical—there can be only one peak. The completed fairings provide data that describe the maximum suction parameter and the corresponding optimum leading- and trailing-edge deflection angles and canard incidence angles (the arrows) as a function of the lift coefficient.

Envelope data from the dashed curves of figure 7 and similar data for theoretical results (not

5

presented) are shown in figure 8. Optimum matched leading- and trailing-edge-flap deflection angles, optimum canard incidence angle, and maximum suction parameter for this limited family are shown as a function of lift coefficient. The theory with attainable thrust and vortex force estimates gives a good prediction of the maximum suction parameter and the required deflection and incidence angles. In the absence of any moment considerations, the optimum canard incidence results in a surface that is nearly aligned with the free stream and produces little or no lift. Apparently, the downwash-upwash field produced by a lifting canard has an unfavorable effect on the leading-edge-flap loadings responsible for the flap performance benefits. In the section "Examples of Configuration Optimization," the problem of selecting optimum angles when leading-edge-flap deflection, trailing-edge-flap deflection, and canard incidence may be varied independently is addressed. Solutions subject to moment constraints, as well as fully optimized solutions, are considered.

An examination of figure 8 in conjunction with a reexamination of figure 5 shows that a good correlation of theory and experiment is obtained for flap and canard settings that result in near-maximum performance for the lift-coefficient range of interest. Poorer but still acceptable correlation is displayed for settings far from the optimum. If canard-generated lift is required to provide airplane trim, these data indicate that the code can provide a reasonable estimate of trim drag penalties.

Figure 9 provides data similar to those of figure 5, but for a Mach number of 0.8. Data for the code prediction without attainable thrust and vortex forces, as well as the theoretical bounds, are omitted because the primary purpose here is to assess the effect of Mach number on the experimental-theoretical correlation. It is not surprising that the correlation of theory and experiment at this higher Mach number is somewhat poorer. For undeflected flaps and a canard incidence of zero, there is a breakaway in axial force for the experimental data (probably caused by shock development) above an angle of attack of about 8° or above a lift coefficient of about 0.5. When the flap deflections are increased to 20° with a canard incidence of −10°, there is evidence of trailing-edge-flap flow separation (failure to develop the predicted C_N increment) and shock effects, and the overall correlation is relatively poor.

44°-Swept Trapezoidal-Wing Fighter With Horizontal Tail

The 44°-swept-wing fighter of reference 11 was also tested with a horizontal tail instead of the canard. Figure 10 presents data for matched leading-and trailing-edge-flap deflection angles ($\delta_{L,n} = \delta_{T,n} = 0°, 12°$, and 20°) with selected horizontal-tail incidence angles. In figure 10(a), for undeflected surfaces, there is evidence of a significant attainable thrust contribution to axial force, as was the case for the canard configuration. However, there is little evidence of the predicted vortex-force contribution to normal force. A similar failure of the predicted vortex force to materialize for a 45°-swept delta wing was noted in reference 12. A reasonable prediction of drag is obtained only for lift coefficients below about 0.5 for all the data with undeflected flaps (figs. 10(a) to 10(c)). There is also a significant discrepancy between experimental and theoretical pitching-moment coefficient for the higher lift coefficients. Similar discrepancies occurred for this configuration with undeflected flaps and without a canard or a horizontal tail. (See ref. 4.) For the 12° and 20° deflection of both flaps in the remaining parts of figure 10 (figs. 10(d) to 10(i)), there is generally a better prediction of drag at the higher lift coefficients. For $\delta_H = 0°$ and $\delta_H = 10°$, which produce relatively good performance, the correlation is reasonably good. The greatest discrepancy between theory and experiment is for $\delta_H = -10°$, an incidence angle which produces poor performance. However, the measured drag penalty is less than that predicted. For these deflected-flap cases, there is also reasonable agreement between the level of theoretical and experimental pitching moment for horizontal-tail deflections that produce good performance. The derivative dC_m/dC_L, however, is not well predicted, because the vortex contribution is overestimated.

Suction-parameter data for all the combinations of flap deflection and horizontal-tail incidence covered in figure 10 are shown as functions of lift coefficient in figure 11. Figure 12 shows suction parameter as a function of matched leading- and trailing-edge-flap deflection angle and horizontal-tail incidence angle for each of four selected lift coefficients. This figure is similar to figure 7 for the previous canard configuration. A detailed description of the generation of these plots and their use is given in the preceding section.

Envelope data from figure 12 and similar data from theoretical results (not presented) are shown in figure 13. Optimum matched leading- and trailing-edge-flap deflection angles, optimum horizontal-tail incidence angles, and the maximum suction parameter are plotted as functions of lift coefficient. The theoretical data with attainable thrust and vortex forces included provide a good estimate of the maximum suction parameter and the required deflection and incidence angles. In the section "Examples of Configuration Optimization," the

problem of selecting optimum angles when leading-edge-flap deflection, trailing-edge-flap deflection, and horizontal-tail incidence may be varied independently is addressed.

An examination of figure 13 in conjunction with a reexamination of figure 10 shows that a reasonably good correlation of theory and experiment is obtained for flap and horizontal-tail settings that result in near-maximum performance for the lift-coefficient range of interest. Poor correlation is displayed for settings far from the optimum. These discrepancies for the horizontal-tail configuration are much larger than those for the canard configuration and present a problem if negative horizontal-tail incidence angles are required to trim the airplane. One saving feature is that the code provides a reasonable estimate of the pitching-moment change due to a change in horizontal-tail incidence and provides a conservative estimate of trim drag penalties.

Figure 14 provides data similar to those of figure 10, but for a Mach number of 0.8. Data for the prediction without attainable thrust and vortex forces, as well as the theoretical bounds, are omitted, because the primary purpose here is to assess the effect of Mach number on the experimental-theoretical correlation. It is not surprising that the correlation of theory and experiment at this higher Mach number is poorer. For undeflected flaps and a horizontal-tail incidence of zero, there is a breakaway in axial force for the experimental data (probably caused by shock development) above an angle of attack of about 6° or a lift coefficient of about 0.4. With the flap deflections increased to 20° with a horizontal-tail incidence of 10°, there is evidence of trailing-edge-flap flow separation (failure to achieve the predicted C_N increment) as well as shock effects, and the overall correlation is relatively poor.

60°-Swept Delta-Wing Fighter With Canard

Reference 11, which provided data for the previous two configurations, also provides data for a 60°-swept delta-wing fighter tested in the Langley 7- by 10-Foot High-Speed Tunnel at $M = 0.4$ and $R = 2.4 \times 10^6$. Figure 15 presents data for matched leading- and trailing-edge-flap deflection angles ($\delta_{L,n} = \delta_{T,n} = 0°$, 10°, and 20°) with selected canard incidence angles. As in the case of the 44°-swept trapezoidal-wing–canard configuration, the theory generally provides a reasonably good estimate of the force-and-moment characteristics. Again, correlation is best for negative incidence angles because they offer reduced drag.

Suction-parameter data for all the flap-deflection–canard incidence combinations in figure 15 are shown as functions of lift coefficient in figure 16. Figure 17

shows suction parameter as a function of matched leading- and trailing-edge-flap deflection angles and canard-incidence angles for each of four selected lift coefficients. This figure is similar to figure 7 for the previous canard configuration. A detailed description of the generation of these plots and their use is given in the preceding section.

Envelope data from figure 17 and similar data from theoretical results (not presented) are shown in figure 18. Optimum matched leading- and trailing-edge deflection angles, optimum canard incidence angles, and the maximum suction parameter are plotted as functions of lift coefficient. The theoretical data with attainable thrust and vortex forces included provide a reasonably good estimate of the maximum suction parameter and the required deflection and incidence angles. As for the 44°-swept trapezoidal-wing-canard configuration, the optimum canard incidence in the absence of moment restraints results in a surface that is nearly aligned with the free stream.

Figure 19 provides data similar to those of figure 15, but for a Mach number of 0.8. There is some deterioration in the ability of the theory to predict the aerodynamic characteristics at this higher Mach number, but not as much as for the 44°-swept trapezoidal-wing configuration. The higher sweep angle probably delays the onset of shock-induced separation.

60°-Swept Delta-Wing Fighter With Horizontal Tail

Data for the 60°-swept delta-wing fighter with a horizontal tail (ref. 11) are shown in figure 20. The theory generally provides a better prediction of measured characteristics than it did for the 44°-swept horizontal-tail configuration. Again, however, there is some deterioration in the prediction ability of the theory for conditions which produce poor aerodynamic efficiency.

Figures 21 to 23 are similar to figures 11 to 13 for the 44°-swept trapezoidal-wing fighter with horizontal tail and again provide data for the determination of optimum flap and horizontal-tail settings and the maximum suction parameter.

An examination of figure 23 in conjunction with a reexamination of figure 20 shows that, as for the previous configurations, a reasonably good correlation of theory and experiment is obtained for flap and horizontal-tail settings that result in near-maximum performance for the lift-coefficient range of interest. Poorer correlation is displayed for settings far from the optimum.

Figure 24 provides data similar to those of figure 20, but for a Mach number of 0.8. There again is some deterioration in the ability of the theory to

predict the aerodynamic characteristics at this higher Mach number.

Forward-Swept-Wing Fighter With Canard

Figure 25 presents data for a fighter configuration with a forward-swept wing, employing twist and camber, and a canard surface. The data taken from reference 13 were measured in the Langley 16-Foot Transonic Tunnel at $M = 0.6$ and $R = 2.5 \times 10^6$. Data for undeflected flaps and for a canard at $\delta_C = 0°$ (fig. 25(a)) show good agreement between theory and measured results for lift coefficients up to about 1.0. The wing apparently has a highly efficient camber surface as evidenced by the close approach of measured drag to the theoretical lower limit for $C_L \approx 0.4$ to $C_L \approx 0.8$. The canard incidence angle of 10° in figure 25(b) causes a severe loss in aerodynamic efficiency, depicted by the departure from the minimum curve, which is predicted by the theory. As shown in figure 25(c), a canard incidence angle of $-10°$ offers good performance, which equates to suction parameters of 0.9 or greater, for $C_L \approx 0.5$ to $C_L \approx 0.8$. Figures 25(d) to 25(f) form a series in which the leading-edge-flap deflection varies while the trailing-edge-flap deflection remains fixed at 10° and the canard remains fixed at $\delta_C = 0°$. The pitching moment is poorly predicted, especially at the lower lift coefficients. The prediction of lift and drag, however, is excellent in all three of the figures for $C_L = 0.4$ to $C_L = 1.2$.

Figure 26 demonstrates the ability of the theory to predict the variation of drag with changes in canard incidence for each of four selected lift coefficients. These data for undeflected flaps were obtained from figures 25(a), 25(b), and 25(c). As might be expected, the optimum canard incidence angle (δ_C for a minimized drag coefficient) becomes more negative with increasing lift coefficient. For $C_L = 0.8$, the optimum canard incidence is close to $-10°$. As shown in figure 25(c), a lift coefficient of 0.8 requires an angle of attack of about 9°. The result is that, as before, the canard at optimum incidence is nearly aligned with the free stream and produces little or no lift. Optimum canard incidence angle is discussed further in the section "Examples of Configuration Optimization."

The ability of the theory to predict aerodynamic performance at high Mach numbers is shown in figure 27. These data apply only to undeflected flaps and a canard at $\delta_C = 0°$. A comparison of figure 27(a) with 25(a) shows that there is only a small deterioration in the code prediction at $M = 0.8$. At $M = 0.9$, however, appreciable discrepancies appear at $C_L \approx 0.8$, and the correlation becomes progressively poorer as C_L increases. The code is obviously not applicable to transonic speeds, which are above the drag-rise Mach number.

Arrow-Wing Supersonic Transport

The application of the computer code to a highly swept arrow-wing supersonic transport with a horizontal tail may be examined with the aid of figure 28. Experimental results for this configuration were obtained from reference 14. The wing is twisted and cambered for supersonic cruise at a Mach number of 2.2 (wing W_2 of ref. 15) and is equipped with leading- and trailing-edge flaps. The leading-edge flap is full span and is broken into six segments. The trailing-edge-flap system is composed of inboard and outboard segments of single-slotted flaps (ref. 14). The tests were run in the Langley 30- by 60-Foot Tunnel at $M = 0.09$ and $R = 4.19 \times 10^6$ (based on $\bar{c}$).

The deflections of the horizontal tail and the flaps in reference 14 were not sufficient to determine optimum settings. However, sufficient configurations were tested to determine the accuracy of the code and to examine some trends.

Figures 28(a) to 28(f) show results for zero flap deflections. Figure 28(a) shows data with the tail and nacelles removed, and the other figures show data for various tail incidence angles. The theory gives a good prediction of the force data for each of the configurations shown. The most accurate prediction of the drag at the higher lift coefficients occurs with the tail off and with tail incidence set to 0° or 5°. These configurations also produce the best performance (lowest drag) and the smallest pitching moment for a typical low-speed lift coefficient of 0.6. The axial-force calculations show the effect of the attainable leading-edge thrust, and the normal-force calculations show the effect of the vortex force. The mildness of the wing twist and camber is shown by the slight slope in the axial force without attainable leading-edge thrust and vortex force that results from distributed thrust on the wing camber surface.

Significant discrepancies between theory and experiment occur in the pitching moment for some conditions. The theory provides for a reasonably good estimate of the pitching moment with the tail off and with it set to 0° or 5°. These are the configurations that produced the lowest drag. For the negative tail incidence angles, the moment is well predicted at low positive lift coefficients.

Figures 28(g) to 28(i) show results with the leading- and trailing-edge flaps deflected and with three tail deflections. Although the theory does not model the flow through the trailing-edge-flap slot, the theory gives a reasonably good prediction of the lift

and drag characteristics. The most accurate prediction of the drag at the higher lift coefficients corresponds to conditions for which the measured drag comes closest to the lower bound ($C_L = 0.4$ to 0.6). The prediction also tends to be better for $\delta_H = 0°$. The prediction of the pitching moment is also best where the drag comes closest to the minimum curve.

The normal-force results indicate that a significant vortex did not develop in the experiment. The axial-force results indicate that the experimental data have more leading-edge thrust at the higher angles of attack than is predicted by the theory. These effects tend to counteract each other, so that the lift and drag prediction is good.

Results for the drag and pitching moment at several lift coefficients are summarized in figures 29 and 30 as a function of tail incidence. These figures show, for example, that at $C_L = 0.2$, where lower drag occurs with the flaps undeflected, the best correlation between theory and experiment for the pitching moment also occurs with the flaps undeflected. At $C_L = 0.4$ and 0.6, where flap deflection reduces drag, the best correlation for pitching moment occurs with the flaps deflected.

Examples of Configuration Optimization

The experimental data used in the preceding section of this paper for configuration performance optimization were limited. The search for optimum arrangements was restricted to a special case in which leading- and trailing-edge-flap deflections measured normal to the hinge line were equal ($\delta_{L,n} = \delta_{T,n}$). The theory, however, has no such restrictions and permits an optimization process in which leading-edge-flap deflection, trailing-edge-flap deflection, and canard or horizontal-tail incidence angle may be varied independently. Performance contour maps serve as the basis of a graphical optimization process. The procedures that may be employed are discussed for two examples, one with a canard and one with a horizontal tail.

44°-Swept Trapezoidal-Wing Fighter With Canard

Figure 31 is a comparison of theoretical and experimental performance contour maps for the limited family of flap and canard deflections previously discussed. This figure is simply another form of the data presented in figure 5. The maps show contour lines of equal suction parameter (the solid lines) and contour lines of equal moment coefficient (the dashed lines) for a representative lift coefficient of 0.6. The theory shows a reasonable ability to represent the experimental data in the peak performance

region. There is a fairly broad range of angles over which near-maximum performance may be achieved; thus, precise definition of the required angles is not necessary.

The performance contour maps of figure 32 show how independent variation of leading-edge-flap deflection, trailing-edge-flap deflection, and canard incidence angle may be considered in an optimization study. The data were generated by a series of computer entries as follows:

1. $\delta_{L,n} = 10°$; $\delta_{T,n} = 10°$; $\delta_C = 0°, 10°, -10°$

2. $\delta_{L,n} = 10°$; $\delta_{T,n} = 20°$; $\delta_C = 0°, 10°, -10°$

3. $\delta_{L,n} = 20°$; $\delta_{T,n} = 10°$; $\delta_C = 0°, 10°, -10°$

4. $\delta_{L,n} = 20°$; $\delta_{T,n} = 20°$; $\delta_C = 0°, 10°, -10°$

These input data sets also provided results for combinations of leading- and trailing-edge deflections in which one or both of the deflections is zero through the use of TXMLEFD and TXMTEFD factors described in appendix A. Data for the three canard incidence angles were obtained in one computer entry by use of the successive-run provision described in appendix A. The matrix of nine points used in the generation of the contour maps provides a general, but not detailed, description of the variation of suction parameter with changes in flap deflection angles. That matrix, however, permits a sufficiently accurate representation for illustration purposes.

Figure 33 uses data obtained from figure 32 to show the variation of suction parameter with leading-edge-flap deflection angle, subject to a restraint of $C_m = 0°$. The variations of the required trailing-edge-flap deflection angle and the canard incidence angle are also shown. A peak suction parameter of about 0.82 is obtained for a trailing-edge-flap deflection of about $3°$, a canard incidence of about $-7°$, and a leading-edge-flap deflection of about $17°$. These data and similar data for plots with other moment restraints (not shown) were used in derivation of the curves shown in figure 34. In this figure, maximum suction parameter is shown as a function of the imposed moment restraint. The required flap deflection angles and the required canard incidence angle are also shown. There is a substantial variation in aerodynamic performance over the range of moment coefficients shown. A peak suction parameter of about 0.91 is obtained for a moment coefficient of about -0.09. The required leading-edge-flap deflection is about $15°$, the trailing-edge-flap deflection is about $11°$, and the canard incidence angle is about $-9°$. This peak performance is very close to that

achieved by the wing-alone configuration analyzed in reference 4. The flap deflection angles required for optimization are also very close to those required for the wing-along configuration. Sketch A depicts the optimized-configuration mean-camber surface. At the angle of attack ($\approx 7.5°$) required to generate a lift coefficient of 0.6, the optimum canard incidence angle results in a surface nearly aligned with the free-stream flow so as to produce only a small amount of lift (in this case, slightly negative). The optimum canard setting apparently alters the flow about an optimized wing-alone configuration to a very small degree. In these circumstances, the near equivalence of the drag-due-to-lift performance of the optimized wing-canard configuration and the wing-alone configuration is not surprising.
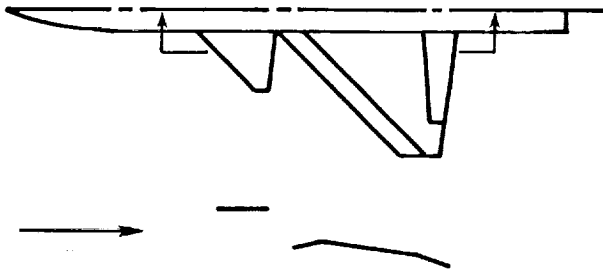
Sketch A

The curves of figure 34 show that preservation of maximum performance over a range of moment coefficients requires large changes in trailing-edge-flap deflection but only small changes in the canard incidence angle. An examination of tabulated code theoretical data (not presented here) shows that the change in trailing-edge-flap deflection from 13° to −3° is responsible for about 85 percent of the change in moment coefficient from −0.12 to 0.08. There are no experimental data to validate the theoretical prediction of the variation of lifting efficiency S_s with pitching moment for these theoretically optimized arrangements. Sketch B gives some indication of the degree of correlation that might be expected. This correlation is for the previous limited set of experimental data ($\delta_{L,n} = \delta_{T,n}$) for this same configuration presented in figure 31. Because the optimized arrangements, wherein leading- and trailing-edge flaps are free to vary independently, should be more efficient, the correlation should be somewhat better than that shown in sketch B.

The small contribution of the canard to the forces generated by an optimized configuration may be explained by the following arguments. A canard
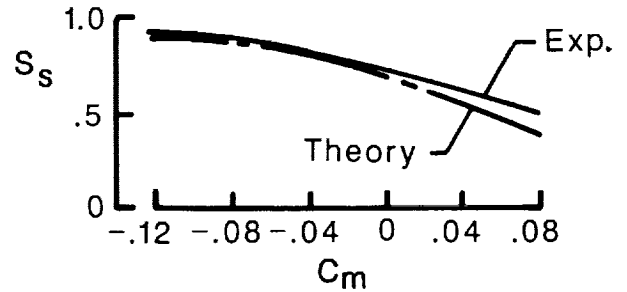
Sketch B

inclined at a positive angle with respect to the free stream so as to produce a lifting force also produces a downwash along the wing leading edge behind the canard. This downwash reduces the thrust force created by the deflected leading-edge flap, and some of the flap benefits are lost. Upwash acting on the wing leading edge outboard of the canard tips is not strong enough to counteract the unfavorable effect.

A canard inclined at a negative angle with respect to the free stream could, in the presence of a strong upwash field, produce a favorable thrust force, as does a leading-edge flap; but the wing-generated upwash field ahead of the wing in the vicinity of the canard is too weak to produce a significant benefit. Perhaps a more efficient arrangement for a lifting canard configuration would employ segmented wing leading-edge flaps with different deflections inboard and outboard of the canard. The wing-design program described in reference 4 provides a capability for the design of flap surfaces in the presence of interference flow fields and can be used to explore these possibilities.

44°-Swept Trapezoidal-Wing Fighter With Horizontal Tail

Figure 35 is a comparison of theoretical and experimental performance contour maps for the previously treated limited family of flap deflections for the horizontal-tail configuration. The lift coefficient for configuration optimization is again selected as 0.6. As for the canard configuration, the theory shows a reasonable ability to represent the experimental data in the peak performance region.

Figure 36 presents contour maps for the horizontal-tail configuration that allow independent variation of leading-edge-flap deflection, trailing-edge-flap deflection, and horizontal-tail incidence. These maps were generated in a manner similar to that for the previously described maps in figure 32.

Figure 37 uses data derived from figure 36 to show the variation of maximum suction parameter with leading-edge-flap deflection angle subject to a

restraint of $C_m = 0°$. The required trailing-edge-flap deflection angle and the horizontal-tail incidence angle are also shown. A peak suction parameter of about 0.82 is obtained for a trailing-edge-flap deflection of about 5°, a horizontal-tail deflection angle of about −2°, and a leading-edge-flap deflection of about 16°. These data and similar data for plots with other moment restraints (not shown) were used in the derivation of the curves shown in figure 38. In this figure, which is similar to figure 34 for the canard configuration, maximum suction parameter is shown as a function of the imposed moment restraint. A peak suction parameter of about 0.91 is obtained for a moment coefficient of about −0.09. The required leading-edge-flap deflection is about 15°, the trailing-edge-flap deflection is about 10°, and the horizontal-tail incidence angle is about 4°. This performance level is very close to that achieved for the canard configuration (fig. 34) and for the wing-alone configuration (ref. 4). The required flap deflection angles are also similar. Sketch C shows the mean-camber surface of the optimized arrangement. The trailing-edge-flap deflection provides a benefit by reducing the angle of attack for a given lift coefficient. The horizontal-tail deflection serves the same purpose.
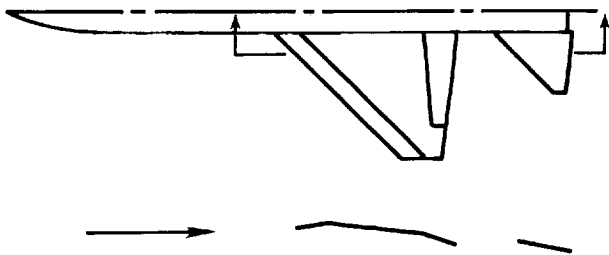
Sketch C

The curves of figure 38 show that preservation of maximum performance over a range of moment coefficients requires large changes in the horizontal-tail incidence angle and moderate changes in the trailing-edge-flap deflection. Theoretical estimates show that the change in horizontal-tail incidence angle from 6° to −8° is responsible for 95 percent of the change in moment coefficient from −0.12 to 0.08. Sketch D gives some indication of the ability of the theory to predict the variation of lifting efficiency S_s with pitching moment for these theoretically optimized arrangements. The correlation of sketch D is for the previous limited set of experimental data $(\delta_{L,n} = \delta_{T,n})$ for the same configuration presented in figure 35. Because the optimized arrangements, wherein both leading- and trailing-edge flaps are free

to vary independently, should be more efficient, the correlation for that case should be better than that shown in sketch D.
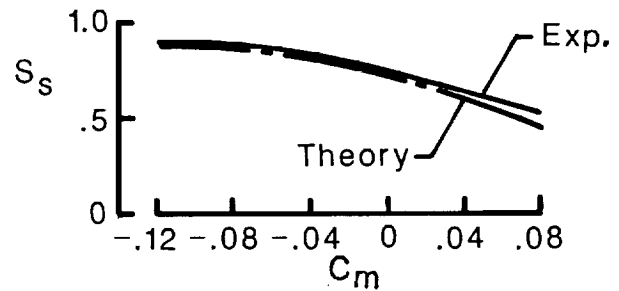
Sketch D

Comparison of Canard and Horizontal-Tail Configurations

In the absence of moment constraints, the canard and horizontal-tail configurations for the 44°-swept trapezoidal wing offered comparable performance. In both cases, a peak suction parameter of about 0.91 was obtained for a moment coefficient of about −0.09. There is, however, a significant variation of aerodynamic performance with C_m, and $C_m = −0.09$ may be far from that required to trim the configurations with a realistic center-of-gravity location and a practical stability level. Figure 39 is a comparison of the aerodynamic performance of the canard configuration with that of the horizontal-tail configurations at equal stability levels. The suction parameters shown here were obtained from figures 34 and 38 using the relationship

$$C_m = \left(SM + \frac{dC_m}{dC_L}\right) C_L \quad \text{where } SM = -\frac{dC_{m,cg}}{dC_L}$$

where dC_m/dC_L is the moment derivative given by the code at $C_L = 0$ for the wing without flap deflections and with no incidence of the second surface. For this example, $dC_m/dC_L = 0.164$ for the canard, and $dC_m/dC_L = −0.048$ for the horizontal tail. Actual values of these derivatives at the optimized settings for $C_L = 0.6$ and at the specified flap and second-surface settings are only slightly different. The derivatives listed above agree with the experimental data for near-optimum settings (as close as the data provides) better than the full theory, which includes a vortex contribution that apparently does not fully materialize. For comparison purposes, figure 39 also shows similar data for a wing-fuselage configuration (ref. 4).

Figure 39 indicates that the canard configuration can be competitive with the horizontal-tail configuration in aerodynamic efficiency only if it can be flown in a statically unstable mode. However, the point to be made from this example does not concern the relative merits of the two configurations, but rather the usefulness of the computer code in the conduct of preliminary design trade-off studies.

The other configurations treated in this report were not subjected to the same detailed theoretical analysis. However, an inspection of the available data indicates that, for the most part, the observations made for the 44°-swept trapezoidal-wing fighter are supported, and are in no case contradicted. In general, an optimized canard configuration with no applied moment restraints has a canard that generates little or no lift with a surface nearly aligned with the free stream. When trim moment restraints are applied, most of the moment increment (from the unrestrained solution) will be supplied by trailing-edge flaps rather than the canard. An optimized horizontal-tail configuration with no applied moment restraints will have a horizontal tail that generates appreciable lift. When trim moment restraints are applied, most of the moment increment will be supplied by a change in horizontal-tail incidence. For both the canard and horizontal tail in the absence of moment restraints, suction parameters about the same as those for the corresponding wing-alone configuration can be achieved for a properly optimized combination of flap deflections and canard or horizontal-tail incidence angles. Also, the optimum leading- and trailing-edge-flap deflections are not much different from those of the wing-alone configuration.

Conclusions

An analysis of the subsonic aerodynamic performance of wing-canard and wing–horizontal-tail configurations which may employ wing leading- and trailing-edge flaps has led to the following conclusions:

1. Linearized-theory, attached-flow, computer-code methods (with estimated attainable leading-edge thrust and an approximate representation of vortex forces) provide a rational basis for the estimation and optimization of aerodynamic performance at subsonic speeds below the drag-rise Mach number.

2. Optimization of aerodynamic performance requires specified flap and canard or horizontal-tail settings which can be predicted with reasonable accuracy by numerical methods. Near-maximum performance, however, can be achieved over a fairly broad range of deflection and incidence angles.

3. Generally, good prediction of aerodynamic performance, as measured by the suction parameter, and reasonably good prediction of pitching moment can be expected for near-optimum combinations of canard or horizontal-tail incidence angle and leading- and trailing-edge-flap deflection at a given lift coefficient; these conditions tend to produce a predominantly attached flow.

4. For canard configurations, maximum performance in the absence of pitching-moment restraints is achieved with a canard that is nearly aligned with the free stream and produces little or no lift. When pitching-moment restraints are applied, the most efficient arrangements call for most of the moment increment to be supplied by the wing trailing-edge flap rather than by the canard.

5. For horizontal-tail configurations, maximum performance in the absence of pitching-moment restraints is achieved with a positive horizontal-tail incidence angle that produces a significant amount of lift. When pitching-moment restraints are applied, the most efficient arrangements call for most of the moment increment to be supplied by the horizontal tail rather than by the wing flaps.

6. For both canard and horizontal-tail configurations in the absence of moment restraints, suction parameters about the same as those for the corresponding wing-alone configuration can be achieved for a properly optimized combination of flap deflections and canard or horizontal-tail incidence angles. Also, the optimum leading- and trailing-edge-flap deflections are not much different from those of the wing-alone configuration. These settings are a good starting point in the search for optimized canard or horizontal-tail configurations, even if pitching-moment restraints are applied.

Performance degradation brought about by low Reynolds numbers and high Mach numbers was not investigated in this study. The conclusions are thus restricted to Mach numbers below the drag rise and Reynolds numbers sufficiently high to avoid drastic flow separation at or near design conditions.

Appendix A

Code Input and Output Data

The computer code

> AERO2S - Subsonic Aerodynamic
> Analysis of Wings With Leading-
> and Trailing-Edge Flaps in
> Combination With Canard
> or Horizontal Tail Surfaces

used in this paper for the analysis of wing-canard and wing–horizontal-tail combinations that may employ wing leading- and trailing-edge flaps may be obtained for a fee from:

> COSMIC
> Computer Services Annex
> University of Georgia
> Athens, GA 30602
> (404) 542-3265

Request the code by the designation LAR-14178. This code is written in FORTRAN V for use on the Control Data 6600 computer system and on the Control Data Cyber series.

The first record in the input is a code run identification that accepts up to 80 characters. The remainder of the input is placed in NAMELIST format under the name INPT1.

The wing-planform information is specified by a series of leading-edge and trailing-edge breakpoints for a right-hand wing panel. Up to 21 pairs of coordinates may be used to describe the leading edge and up to 21 pairs to describe the trailing edge. The planform input data in program terminology are as follows:

NLEY	number of leading-edge break-points (limit of 21)
TBLEY	table of leading-edge y-values; beginning at $y = 0$; increasing order of y from root to tip
TBLEX	table of leading-edge x-values that correspond to TBLEY table
NTEY	number of trailing-edge break-points (limit of 21)
TBTEY	table of trailing-edge y-values; beginning at $y = 0$; increasing order of y from root to tip
TBTEX	table of trailing-edge x-values that correspond to TBTEY table

XMAX	largest x-ordinate anywhere on planform; includes second surface if present
SREF	wing reference area for use in aerodynamic force-and-moment coefficients
CBAR	wing reference chord for use in aerodynamic moment coefficients
XMC	x-location of moment reference center
JBYMAX	integer designating number of elements in spanwise direction (limit of 41)
ELAR	element aspect ratio

The size of the wing in code dimensions is controlled by the entry JBYMAX. The necessary scaling is done within the code by use of a scale factor $2(\text{JBYMAX})/\beta b)$. The number of complete wing elements N corresponding to a given JBYMAX may be approximated as

$$N = 4(\text{JBYMAX}^2)\left(\frac{\text{ELAR}}{\text{AR}}\right)$$

The code has been written to accommodate 2000 right-hand panel elements. Generally, the JBYMAX integer is much less than the limit of 41. The normal range is 8 to 20. Computational costs tend to increase as the square of the number of elements.

For flat and mildly cambered wings, an element aspect ratio approximately one-half the full-wing aspect ratio is recommended. For small chord leading- or trailing-edge flaps it may be necessary to use a large element aspect ratio to place at least two elements within the chord. The number of elements in a given chord, c_L or c_T, may be approximated as

$$N = \frac{c_L}{b/2}(\text{JBYMAX})(\text{ELAR})$$

or

$$N = \frac{c_T}{b/2}(\text{JBYMAX})(\text{ELAR})$$

Because computational costs tend to increase as the fourth power of JBYMAX and the second power of ELAR, an increase in the element aspect ratio is the more efficient means of providing for improved definition.

The wing mean-camber surface must be specified by exactly 26 chordwise ordinates at up to 21 span stations. When fewer than 26 camber coordinates are

13

used to define the sections, the ordinate tables must be filled with enough zeros to complete the list of 26. The necessary section information is as follows:

NYC — number of spanwise stations at which chordwise sections are used to define mean-camber surface (limit of 21)

TBYC — table of y-values for chordwise camber-surface sections; beginning at $y = 0$; increasing order of y from root to tip

NPCTC — number of chordwise stations used in definition of mean-camber surface (limit of 26)

TBPCTC — table of chordwise stations, in percent chord, at which mean-camber-surface ordinates are defined; increasing order from leading edge to trailing edge

TZORDC — table of mean-camber-surface z-ordinates that correspond to TBPCTC table; the full 26 values for root chord (including zeros for values in excess of NPCTC) are given first, followed by similar information for all spanwise stations in increasing order of y

TZSCALE — multiplying factor applied to TZORDC table to change camber-surface ordinates, default 1.0

The TZORDC table may be multiplied by a scale factor TZSCALE. This factor may be useful if the original tabulated ordinates are nondimensionalized with respect to a single measurement (e.g., the wing root chord) or if it is necessary to evaluate the effect of a change in camber-surface severity.

The following wing-section information is required for the calculation of attainable leading-edge thrust and leading-edge separation forces:

NYR — number of spanwise stations at which information on airfoil sections is supplied (limit of 21)

TBYR — table of y-values for airfoil section information; beginning at $y = 0$; increasing order of y-values from root to tip

TBTOC — table of airfoil maximum thickness as a fraction of chord, $(t/c)_{max}$

TBETA — table of section locations of maximum thickness as a fraction of chord, η

TBROC — table of leading-edge radii as a fraction of chord, r/c

IVOROP — vortex location option as follows:

0 full vortex force acts normal to wing reference plane at wing leading edge; does not contribute to axial force

1 vortex center given by empirical relationships derived from delta-wing experimental data (default)

2 vortex center given by method of Lan (ref. 16)

YAPEX — spanwise location of vortex flow-field origin

For special planforms such as forward-swept wings or other wings with an apex away from the centerline, this input can help provide a better estimate of vortex-induced flow fields and forces (default YAPEX = 0.0)

The flight or test conditions are specified as follows:

XM — free-stream Mach number

RN — free-stream Reynolds number (based on $\bar{c}$) $\times 10^{-6}$

NALPHA — number of angles of attack to be calculated (limit of 19)

TALPHA — table of angles of attack to be calculated, deg

NADRN — number of additional Reynolds numbers (default 0)

TADRN — table of additional Reynolds numbers (limit of 3)

The commonly accepted practice of performing subsonic calculations for a Mach number of 0.0 is not appropriate for this code. Realistic estimates of attainable thrust can be made only if both the Mach number and the Reynolds number correspond to actual conditions. In fact, the code stops and writes an error message when XM = 0.0 is input.

The following information makes possible the calculation of loadings and forces on deflected leading-edge and trailing-edge flaps. If flap data are not desired, simply omit these entries.

NLEFY — number of breakpoints in leading-edge-flap chord distribution (limit of 21)

TBLEFY — table of y-values at breakpoints in leading-edge-flap chord distribution; beginning at $y = 0$; increasing order of y from root to tip

TBLEFC — table of streamwise leading-edge-flap chords corresponding to TBLEFY table

TBLEFD — table of flap deflections in degrees (positive for leading edge down) corresponding to TBLEFY table

NADLEFD — number of leading-edge-flap deflection multipliers other than 1.0 (limit of 4) (default 0)

TXMLEFD — table of leading-edge-flap deflection multipliers (applied as a multiplier of tangents of input flap deflections)

LEFTYPE — type of leading-edge deflection

1 linear (default)
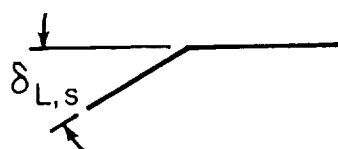
2 parabolic

NTEFY — number of breakpoints in trailing-edge-flap chord distribution (limit of 21)

TBTEFY — table of y-values at breakpoints in trailing-edge-flap chord distribution; beginning at $y = 0$; increasing order of y from root to tip

TBTEFC — table of streamwise trailing-edge-flap chords that correspond to TBTEFY table

TBTEFD — table of flap deflections in degrees (positive for trailing edge down) that correspond to TBTEFY table

NADTEFD — number of trailing-edge-flap deflection multipliers other than 1.0 (limit of 4) (default 0)

TXMTEFD — table of trailing-edge-flap deflection multipliers (applied as a multiplier to tangents of input flap deflections)

CLDES — additional lift coefficient for which flap-system aerodynamic performance is to be specified; code aerodynamic characteristics are given only for angles of attack in input TALPHA table unless CLDES is specified

Spanwise tables must begin with $y = 0$ and extend to $y = b/2$ (with chords of 0 where there are no flaps). At spanwise positions where there are discontinuities in either flap chord or deflection, it is necessary to make closely spaced tabular entries inboard and outboard of the discontinuity.

The program requires flap deflection angles measured in the x-z plane. Flap deflection angles measured normal to the flap hinge line may be converted to code input angles by

$$\delta_{L,s} = \tan^{-1}(\cos \Lambda_{h,L} \tan \delta_{L,n})$$

$$\delta_{T,s} = \tan^{-1}(\cos \Lambda_{h,T} \tan \delta_{T,n})$$

The code provides solutions for wing surfaces composed of all possible combinations of leading-edge and trailing-edge-flap settings provided by the original deflections (TBLEFD and TBTEFD) and by the flap deflection multipliers (TXMLEFD and TXMTEFD). Up to 25 pairs of leading-edge and trailing-edge-flap deflection schedules may thus be treated simultaneously. Solutions obtained by using the multipliers (values other than 0 or 1) are determined by a perturbation process; thus, they are not as accurate as solutions for the original or nominal input deflections. When increased accuracy is required, or when the change in performance with the change in deflection must be evaluated—as in the construction of suction-parameter contour maps—individual solutions without recourse to multipliers may be required. There is, however, a strategy that may be

used to obtain a set of data nearly as accurate as the code is capable of providing with the use of only two code runs. The procedure is described in detail in appendix B of reference 4.

The code also provides for an improved accounting of hinge-line singularities in determination of wing forces and moments. The technique used is described in appendix B of reference 4.

To determine lifting-surface perturbation velocity distributions, the code provides for a maximum of 70 iterations. If this number is reached without the convergence criteria being met, the results for the 70th iteration are printed with a warning of the failure to meet the criteria. The maximum number of iterations may be increased or decreased by the entry

> ITRMAX   maximum number of perturbation velocity iterations (default 70)

The code convergence criteria are met when, for all four wing surfaces and for two successive iterations, the average difference in perturbation velocity between iterations is less than half of 1 percent of the average velocity over the wing. If the average velocity for the camber surface or either of the flap surfaces is less than the average velocity for the flat surface at $\alpha = 1°$, the flat-wing surface value is used instead. In many instances, these criteria may be more stringent than necessary. If desired, the convergence criteria may be changed by the entry

> CNVGTST   perturbation velocity convergence criteria (default 0.005)

The following set of input data is required for the handling of wing-canard or wing–horizontal-tail configurations. If wing-alone solutions are desired, simply omit these entires.

> ILS2   second surface identifier
>
> 0 no second surface (default)
>
> 1 canard
>
> 2 horizontal tail

If a second surface is to be employed (ILS2 = 1 or 2) the following planform information must be supplied:

> NLEY2   number of leading-edge breakpoints (limit of 21)
>
> TBLEY2   table of leading-edge y-values; need not begin at $y = 0$; increasing order of y

> TBLEX2   table of leading-edge x-values that correspond to TBLEY2 table
>
> NTEY2   number of second-surface trailing-edge breakpoints (limit of 21)
>
> TBTEY2   table of trailing-edge y-values; need not begin at $y = 0$ but initial and final values must be the same as the TBLEX2 initial and final values; increasing order of y
>
> TBTEX2   table of trailing-edge x-values that correspond to TBTEY2 table

The second-surface, mean-camber surface must be specified by exactly 26 chordwise ordinates at up to 21 span stations. When fewer than 26 camber coordinates are used to define the sections, the ordinate tables must be filled with enough zeros to complete the list of 26. The necessary section information is as follows:

> NYC2   number of spanwise stations at which chordwise sections are used to define mean-camber surface (limit of 21)
>
> TBYC2   table of y-values for chordwise camber-surface sections; increasing order of y
>
> NPCTC2   number of chordwise stations used in definition of mean-camber surface (limit of 26)
>
> TBPCTC2   table of chordwise stations, in percent chord, at which mean-camber-surface ordinates are defined; increasing order from leading edge to trailing edge
>
> TZORDC2   table of mean-camber-surface z-ordinates that correspond to TBPCTC2 table; the full 26 values for root chord (including zeros for values in excess of NPCTC2) are given first, followed by similar information for all spanwise stations in increasing order of y
>
> TZSCAL2   multiplying factor applied to TZORDC2 table to change camber-surface ordinates (default 1.0)

16

The following canard or horizontal-tail section information is required for the calculation of attainable leading-edge thrust and leading-edge separation forces:

NYR2   number of spanwise stations at which information on airfoil sections is supplied (limit of 21)

TBYR2   table of y-values for airfoil section information; increasing order of y

TBTOC2   table of airfoil maximum thickness as a fraction of chord, $(t/c)_{max}$

TBETA2   table of section locations of maximum thickness as a fraction of chord, η

TBROC2   table of leading-edge radii as a fraction of chord, r/c

YAPEX2   spanwise location of second-surface vortex flow-field origin

For special planforms such as forward-swept surfaces or other surfaces with an apex away from the centerline, this input can help provide a better estimate of vortex-induced flow fields and forces. The default is YAPEX2 = 0.0.

DELTA2   incidence of the second surface with respect to the wing reference plane, deg (default DELTA2 = 0.0)

The code is constructed so that successive runs may be made with a given code entry. To make additional runs, it is necessary only to add an identification record and namelist data that are to be changed from the previous run.

The printed code results include the following:

1. An iteration-by-iteration history of the convergence parameters.

2. A listing of theoretical pressure distributions for the combined camber surface at $\alpha = 0°$ and for the combined flat surface at $\alpha = 1°$. For each of the program spanwise stations (controlled by JBYMAX), interpolated or extrapolated pressure coefficients are given for a set of chordwise stations.

3. A listing of the spanwise distribution of section normal, axial, and pitching-moment coefficients for the combined cambered surface at $\alpha = 0°$ and for the combined flat surface at $\alpha = 1°$. The interference axial-force coefficient caused by the flat-surface loading acting on the camber surface and the theoretical thrust parameters are also printed.

4. A listing of overall theoretical aerodynamic coefficients $C_N, C_A, C_m, C_L,$ and C_D with no thrust and with full theoretical thrust as a function of angle of attack.

5. A listing of the spanwise distribution of the flat-wing, angle-of-attack range for full theoretical leading-edge thrust (for wing-alone solution only).

6. A listing of overall estimated aerodynamic coefficients, including $C_N, C_A,$ and C_m for the basic pressure loading, ΔC_N and ΔC_A for attainable thrust and vortex-force increments, and $C_N, C_A, C_m, C_L, C_D,$ and S_s for the total loading.

Additional tabulated output data may be selected by using the following print options:

IPRCPD = 1   theoretical pressure distributions for each selected angle of attack

IPRSLDT = 1   theoretical span load distribution of $C_N, C_A, C_m, C_L,$ and C_D with no thrust and with full theoretical thrust for each selected angle of attack

IPRSLDA = 1   estimated span load distribution of $C_N, C_A, C_m, C_L,$ and C_D with attainable thrust and vortex-force effects for each selected angle of attack

IPRALL = 1   the preceding print control options apply only to the first set of flap deflections. Select this option if the three preceding options are to apply to all flap deflection combinations. Selection of this option could result in a very large volume of printed output.

Appendix B

Notes on Computer-Code Application

Table I presents sample input data for the flap-system analysis code for each of the test configurations studied. The wing lifting surface includes contributions of the fuselage planform as well as the wing planform. The canard or horizontal-tail lifting surface is restricted to span positions outside the fuselage to avoid overlap. The camber ordinates, TZORDC, were determined from the mean ordinates of the wing and fuselage combination.

As with any numerical solution of mathematical theory, the problem is to find a sufficiently detailed discretization that provides accurate answers without incurring prohibitive costs. To sufficiently represent the flap geometry of the study configurations, the number of semispan elements, JBYMAX, and the element aspect ratio, ELAR, were chosen so that, for the most part, two or more elements would be contained in any given flap chord. This resulted in element aspect ratios ranging from 1.84 to 6.0 and from 8 to 10 semispan elements. Generally, the whole-wing-body planform was represented by 400 to 600 elements.

To obtain estimates of attainable leading-edge thrust, Reynolds number, RN ($R \times 10^{-6}$), and Mach number, XM, are both specified and the section geometric characteristics of $t/c, r/c,$ and η are entered in the appropriate tables. For evaluation of the estimated forces caused by leading-edge vortex separation, the vortex location option IVOROP = 1 was chosen for all the wings with swept leading edges. Option 0 was used only for the unswept wing.

The wing evaluation program has a feature that permits simultaneous solutions for a number of combinations of leading- and trailing-edge-flap deflections by use of a perturbation process. This time-saving code option is sufficiently accurate for small deflection angles (streamwise angles of about 15° or less), but because of the large deflection angles often considered in this investigation and the need for a high degree of accuracy, this feature was not used to its full capacity. When required, individual computer runs were performed for each pair of leading- and trailing-edge deflections; however, a single computer run can be made to yield as accurate a prediction as the method is capable of for a set of four deflection-angle combinations which include zero deflections of leading- and trailing-edge flaps. The code input data of table I provide for flap deflection multipliers, TXMLEFD and TXMTEFD, of 0.0, which produce results for a leading-edge-flap deflection with no trailing-edge-flap deflection, a trailing-edge-flap deflection with no leading-edge-flap deflection, no leading-edge-flap deflection with no trailing-edge-flap deflection, and the leading- and trailing-edge-flap deflections in combination.

Also, some of the input data of table I provide for a second computer run in which only the leading-edge-flap deflection and/or the trailing-edge-flap deflection are changed. It is unnecessary to repeat the other data.

References

1. Carlson, Harry W.; and Walkley, Kenneth B.: *A Computer Program for Wing Subsonic Aerodynamic Performance Estimates Including Attainable Thrust and Vortex Lift Effects.* NASA CR-3515, 1982.

2. Carlson, Harry W.; and Walkley, Kenneth B.: *An Aerodynamic Analysis Computer Program and Design Notes for Low Speed Wing Flap Systems.* NASA CR-3675, 1983.

3. Carlson, Harry W.; and Darden, Christine M.: *Applicability of Linearized-Theory Attached-Flow Methods to Design and Analysis of Flap Systems at Low Speeds for Thin Swept Wings With Sharp Leading Edges.* NASA TP-2653, 1987.

4. Carlson, Harry W.; and Darden, Christine M.: *Validation of a Pair of Computer Codes for Estimation and Optimization of Subsonic Aerodynamic Performance of Simple Hinged-Flap Systems for Thin Swept Wings.* NASA TP-2828, 1988.

5. Margason, Richard J.; and Lamar, John E.: *Vortex-Lattice FORTRAN Program for Estimating Subsonic Aerodynamic Characteristics of Complex Planforms.* NASA TN D-6142, 1971.

6. Woodward, F. A.: *An Improved Method for the Aerodynamic Analysis of Wing-Body-Tail Configurations in Subsonic and Supersonic Flow. Part I—Theory and Application.* NASA CR-2228, Pt. I, 1973.

7. Magnus, Alfred E.; and Epton, Michael A.: *PAN AIR—A Computer Program for Predicting Subsonic or Supersonic Linear Potential Flows About Arbitrary Configurations Using a Higher Order Panel Method. Volume I—Theory Document (Version 1.0).* NASA CR-3251, 1980.

8. Polhamus, Edward C.: Predictions of Vortex-Lift Characteristics by a Leading-Edge Suction Analogy. *J. Aircr.,* vol. 8, no. 4, Apr. 1971, pp. 193–199.

9. Feistel, T. W.; Corsiglia, V. R.; and Levin, D. B.: Wind-Tunnel Measurements of Wing-Canard Interference and a Comparison With Various Theories. *SAE 1981 Transactions,* Section 2, Volume 90, 1982, pp. 2026–2039. (Available as SAE Paper 810575.)

10. Gloss, Blair B.: *Effect of Canard Location and Size on Canard-Wing Interference and Aerodynamic-Center Shift Related to Maneuvering Aircraft at Transonic Speeds.* NASA TN D-7505, 1974.

11. Nicholas, W. U.; and Naville, G. L.: *An Evaluation of the Relative Merit of Wing-Canard, Wing-Tail, and Tailless Arrangements for Advanced Fighter Applications.* FZA-547, Fort Worth Div., General Dynamics, Apr. 19, 1984.

12. Lamar, John E.: Recent Studies of Subsonic Vortex Lift Including Parameters Affecting Stable Leading-Edge Vortex Flow. *J. Aircr.,* vol. 14, no. 12, Dec. 1977, pp. 1205–1211.

13. Mann, Michael J.; and Mercer, Charles E.: *Forward-Swept-Wing Configuration Designed for High Maneuverability by Use of a Transonic Computational Method.* NASA TP-2628, 1986.

14. Yip, Long P.; and Parlett, Lysle P.: *Low-Speed Wind-Tunnel Tests of a 1/10-Scale Model of an Advanced Arrow-Wing Supersonic Cruise Configuration Designed for Cruise at Mach 2.2.* NASA TM-80152, 1979.

15. Radkey, R. L.; Welge, H. R.; and Felix, J. E.: *Aerodynamic Characteristics of a Mach 2.2 Advanced Supersonic Cruise Aircraft Configuration at Mach Numbers From 0.5 to 2.4.* NASA CR-145094, 1977.

16. Lan, C. Edward; and Chang, Jen-Fu: *Calculation of Vortex Lift Effect for Cambered Wings by the Suction Analogy.* NASA CR-3449, 1981.

Table I. Sample Input Data for AERO2S Code

(a) Unswept wing with canard

```
RECTANGULAR WING-CANARD - FEISTEL, SAE 810575
$INPT1   XM=.2,RN=1.4,JBYMAX=10,ELAR=3.0,IVOROP=0,IPRSLDA=1,
SREF=6.0,CBAR=1.0,XMC=1.2642, XMAX=2.5575,
NALPHA=16,TALPHA=-6.0,-4.0,-2.0,0.0,2.0,
   4.0,6.0,8.0,10.0,12.0,14.0,16.0,18.0,20.0,22.0,24.0,
NLEY=2,TBLEY=0.0000,3.0000,
        TBLEX=1.5575,1.5575,
NTEY=2,TBTEY=0.0000,3.0000,
        TBTEX=2.5575,2.5575,
NYR=2,TBYR=0.000,3.000,
     TBTOC=.1300,.1300,
     TBROC=.0130,.0130,
     TBETA=.4000,.4000,
NYC=2,TBYC=0.0,3.0,
NPCTC=13,TBPCTC=0.0,2.50,5.00,10.0,20.0,30.0,40.0,50.0,60.0,
           70.0,80.0,90.0,100.0,
        TZORDC=0.0,.007,.010,.013,.016,.018,.020,.021,.0215,
           .021,.018,.012,-.005,13*0.0,
              0.0,.007,.010,.013,.016,.018,.020,.021,.0215,
           .021,.018,.012,-.005,13*0.0,
NLEY2=2,TBLEY2=0.00,2.12,
        TBLEX2=0.00,0.00,
NTEY2=2,TBTEY2=0.00,2.12,
        TBTEX2=.710,.710,
NYR2=2,TBYR2=0.00,2.12,
     TBTOC2=.130,.130,
     TBROC2=.013,.013,
     TBETA2=.400,.400,
NYC2=2,TBYC2=0.0,2.12,
NPCTC2=13,TBPCTC2=0.0,2.50,5.00,10.0,20.0,30.0,40.0,50.0,60.0,
           70.0,80.0,90.0,100.0,
        TZORDC2=0.0,.007,.010,.013,.016,.018,.020,.021,.0215,
           .021,.018,.012,-.005,13*0.0,
              0.0,.007,.010,.013,.016,.018,.020,.021,.0215,
           .021,.018,.012,-.005,13*0.0, `
DELTA2=2.0,ILS2=1,      $
```

Table I. Continued

(b) 60°-swept trapezoidal-wing fighter with canard

```
CANARD LOCATION MODEL - GLOSS, TN D7505
$INPT1 XM=.70,RN=1.35,JBYMAX=10,ELAR=2.5,IVOROP=1,IPRSLDA=1,
SREF=160.0,CBAR=9.18,XMC=23.3,XMAX=38.0,
NLEY=4,TBLEY=0.00,1.40,1.50,10.0,
       TBLEX=0.00,6.00,18.8,33.5,
NTEY=4,TBTEY=0.00,1.40,1.50,10.0,
       TBTEX=38.0,38.0,30.5,36.2,
NYC=2,TBYC=0.00,10.0,NPCTC=2,TBPCTC=0.00,100.0,
TZORDC=52*0.0,
NYR=4,TBYR=0.000,1.400,1.500,10.00,
     TBTOC=0.000,0.000,0.060,0.040,
     TBROC=0.000,0.000,.0002,.0007,
     TBETA=0.500,0.500,0.500,0.500,
NALPHA=13,TALPHA=-4.0,-2.0,0.0,2.0,4.0,6.0,8.0,10.0,12.0,
14.0,16.0,18.0,20.0,
NLEY2=2,TBLEY2=1.50,6.79,
        TBLEX2=11.8,18.5,
NTEY2=2,TBTEY2=1.50,6.79,
        TBTEX2=18.9,20.0,
NYC2=2,TBYC2=1.50,6.79,NPCTC2=2,TBPCTC2=0.00,100.0,
TZORDC2=52*0.0,
NYR2=2,TBYR2=1.500,6.790,
     TBTOC2=0.060,0.040,
     TBROC2=.0003,.0014,
     TBETA2=0.500,0.500,
YAPEX=1.5,YAPEX2=1.5,
DELTA2=0.0,ILS2=1,     $
```

Table I. Continued

(c) 44°-swept trapezoidal-wing fighter with canard

```
44 DEG TRAPEZOIDAL WING FIGHTER - NICHOLAS, GD FZA 547 - DLN=12,DTN=12
$INPT1 XM=.40,RN=1.91,JBYMAX=10,ELAR=2.5,IVOROP=1,IPRSLDA=1,
SREF=160.0,CBAR=9.17,XMC=23.39,XMAX=38.03,
NLEY=4,TBLEY=0.000,1.400,1.500,10.00,
       TBLEX=0.000,4.250,18.78,27.00,
NTEY=4,TBTEY=0.000,1.400,1.500,10.00,
       TBTEX=38.03,38.03,30.51,29.66,
NYC=2,TBYC=0.0,10.0,NPCTC=2,TBPCTC=0.0,100.0,TZORDC=52*0.0,
NYR=3, TBYR=0.000,1.500,10.00,
       TBTOC=.0000,.0600,.0400
       TBROC=.0000,.0025,.0011,
       TBETA=.4000,.4000,.4000,
NLEFY=4,TBLEFY=0.00,1.40,1.50,10.0,
       TBLEFC=0.00,0.00,1.80,1.80,
       TBLEFD=0.00,0.00,8.70,8.70,
NTEFY=6,TBTEFY=0.00,1.40,1.50,7.47,7.57,10.0,
       TBTEFC=0.00,0.00,2.32,1.04,0.00,0.00,
       TBTEFD=0.00,0.00,12.0,12.0,0.00,0.00,
NADLEFD=1,TXMLEFD=0.00,
NADTEFD=1,TXMTEFD=0.00,
NALPHA=15,TALPHA=-4.0,-2.0,0.0,2.0,4.0,6.0,8.0,10.0,12.0,14.0,16.0,
18.0,20.0,22.0,24.0,
NLEY2=2,TBLEY2=1.500,5.500,
       TBLEX2=13.22,17.10,
NTEY2=2,TBTEY2=1.500,5.500,
       TBTEX2=18.55,18.17,
NYC2=2,TBYC2=1.500,5.500,
NPCTC2=2,TBPCTC2=0.000,100.0,
TZORDC2=52*0.0,
NYR2=2,TBYR2=1.500,5.500,
       TBTOC2=.0600,.0400,
       TBROC2=.0000,.0000,
       TBETA2=.5000,.5000,
DELTA2=0.0,ILS2=1,     $
DELTA2=10.0
$INPT1 DELTA2=10.0,     $
DELTA2=-10.0
$INPT1 DELTA2=-10.0,     $
```

Table I. Continued

(d) 44°-swept trapezoidal-wing fighter with horizontal tail

```
44 DEG TRAPEZOIDAL WING FIGHTER - NICHOLAS  GD FZA 547 - DLN=12,DTN=12
$INPT1 XM=.40,RN=1.91,JBYMAX=10,ELAR=2.5,IVOROP=1,IPRSLDA=1,
SREF=160.0,CBAR=9.17,XMC=23.39,XMAX=38.47,
NLEY=4,TBLEY=0.000,1.400,1.500,10.00,
       TBLEX=0.000,4.250,18.78,27.00,
NTEY=4,TBTEY=0.000,1.400,1.500,10.00,
       TBTEX=38.03,38.03,30.51,29.66,
NYC=2,TBYC=0.0,10.0,NPCTC=2,TBPCTC=0.0,100.0,TZORDC=52*0.0,
NYR=3, TBYR=0.000,1.500,10.00,
       TBTOC=.0000,.0600,.0400,
       TBROC=.0000,.0025,.0011,
       TBETA=.4000,.4000,.4000,
NLEFY=4,TBLEFY=0.00,1.40,1.50,10.0,
        TBLEFC=0.00,0.00,1.80,1.80,
        TBLEFD=0.00,0.00,8.70,8.70,
NTEFY=6,TBTEFY=0.00,1.40,1.50,7.47,7.57,10.0,
        TBTEFC=0.00,0.00,2.32,1.04,0.00,0.00,
        TBTEFD=0.00,0.00,12.0,12.0,0.00,0.00,
NADLEFD=1,TXMLEFD=0.00,
NADTEFD=1,TXMTEFD=0.00,
NALPHA=15,TALPHA=-4.0,-2.0,0.0,2.0,4.0,6.0,8.0,10.0,12.0,14.0,16.0,
18.0,20.0,22.0,24.0,
NLEY2=2,TBLEY2=1.500,5.500,
        TBLEX2=33.14,37.02,
NTEY2=2,TBTEY2=1.500,5.500,
        TBTEX2=38.47,38.09,
NYC2=2,TBYC2=1.500,5.500,
NPCTC2=2,TBPCTC2=0.000,100.0,
TZORDC2=52*0.0,
NYR2=2,TBYR2=1.500,5.500,
       TBTOC2=.0600,.0400,
       TBROC2=.0000,.0000,
       TBETA2=.5000,.5000,
DELTA2=0.0,ILS2=2,    $
DELTA2=10.0
$INPT1 DELTA2=10.0,    $
DELTA2=-10.0
$INPT1 DELTA2=-10.0,    $
```

Table I. Continued

(e) 60°-swept delta-wing fighter with canard

```
 60 DEG DELTA GENERIC FIGHTER - NICHOLAS, GD FZA 547 - DLN=20,DTN=20
$INPT1 XM=.40,RN=2.52,JBYMAX=10,ELAR=2.5,IVOROP=1,IPRSLDA=1,
SREF=181.94,CBAR=12.13,XMC=23.74,XMAX=41.63,
NLEY=4,TBLEY=0.000,1.400,1.500,10.00,
       TBLEX=0.000,4.250,17.53,32.25,
NTEY=4,TBTEY=0.000,1.400,1.500,10.00,
       TBTEX=41.63,41.63,33.00,32.25,
NYC=2,TBYC=0.0,10.0,NPCTC=2,TBPCTC=0.0,100.0,TZORDC=52*0.0,
NYR=3, TBYR=0.000,1.500,10.00,
       TBTOC=.0000,.0600,.0400,
       TBROC=.0000,.0025,.0011,
       TBETA=.4000,.4000,.4000,
NLEFY=5,TBLEFY=0.00,1.40,1.50,8.50,10.0,
       TBLEFC=0.00,0.00,1.37,2.62,0.00,
       TBLEFD=0.00,0.00,9.60,9.60,9.60,
NTEFY=6,TBTEFY=0.00,1.40,1.50,7.00,7.10,10.0,
       TBTEFC=0.00,0.00,1.69,1.21,0.00,0.00,
       TBTEFD=0.00,0.00,20.0,20.0,0.00,0.00,
NADLEFD=1,TXMLEFD=0.00,
NADTEFD=1,TXMTEFD=0.00,
NALPHA=15,TALPHA=-4.0,-2.0,0.0,2.0,4.0,6.0,8.0,10.0,12.0,14.0,16.0,
18.0,20.0,22.0,24.0,
NLEY2=2,TBLEY2=1.500,5.500,
       TBLEX2=11.58,15.46,
NTEY2=2,TBTEY2=1.500,5.500,
       TBTEX2=16.91,16.53,
NYC2=2,TBYC2=1.500,5.500,
NPCTC2=2,TBPCTC2=0.000,100.0,
TZORDC2=52*0.0,
NYR2=2,TBYR2=1.500,5.500,
      TBTOC2=.0600,.0400,
      TBROC2=.0000,.0000,
      TBETA2=.5000,.5000,
DELTA2=0.0,ILS2=1,     $
DELTA2=10.0
$INPT1 DELTA2=10.0,    $
DELTA2=-10.0
$INPT1 DELTA2=-10.0,   $
```

Table I. Continued

(f) 60°-swept delta-wing fighter with horizontal tail

```
 60 DEG DELTA GENERIC FIGHTER - NICHOLAS, GD FZA 547 - DLN=20,DTN=20
$INPT1 XM=.40,RN=2.52,JBYMAX=10,ELAR=2.5,IVOROP=1,IPRSLDA=1,
SREF=181.94,CBAR=12.13,XMC=23.74,XMAX=41.63,
NLEY=4,TBLEY=0.000,1.400,1.500,10.00,
       TBLEX=0.000,4.250,17.53,32.25,
NTEY=4,TBTEY=0.000,1.400,1.500,10.00,
       TBTEX=41.63,41.63,33.00,32.25,
NYC=2,TBYC=0.0,10.0,NPCTC=2,TBPCTC=0.0,100.0,TZORDC=52*0.0,
NYR=3, TBYR=0.000,1.500,10.00,
       TBTOC=.0000,.0600,.0400,
       TBROC=.0000,.0025,.0011,
       TBETA=.4000,.4000,.4000,
NLEFY=5,TBLEFY=0.00,1.40,1.50,8.50,10.0,
        TBLEFC=0.00,0.00,1.37,2.62,0.00,
        TBLEFD=0.00,0.00,9.60,9.60,9.60,
NTEFY=6,TBTEFY=0.00,1.40,1.50,7.00,7.10,10.0,
        TBTEFC=0.00,0.00,1.69,1.21,0.00,0.00,
        TBTEFD=0.00,0.00,20.0,20.0,0.00,0.00,
NADLEFD=1,TXMLEFD=0.00,
NADTEFD=1,TXMTEFD=0.00,
NALPHA=15,TALPHA=-4.0,-2.0,0.0,2.0,4.0,6.0,8.0,10.0,12.0,14.0,16.0,
18.0,20.0,22.0,24.0,
NLEY2=2,TBLEY2=1.500,5.500,
        TBLEX2=36.24,40.12,
NTEY2=2,TBTEY2=1.500,5.500,
        TBTEX2=41.57,41.19,
NYC2=2,TBYC2=1.500,5.500,
NPCTC2=2,TBPCTC2=0.000,100.0,
TZORDC2=52*0.0,
NYR2=2,TBYR2=1.500,5.500,
       TBTOC2=.0600,.0400,
       TBROC2=.0000,.0000,
       TBETA2=.5000,.5000,
DELTA2=0.0,ILS2=2,      $
DELTA2=10.0
$INPT1 DELTA2=10.0,     $
DELTA2=-10.0
$INPT1 DELTA2=-10.0,       $
```

Table I. Continued

(g) Forward swept-wing fighter with canard

```
FORWARD SWEEP FIGHTER - MANN,TP 2628 - DLS=0,DTS=0,C=0
$INPT1 XM=.60,RN=2.5,JBYMAX=8,ELAR=4.0,IVOROP=1,IPRSLDA=1,
SREF=216.0,CBAR=9.26,XMC=23.77,XMAX=37.77,YAPEX=13.32,
NLEY=4,TBLEY=0.000,1.740,1.750,13.32,
       TBLEX=0.000,12.75,23.75,19.48,
NTEY=2,TBTEY=0.000,13.32,
       TBTEX=37.77,22.35,
NYC=9,TBYC=0.000,1.740,1.750,2.660,5.590,8.000,10.65,11.98,13.32,
NPCTC=10,
TBPCTC=0.000,5.000,10.00,20.00,30.00,40.00,50.00,60.00,80.00,100.0,
TZORDC=0.000,0.000,0.000,0.000,0.000,0.000,0.000,0.000,0.000,0.000,16*0.0,
       0.000,0.000,0.000,0.000,0.000,0.000,0.000,0.000,0.000,0.000,16*0.0,
       0.000,.1368,.2067,.2075,.4812,.6205,.7367,.8091,.7814,.3670,16*0.0,
       0.000,.1264,.1916,.3190,.4418,.5671,.6721,.7374,.7074,.3213,16*0.0,
       0.000,.0927,.1428,.2339,.3146,.3948,.4636,.5061,.4686,.1739,16*0.0,
       0.000,.0593,.1012,.1654,.2101,.2434,.2685,.2802,.2289,-.029,16*0.0,
       0.000,.0403,.0596,.0831,.0915,.0920,.0875,.0710,-.015,-.247,16*0.0,
       0.000,.0355,.0529,.0701,.0724,.0639,.0431,.0138,-.080,-.286,16*0.0,
       0.000,.0307,.0462,.0571,.0533,.0538,-.001,-.043,-.145,-.318,16*0.0,
NYR=4,TBYR=0.000,1.740,1.750,13.32,
       TBTOC=0.000,0.000,.0420,.0460,
       TBROC=0.000,0.000,.0020,.0023,
       TBETA=0.250,0.250,0.250,0.250,
NALPHA=13,TALPHA=-4.0,-2.0,0.0,2.0,4.0,6.0,8.0,10.0,12.0,14.0,16.0,
18.0,20.0,
NLEY2=2,TBLEY2=1.750,6.660,
       TBLEX2=12.75,17.66,
NTEY2=2,TBTEY2=1.750,6.660,
       TBTEX2=18.06,19.09,
NYC2=4,TBYC2=1.750,2.000,6.000,6.660,
NPCTC2=6,
TBPCTC2=0.000,20.00,40.00,60.00,80.00,100.0,
TZORDC2=0.000,.0991,.1111,.0892,.0485,-.042,20*0.0,
       0.000,.0961,.1095,.0902,.0522,-.033,20*0.0,
       0.000,.0483,.0845,.1060,.1115,.0974,20*0.0,
       0.000,.0453,.0829,.1070,.1152,.1056,20*0.0,
NYR2=2,TBYR2=1.750,6.660,
       TBTOC2=.0510,.0510,
       TBROC2=.0024,.0024,
       TBETA2=.3000,.3000,
DELTA2=0.0,ILS2=1,     $
C=10
$INPT1 DELTA2=10.0,    $
```

Table I. Concluded

(h) Arrow-wing supersonic transport with horizontal tail

```
SST-YIP,TM 80152 - LEFD=4.3,12.8,12.8,12.8,11.2,17.6,TEFD=30,DELTA2=5,-15
$INPT1 XM=0.09,RN=4.19,JBYMAX=10,ELAR=3.0,IVOROP=1,IPRSLDA=1,
SREF=14400.,CBAR=77.76,XMC=220.91,XMAX=372.,
NALPHA=16,TALPHA=-6.0,-4.0,-2.0,0.0,2.0,4.0,6.0,8.0,10.0,12.0,14.0,
16.0,18.0,20.0,22.0,24.0,
NLEY=4,TBLEY=0.000,7.0000,51.710,81.330,
       TBLEX=0.000,104.70,234.55,280.20,
NTEY=4,TBTEY=0.000,7.0000,25.800,81.330,
       TBTEX=372.0,277.70,277.70,294.97,
NYC=15,TBYC=0.0000,4.4090,13.428,20.899,23.218,27.202,29.498,
           38.294,47.061,49.819,53.701,56.458,67.509,76.399,
           81.330,
NPCTC=10,
TBPCTC=0.000,5.000,10.00,20.00,30.00,40.00,50.00,60.00,80.00,100.0,
TZORDC=14.30,15.20,17.50,17.40,15.40,12.55,10.00,8.000,6.000,10.00,16*0.0,
       13.20,13.20,12.79,11.24,9.250,7.380,5.700,4.250,2.000,.6000,16*0.0,
       6.250,6.780,6.990,6.890,6.200,5.320,4.500,3.770,2.330,1.000,16*0.0,
       4.280,4.850,5.250,5.430,5.130,4.600,4.030,3.500,2.470,1.420,16*0.0,
       4.030,4.600,4.940,5.200,4.980,4.450,3.930,3.430,2.470,1.500,16*0.0,
       3.760,4.270,4.600,4.890,4.660,4.220,3.780,3.300,2.380,1.560,16*0.0,
       3.530,4.000,4.370,4.650,4.430,4.100,3.660,3.200,2.350,1.580,16*0.0,
       1.950,2.430,2.800,3.120,3.070,2.880,2.680,2.450,2.000,1.580,16*0.0,
       0.660,0.960,1.200,1.480,1.600,1.630,1.660,1.630,1.570,1.480,16*0.0,
       0.470,0.700,0.880,1.120,1.250,1.330,1.400,1.420,1.430,1.430,16*0.0,
       0.330,0.450,0.580,0.760,0.900,1.040,1.130,1.210,1.300,1.340,16*0.0,
       0.260,0.370,0.430,0.590,0.720,0.870,0.980,1.070,1.200,1.280,16*0.0,
       0.300,0.310,0.320,0.350,0.410,0.470,0.550,0.620,0.790,0.930,16*0.0,
       0.270,0.270,0.270,0.280,0.290,0.310,0.330,0.360,0.430,0.520,16*0.0,
       0.280,0.280,0.280,0.280,0.280,0.280,0.290,0.300,0.330,0.400,16*0.0,
NYR=7,TBYR=0.00000,4.40900,20.8990,38.2940,51.7000,51.7100,81.3300,
      TBTOC=0.04000,0.02380,0.02870,0.03000,0.03000,0.03000,0.03000,
      TBETA=0.50000,0.66000,0.55000,0.58000,0.60000,0.60000,0.60000,
      TBROC=0.00000,0.00024,0.00050,0.00048,0.00040,.000003,.000013,
NLEFY=10,TBLEFY=0.000,7.000,7.010,17.59,17.60,44.42,51.71,64.00,64.01,81.33,
         TBLEFC=0.000,0.000,18.84,18.80,18.80,18.78,8.370,6.770,6.770,4.510,
         TBLEFD=0.000,0.000,4.300,4.300,12.80,12.80,11.20,11.20,17.60,17.60,
NTEFY=10,TBTEFY=0.000,17.00,17.01,25.80,25.81,36.59,36.60,61.00,61.01,81.33,
         TBTEFC=0.000,0.000,15.93,15.93,0.000,0.000,14.50,9.650,0.000,0.000,
         TBTEFD=0.000,0.000,30.00,30.00,0.000,0.000,30.00,30.00,0.000,0.000,
NLEY2=2,TBLEY2=2.0000,23.700,
        TBLEX2=323.20,348.99,
NTEY2=2,TBTEY2=2.0000,23.700,
        TBTEX2=361.00,355.39,
NYC2=2,TBYC2=2.0000,23.700,
NPCTC2=2,TBPCTC2=0.0000,100.00,
TZORDC2=52*0.0,
NYR2=2,TBYR2=2.000,23.70,
       TBTOC2=0.035,0.035,
       TBETA2=0.500,0.500,
       TBROC2=0.000,0.000,
DELTA2=5.0,ILS2=2,    $
DELTA2=-15.0
$INPT1 DELTA2=-15.0,    $
```
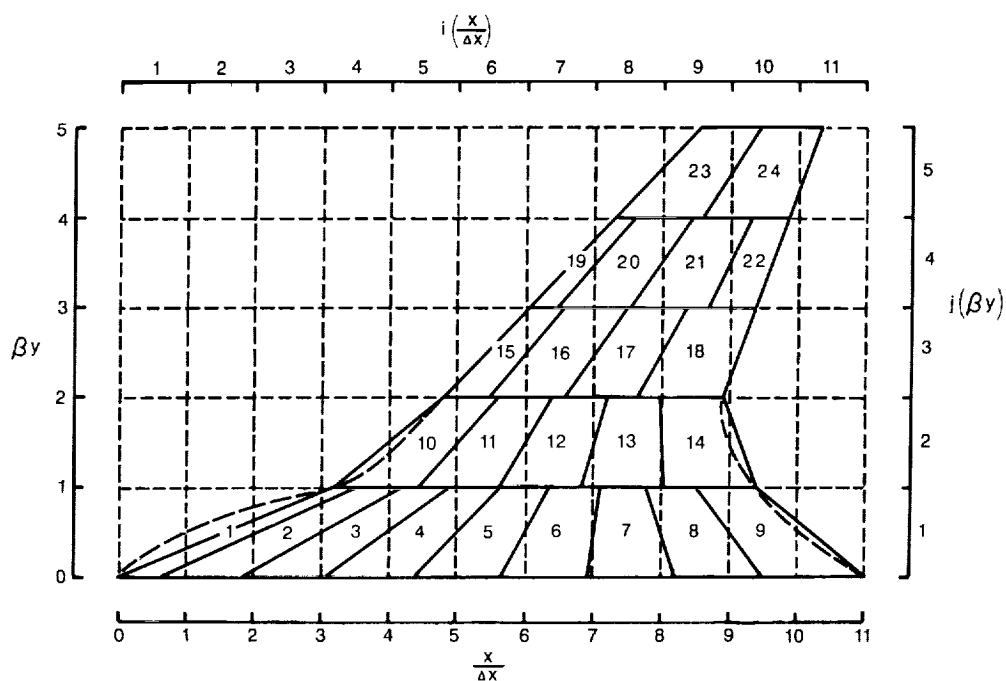
(a) Wing alone.
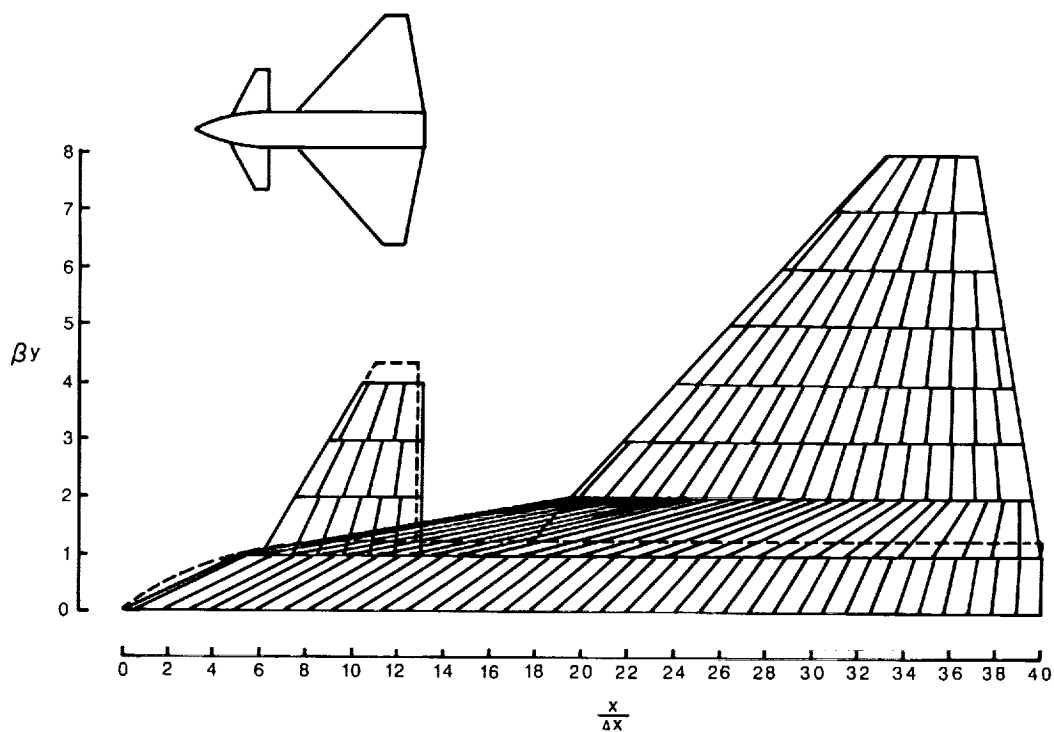
(b) Wing-body-canard configuration.

Figure 1. Typical representation of lifting surfaces used for numerical solution of linearized theory. Dashed line indicates original planform; numbers used to identify individual wing elements.

Actual planform

Code-input planform

Code-generated planform

(a) 60°-swept trapezoidal-wing fighter with canard.

Actual planform

Code-input planform

Code-generated planform
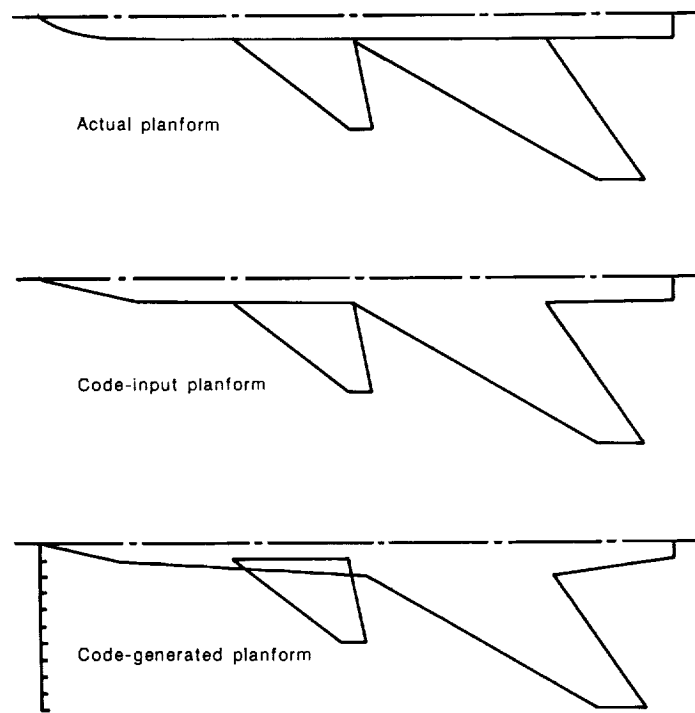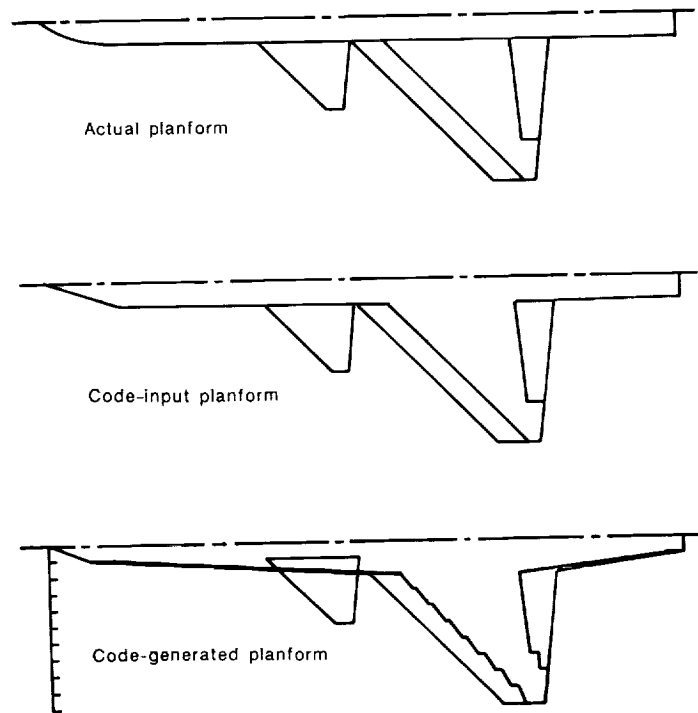
(b) 44°-swept trapezoidal-wing fighter with canard.

Figure 2. Numerical representation of lifting surface for selected configurations used in study.

Actual planform

Code-input planform

Code-generated planform

(c) 60°-swept delta-wing fighter with horizontal tail.

Actual planform

Code-input planform

Code-generated planform
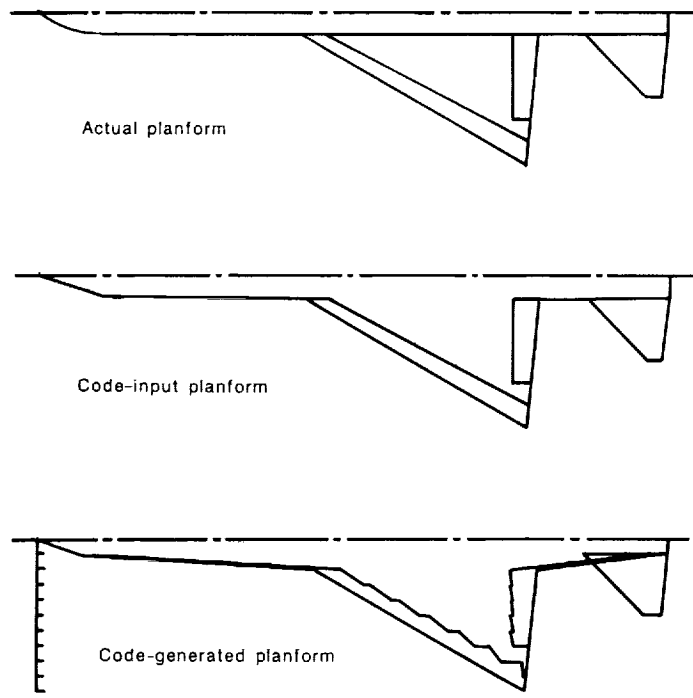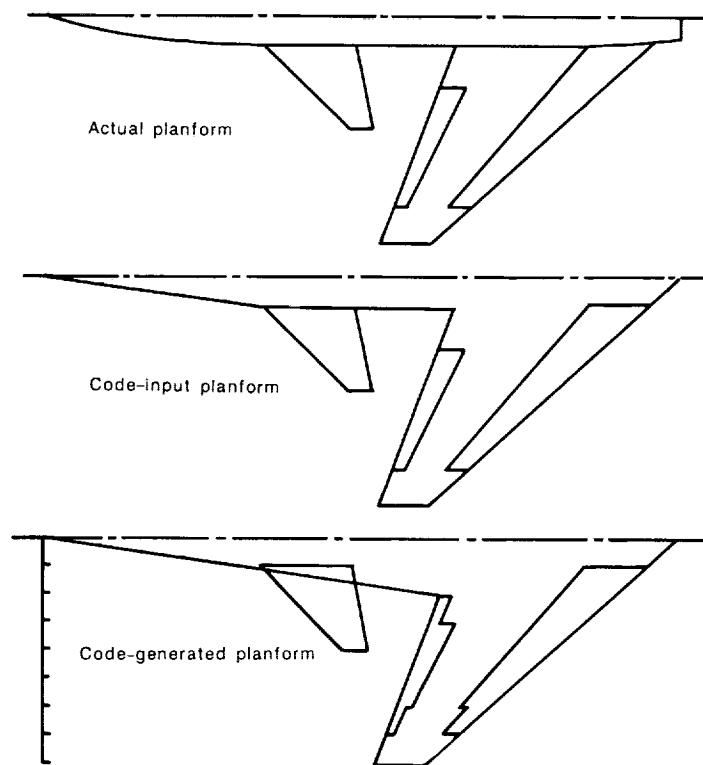
(d) Forward swept-wing fighter with canard.

Figure 2. Continued.

Actual planform

Code-input planform

Code-generated planform
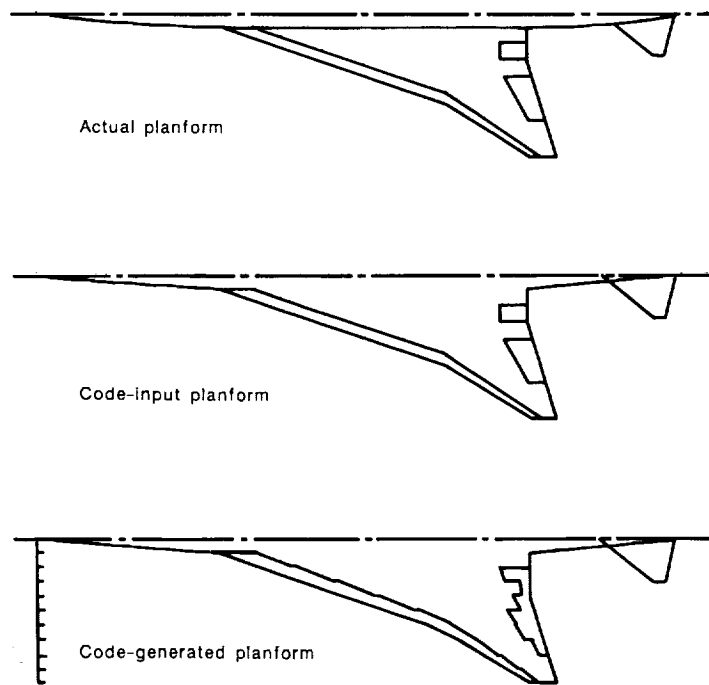
(e) Arrow-wing supersonic transport with horizontal tail.

Figure 2. Concluded.

Legend:
- ○ Experiment
- Theory
  - ━━ ━ ━ With attainable thrust and vortex force
  - ━ ━ ━ ━ Without thrust or vortex
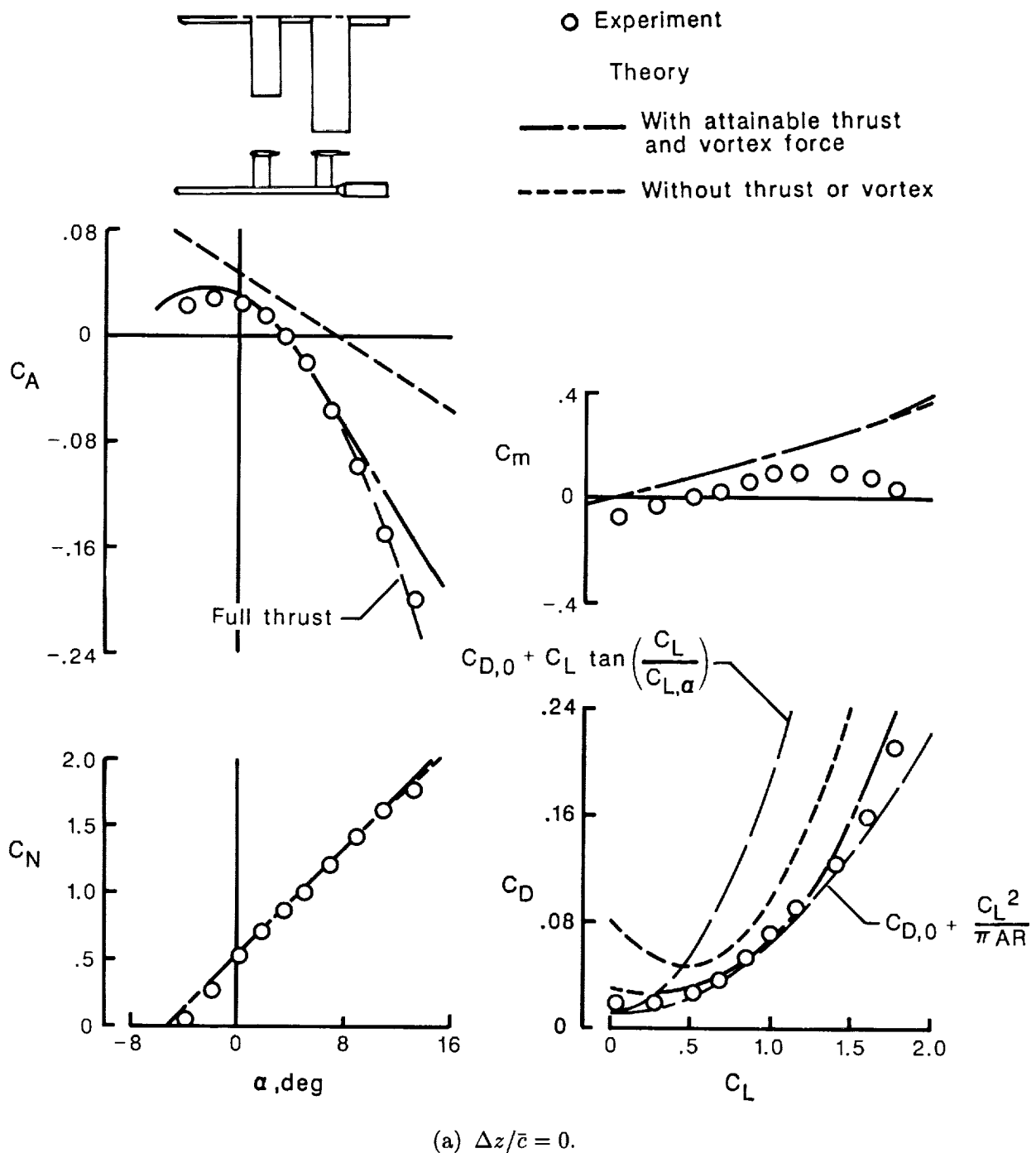
(a) $\Delta z / \bar{c} = 0$.

Figure 3. Theoretical and experimental data for unswept wing-canard configuration at three canard heights. $M = 0.2$; $R = 1.4 \times 10^6$.
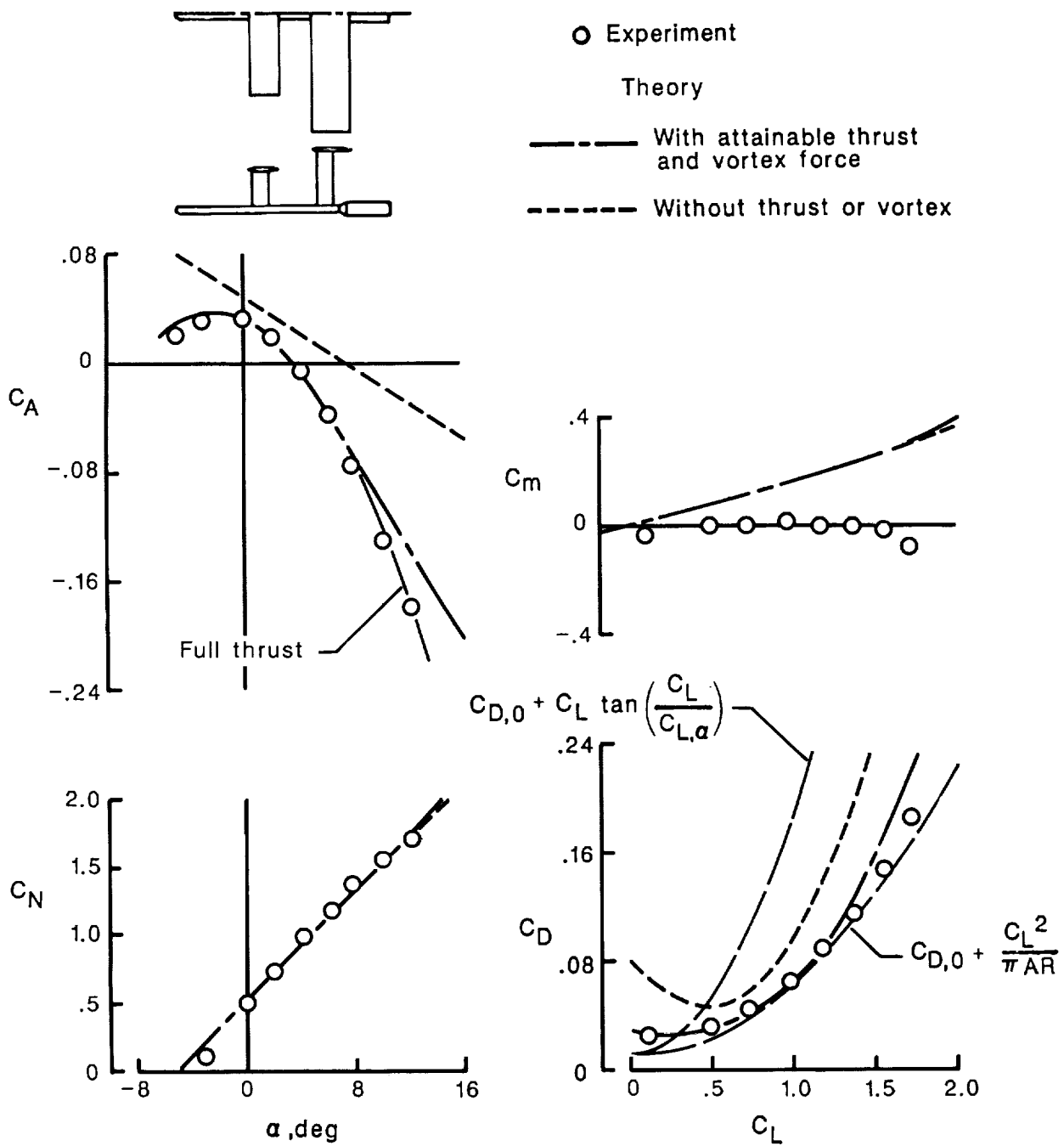
(b) $\Delta z/\bar{c} = -0.5$.

Figure 3. Continued.

O Experiment

Theory

With attainable thrust and vortex force

Without thrust or vortex

(c) $\Delta z / \bar{c} = 0.5$.
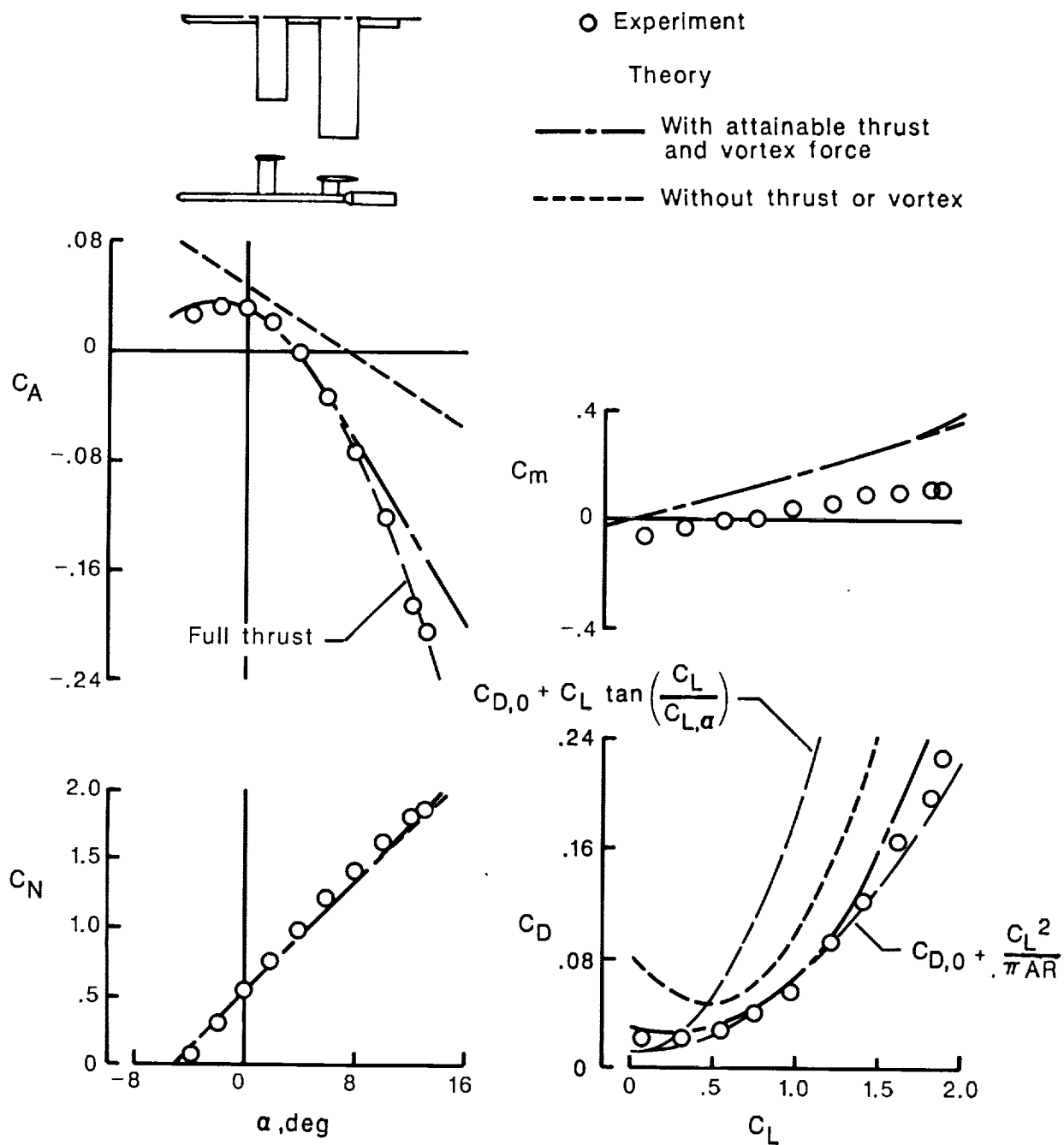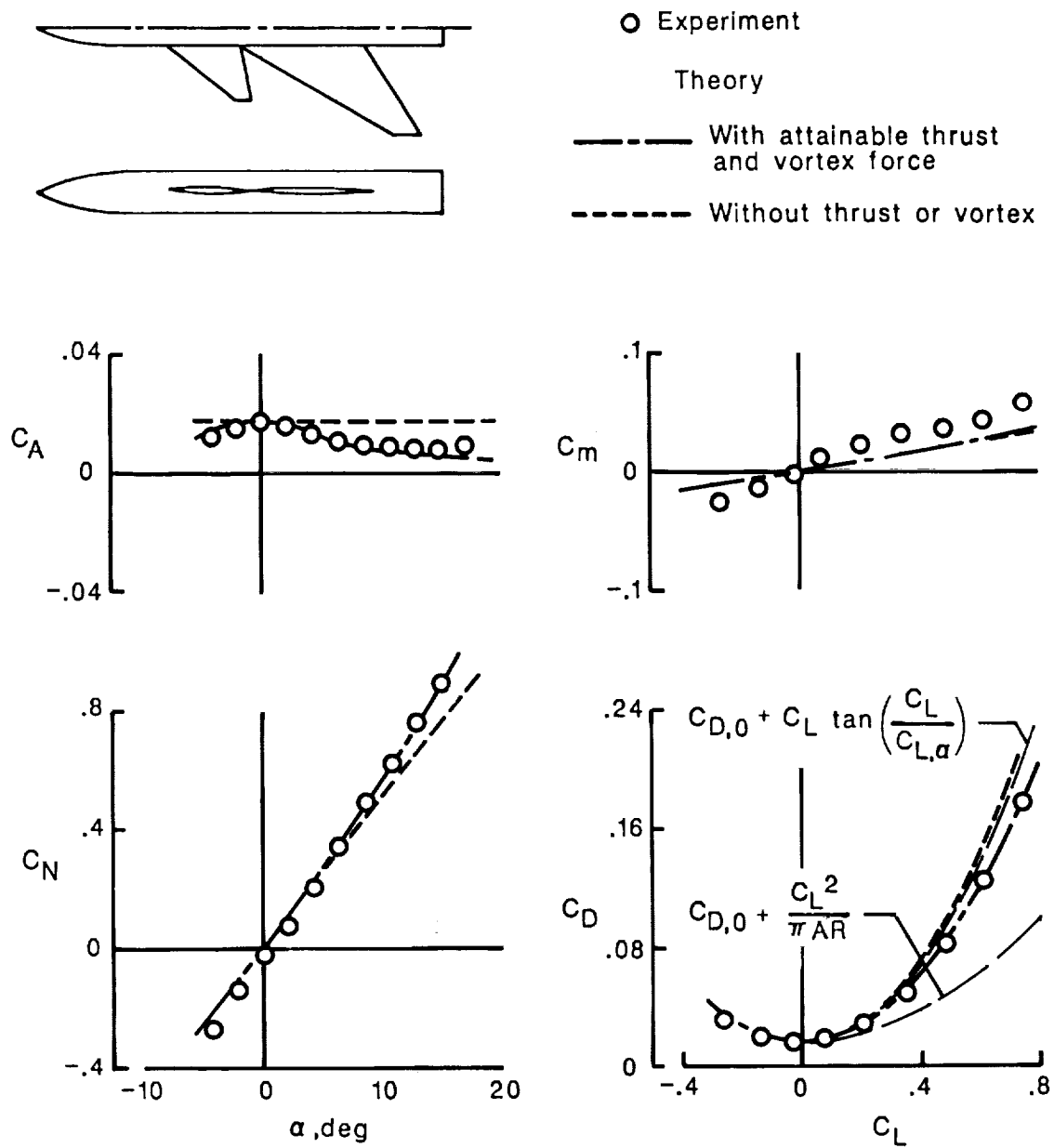
Figure 3. Concluded.

Figure 4. Theoretical and experimental data for 60°-swept trapezoidal-wing fighter with canard at three canard heights. $M = 0.7$; $R = 1.35 \times 10^6$.

(a) $\Delta z/\bar{c} = 0$.

O Experiment

Theory

— - — With attainable thrust
and vortex force

— — — — Without thrust or vortex

$$C_{D,0} + C_L \tan\left(\frac{C_L}{C_{L,\alpha}}\right)$$

$$C_{D,0} + \frac{C_L{}^2}{\pi\,AR}$$
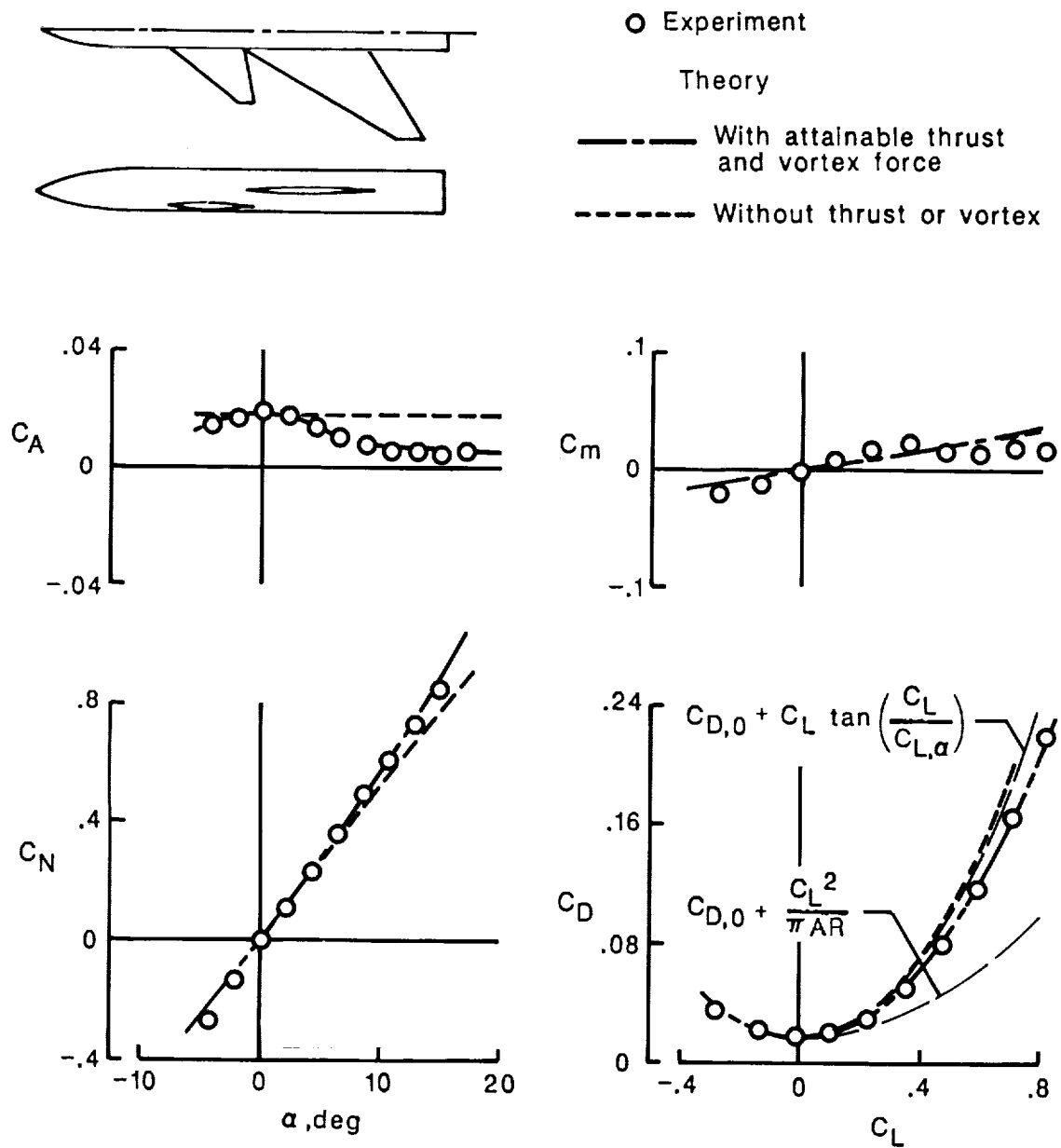
(b) $\Delta z/\bar{c} = -0.185$.

Figure 4. Continued.

Legend:

O Experiment

Theory

——— · ——— With attainable thrust and vortex force

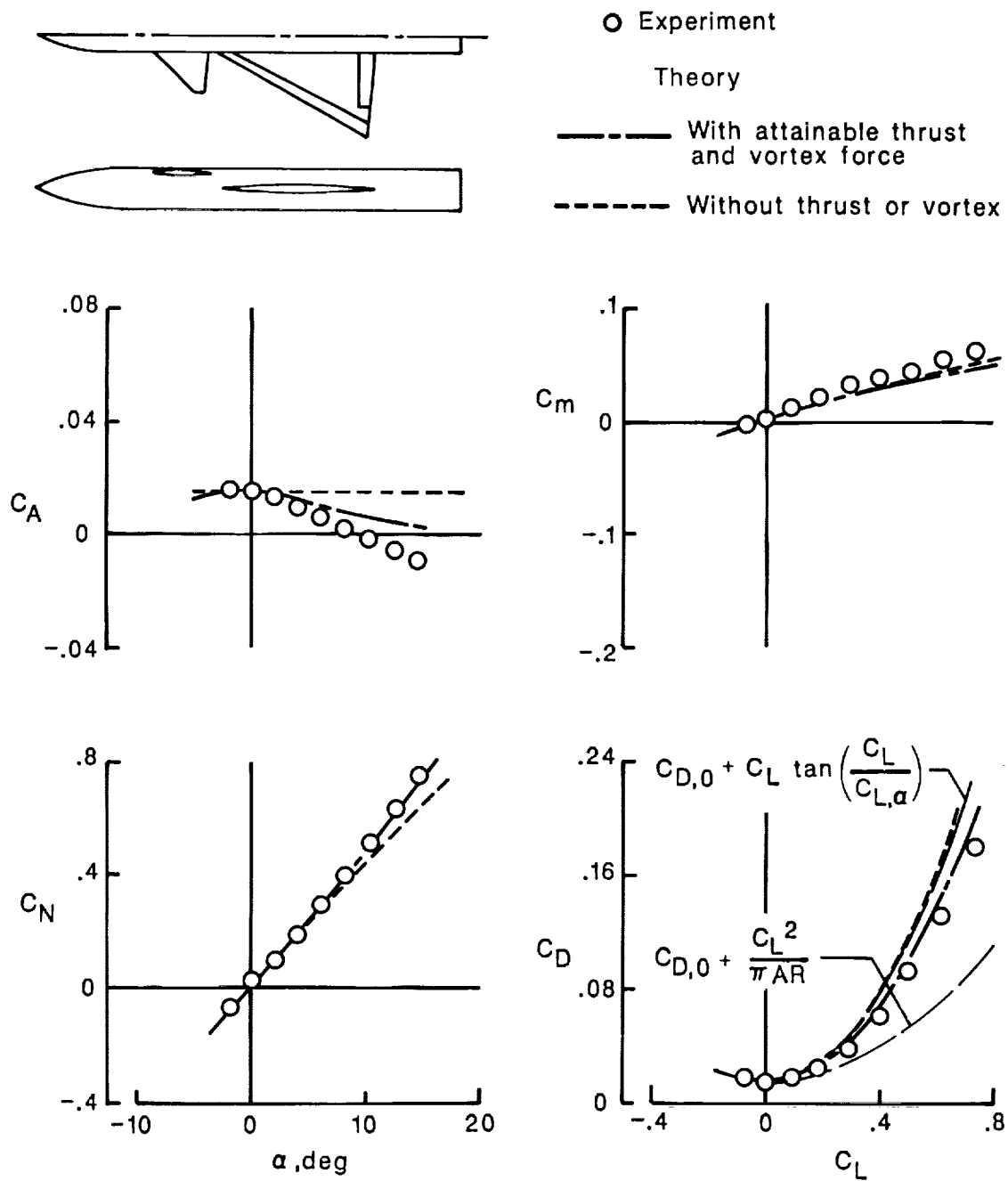— — — — Without thrust or vortex
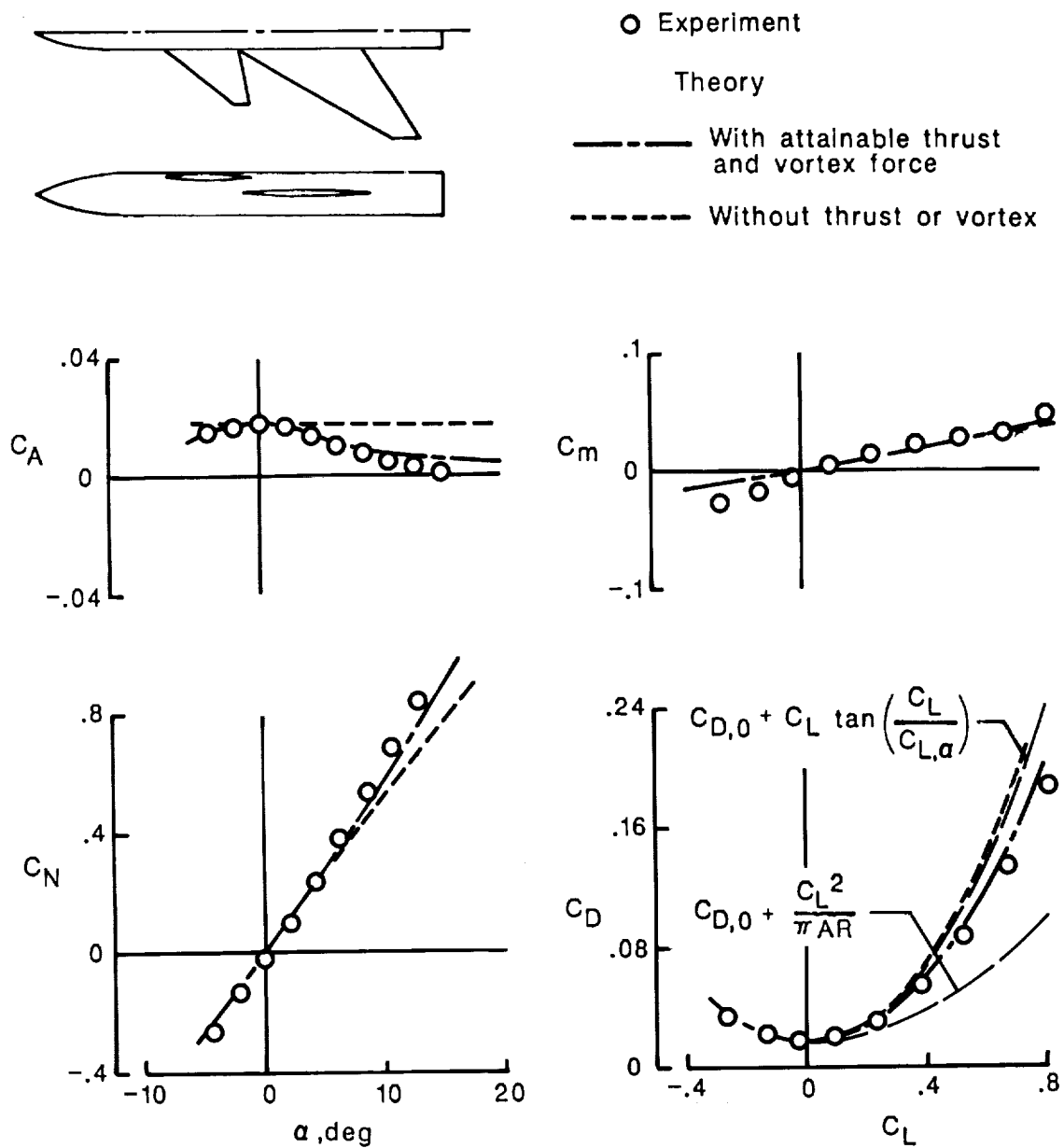
(c) $\Delta z/\bar{c} = 0.185$.

Figure 4. Concluded.
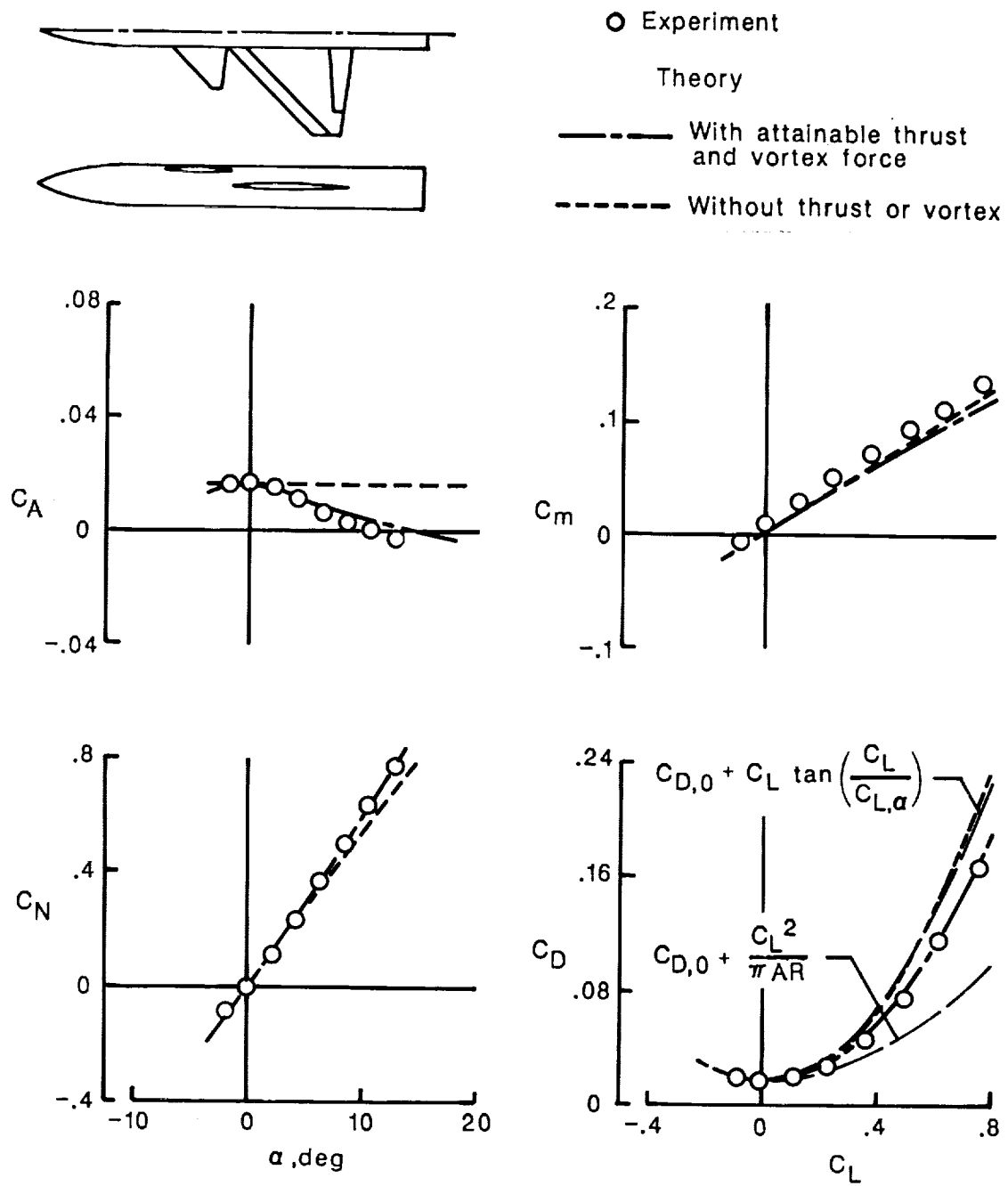
(a) $\delta_{L,n} = 0°$, $\delta_{T,n} = 0°$, $\delta_C = 0°$.

Figure 5. Theoretical and experimental data for 44°-swept trapezoidal-wing fighter with canard. $M = 0.4$; $R = 1.9 \times 10^6$.
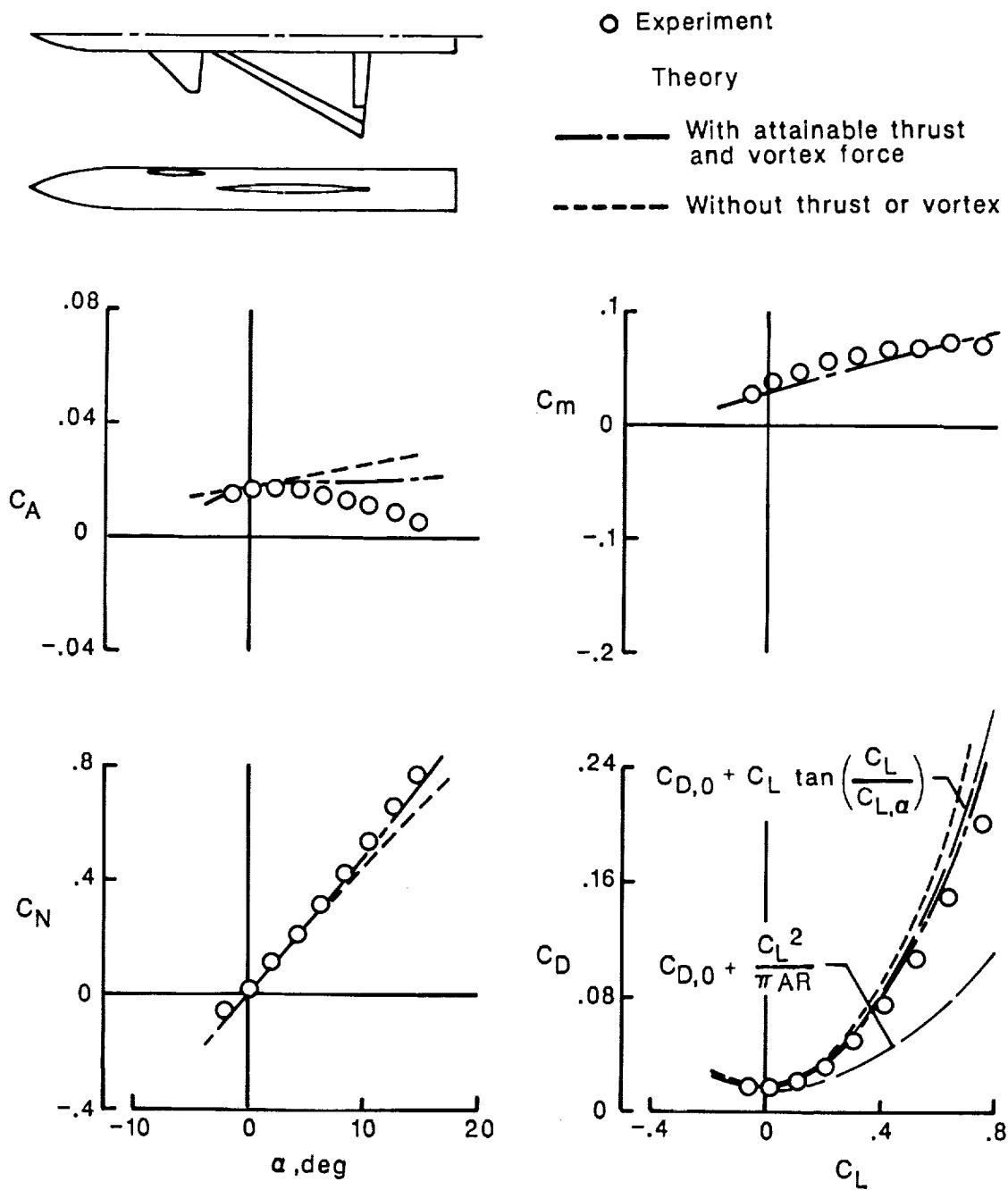
O Experiment

Theory

——— · —— With attainable thrust
and vortex force

— — — — Without thrust or vortex
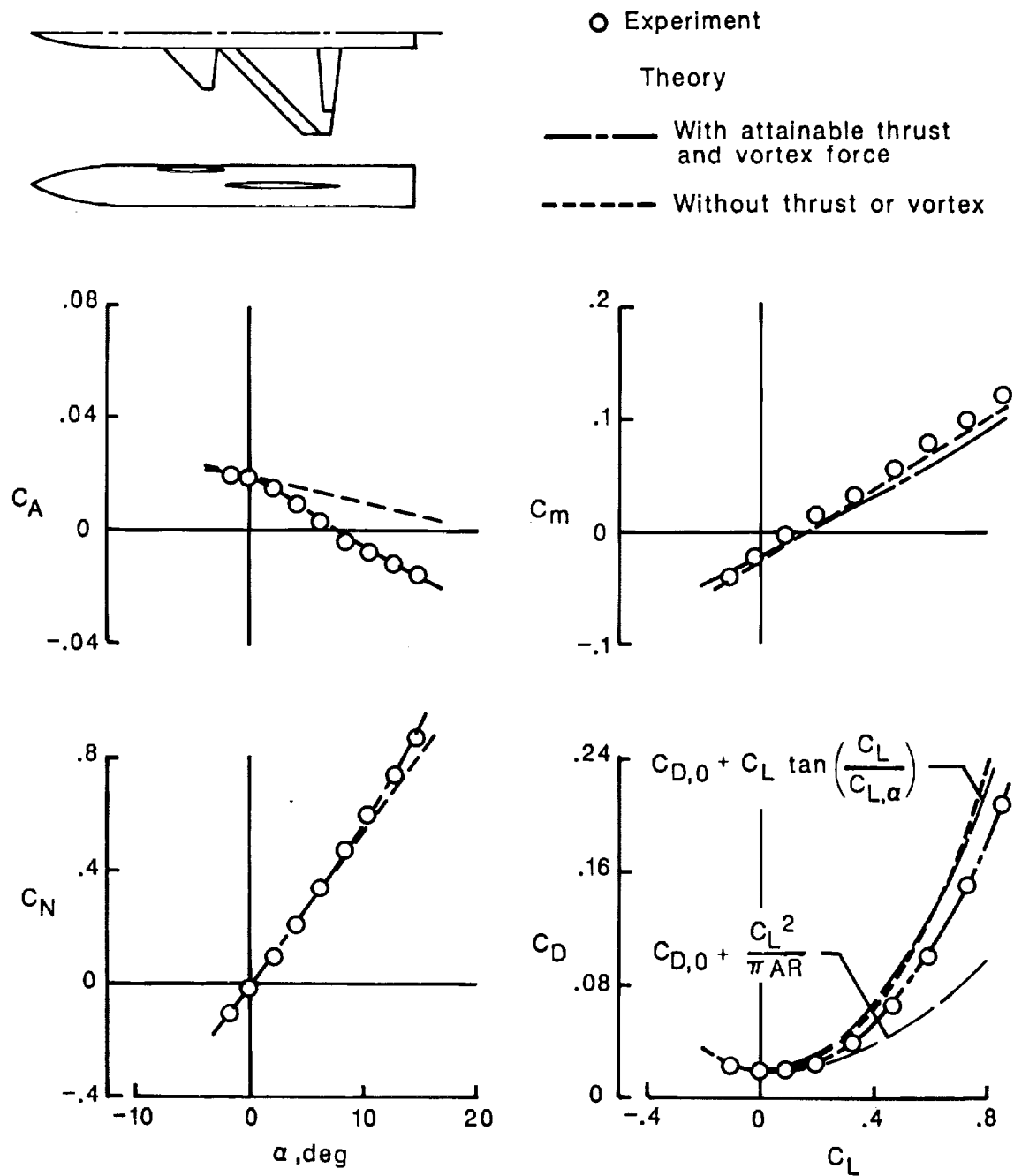
(b) $\delta_{L,n} = 0°$, $\delta_{T,n} = 0°$, $\delta_C = -5°$.

Figure 5. Continued.

○ Experiment

Theory

—— · —— With attainable thrust
and vortex force

— — — — Without thrust or vortex
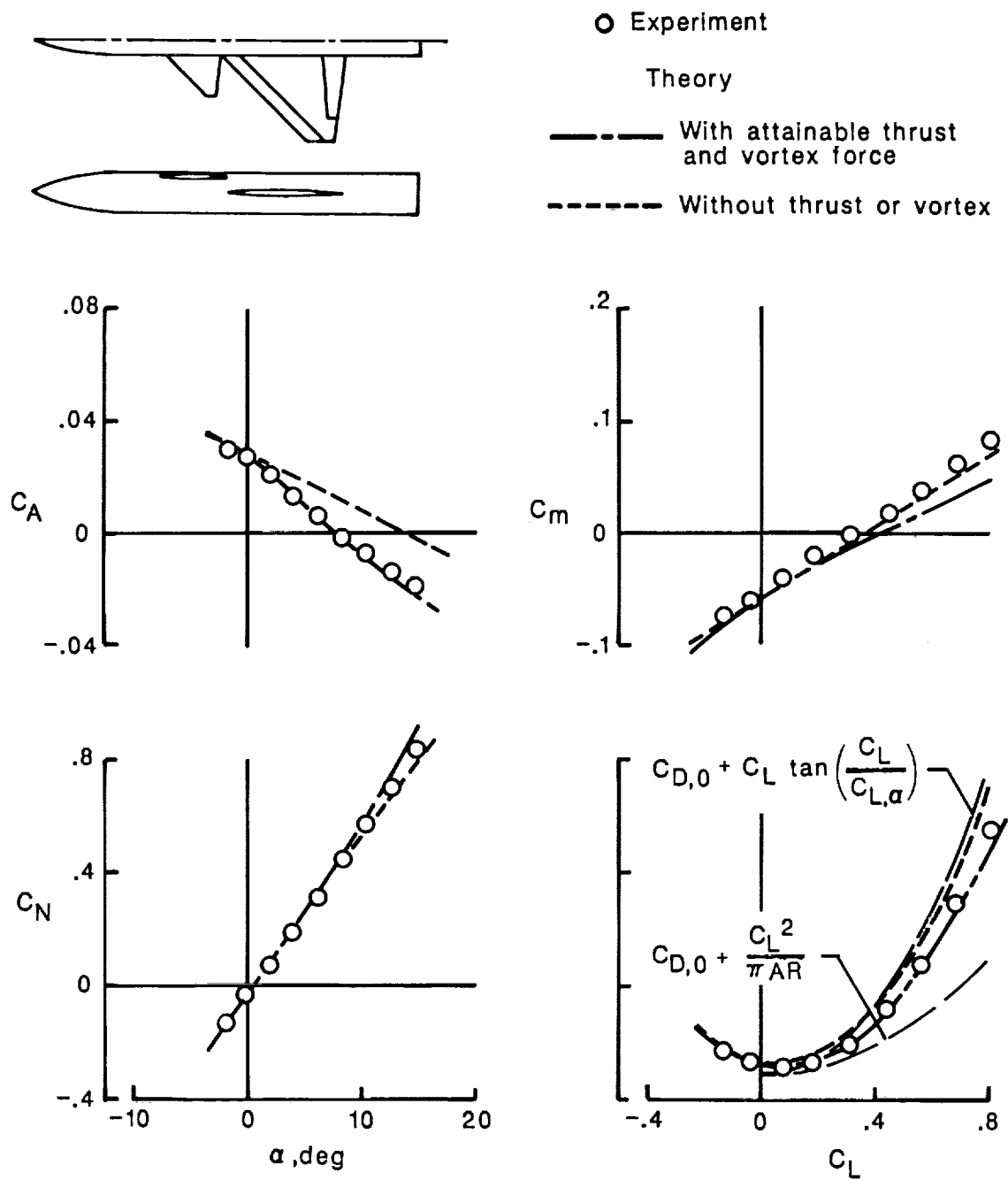
(c) $\delta_{L,n} = 0°$, $\delta_{T,n} = 0°$, $\delta_C = -10°$.

Figure 5. Continued.

O Experiment

Theory

—— —— With attainable thrust
and vortex force

—————— Without thrust or vortex
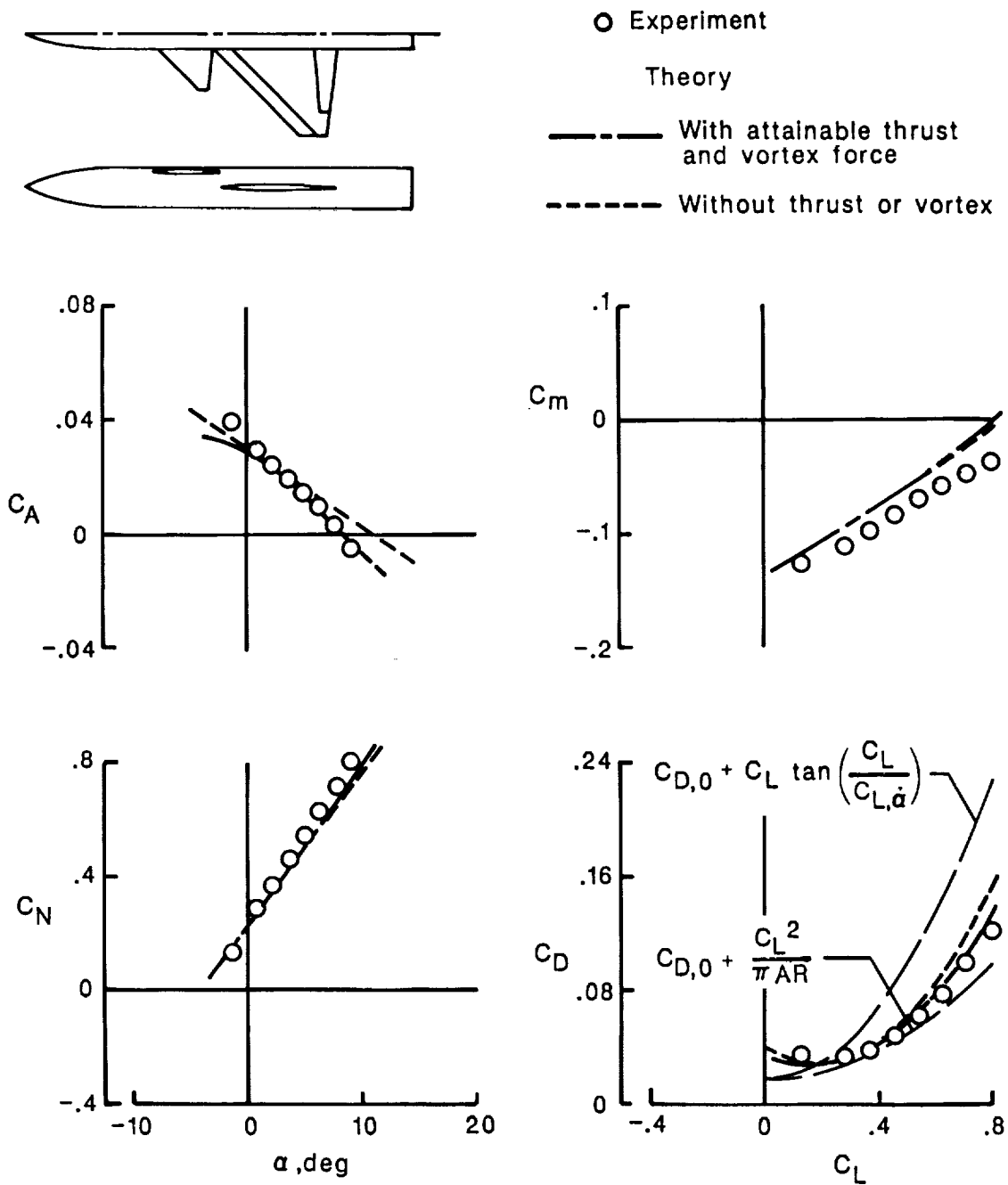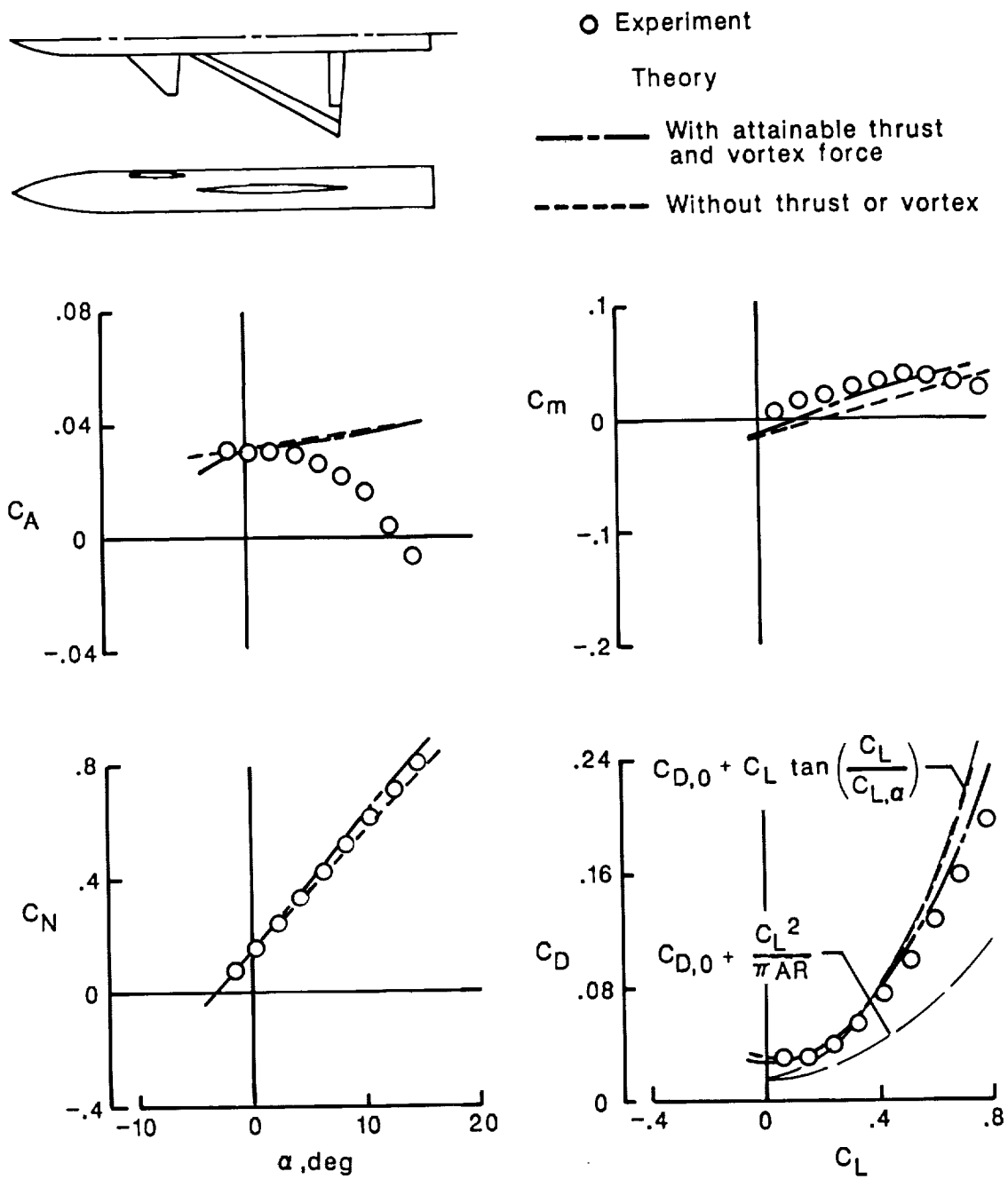
(d) $\delta_{L,n} = 12°$, $\delta_{T,n} = 12°$, $\delta_C = 0°$.

Figure 5. Continued.

(e) $\delta_{L,n} = 12°$, $\delta_{T,n} = 12°$, $\delta_C = -10°$.

Figure 5. Continued.

O Experiment

Theory

With attainable thrust and vortex force

Without thrust or vortex

(f) $\delta_{L,n} = 12°$, $\delta_{T,n} = 12°$, $\delta_C = 10°$.

Figure 5. Continued.

O Experiment

Theory

With attainable thrust and vortex force

Without thrust or vortex
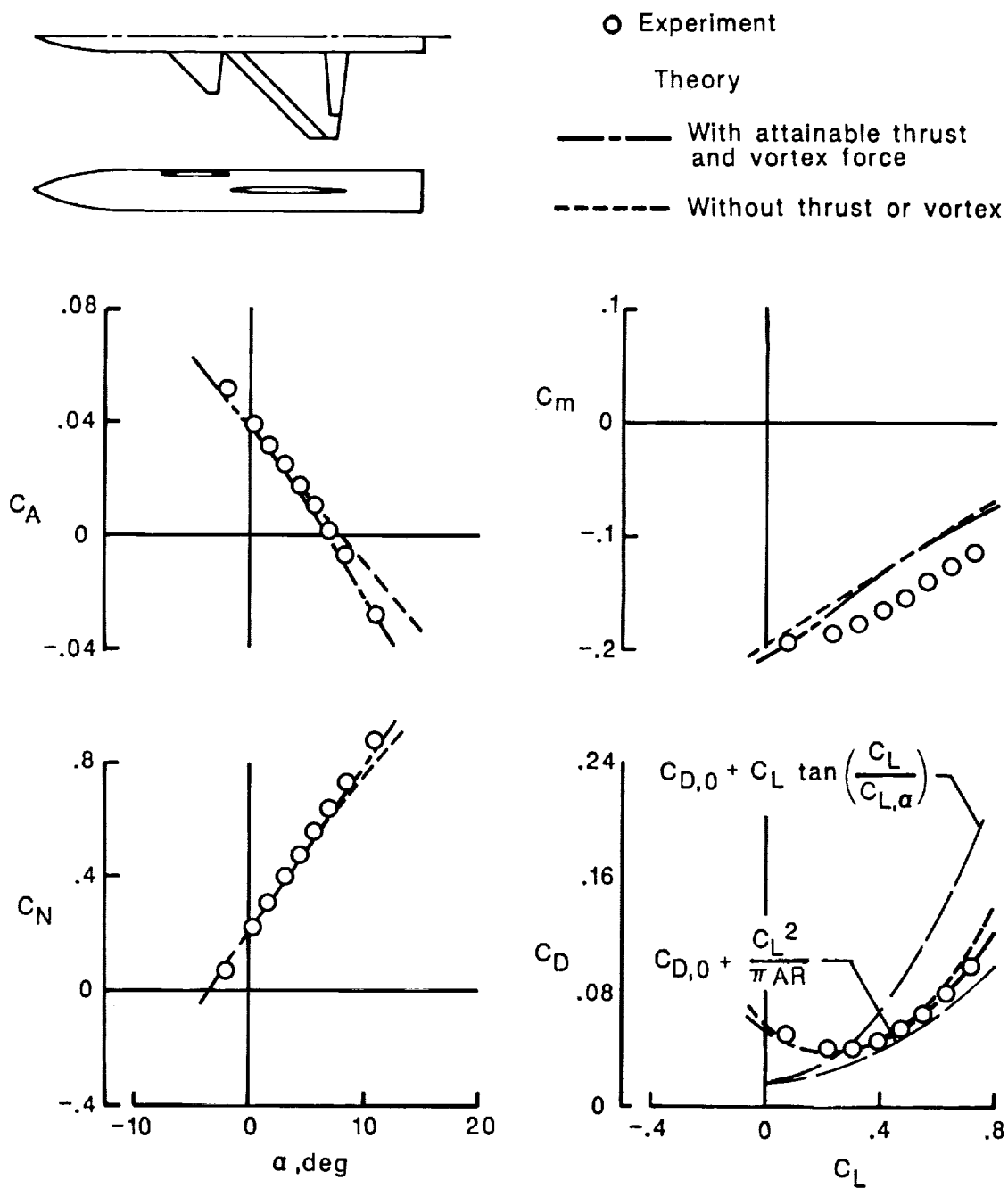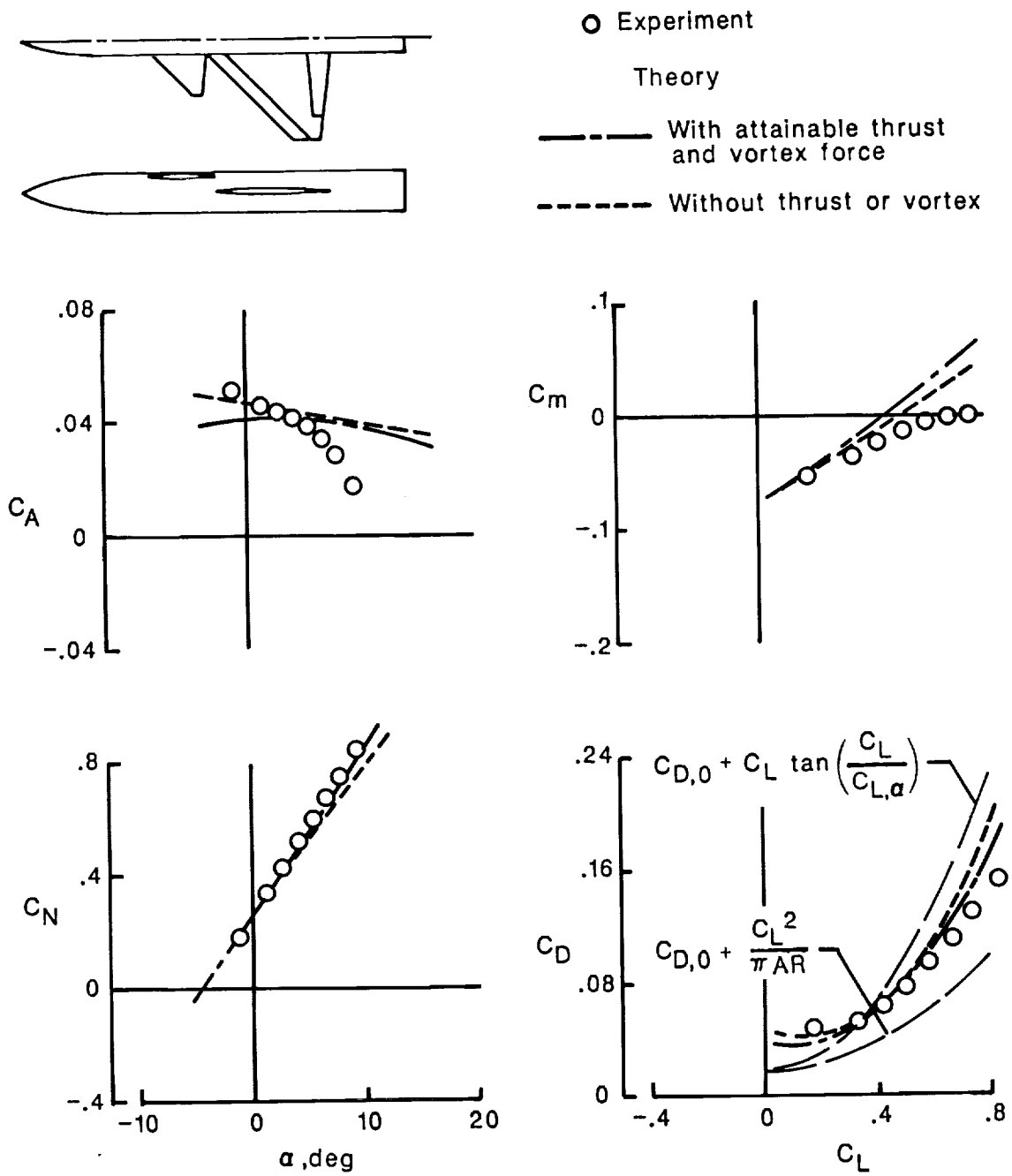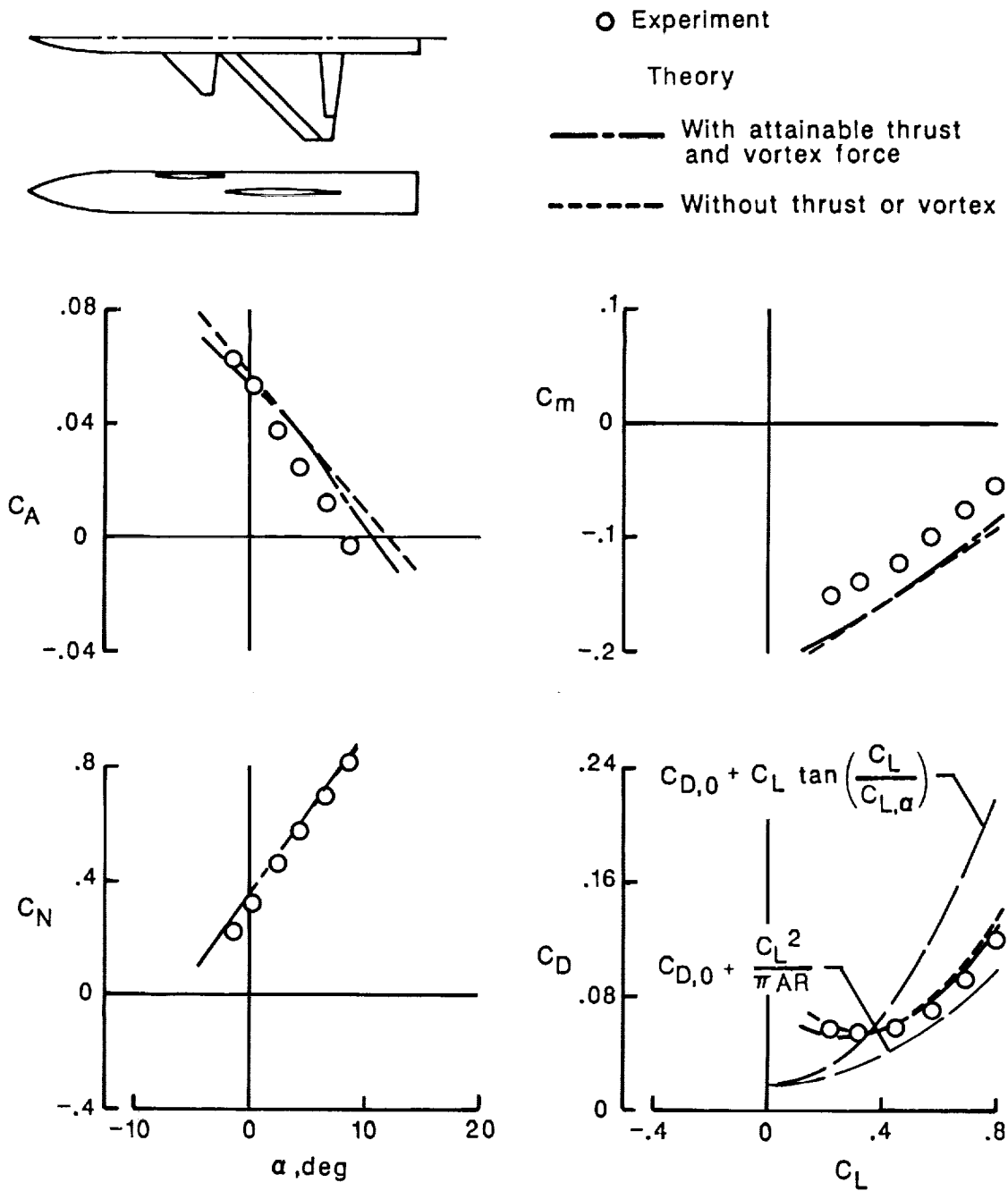
(g) $\delta_{L,n} = 20°$, $\delta_{T,n} = 20°$, $\delta_C = 0°$.

Figure 5. Continued.
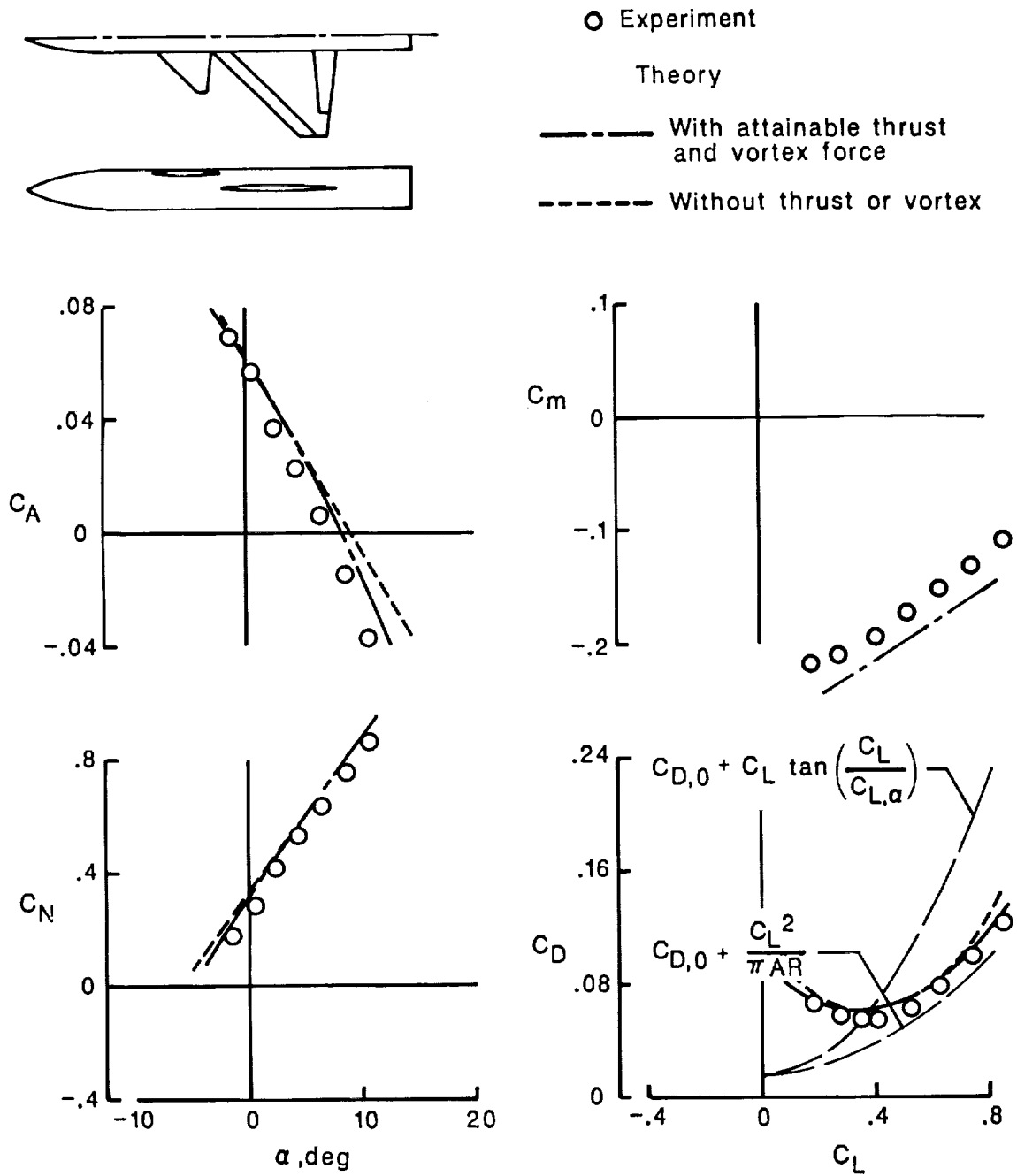
Figure 5. Continued.

(h) $\delta_{L,n} = 20°$, $\delta_{T,n} = 20°$, $\delta_C = -10°$.

(i) $\delta_{L,n} = 20°$, $\delta_{T,n} = 20°$, $\delta_C = 10°$.

Figure 5. Concluded.
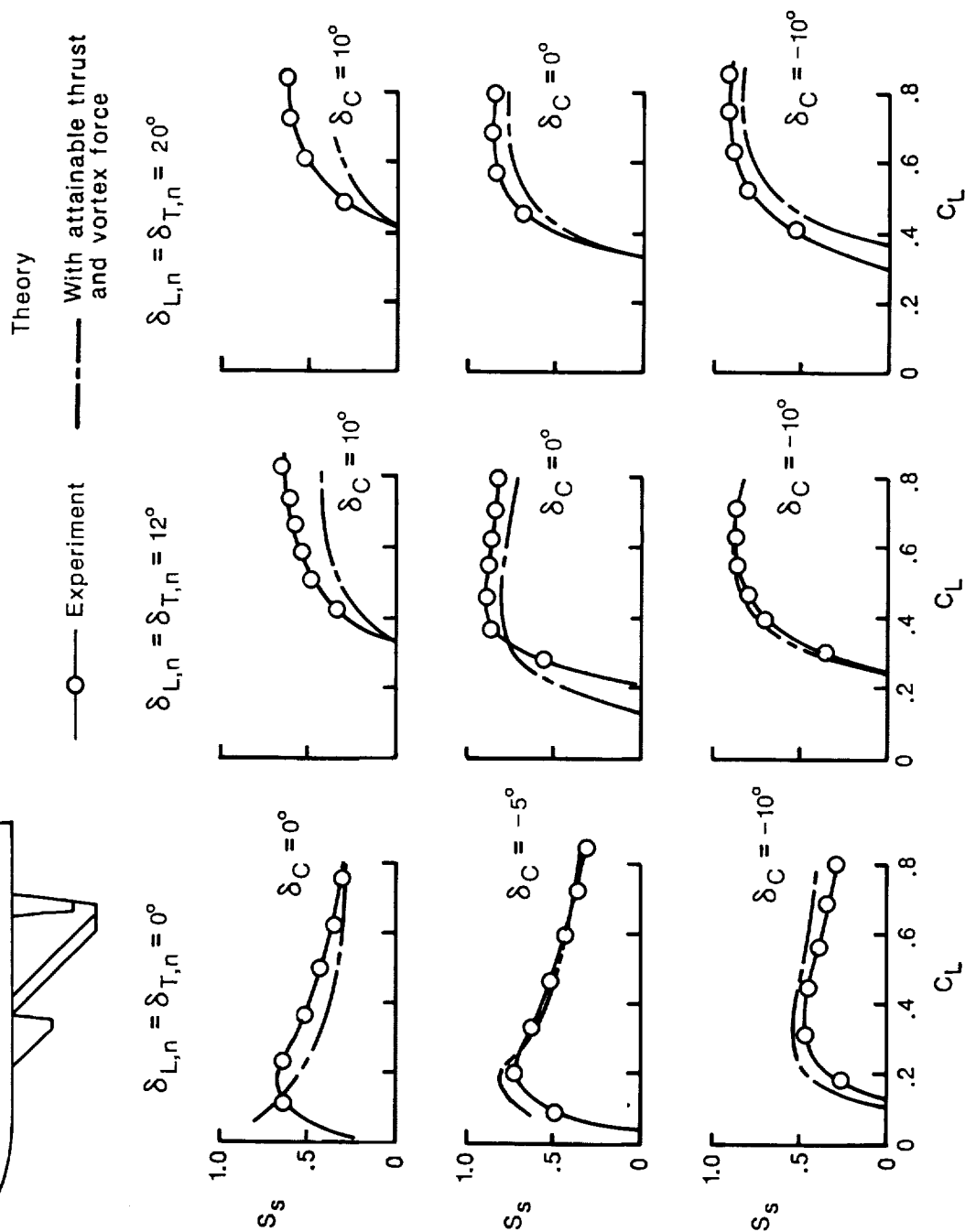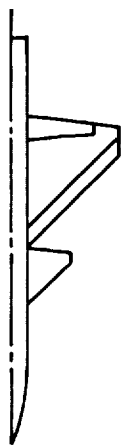
Figure 6. Suction-parameter variation with lift coefficient for various combinations of flap deflection angle and canard incidence angle for 44°-swept trapezoidal-wing fighter with canard. $M = 0.4$; $R = 1.9 \times 10^6$.
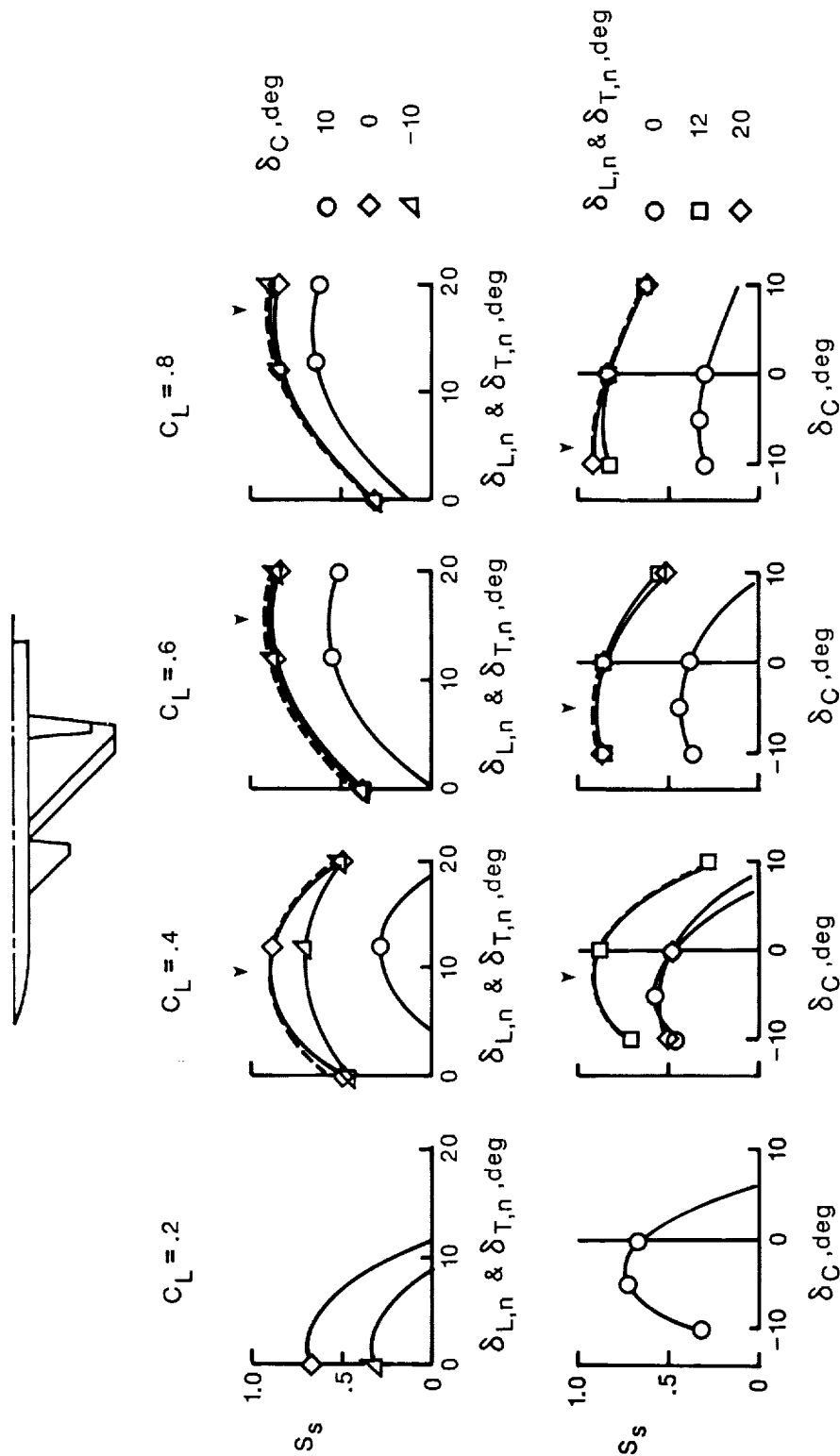
Figure 7. Experimental suction-parameter variation with flap deflection angle and canard incidence angle for selected lift coefficients for 44°-swept trapezoidal-wing fighter with canard. $M = 0.4$; $R = 1.9 \times 10^6$; dashed lines indicate envelope curves, and arrows indicate optimum deflections.

O Experiment

Theory

━━ ━ ━ With attainable thrust
and vortex force
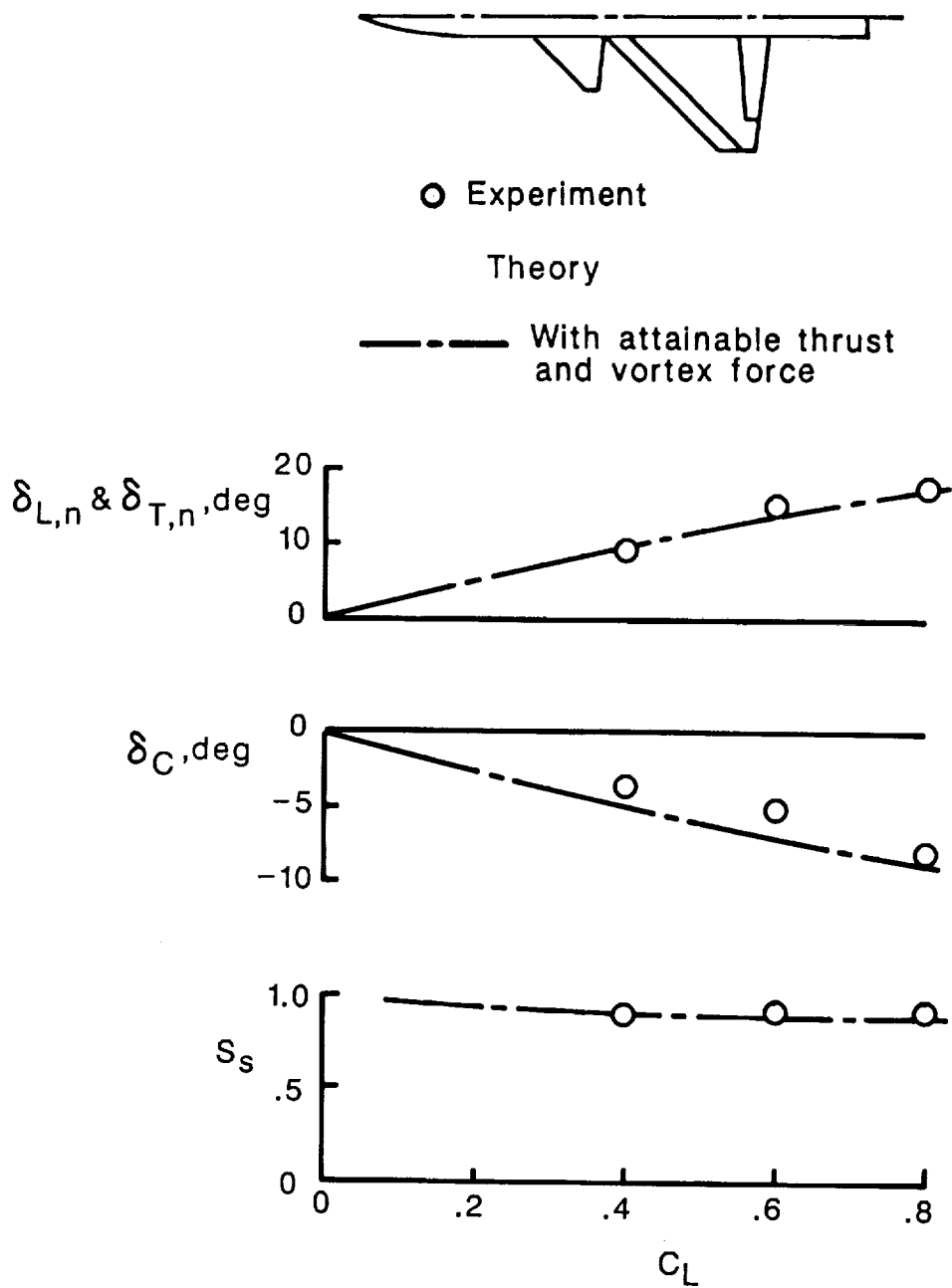
Figure 8. Optimum flap deflection angle, canard incidence angle, and maximum suction-parameter variation with lift coefficient for 44°-swept trapezoidal-wing fighter with canard. $M = 0.4$; $R = 1.9 \times 10^6$.

O Experiment

Theory

— - — With attainable thrust
and vortex force
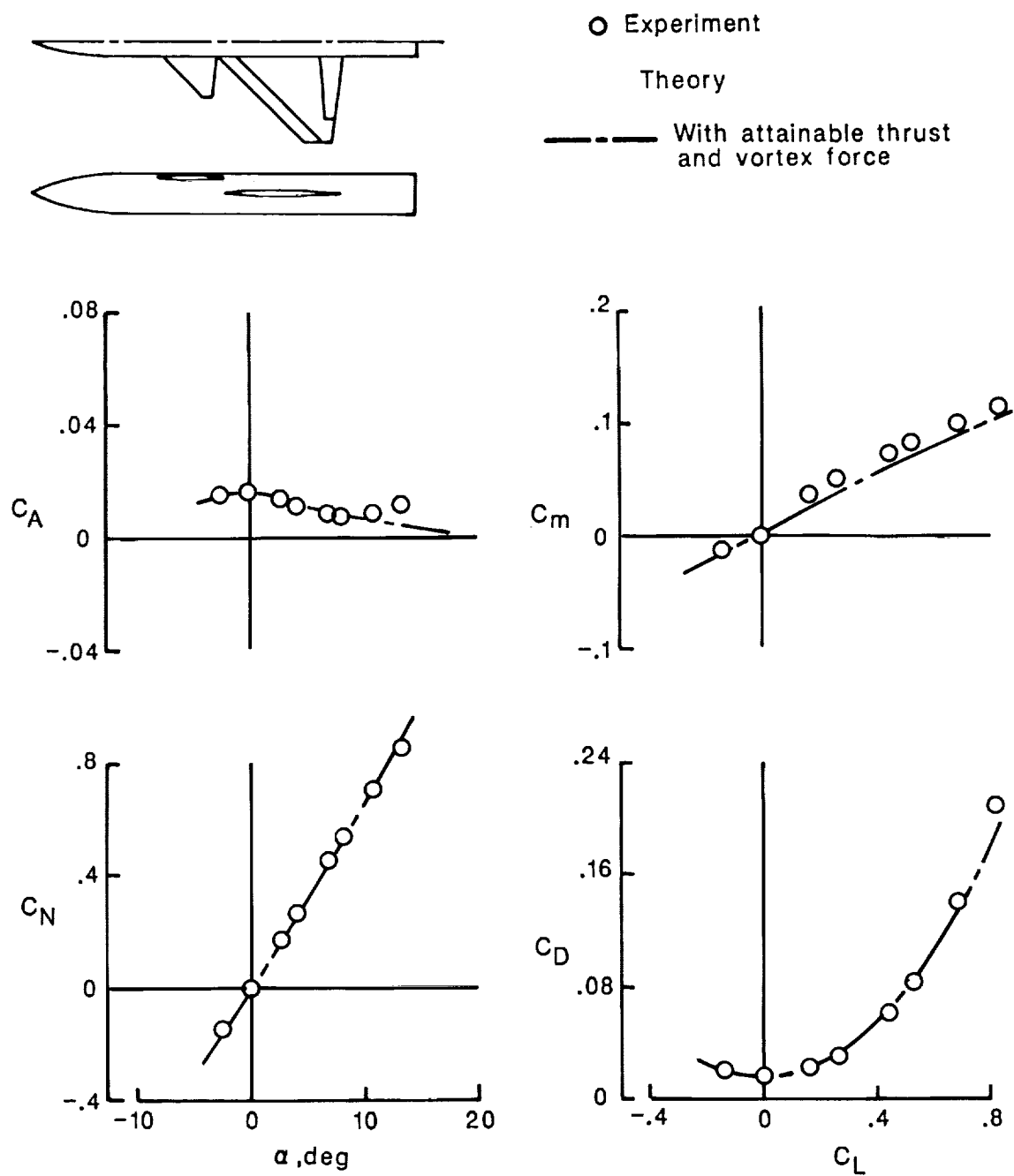
(a) $\delta_{L,n} = 0°$, $\delta_{T,n} = 0°$, $\delta_C = 0°$.

Figure 9. Theoretical and experimental data for 44°-swept trapezoidal-wing fighter with canard. $M = 0.8$; $R = 2.58 \times 10^6$.

O Experiment

Theory

—— — With attainable thrust
and vortex force
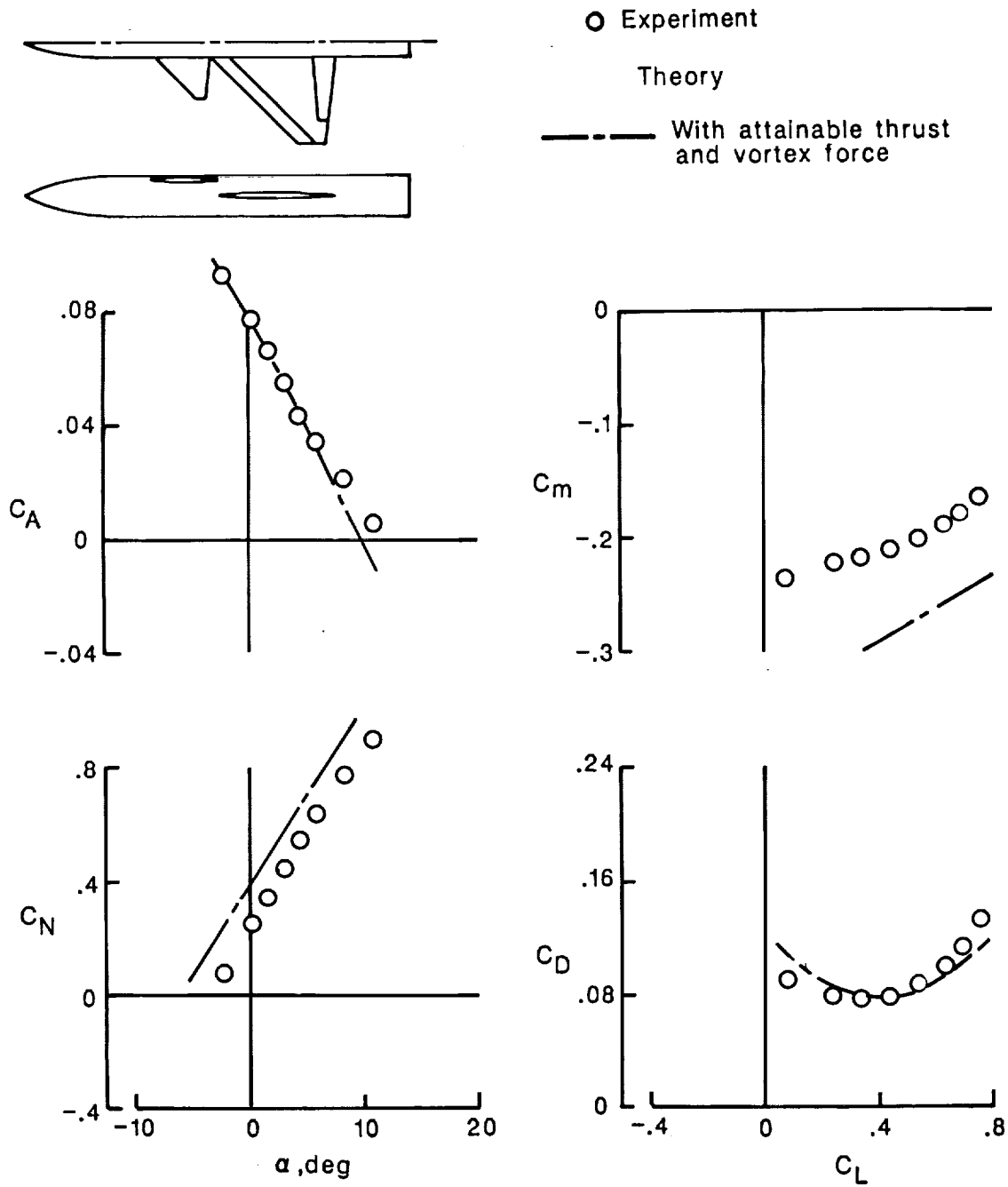
(b) $\delta_{L,n} = 20°$, $\delta_{T,n} = 20°$, $\delta_C = -10°$.

Figure 9. Concluded.

O Experiment

Theory

— ⸱— ⸱ — With attainable thrust and vortex force

— — — — Without thrust or vortex
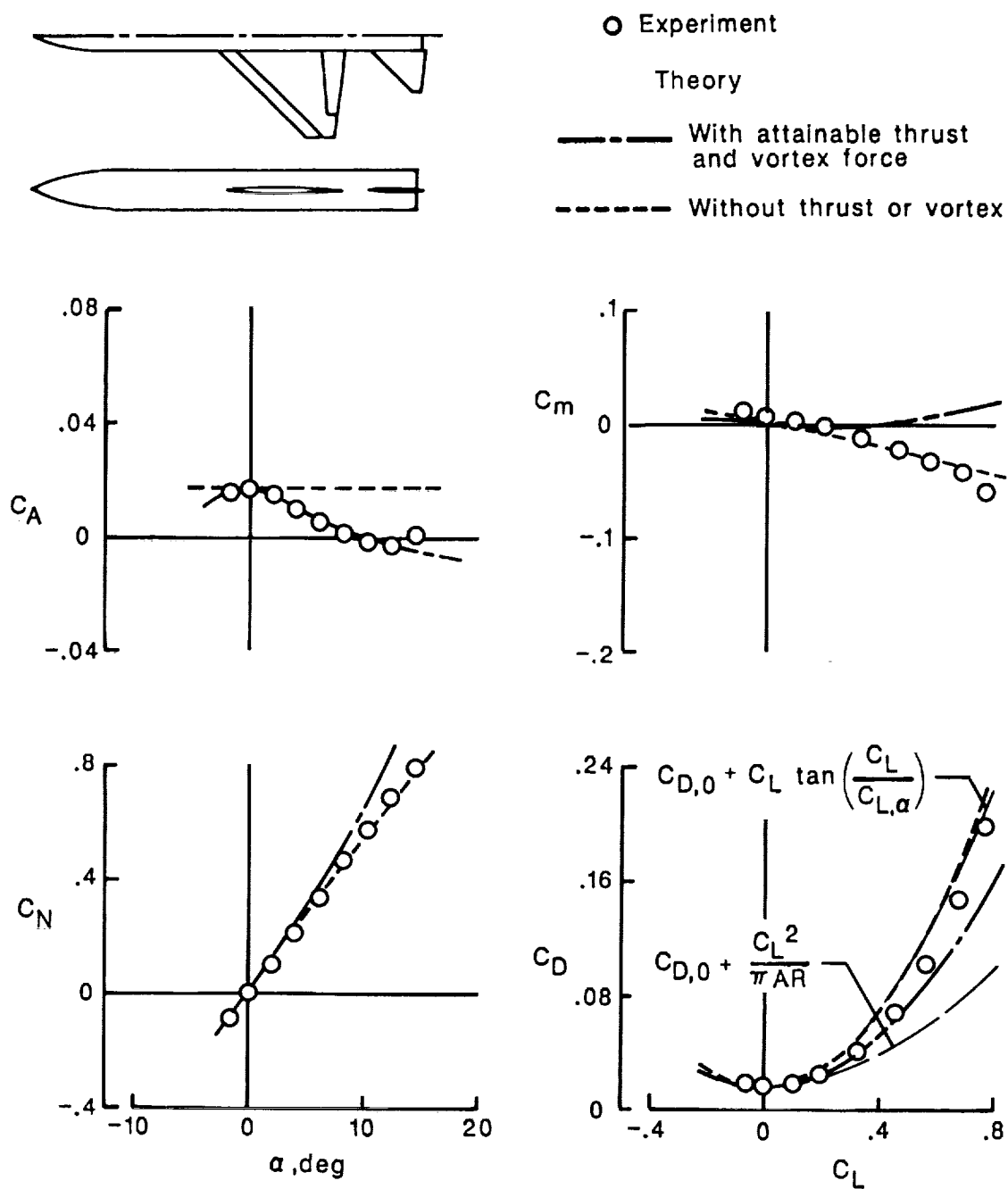
(a) $\delta_{L,n} = 0°$, $\delta_{T,n} = 0°$, $\delta_H = 0°$.

Figure 10. Theoretical and experimental data for 44°-swept trapezoidal-wing fighter with horizontal tail at $M = 0.4$ and $R = 1.9 \times 10^6$.

Legend:

○ Experiment

Theory

— ·· — With attainable thrust and vortex force

— — — — Without thrust or vortex

(b) $\delta_{L,n} = 0°$, $\delta_{T,n} = 0°$, $\delta_H = -5°$.

Figure 10. Continued.

○ Experiment

Theory

—— ·· —— With attainable thrust and vortex force

------- Without thrust or vortex

(c) $\delta_{L,n} = 0°$, $\delta_{T,n} = 0°$, $\delta_H = 5°$.

Figure 10. Continued.

O Experiment

Theory

With attainable thrust and vortex force

Without thrust or vortex
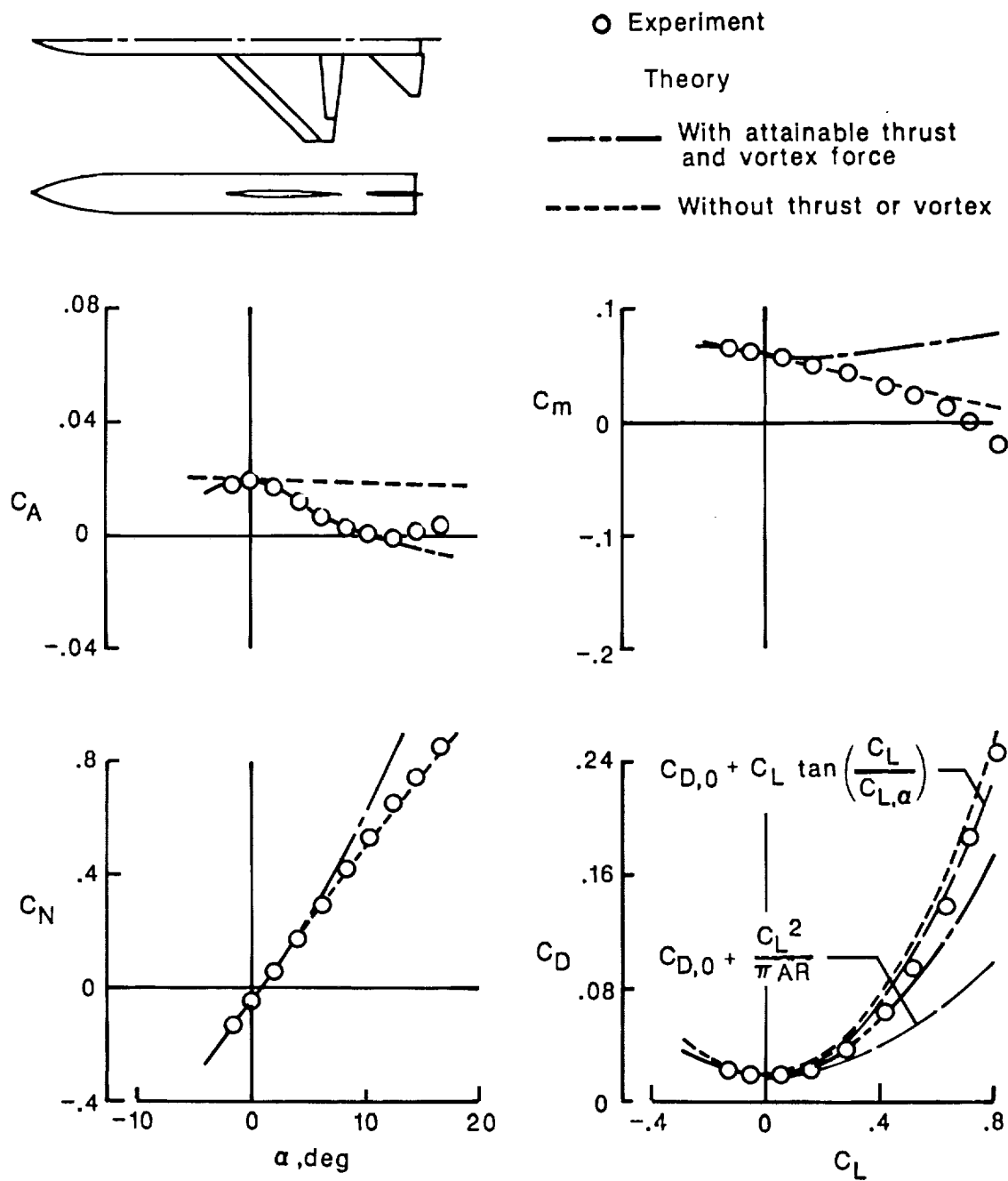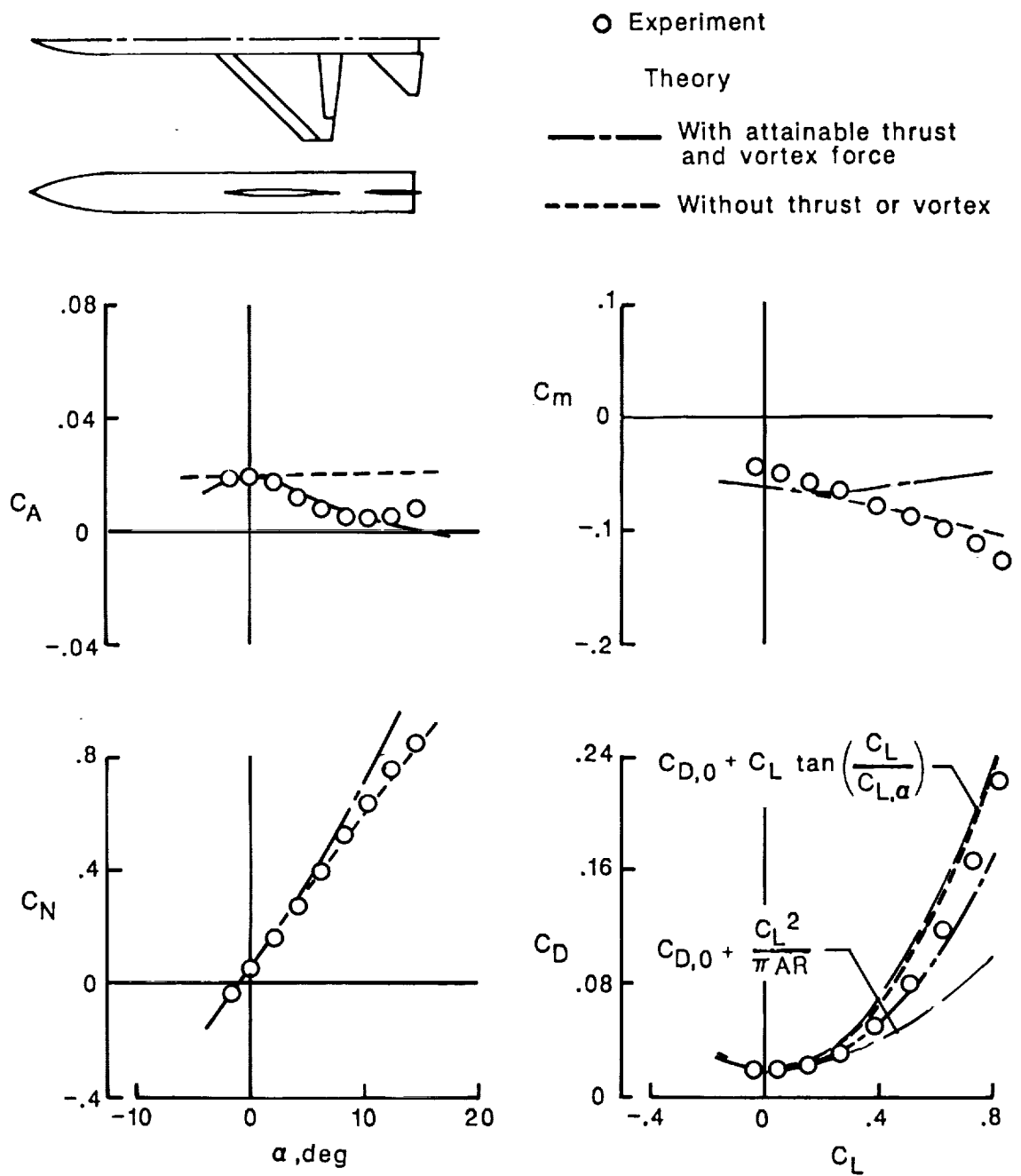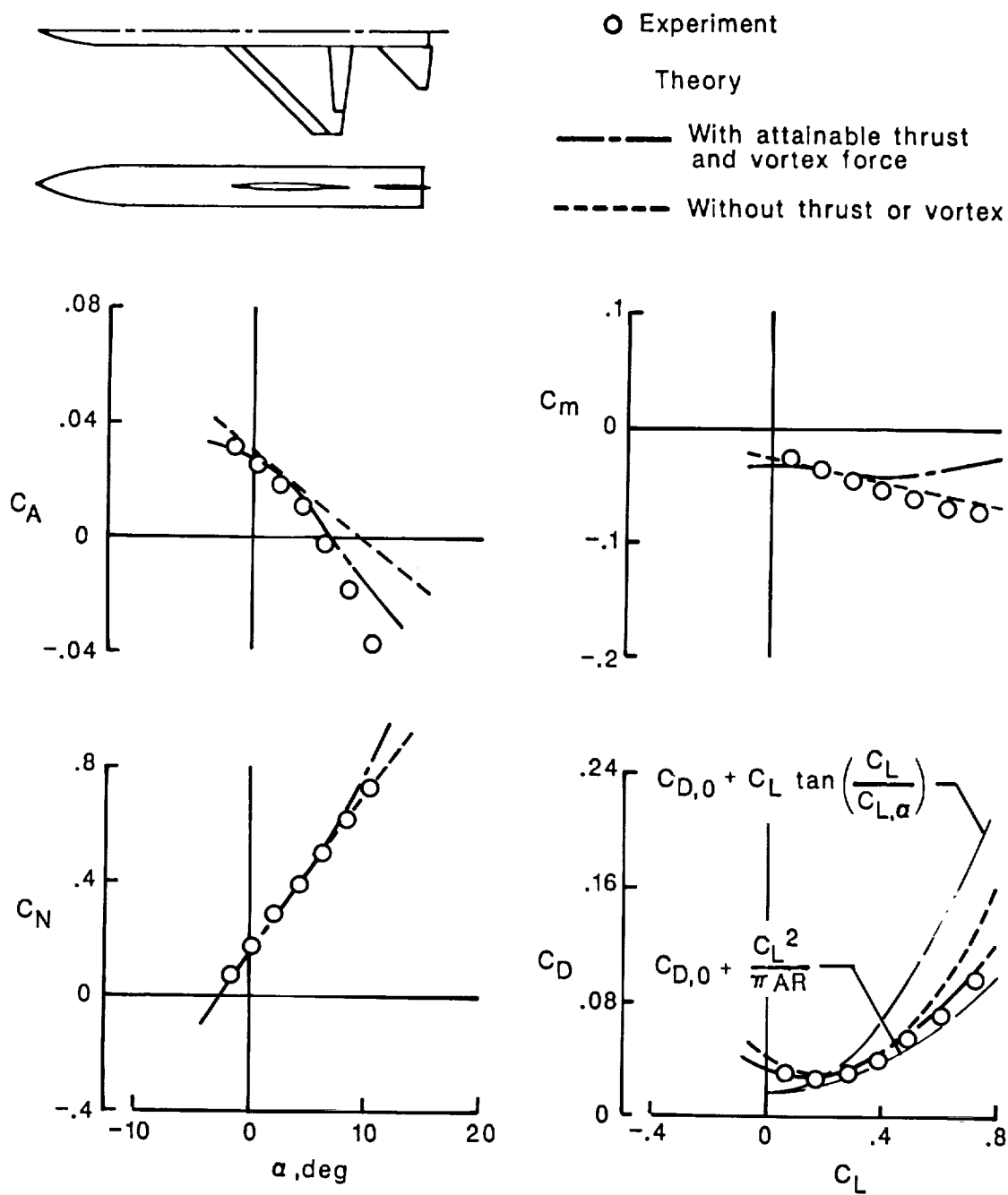
(d) $\delta_{L,n} = 12°$, $\delta_{T,n} = 12°$, $\delta_H = 0°$.

Figure 10. Continued.

○ Experiment

Theory

——— ⋅ ——— With attainable thrust and vortex force

——————— Without thrust or vortex

(e) $\delta_{L,n} = 12°$, $\delta_{T,n} = 12°$, $\delta_H = -10°$.

Figure 10. Continued.

Experiment — ○

Theory

With attainable thrust and vortex force

Without thrust or vortex

C_A, C_m, C_N, C_D plotted against α, deg and C_L.

$$C_{D,0} + C_L \tan\left(\frac{C_L}{C_{L,\alpha}}\right)$$

$$C_{D,0} + \frac{C_L^2}{\pi AR}$$

(f) $\delta_{L,n} = 12°$, $\delta_{T,n} = 12°$, $\delta_H = 10°$.

Figure 10. Continued.

O Experiment

Theory

—— - —— With attainable thrust
and vortex force

— — — — — Without thrust or vortex
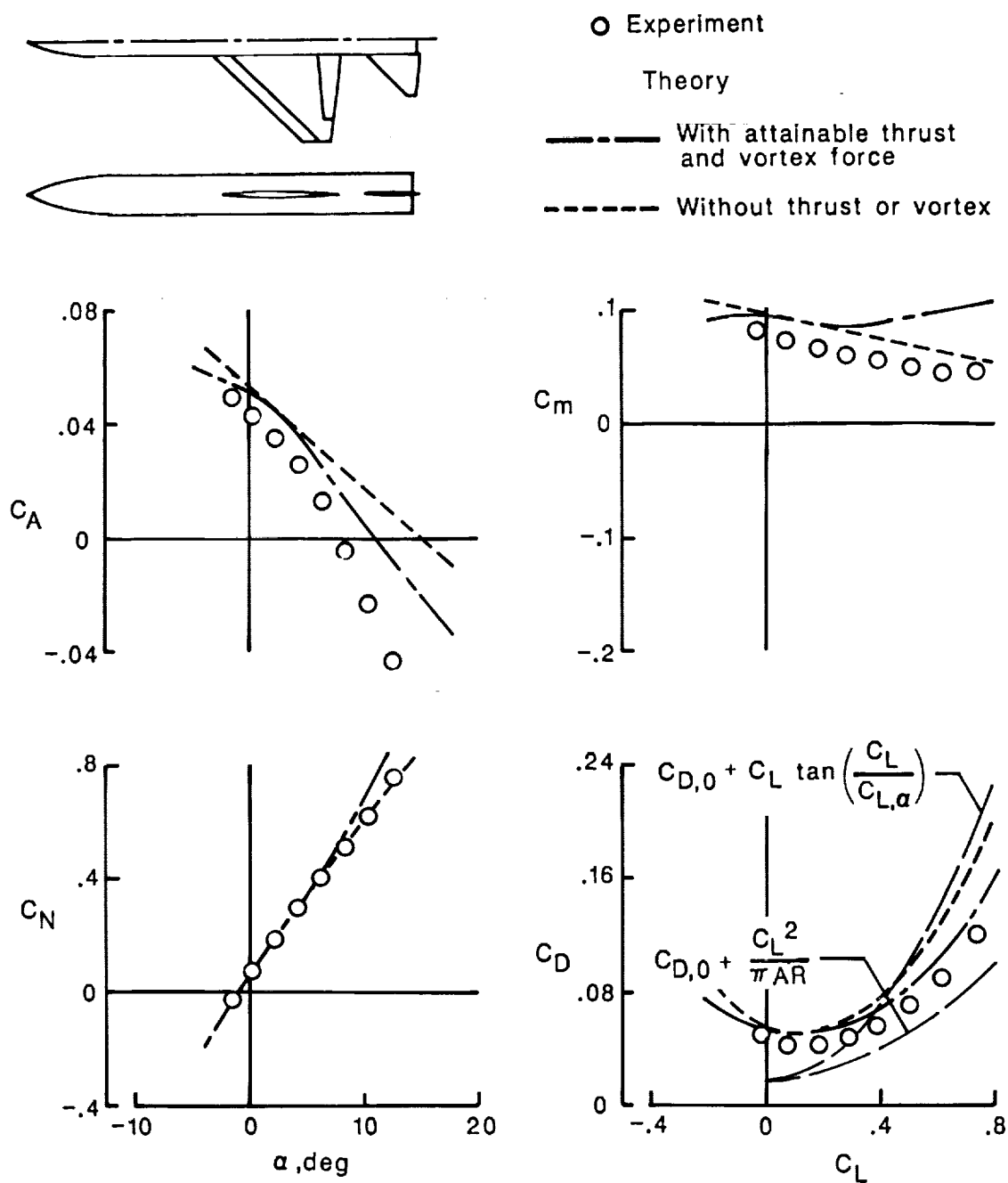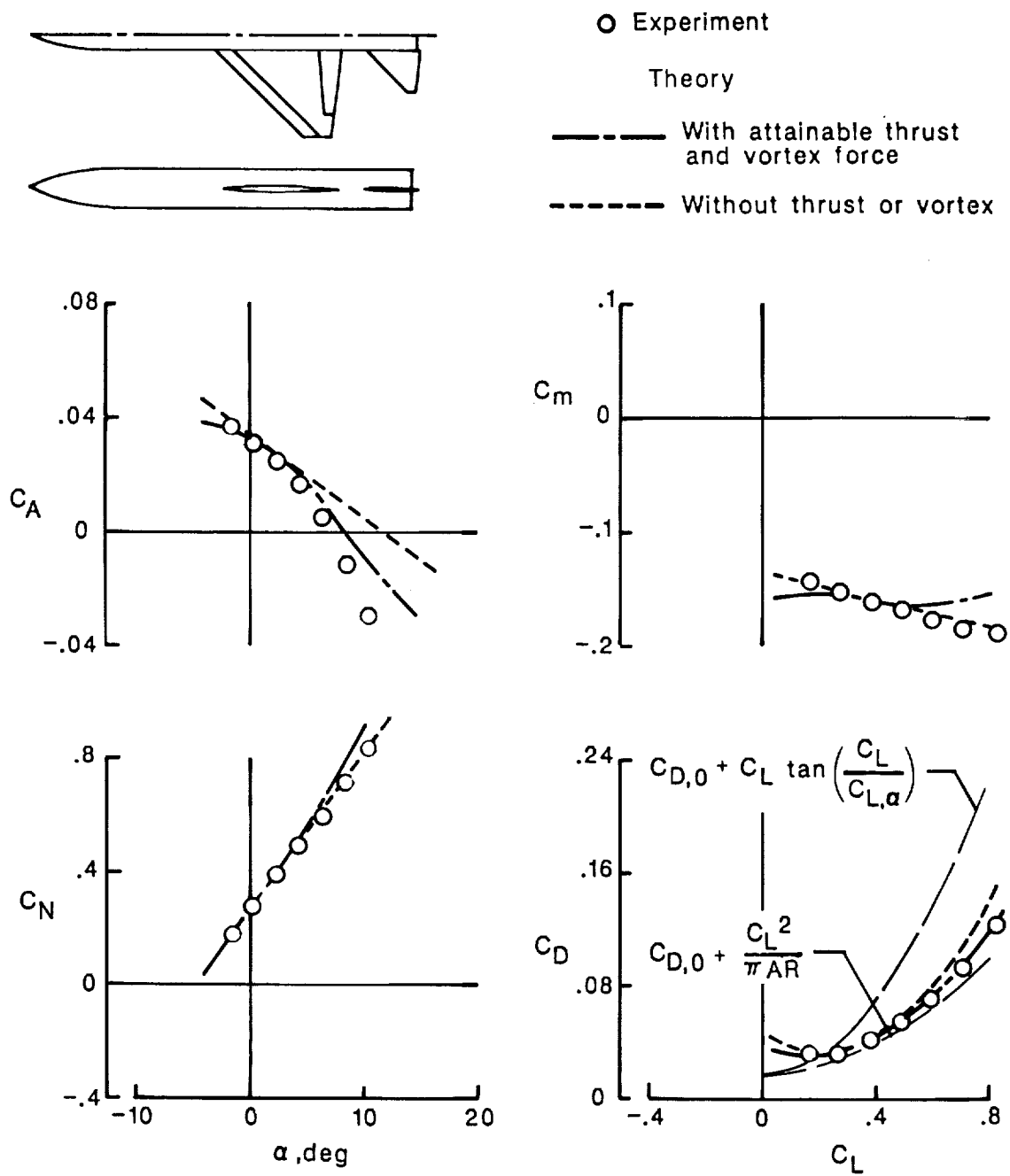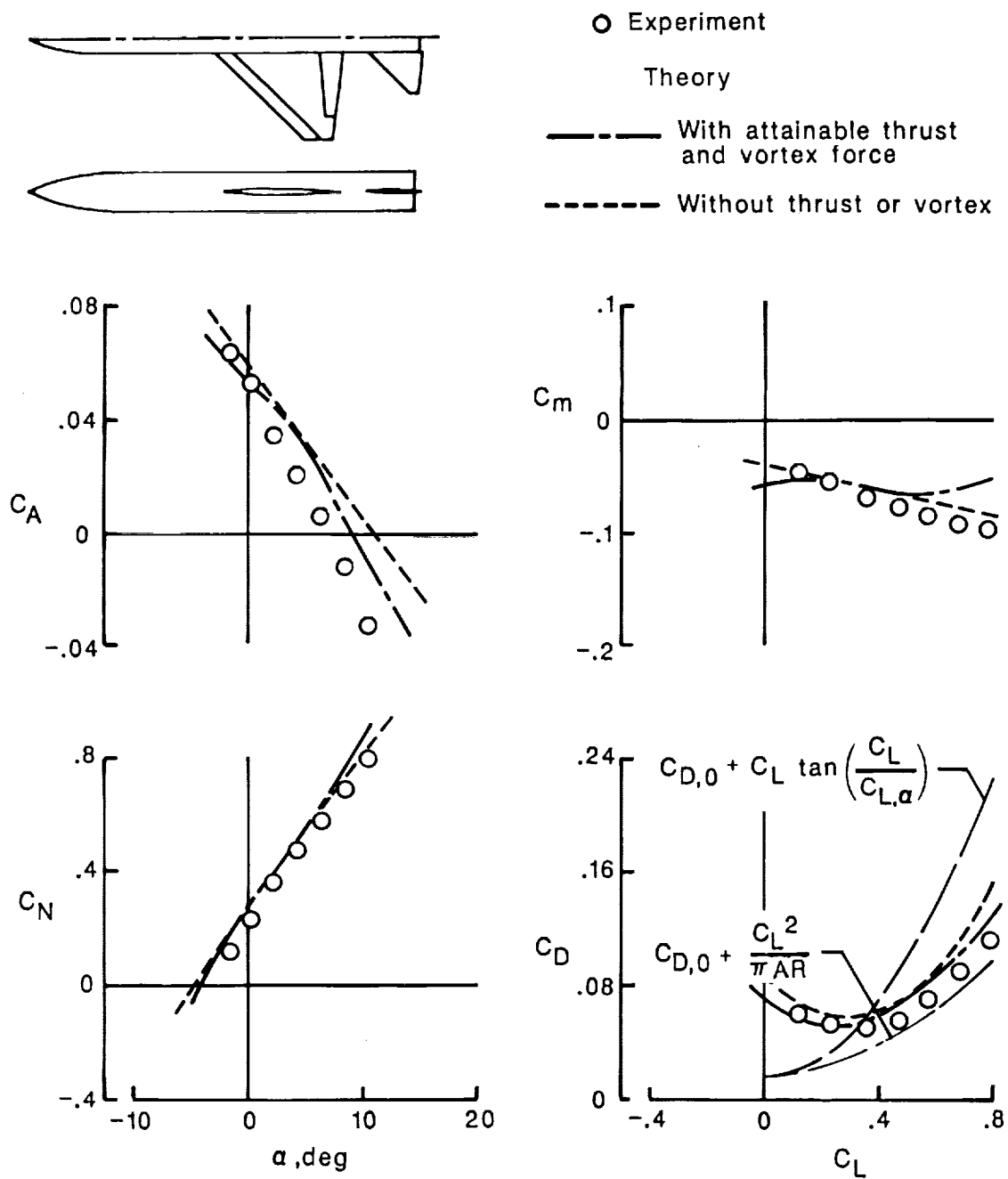
(g) $\delta_{L,n} = 20°$, $\delta_{T,n} = 20°$, $\delta_H = 0°$.

Figure 10. Continued.

Legend:
- O Experiment
- Theory
  - —··— With attainable thrust and vortex force
  - —————— Without thrust or vortex

$$C_{D,0} + C_L \tan\left(\frac{C_L}{C_{L,\alpha}}\right)$$

$$C_{D,0} + \frac{C_L^2}{\pi AR}$$

(h) $\delta_{L,n} = 20°$, $\delta_{T,n} = 20°$, $\delta_H = -10°$.

Figure 10. Continued.

Experiment

Theory

With attainable thrust and vortex force

Without thrust or vortex
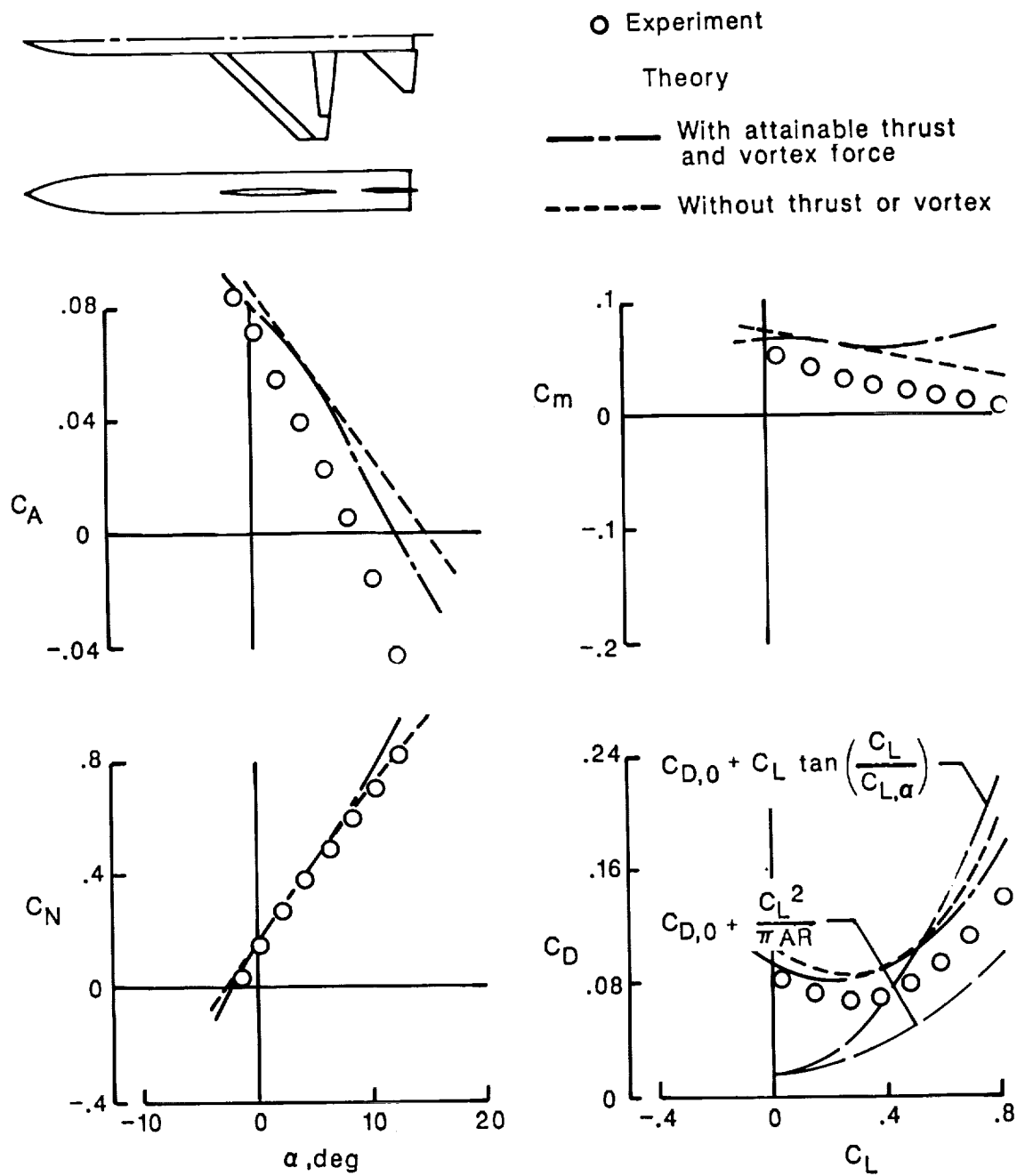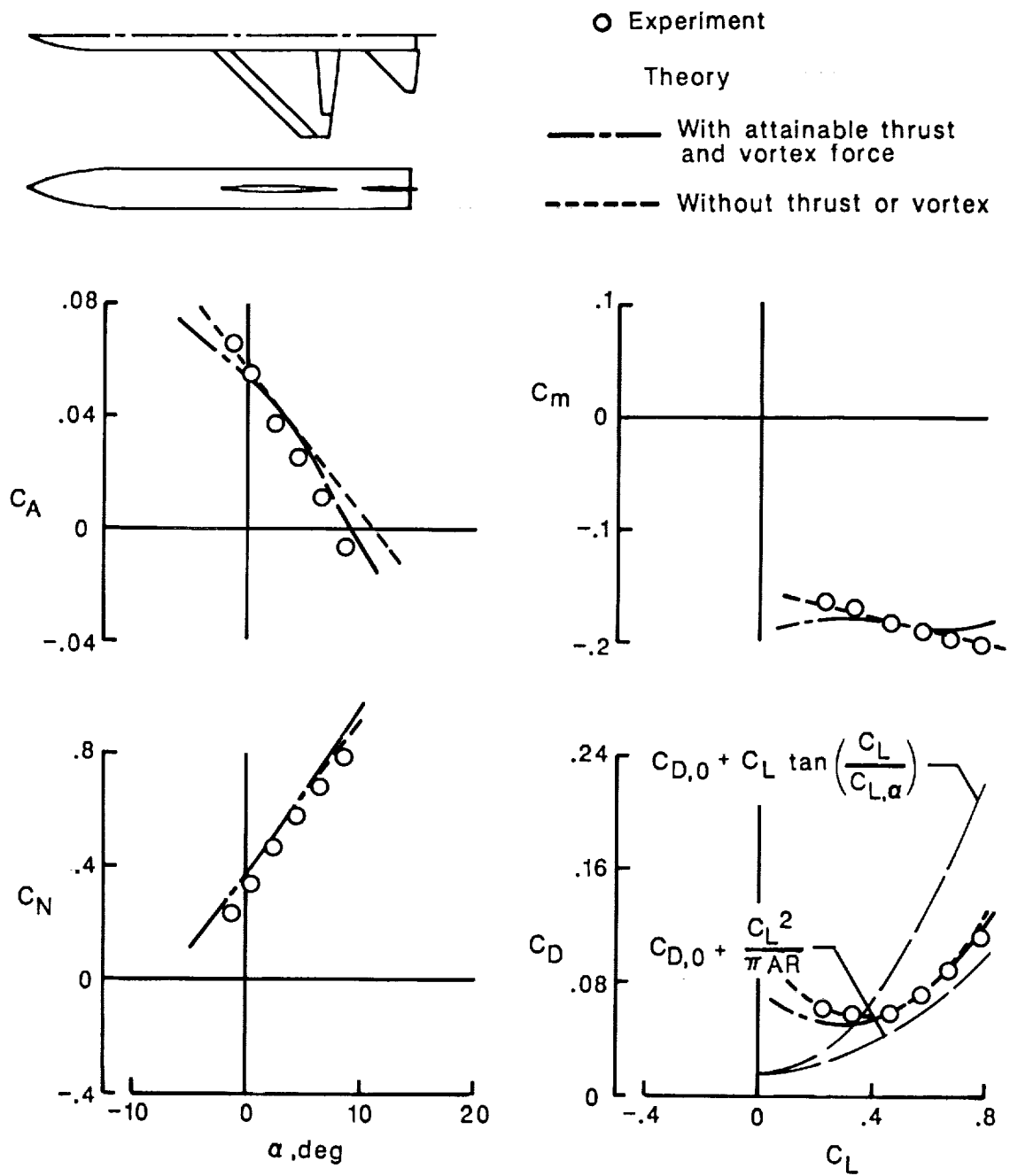
(i) $\delta_{L,n} = 20°$, $\delta_{T,n} = 20°$, $\delta_H = 10°$.

Figure 10. Concluded.
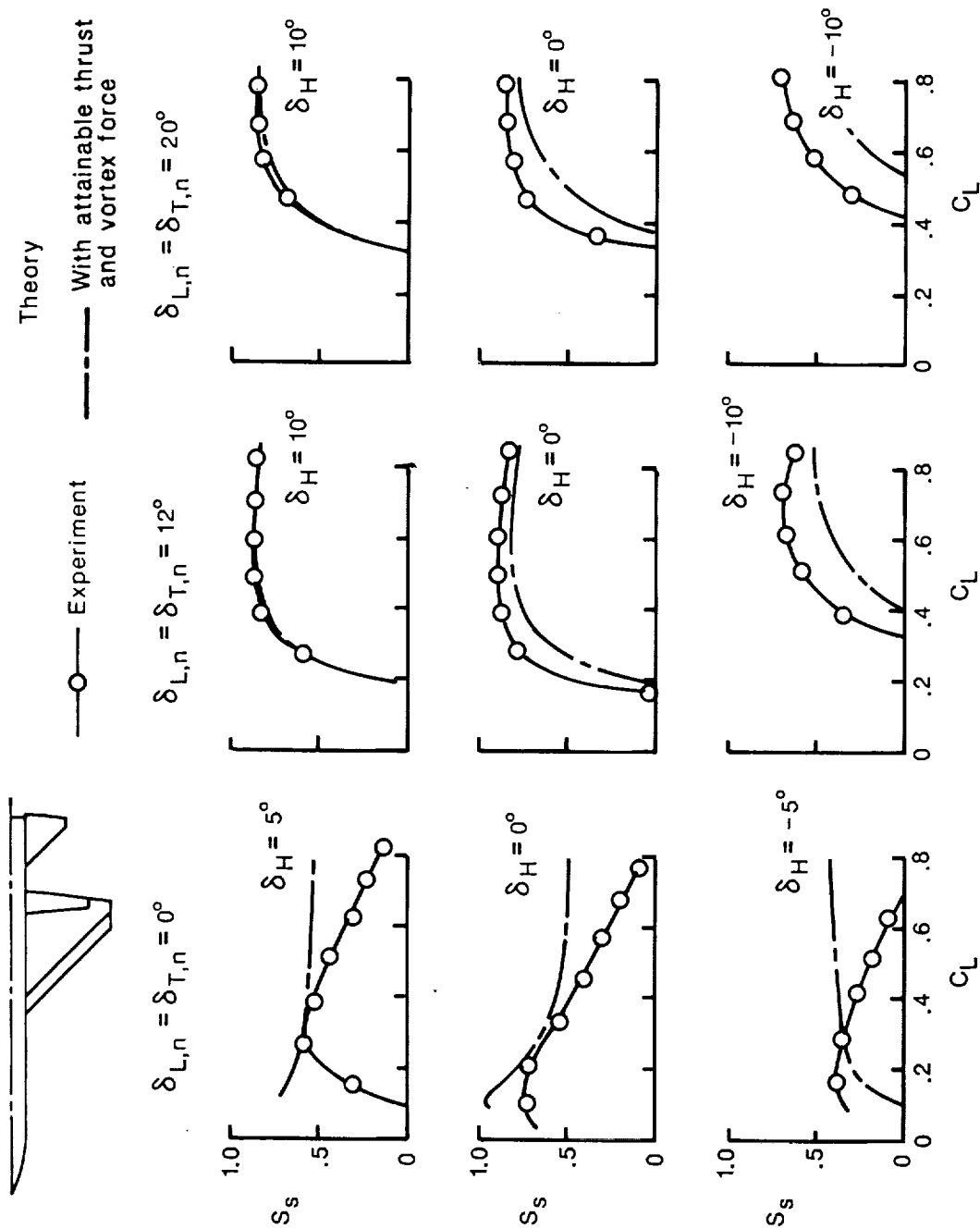
Figure 11. Suction-parameter variation with lift coefficient for various combinations of flap deflection angle and horizontal-tail incidence angle for 44°-swept trapezoidal-wing fighter with horizontal tail. $M = 0.4$; $R = 1.9 \times 10^6$.
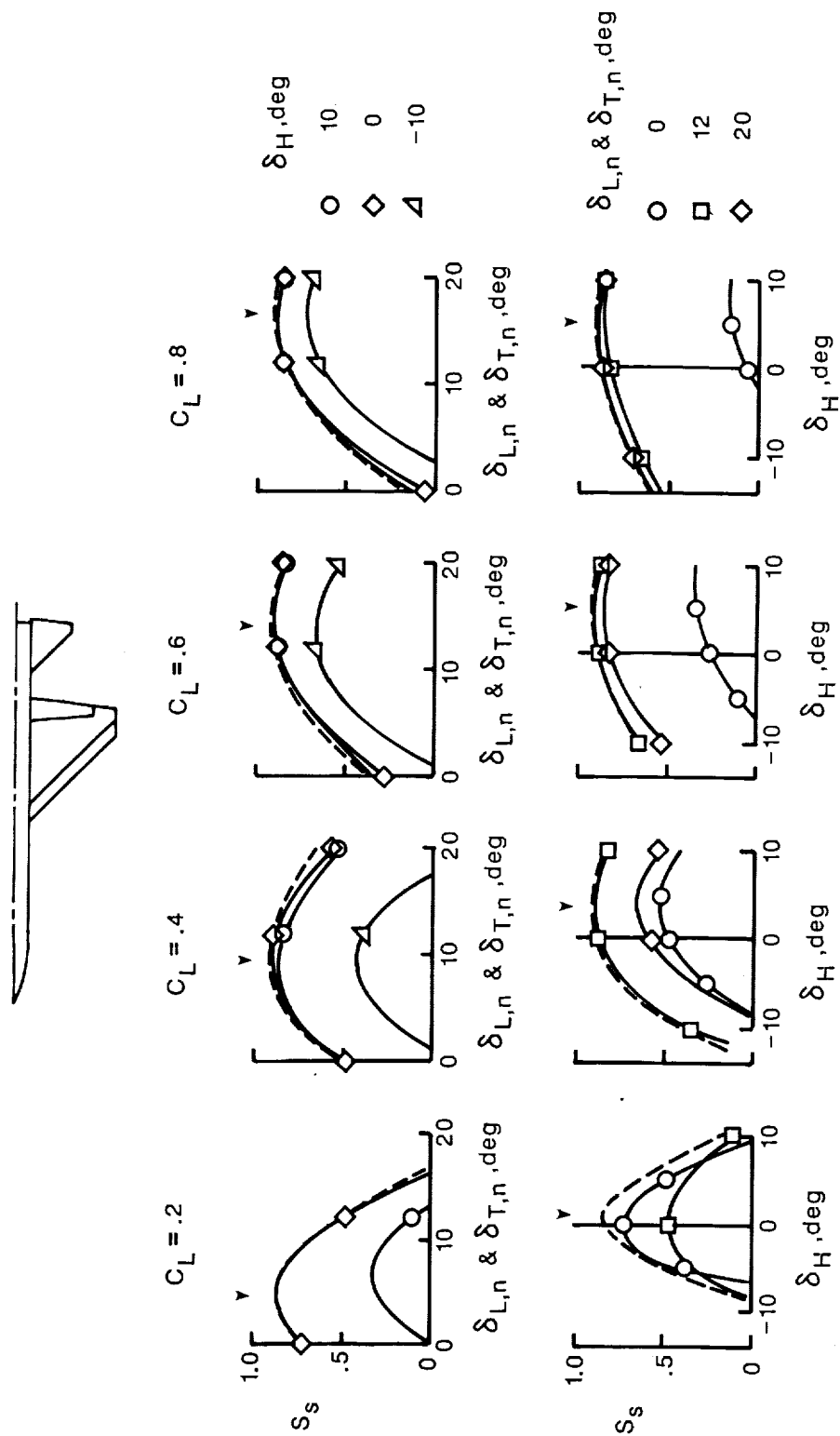
Figure 12. Experimental suction-parameter variation with flap deflection angle and horizontal-tail incidence angle for selected lift coefficients for 44°-swept trapezoidal-wing fighter with horizontal tail. $M = 0.4$; $R = 1.9 \times 10^6$; dashed lines indicate envelope curves, and arrows indicate optimum deflections.
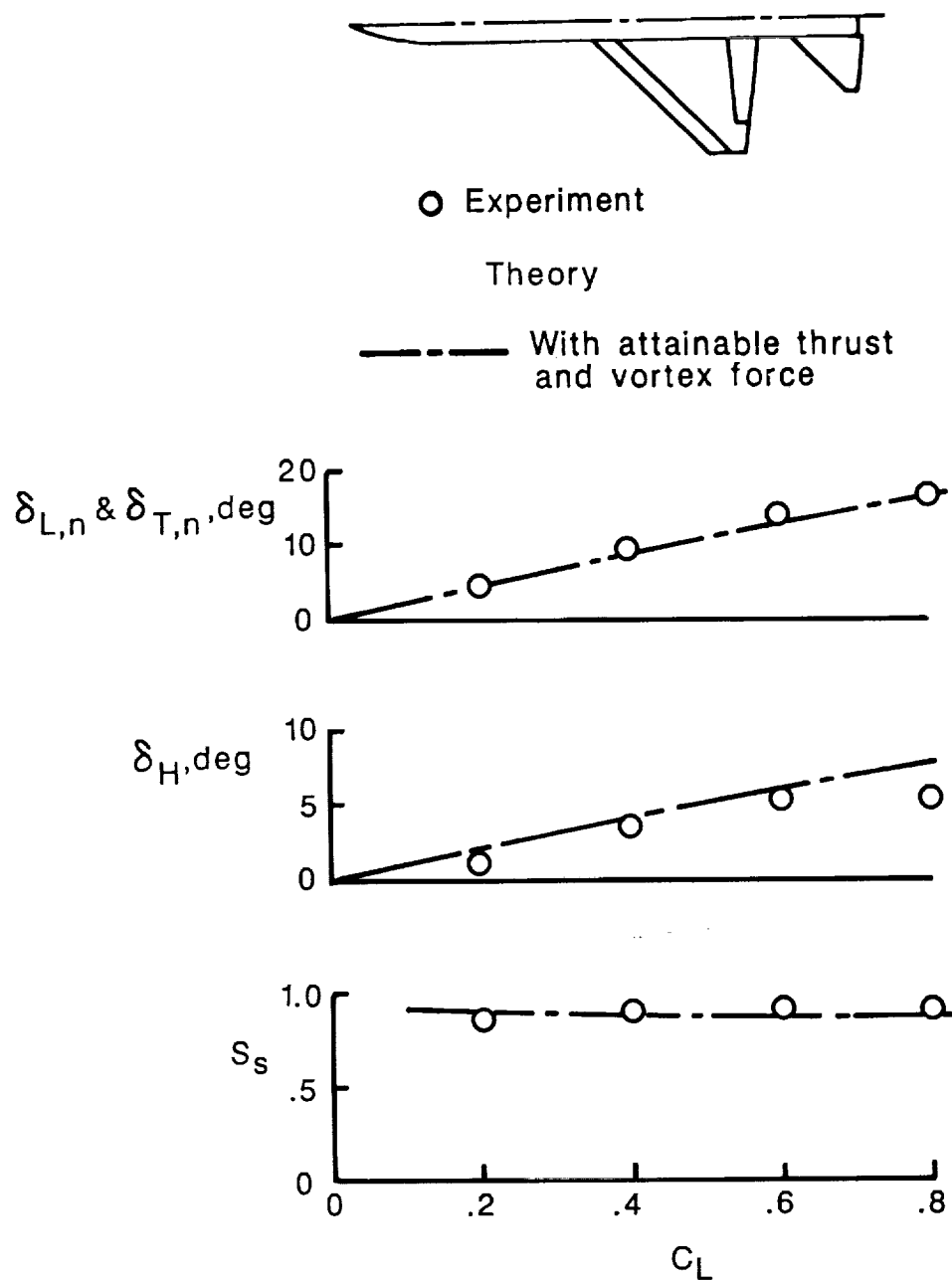
Figure 13. Optimum flap deflection angle, horizontal-tail incidence angle, and maximum suction-parameter variation with lift coefficient for 44°-swept trapezoidal-wing fighter with horizontal tail. $M = 0.4$; $R = 1.9 \times 10^6$.
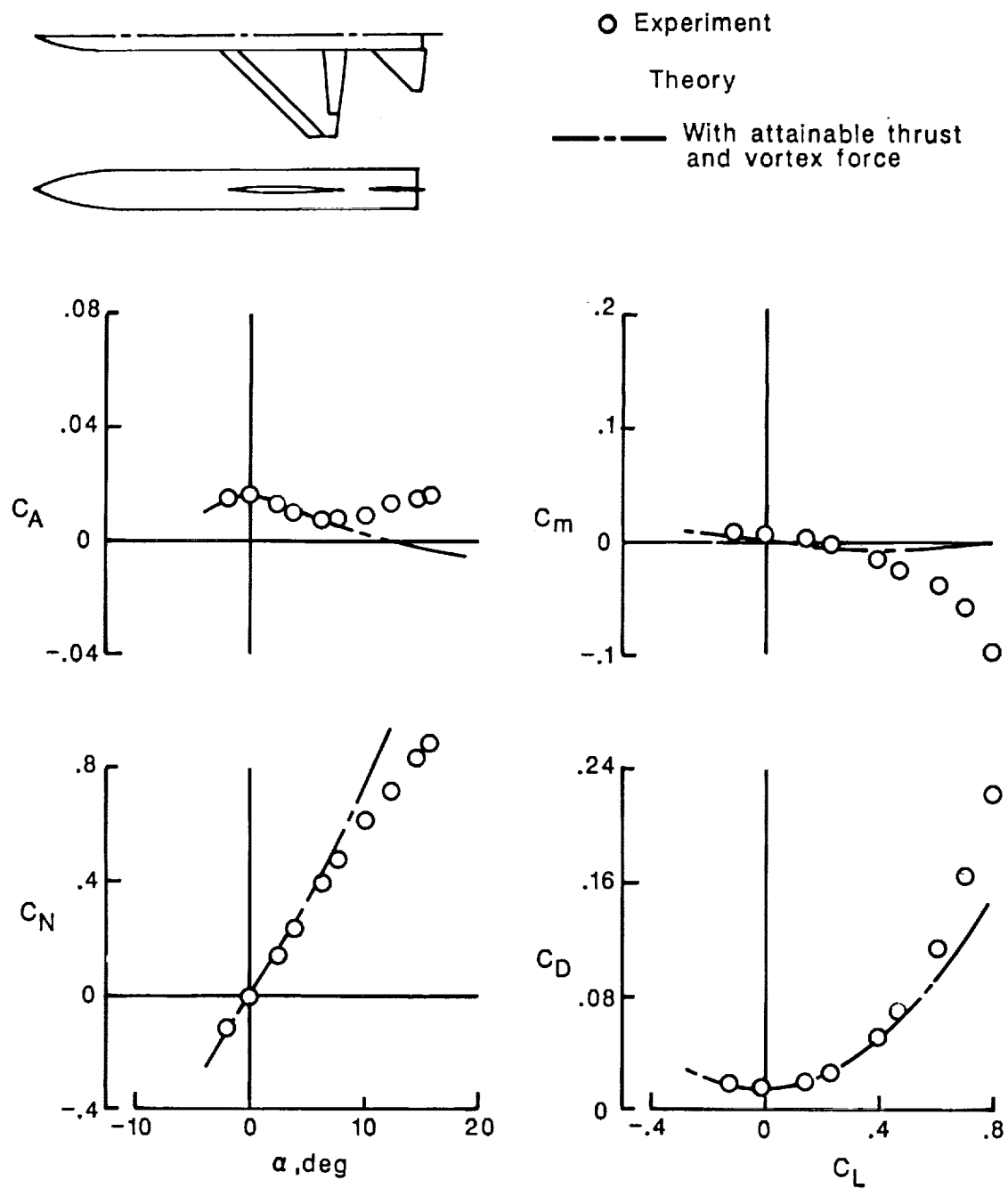
(a) $\delta_{L,n} = 0°$, $\delta_{T,n} = 0°$, $\delta_H = 0°$.

Figure 14. Theoretical and experimental data for 44°-swept trapezoidal-wing fighter with horizontal tail at $M = 0.8$ and $R = 2.58 \times 10^6$.

○ Experiment

Theory

— ·· — With attainable thrust and vortex force
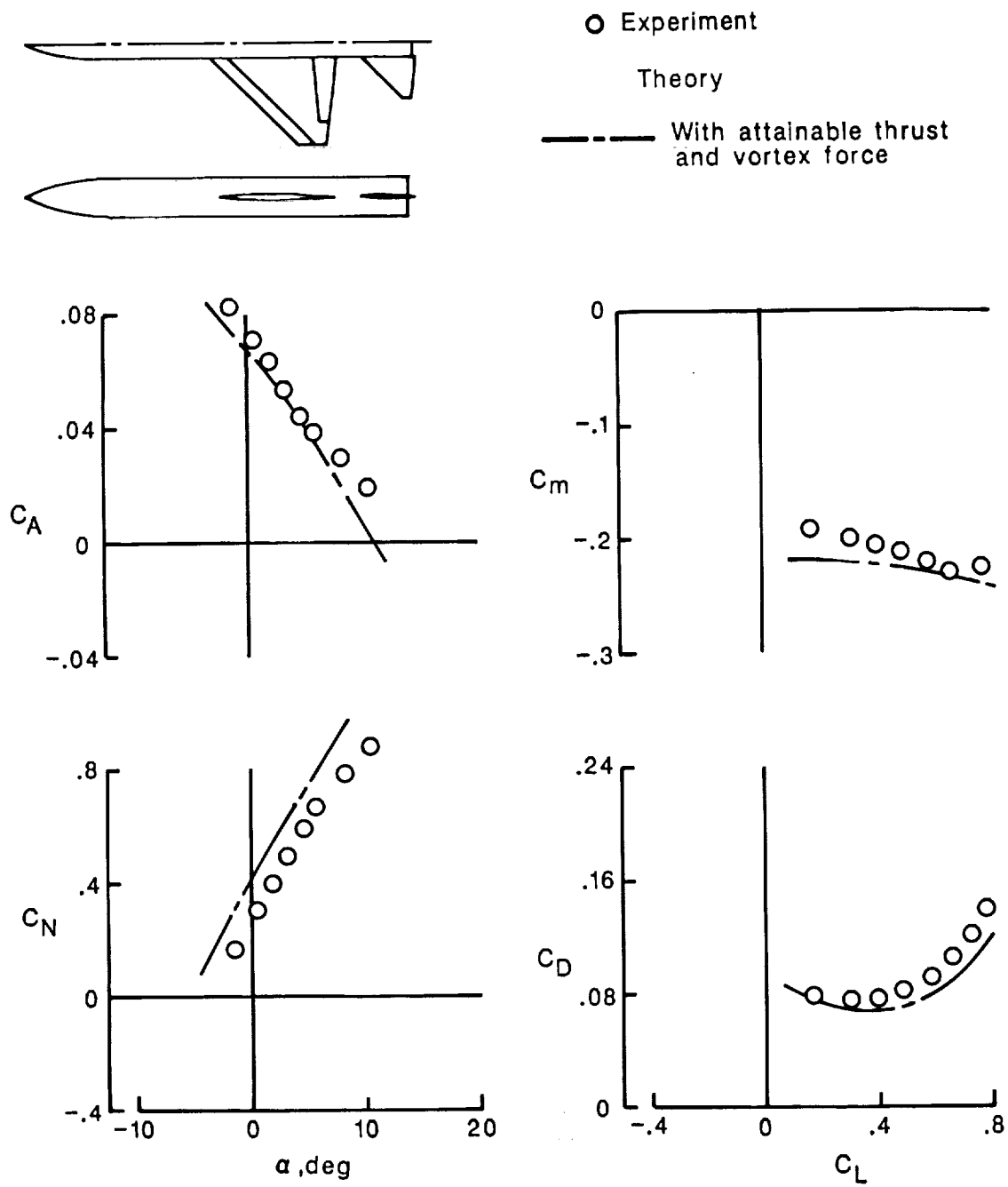
(b) $\delta_{L,n} = 20°$, $\delta_{T,n} = 20°$, $\delta_H = 10°$.

Figure 14. Concluded.

Legend:
- O Experiment

Theory
- ——— ·· ——— With attainable thrust and vortex force
- — — — — Without thrust or vortex

(a) $\delta_{L,n} = 0°$, $\delta_{T,n} = 0°$, $\delta_C = 0°$.

Figure 15. Theoretical and experimental data for 60°-swept delta-wing fighter with canard. $M = 0.4$; $R = 2.52 \times 10^6$.

$$C_{D,0} + C_L \tan\left(\frac{C_L}{C_{L,\alpha}}\right)$$

$$C_{D,0} + \frac{C_L{}^2}{\pi\,AR}$$
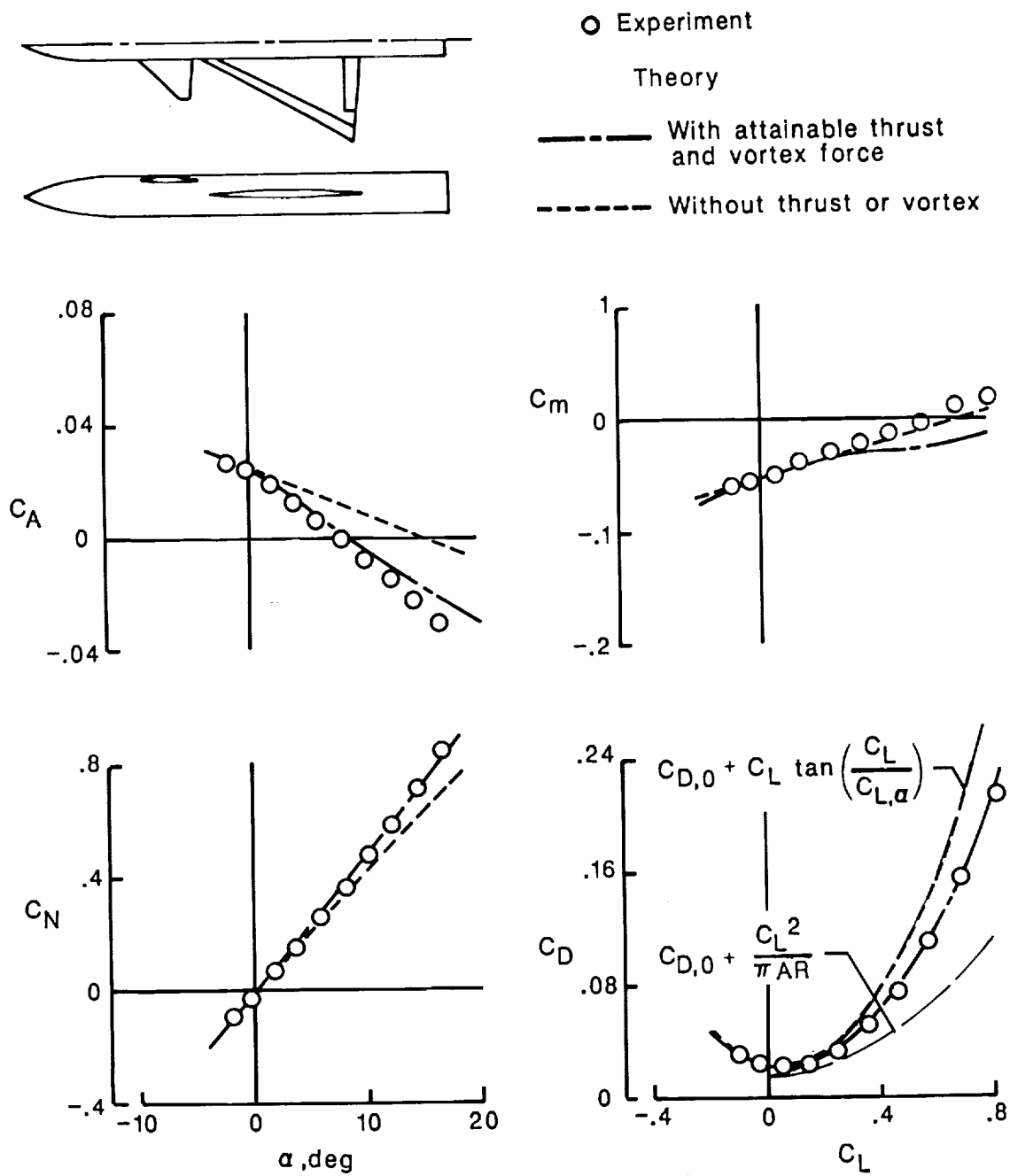
(b) $\delta_{L,n} = 0°$, $\delta_{T,n} = 0°$, $\delta_C = -10°$.

Figure 15. Continued.

Figure 15. Continued.

(c) $\delta_{L,n} = 0°$, $\delta_{T,n} = 0°$, $\delta_C = 5°$.

O Experiment

Theory

With attainable thrust and vortex force

Without thrust or vortex

C_A

C_m

C_N

C_D

$C_{D,0} + C_L \tan\left(\dfrac{C_L}{C_{L,\alpha}}\right)$

$C_{D,0} + \dfrac{C_L{}^2}{\pi\,AR}$

α ,deg

C_L
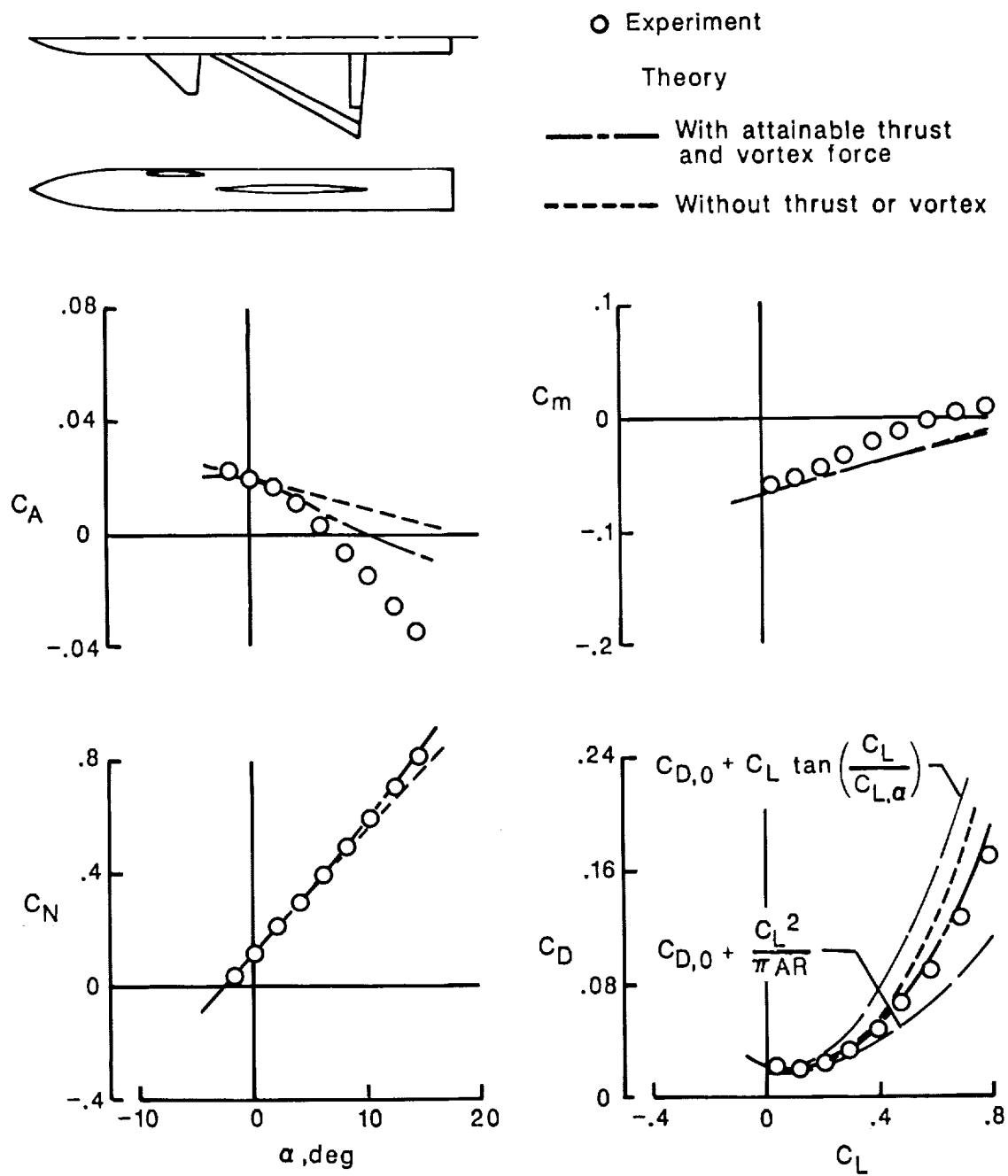
(d) $\delta_{L,n} = 10°$, $\delta_{T,n} = 10°$, $\delta_C = 0°$.

Figure 15. Continued.

O Experiment

Theory

With attainable thrust and vortex force

Without thrust or vortex

(e) $\delta_{L,n} = 10°$, $\delta_{T,n} = 10°$, $\delta_C = -10°$.

Figure 15. Continued.

70

Legend:
○ Experiment
Theory
——— With attainable thrust and vortex force
- - - - - Without thrust or vortex

(f) $\delta_{L,n} = 10°$, $\delta_{T,n} = 10°$, $\delta_C = 10°$.

Figure 15. Continued.

O Experiment

Theory

— ·· — With attainable tnrust and vortex force

— — — — Without thrust or vortex
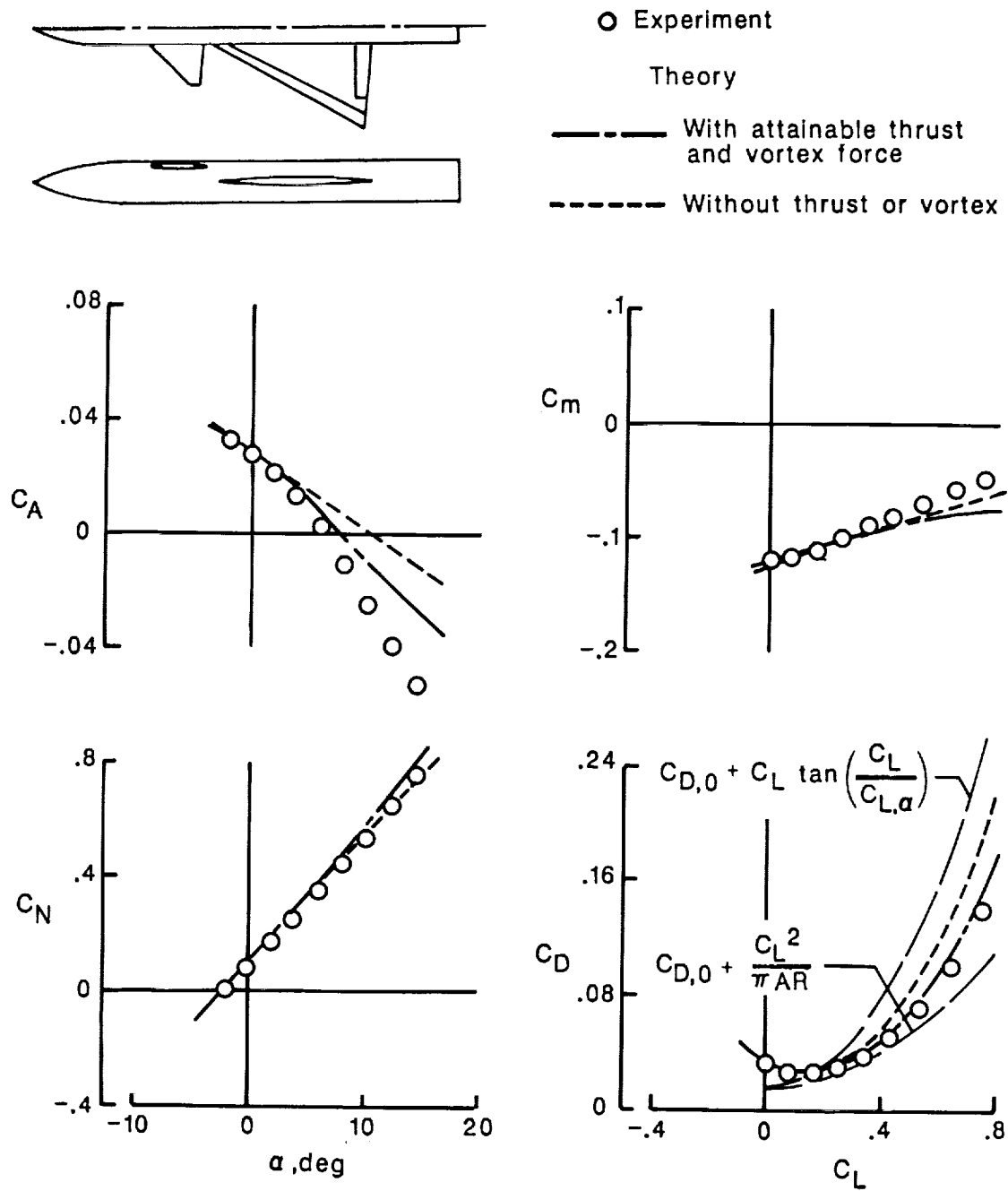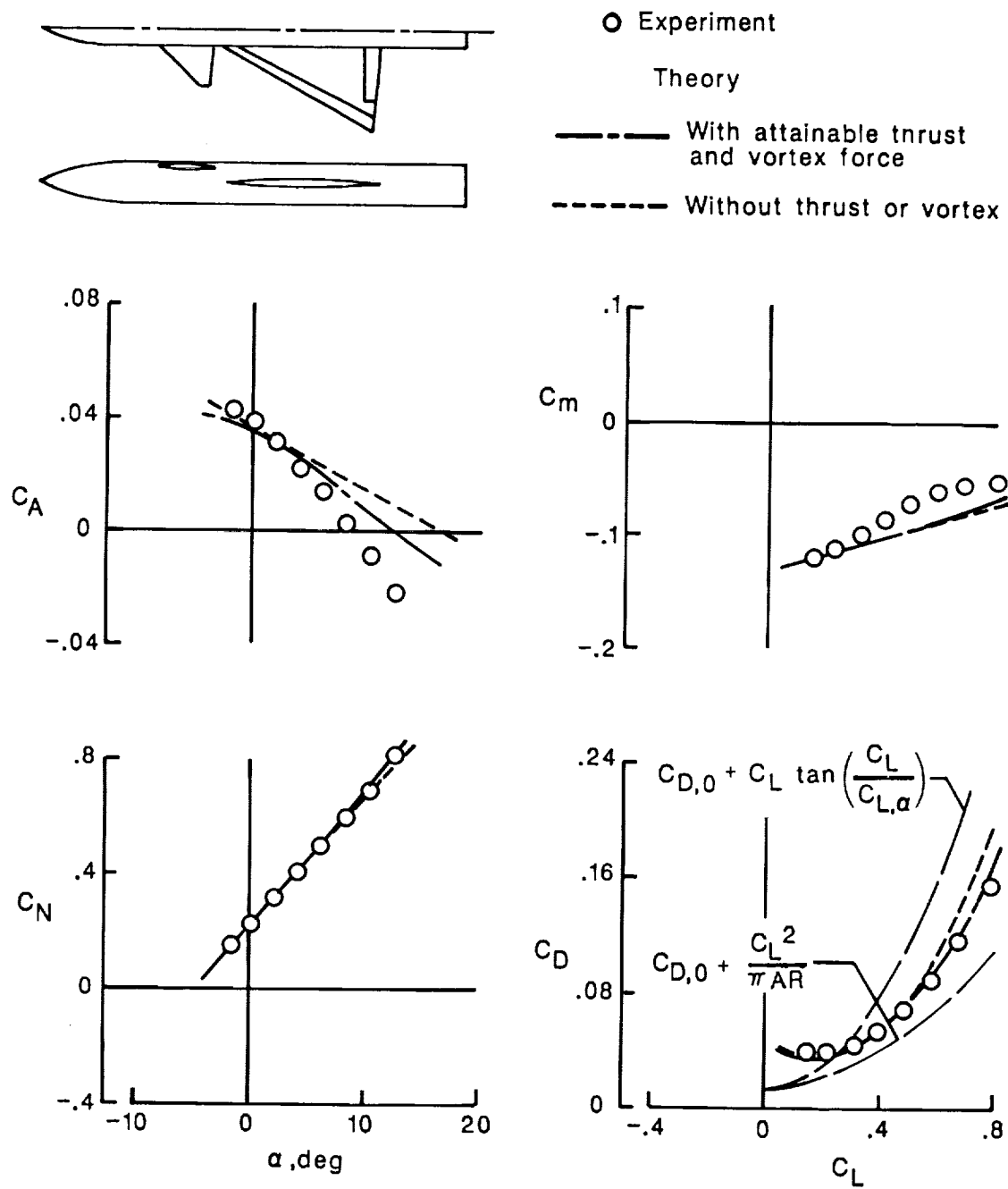
(g) $\delta_{L,n} = 20°$, $\delta_{T,n} = 20°$, $\delta_C = 0°$.

Figure 15. Continued.

72

Figure 15. Continued.
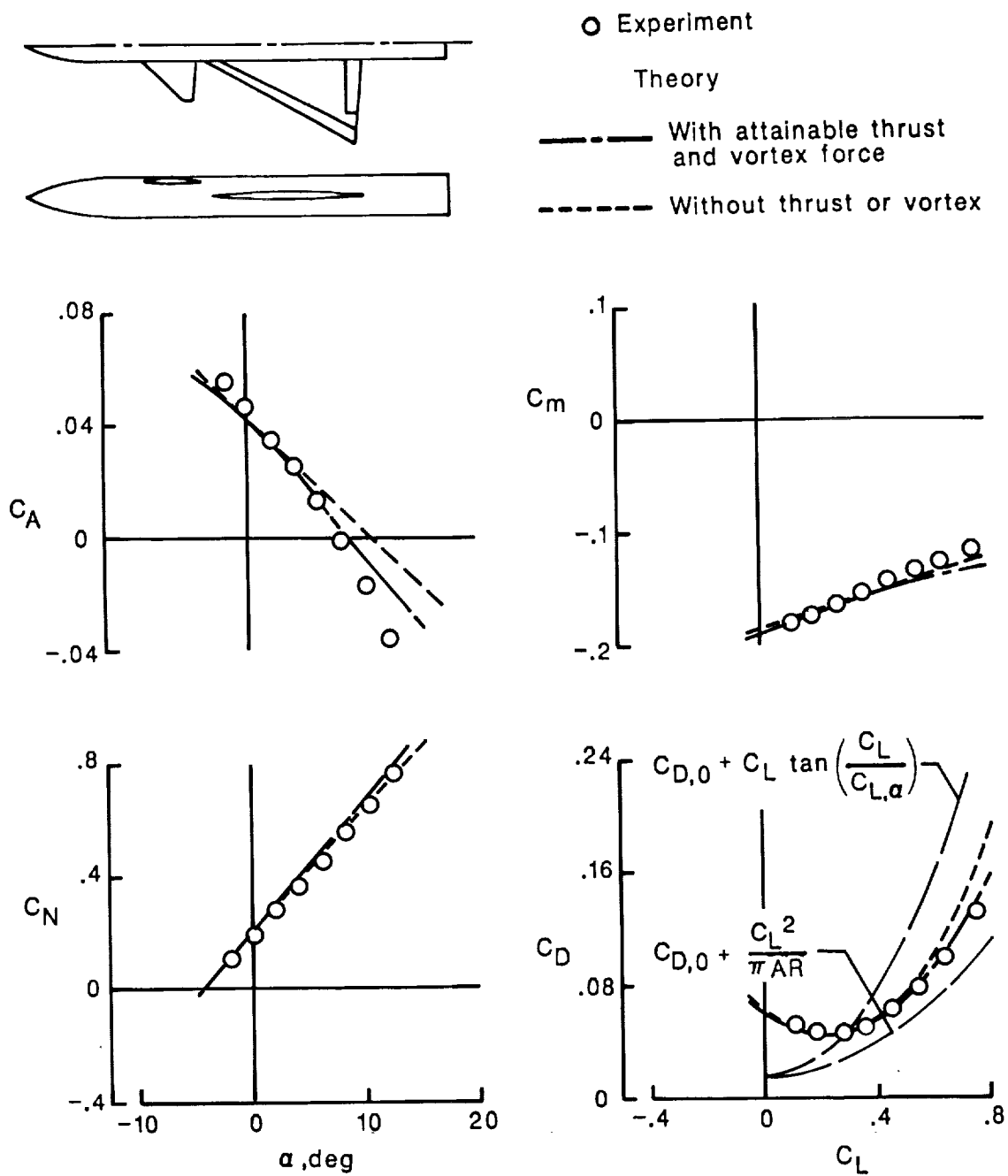
(h) $\delta_{L,n} = 20°$, $\delta_{T,n} = 20°$, $\delta_C = -10°$.

Figure 15. Concluded.

(i) $\delta_{L,n} = 20°$, $\delta_{T,n} = 20°$, $\delta_C = 10°$.
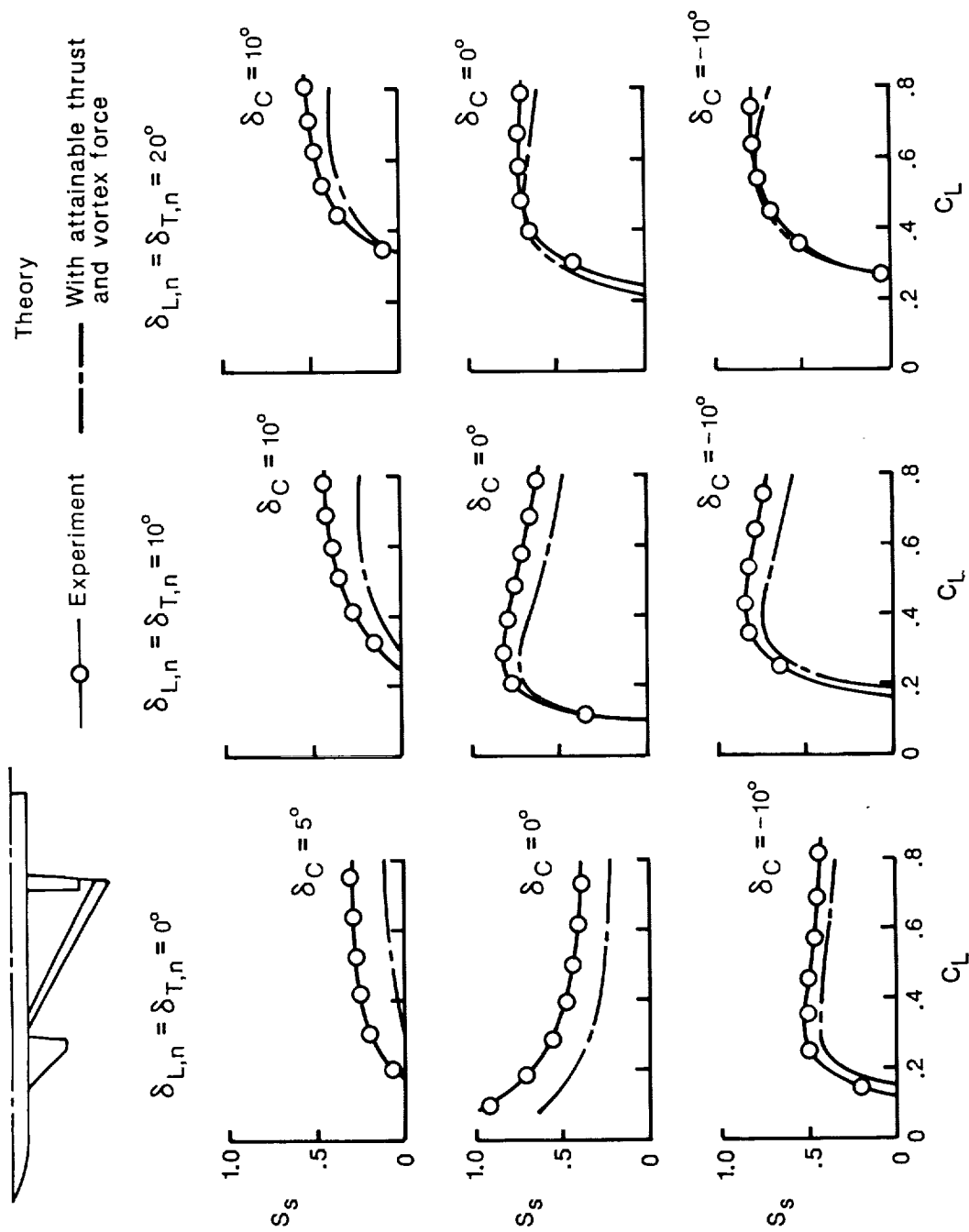
Figure 16. Suction-parameter variation with lift coefficient for various combinations of flap deflection angle and canard incidence angle for 60°-swept trapezoidal-wing fighter with canard. $M = 0.4$; $R = 2.52 \times 10^6$.
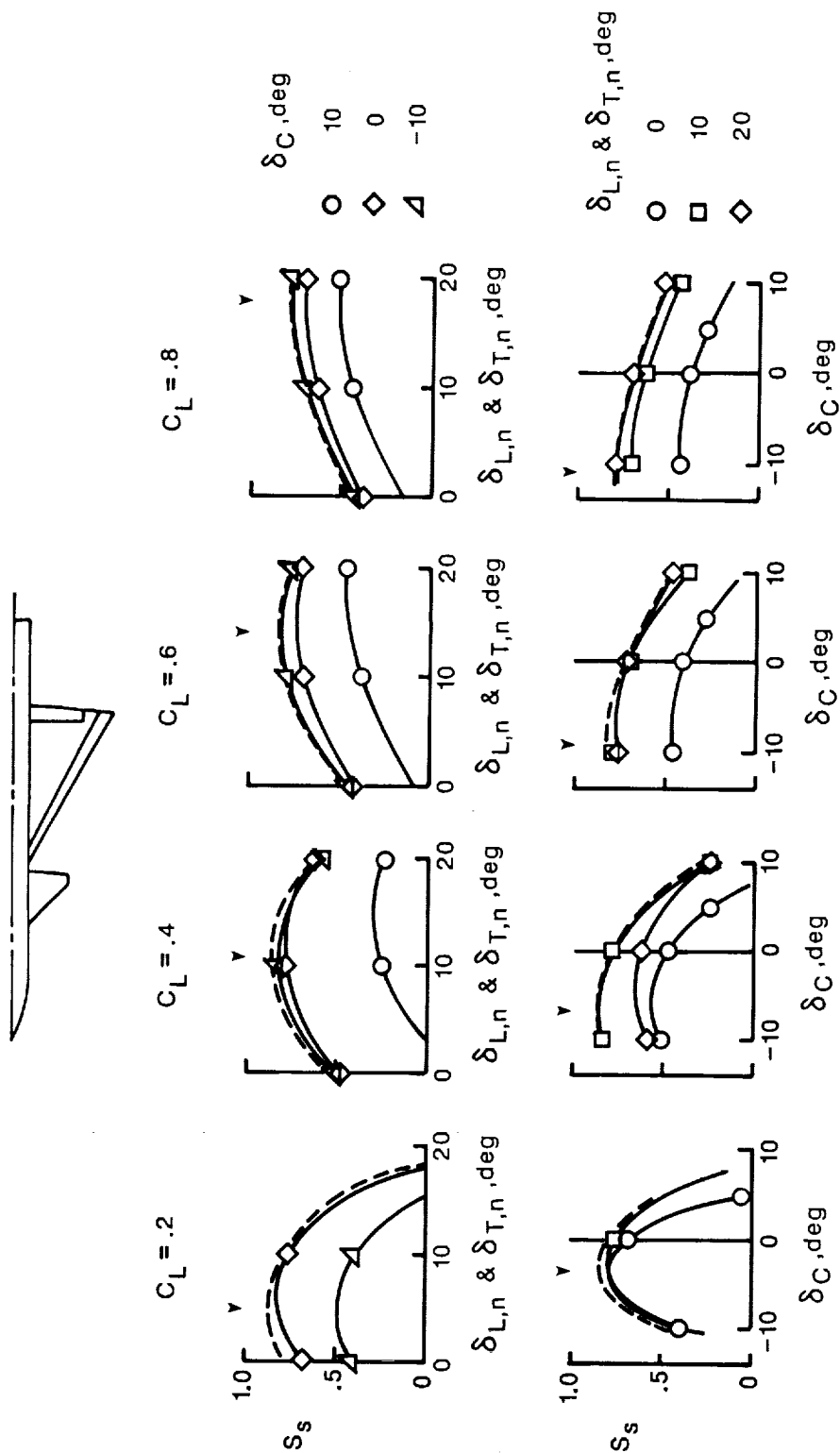
Figure 17. Experimental suction-parameter variation with flap deflection angle and canard incidence angle for selected lift coefficients for 60°-swept delta-wing fighter with canard. $M = 0.4$; $R = 2.52 \times 10^6$; dashed lines indicate envelope curves, and arrows indicate optimum deflections.
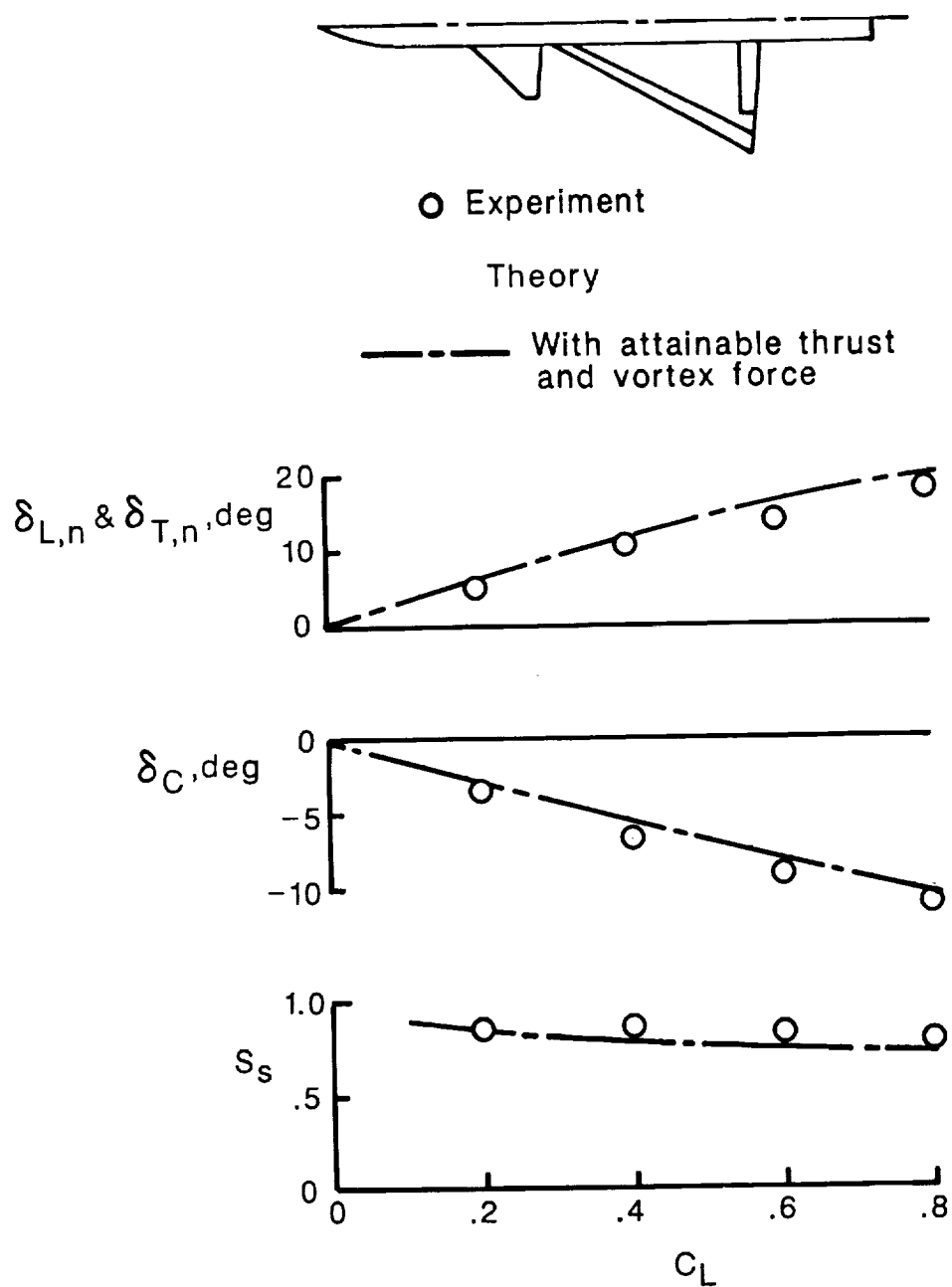
Figure 18. Optimum flap deflection angle, canard incidence angle, and maximum suction-parameter variation with lift coefficient for 60°-swept delta-wing fighter with canard. $M = 0.4$; $R = 2.52 \times 10^6$.
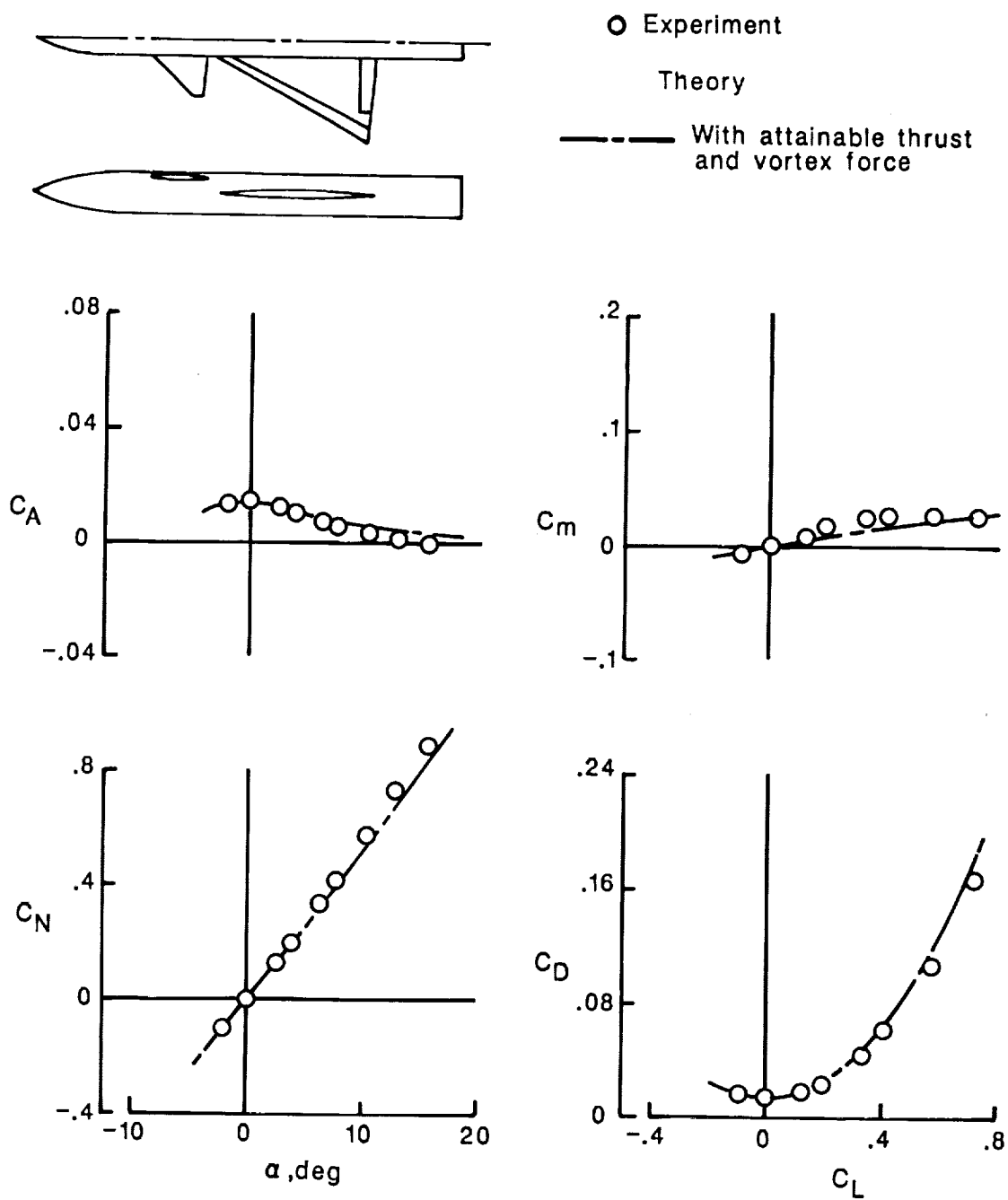
Figure 19. Theoretical and experimental data for 60°-swept delta-wing fighter with canard. $M = 0.8$; $R = 3.4 \times 10^6$.

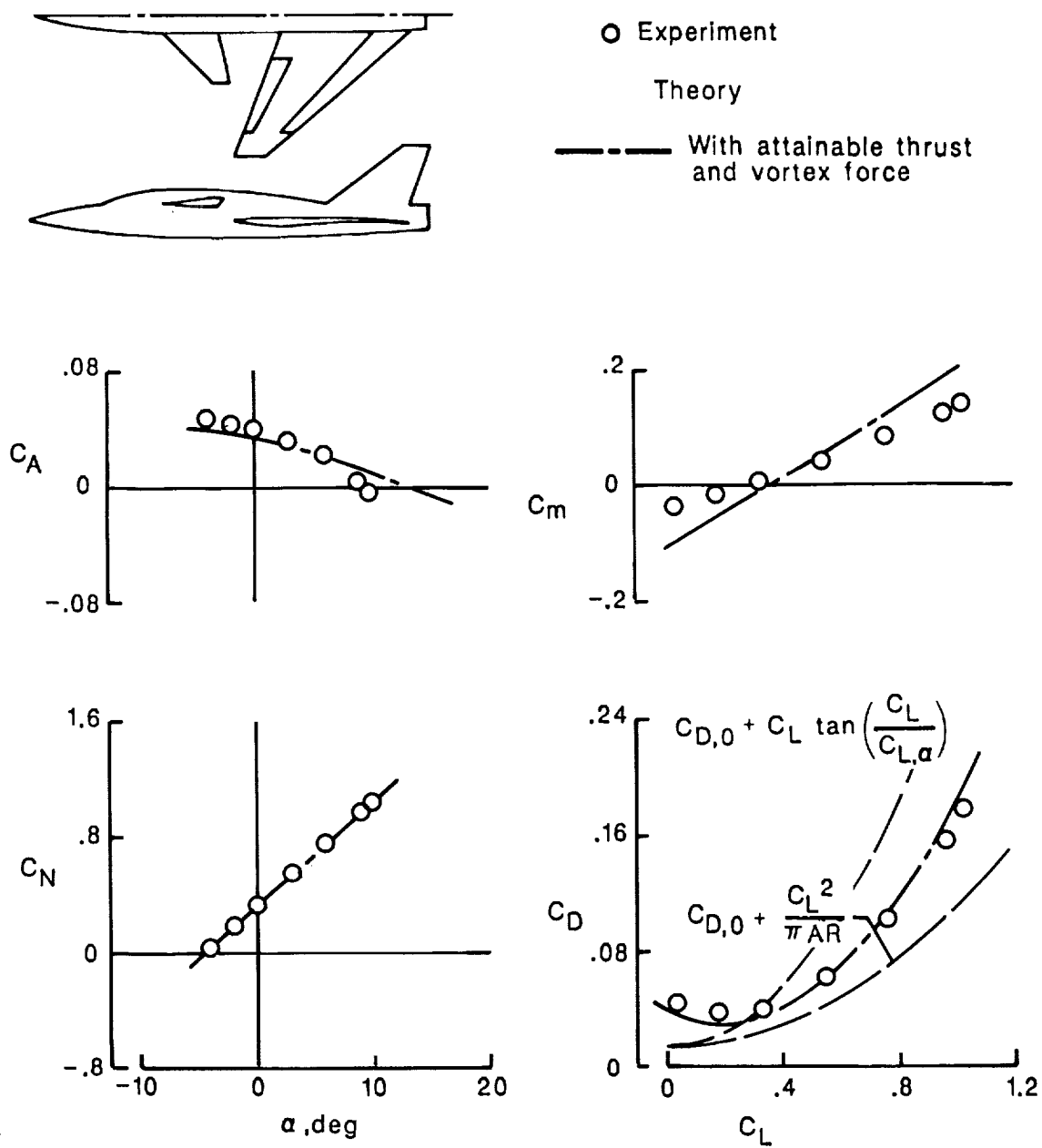(a) $\delta_{L,n} = 0°$, $\delta_{T,n} = 0°$, $\delta_C = 0°$.

O Experiment

Theory

—— ·— With attainable thrust
and vortex force
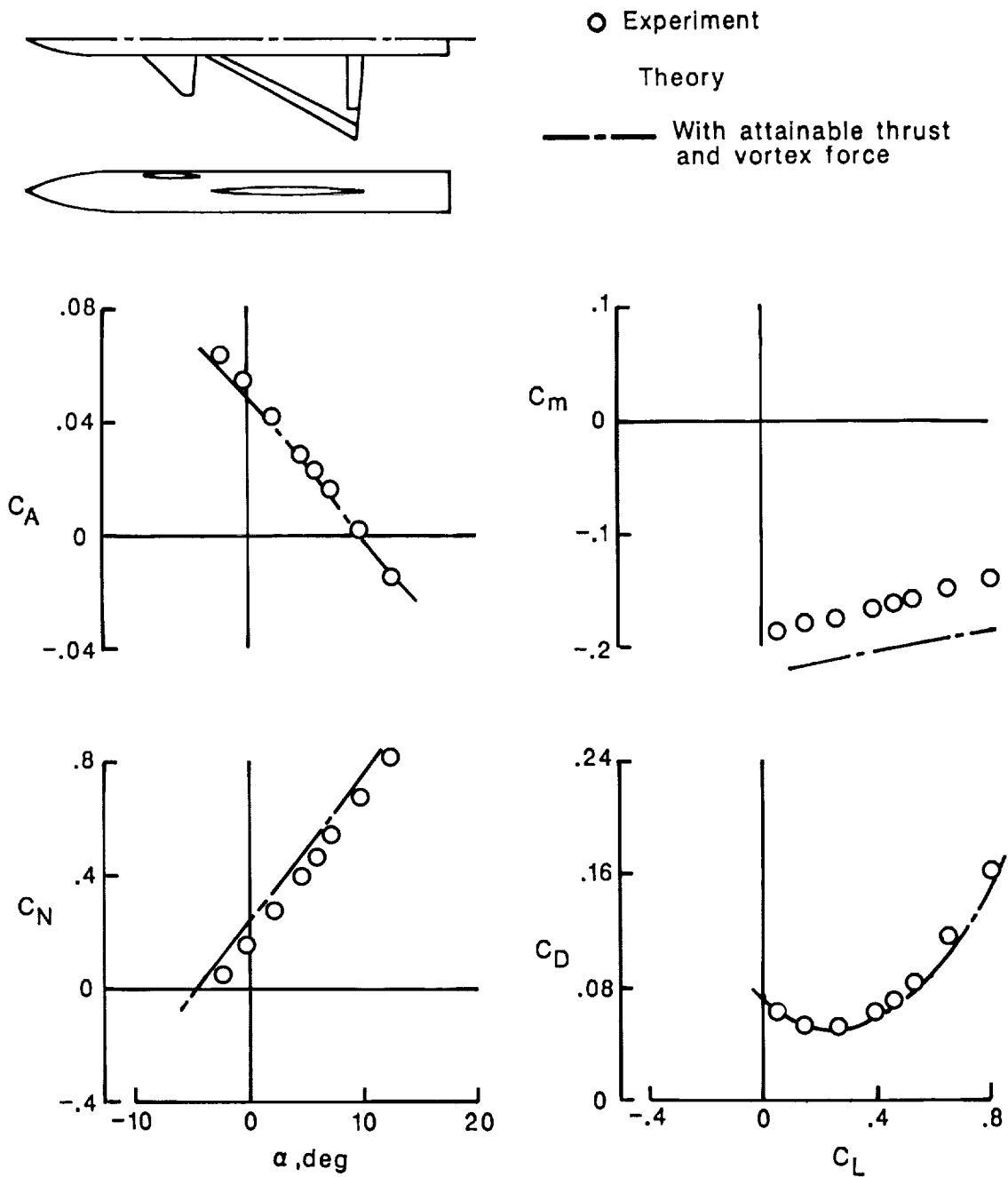
(b) $\delta_{L,n} = 20°$, $\delta_{T,n} = 20°$, $\delta_C = -10°$.

Figure 19. Concluded.
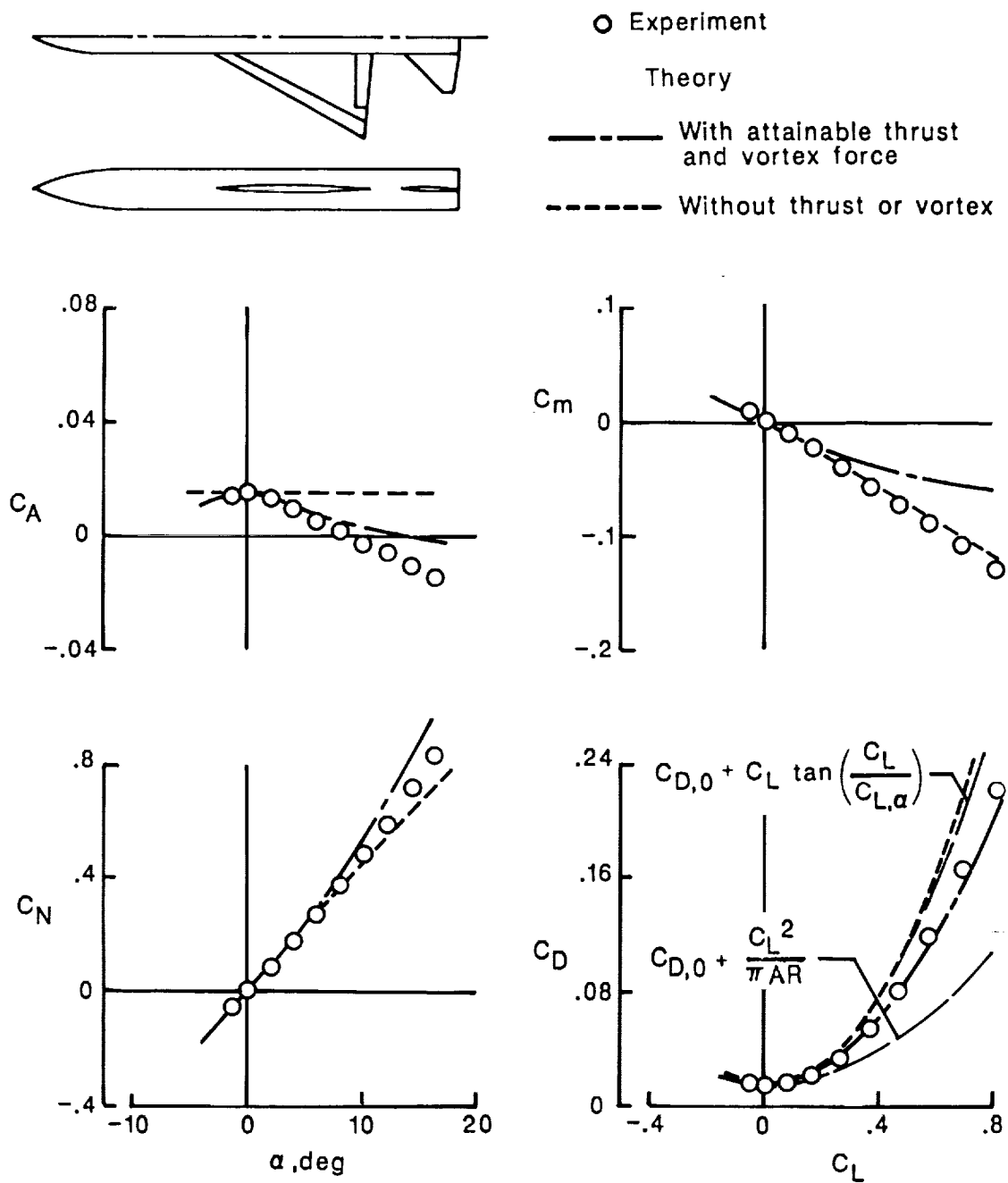
Figure 20. Theoretical and experimental data for 60°-swept delta-wing fighter with horizontal tail. $M = 0.4$; $R = 2.52 \times 10^6$.

(a) $\delta_{L,n} = 0°$, $\delta_{T,n} = 0°$, $\delta_H = 0°$.

Experiment: ○ Experiment

Theory:

— · — With attainable thrust and vortex force

- - - - - Without thrust or vortex

(b) $\delta_{L,n} = 0°$, $\delta_{T,n} = 0°$, $\delta_H = -5°$.

Figure 20. Continued.

O Experiment

Theory

With attainable thrust and vortex force

Without thrust or vortex

(c) $\delta_{L,n} = 0°$, $\delta_{T,n} = 0°$, $\delta_H = 5°$.

Figure 20. Continued.

O Experiment

Theory

— · — · — With attainable thrust and vortex force

— — — — — — Without thrust or vortex
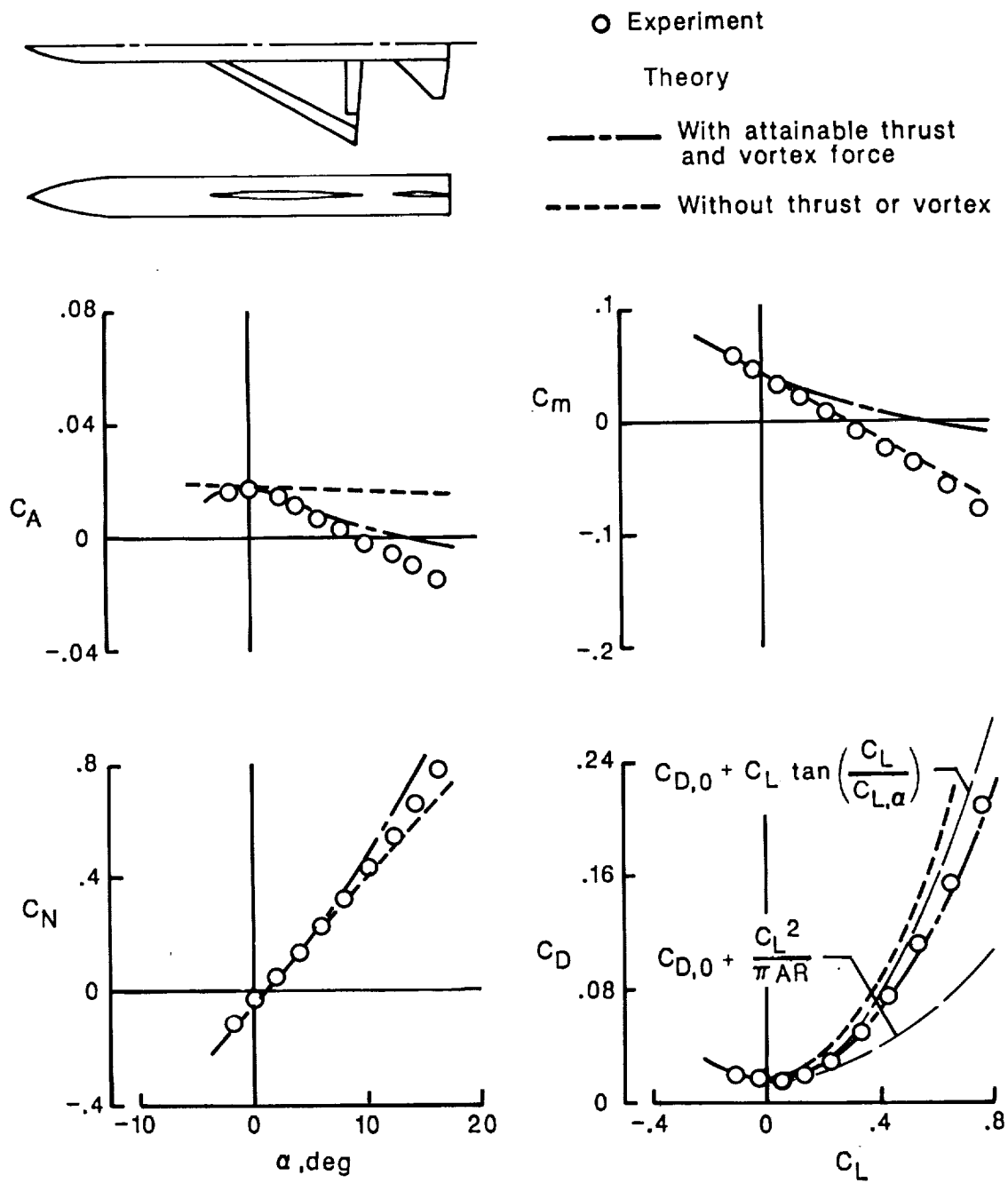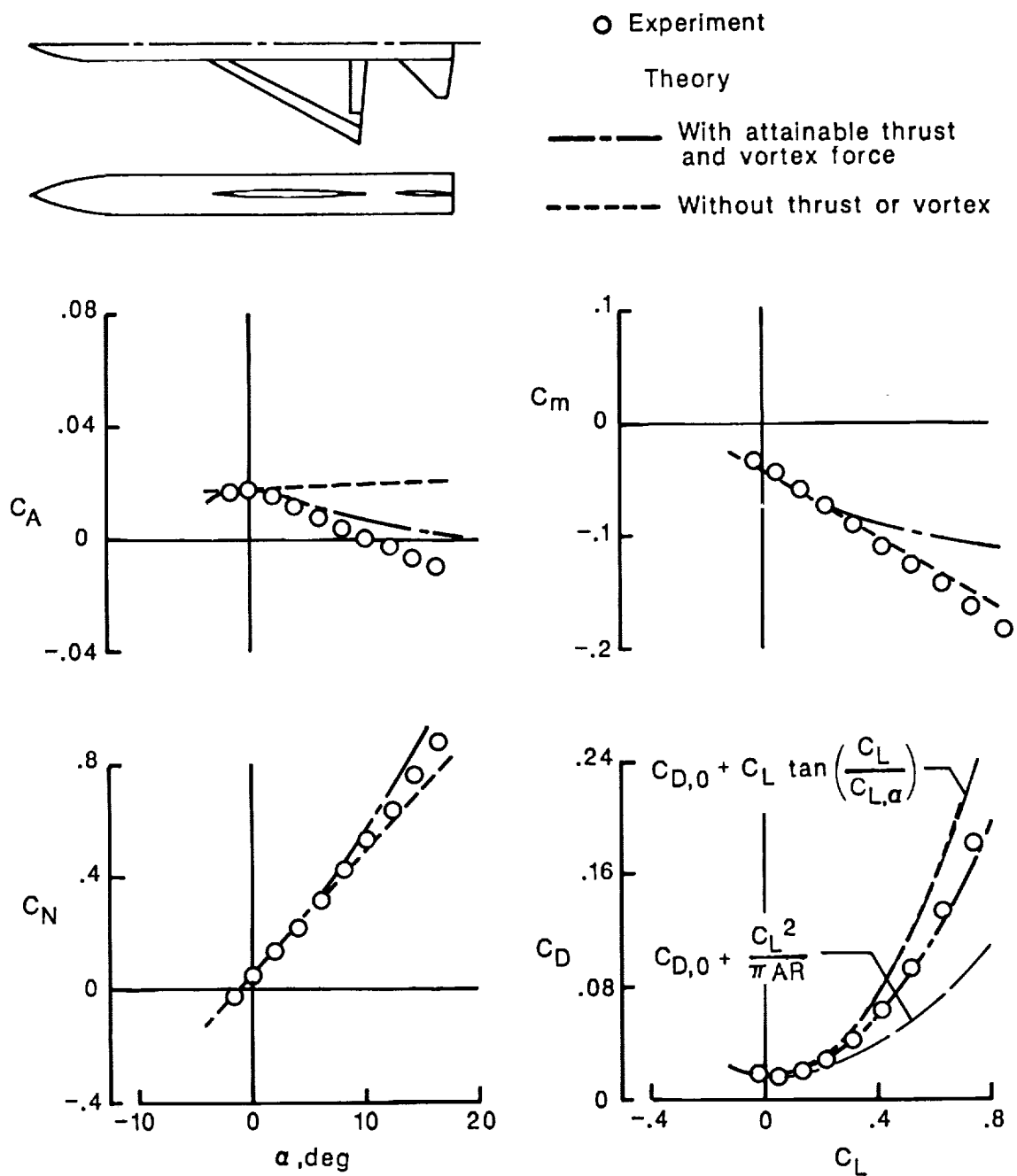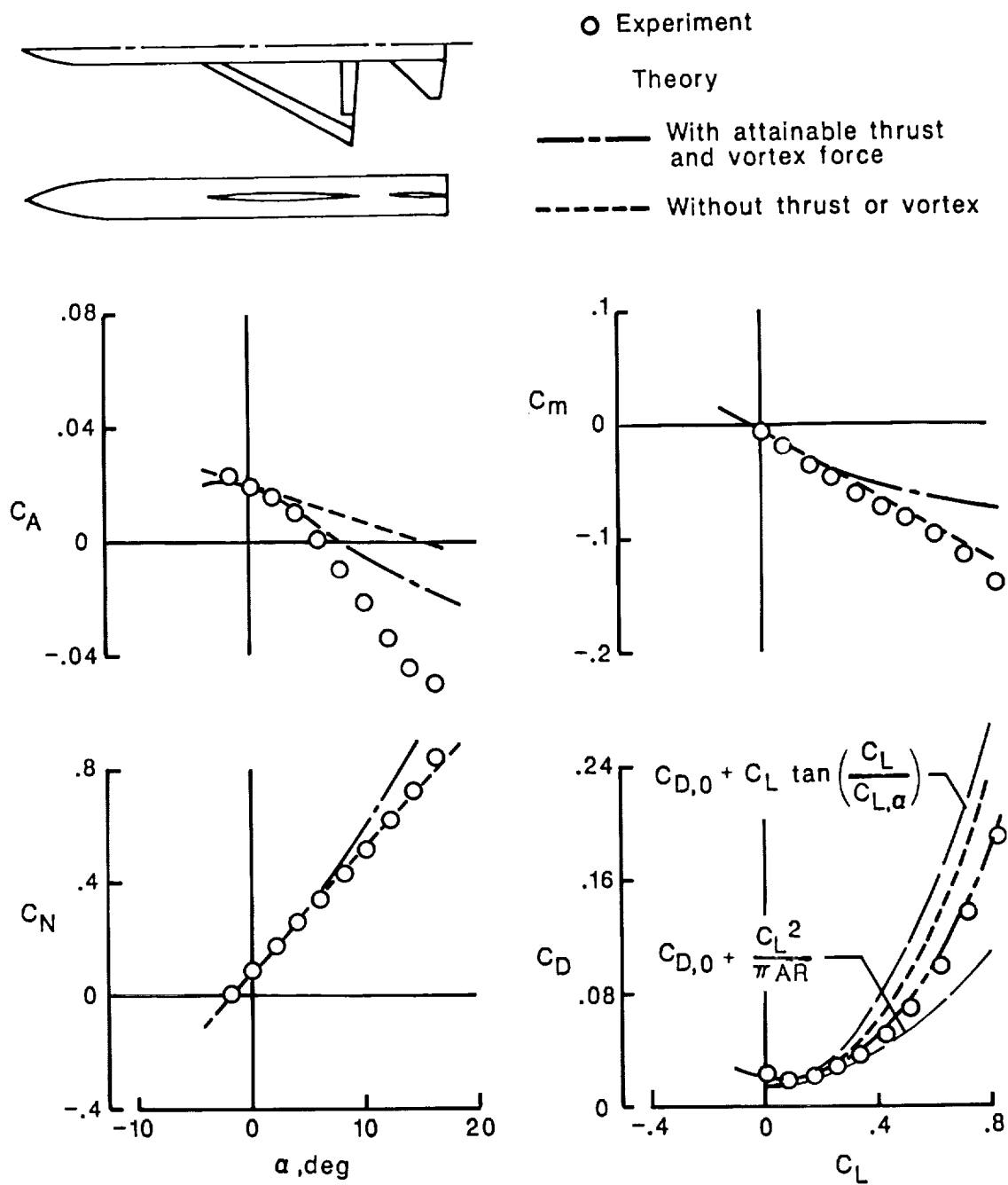
(d) $\delta_{L,n} = 10°$, $\delta_{T,n} = 10°$, $\delta_H = 0°$.

Figure 20. Continued.
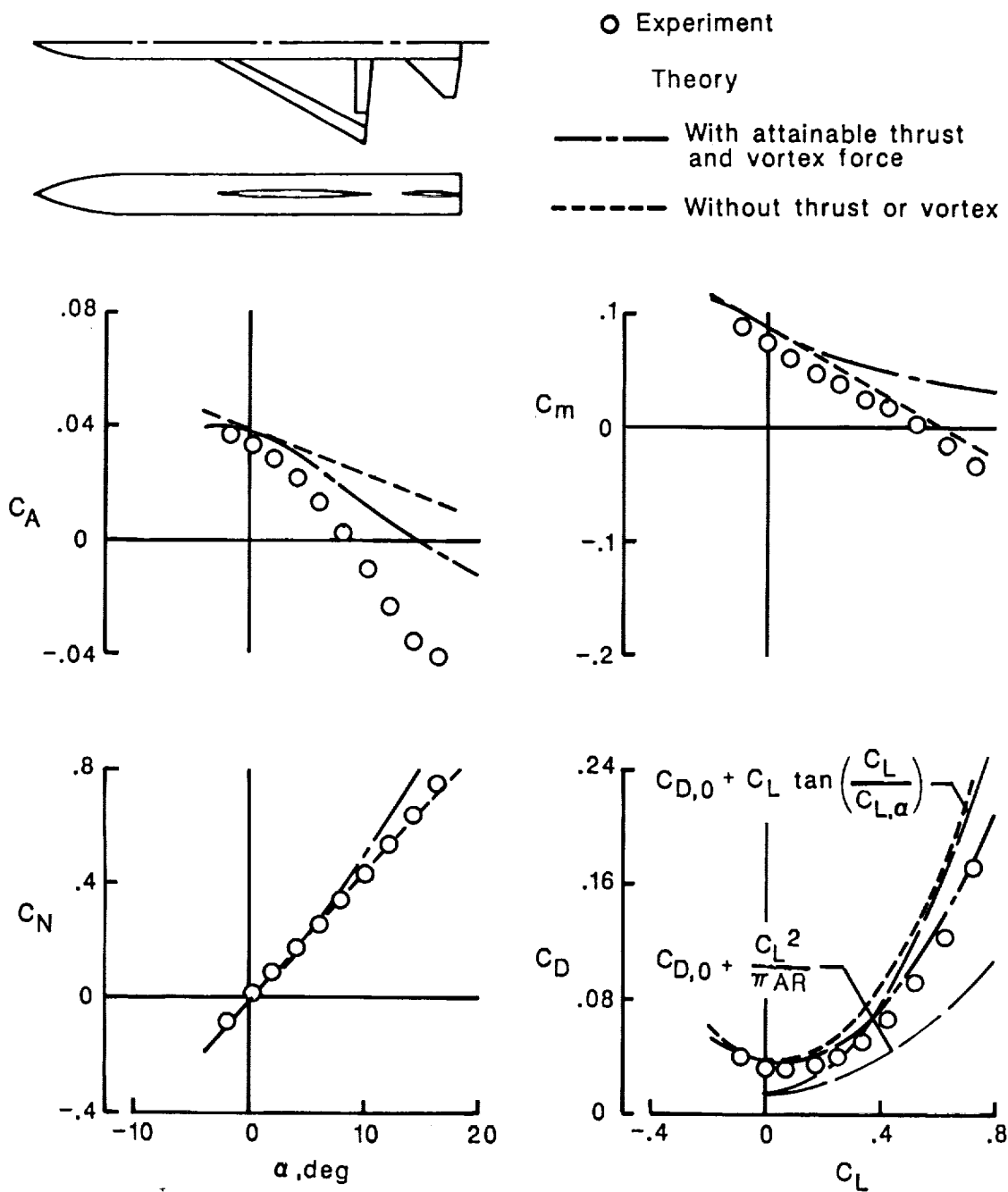
(e) $\delta_{L,n} = 10°$, $\delta_{T,n} = 10°$, $\delta_H = -10°$.

Figure 20. Continued.

Figure 20. Continued.

(f) $\delta_{L,n} = 10°$, $\delta_{T,n} = 10°$, $\delta_H = 10°$.

Experiment

Theory

With attainable thrust and vortex force

Without thrust or vortex
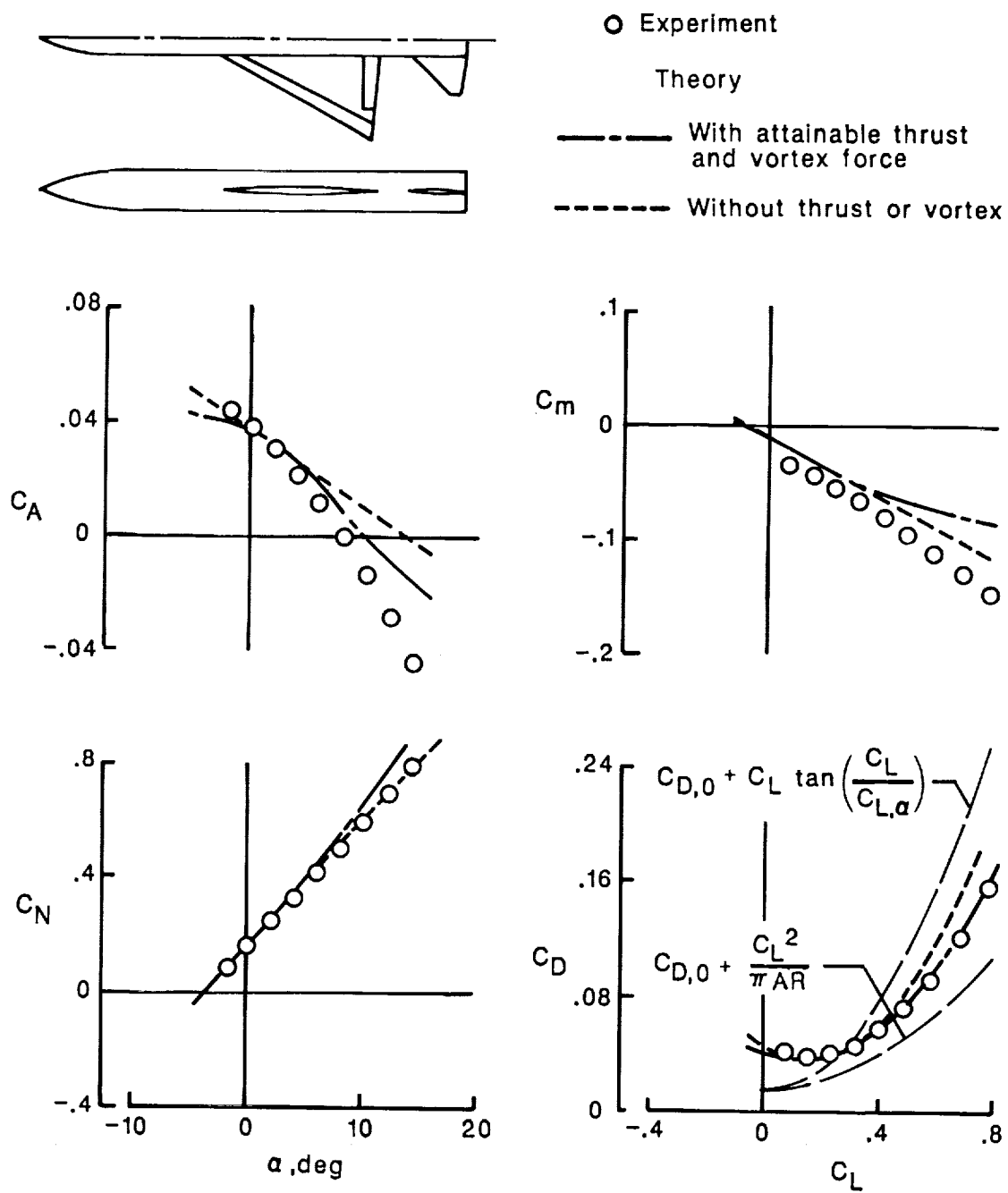
(g) $\delta_{L,n} = 20°$, $\delta_{T,n} = 20°$, $\delta_H = 0°$.

Figure 20. Continued.

(h) $\delta_{L,n} = 20°$, $\delta_{T,n} = 20°$, $\delta_H = -10°$.

Figure 20. Continued.

Experiment: O

Theory:
— · — With attainable thrust and vortex force
– – – Without thrust or vortex
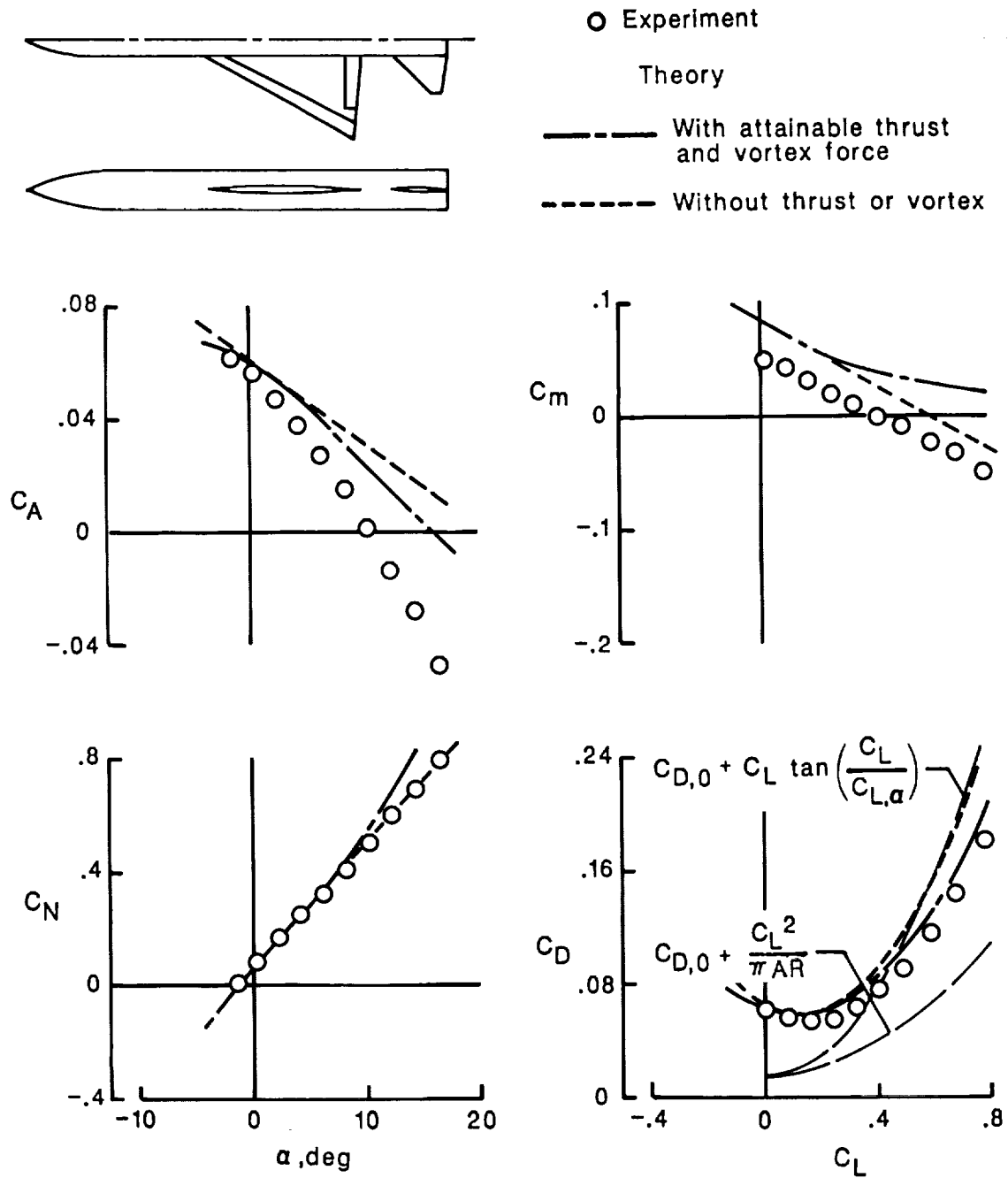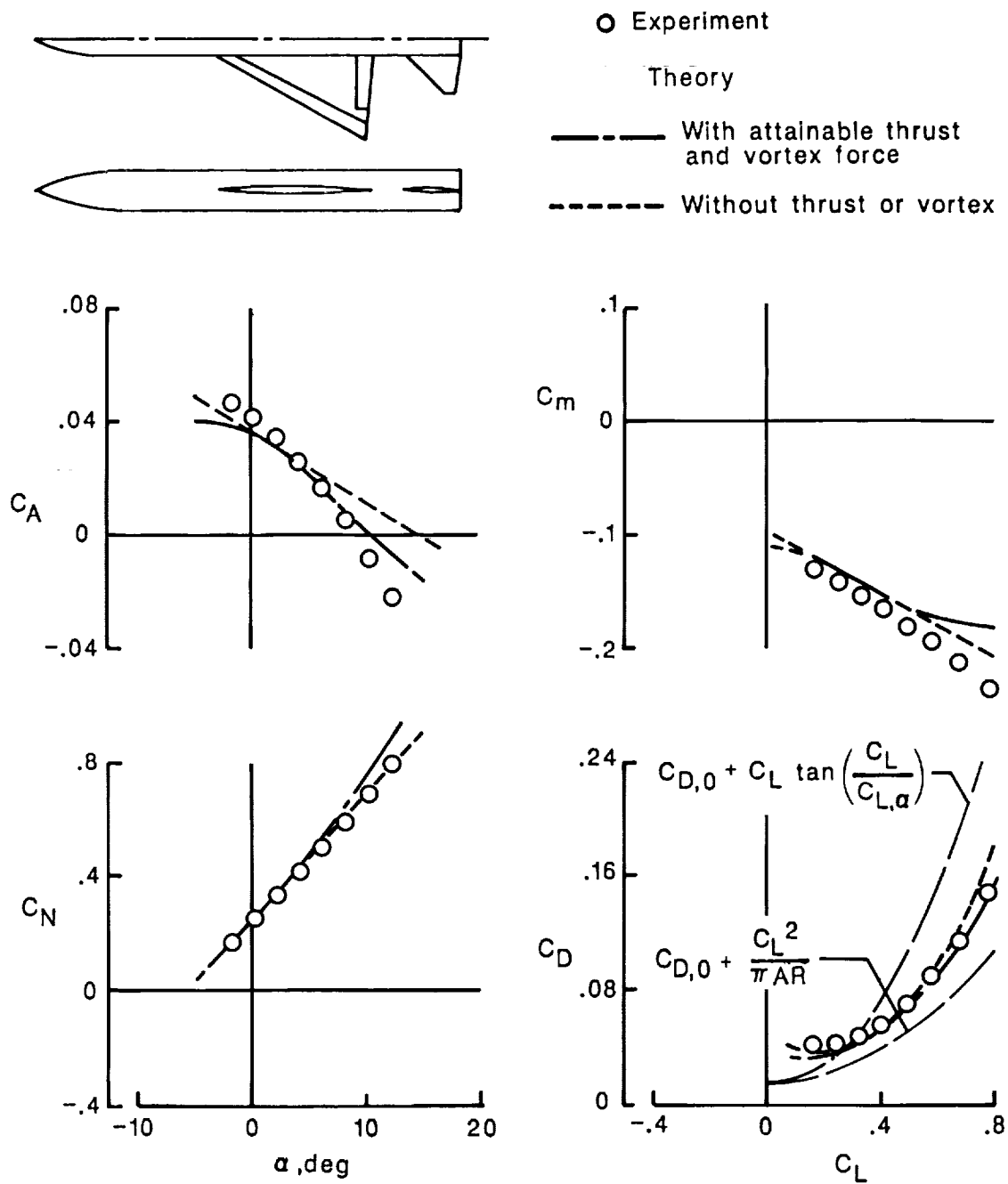
(i) $\delta_{L,n} = 20°$, $\delta_{T,n} = 20°$, $\delta_H = 10°$.

Figure 20. Concluded.
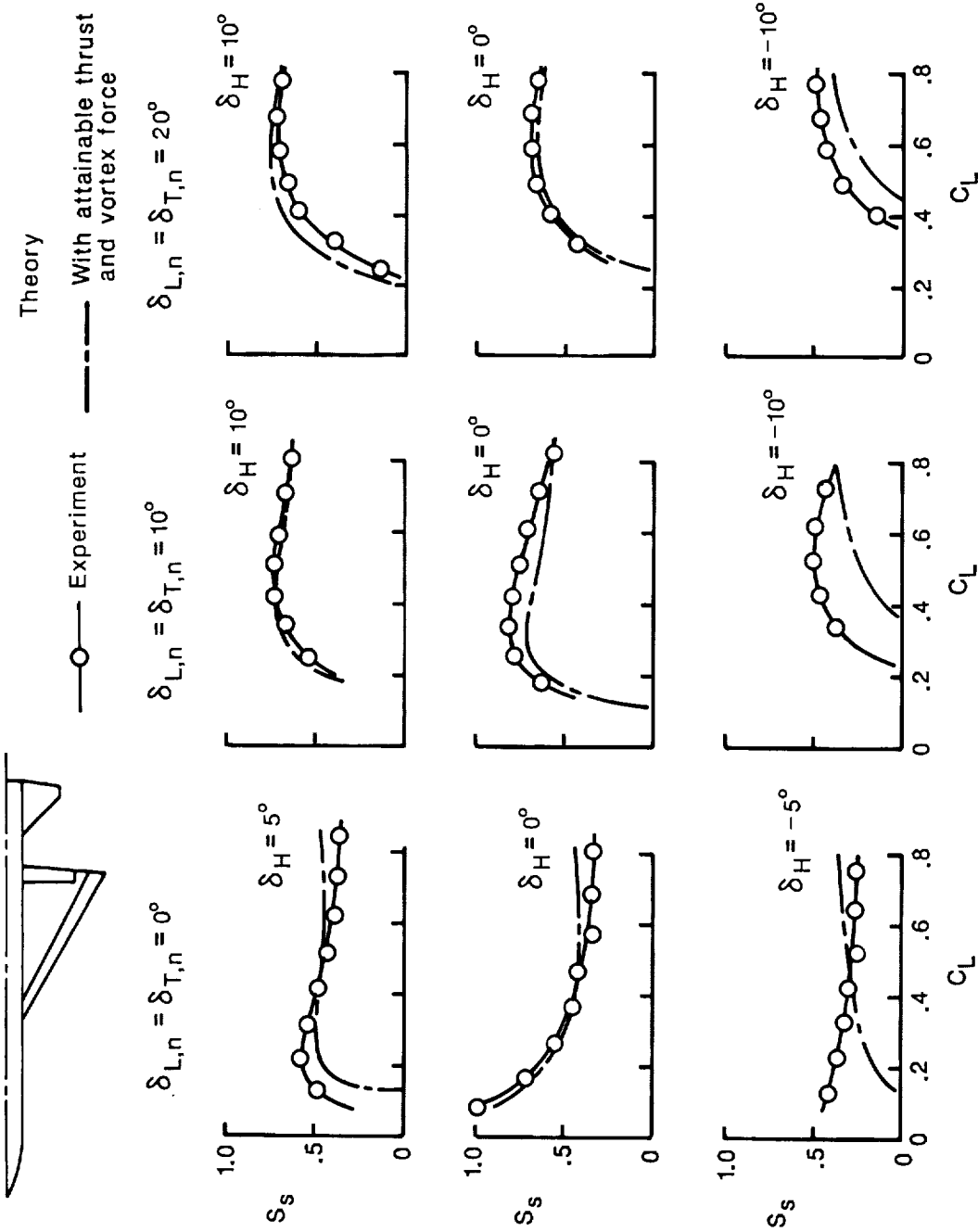
Figure 21. Suction-parameter variation with lift coefficient for various combinations of flap deflection angle and horizontal-tail incidence angle for 60°-swept delta-wing fighter with horizontal tail. $M = 0.4$; $R = 2.52 \times 10^6$.

89
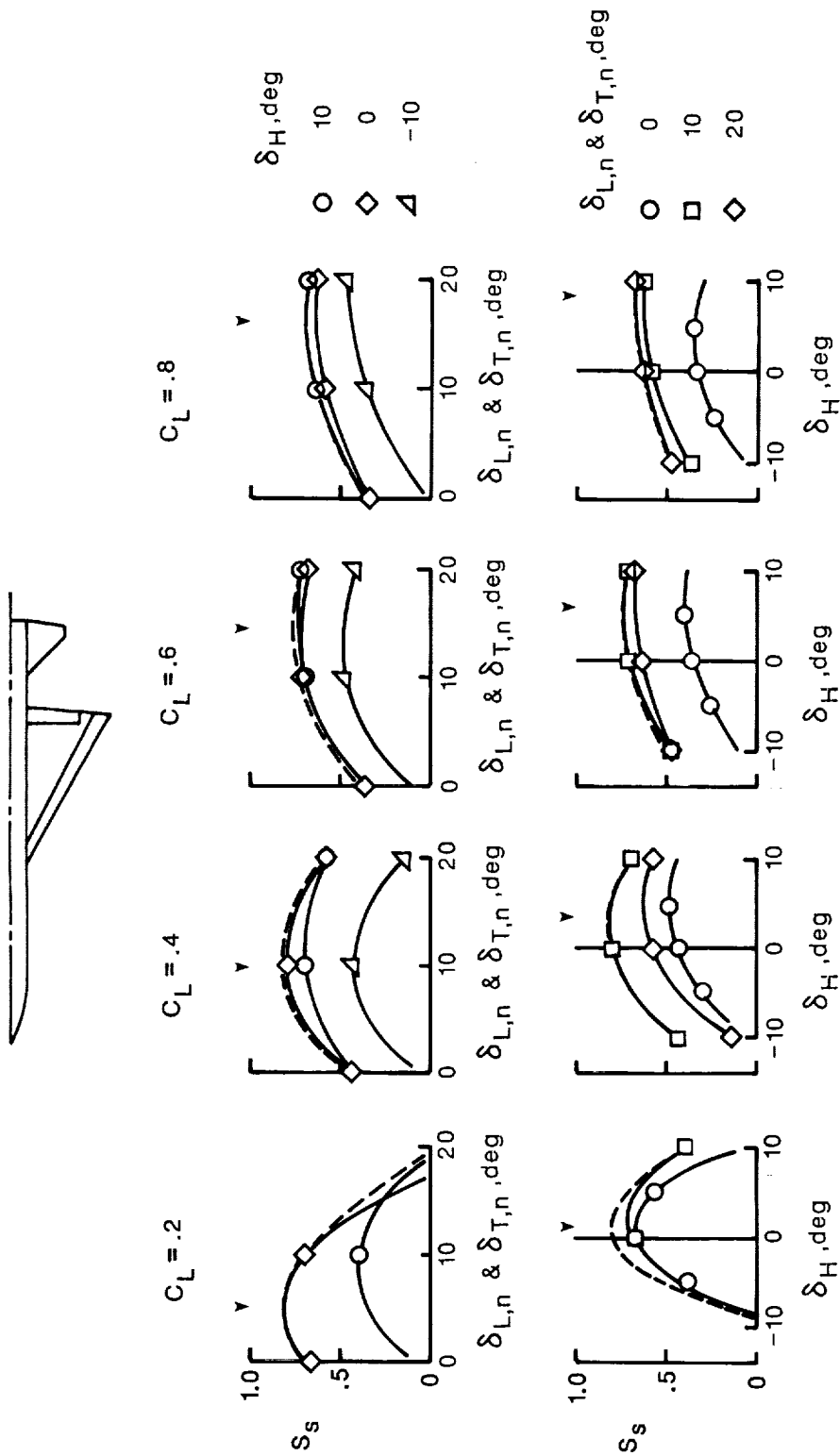
Figure 22. Experimental suction-parameter variation with flap deflection angle and horizontal-tail incidence angle for selected lift coefficients for 60°-swept delta-wing fighter with horizontal tail. $M = 0.4$; $R = 2.52 \times 10^6$; dashed lines indicate envelope curves, and arrows indicate optimum deflections.
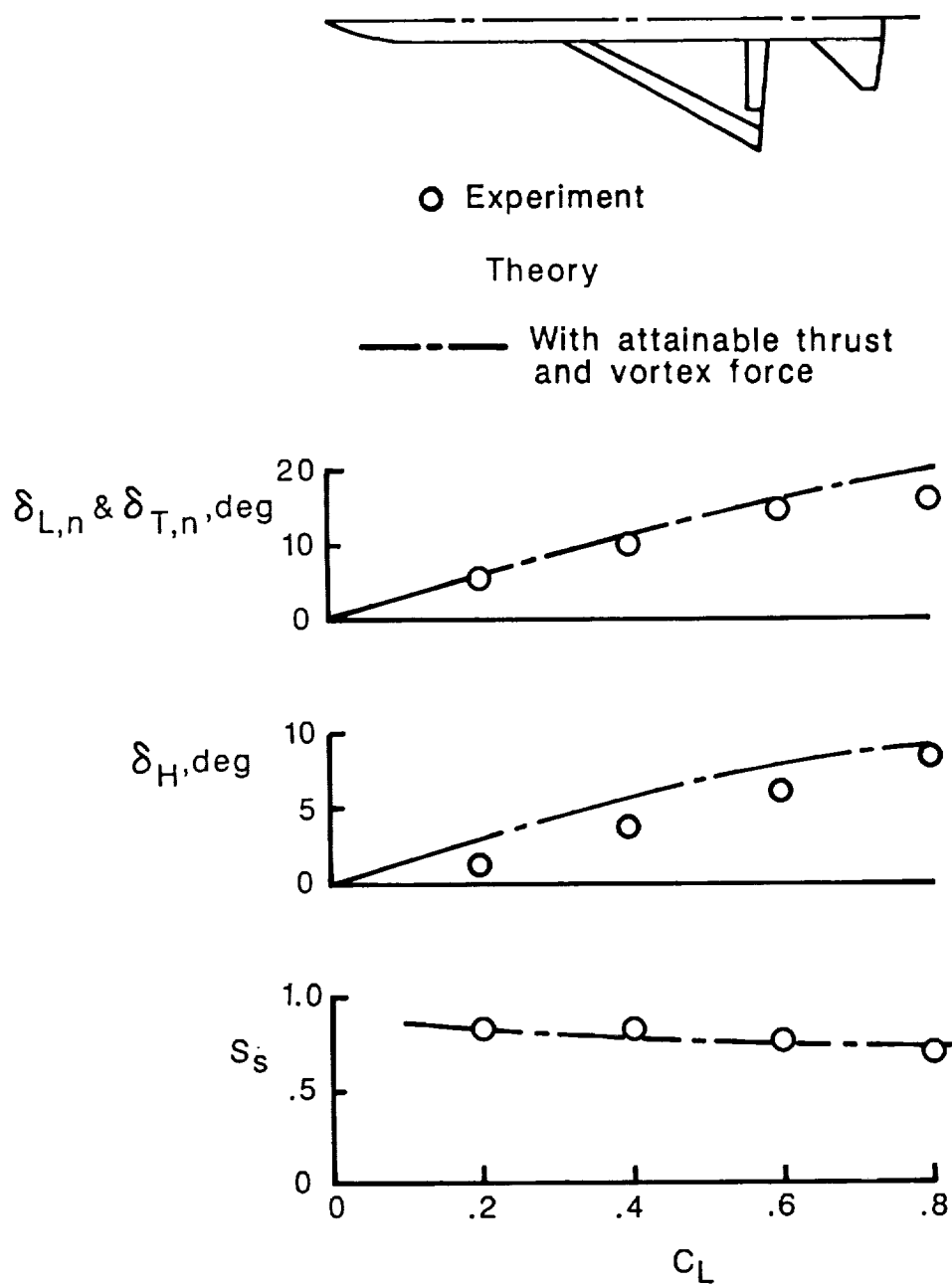
Figure 23. Optimum flap deflection angle, horizontal-tail incidence angle, and maximum suction-parameter variation with lift coefficient for 60°-swept delta-wing fighter with horizontal tail. $M = 0.4$; $R = 2.52 \times 10^6$.
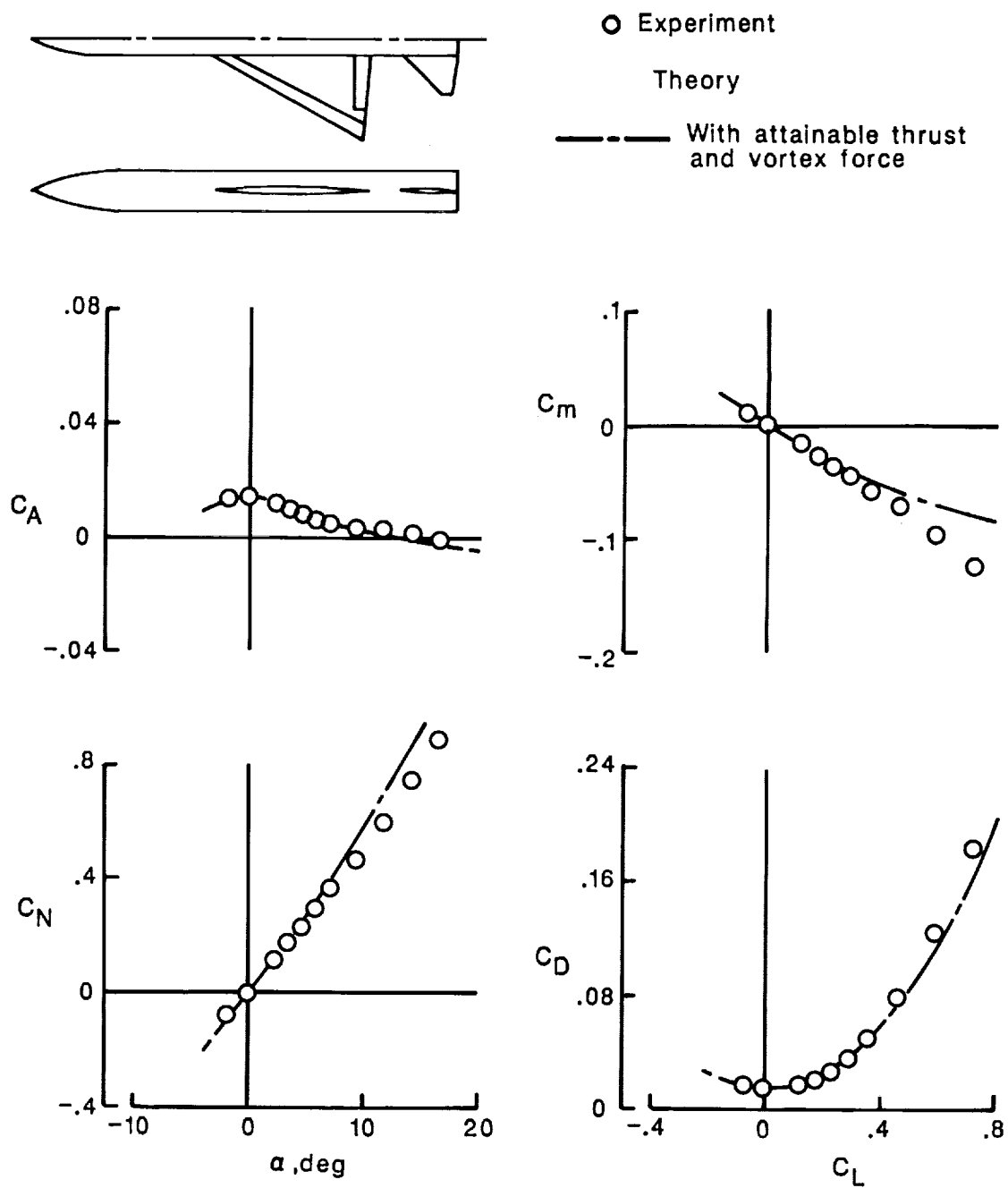
Figure 24. Theoretical and experimental data for 60°-swept trapezoidal-wing fighter with horizontal tail. $M = 0.8$; $R = 3.4 \times 10^6$.

(a) $\delta_{L,n} = 0°$, $\delta_{T,n} = 0°$, $\delta_H = 0°$.

O Experiment

Theory

——— With attainable thrust
and vortex force
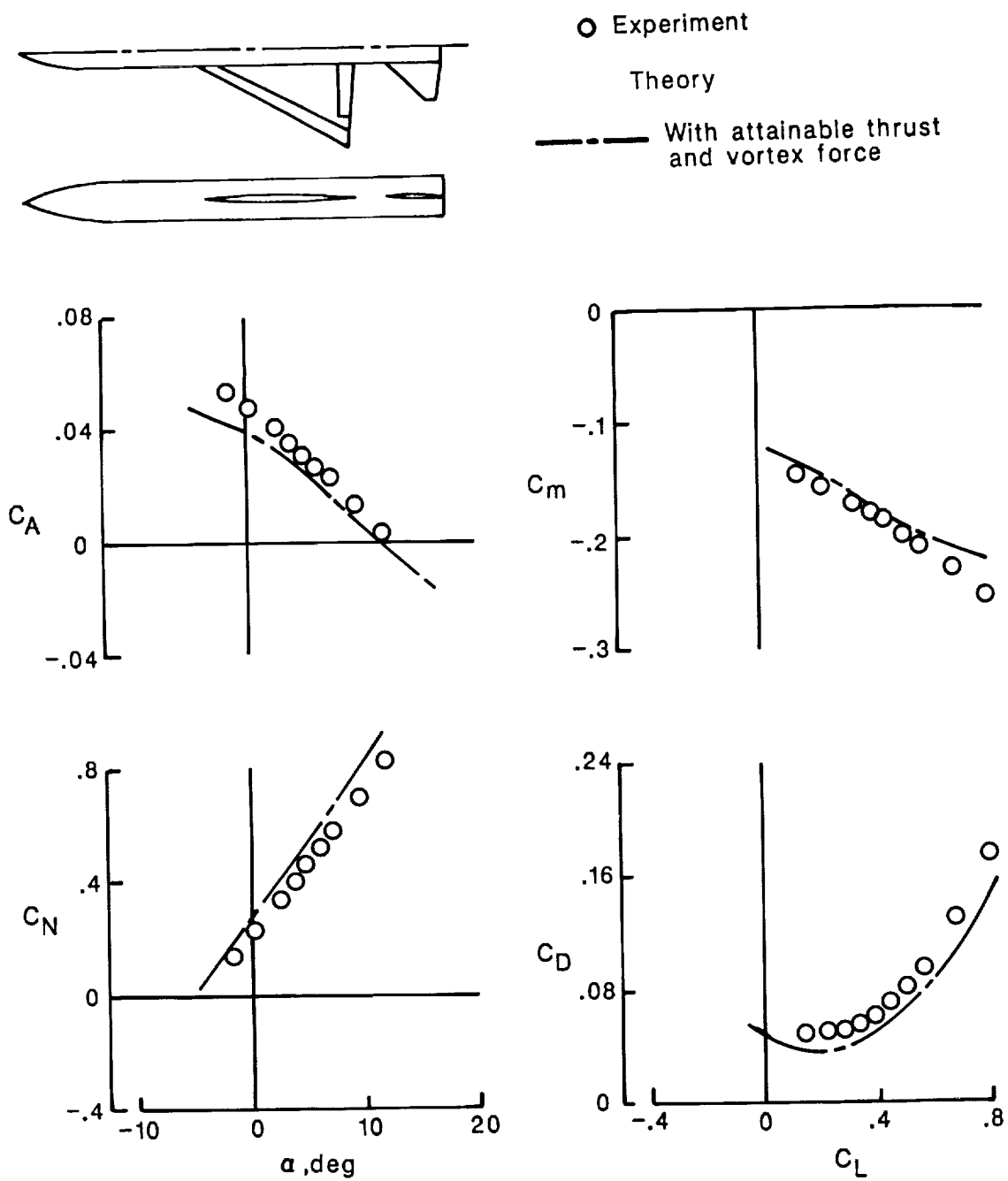
(b) $\delta_{L,n} = 20°$, $\delta_{T,n} = 20°$, $\delta_H = 10°$.

Figure 24. Concluded.

O Experiment

Theory

—— ·· —— With attainable thrust
and vortex force

$$C_{D,0} + C_L \tan\left(\frac{C_L}{C_{L,\alpha}}\right)$$

$$C_{D,0} + \frac{C_L^2}{\pi AR}$$
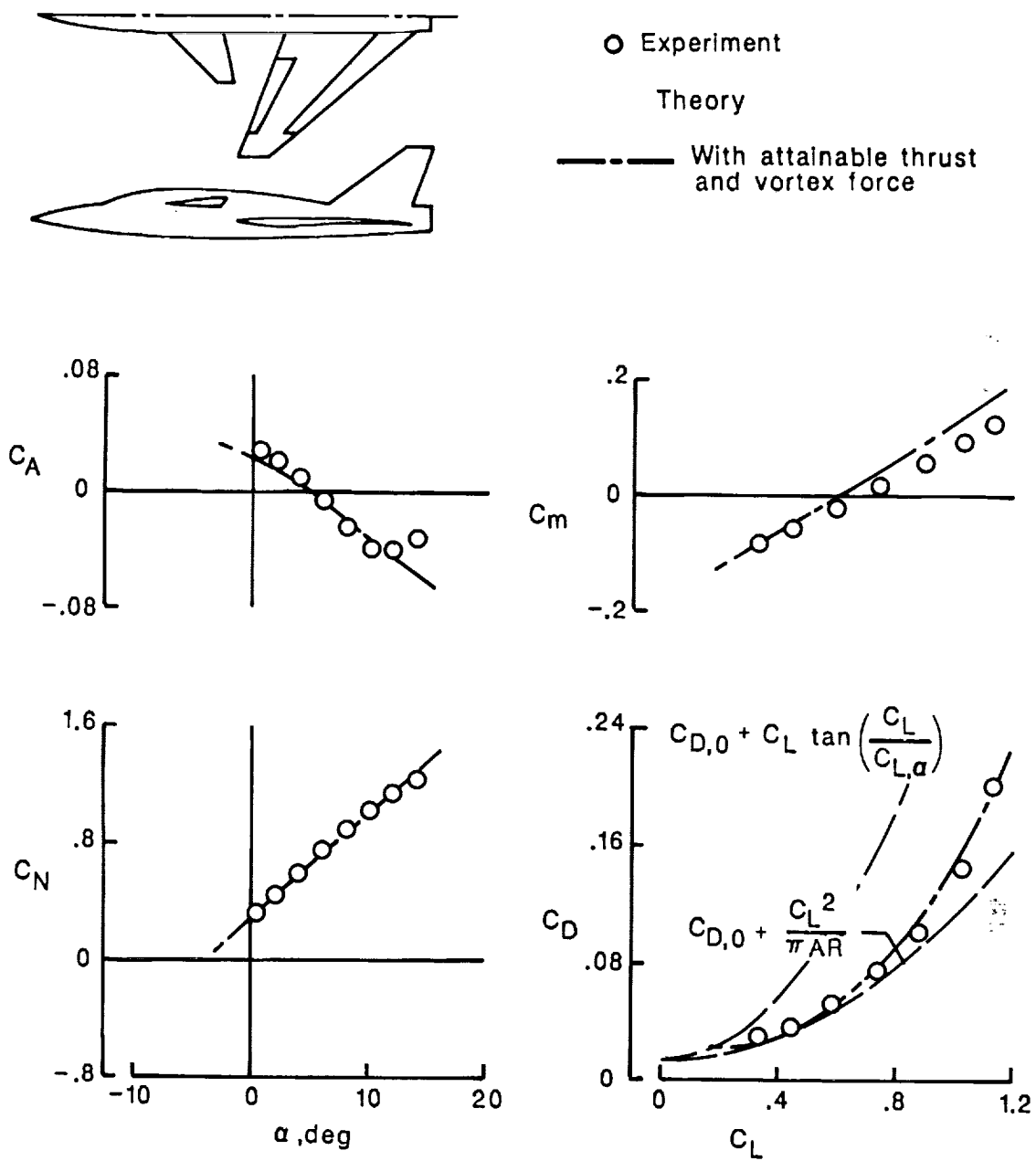
(a) $\delta_{L,s} = 0°$, $\delta_{T,s} = 0°$, $\delta_C = 0°$.

Figure 25. Theoretical and experimental data for forward swept-wing fighter with canard. $M = 0.6$; $R = 2.5 \times 10^6$.
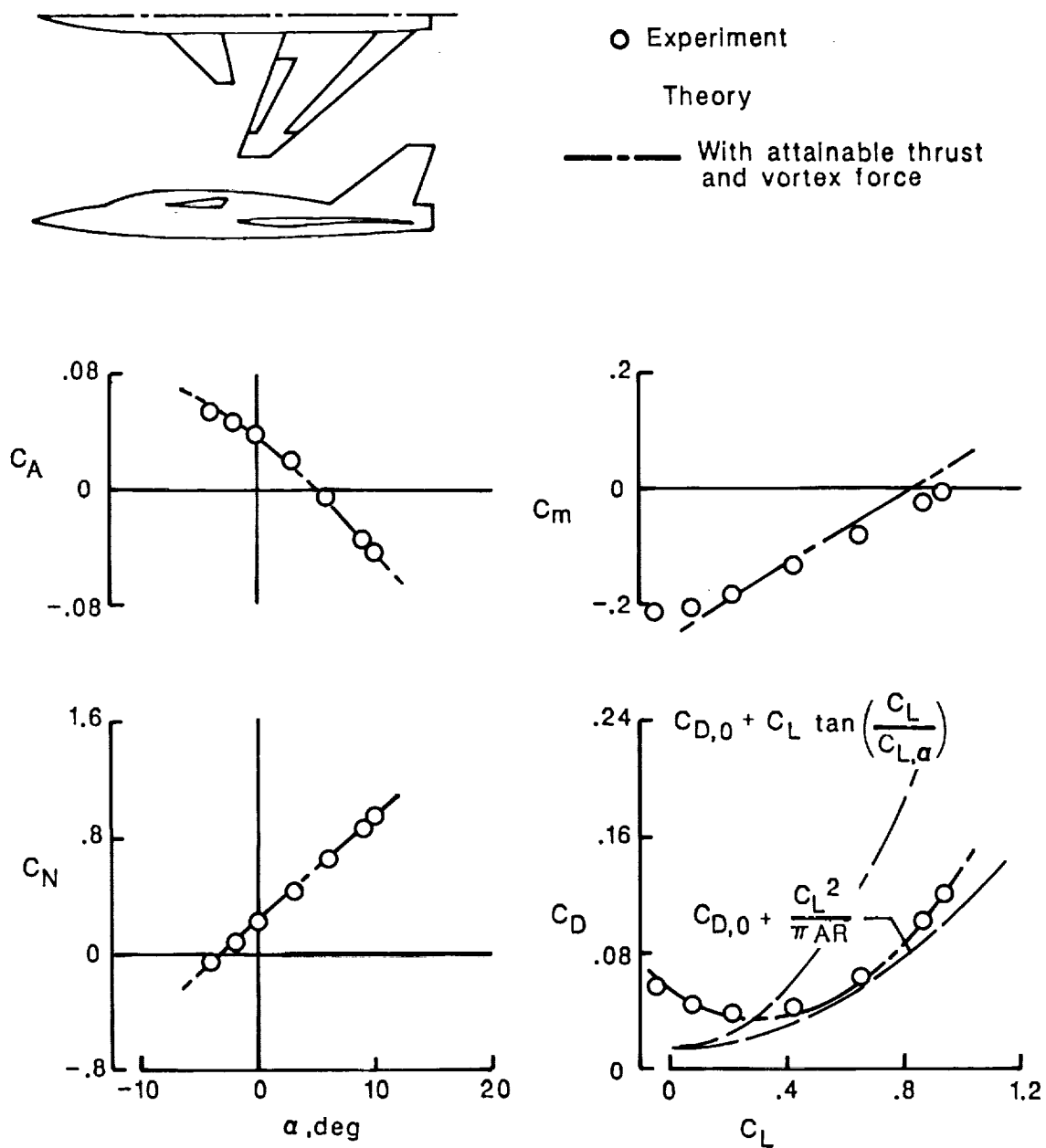
Legend:

O Experiment

Theory

—— With attainable thrust and vortex force

(b) $\delta_{L,s} = 0°$, $\delta_{T,s} = 0°$, $\delta_C = 10°$.

Figure 25. Continued.

○ Experiment

Theory

—— · —— With attainable thrust and vortex force

(c) $\delta_{L,s} = 0°$, $\delta_{T,s} = 0°$, $\delta_C = -10°$.

Figure 25. Continued.

$C - 2$

O Experiment

Theory

With attainable thrust
and vortex force

(d) $\delta_{L,s} = 0°$, $\delta_{T,s} = 10°$, $\delta_C = 0°$.

Figure 25. Continued.

O Experiment

Theory

With attainable thrust
and vortex force

$$C_{D,0} + C_L \tan\left(\frac{C_L}{C_{L,\alpha}}\right)$$

$$C_{D,0} + \frac{C_L{}^2}{\pi\,AR}$$

(e) $\delta_{L,s} = 5°$, $\delta_{T,s} = 10°$, $\delta_C = 0°$.

Figure 25. Continued.

O Experiment

Theory

With attainable thrust and vortex force
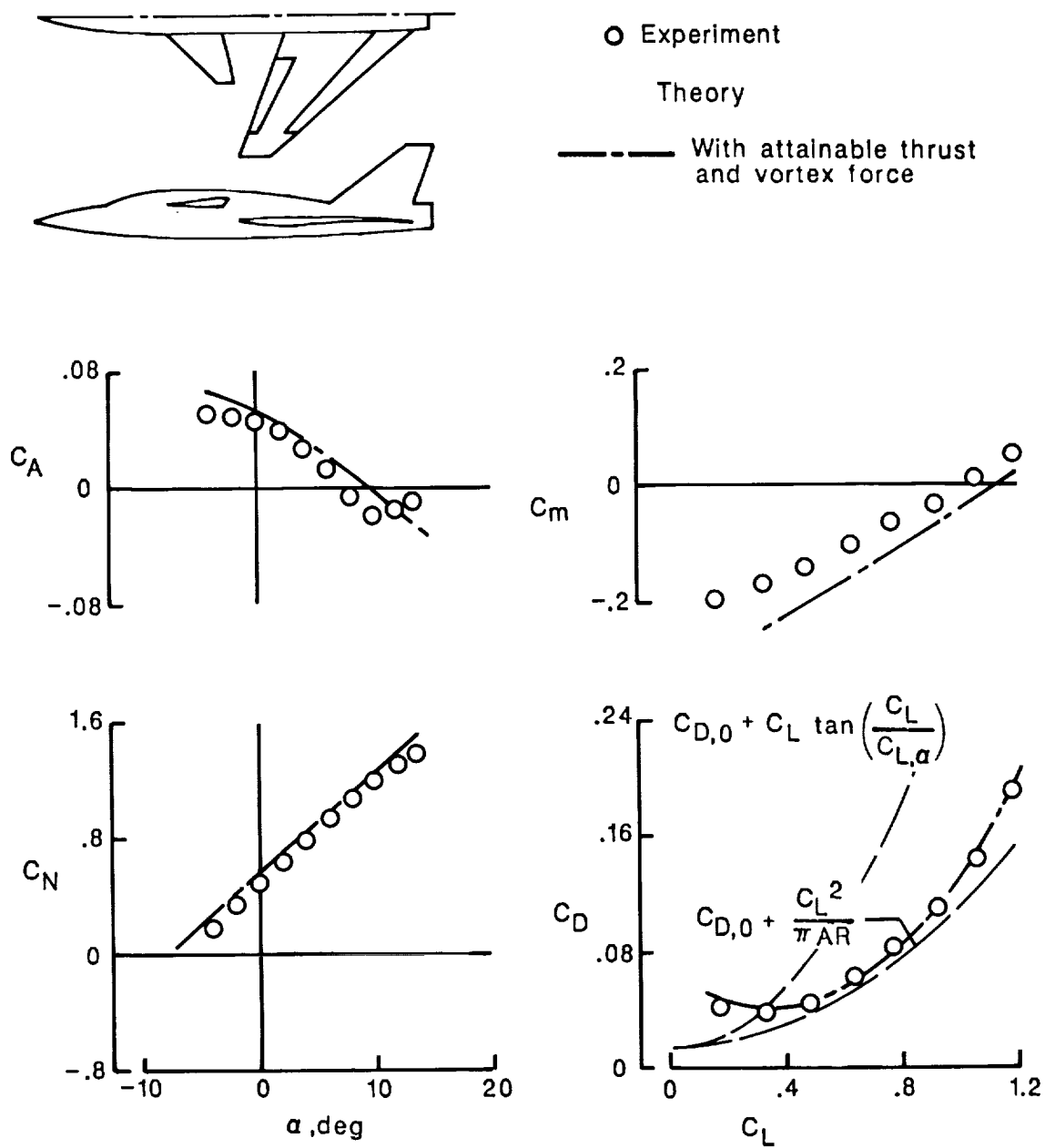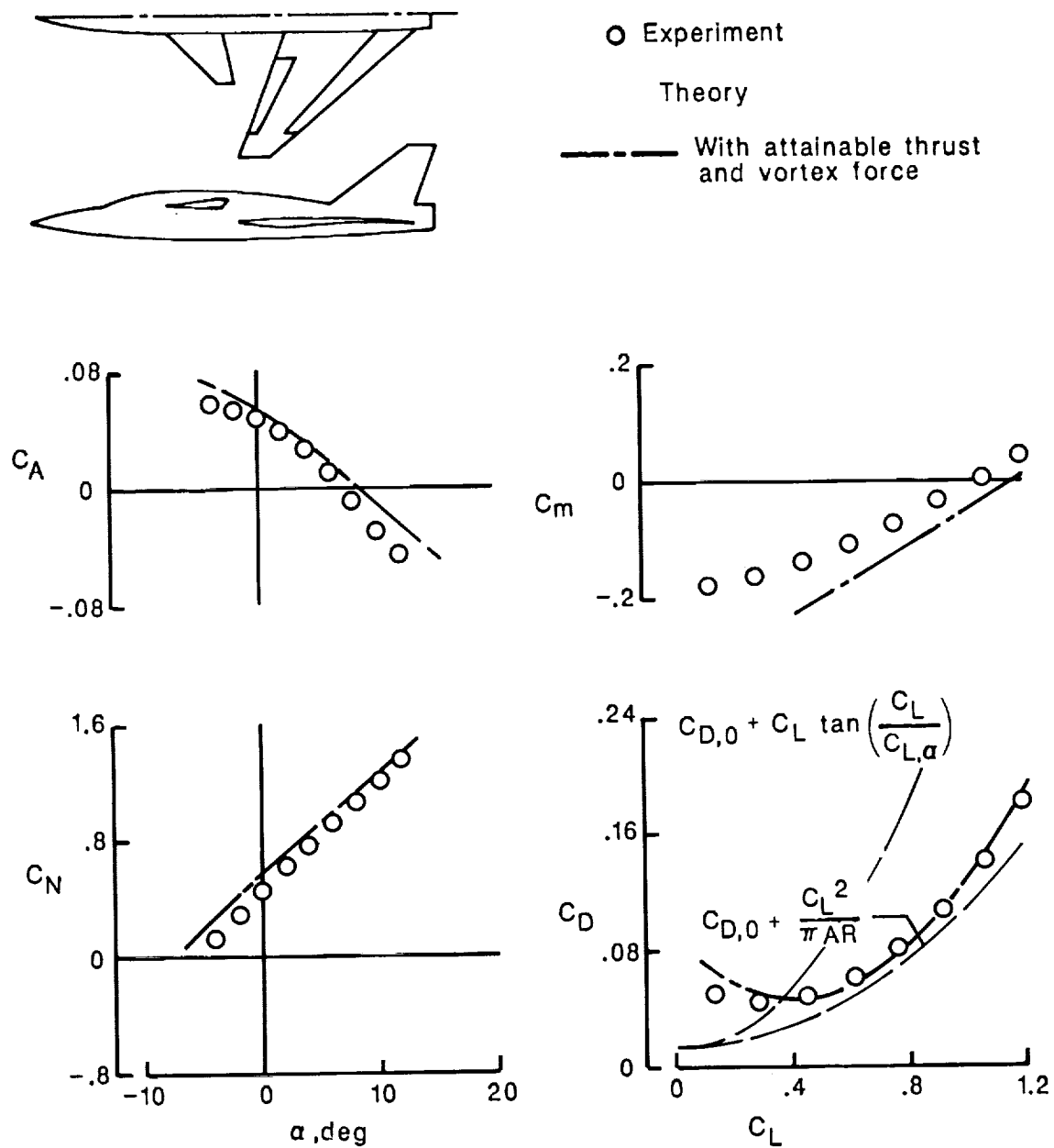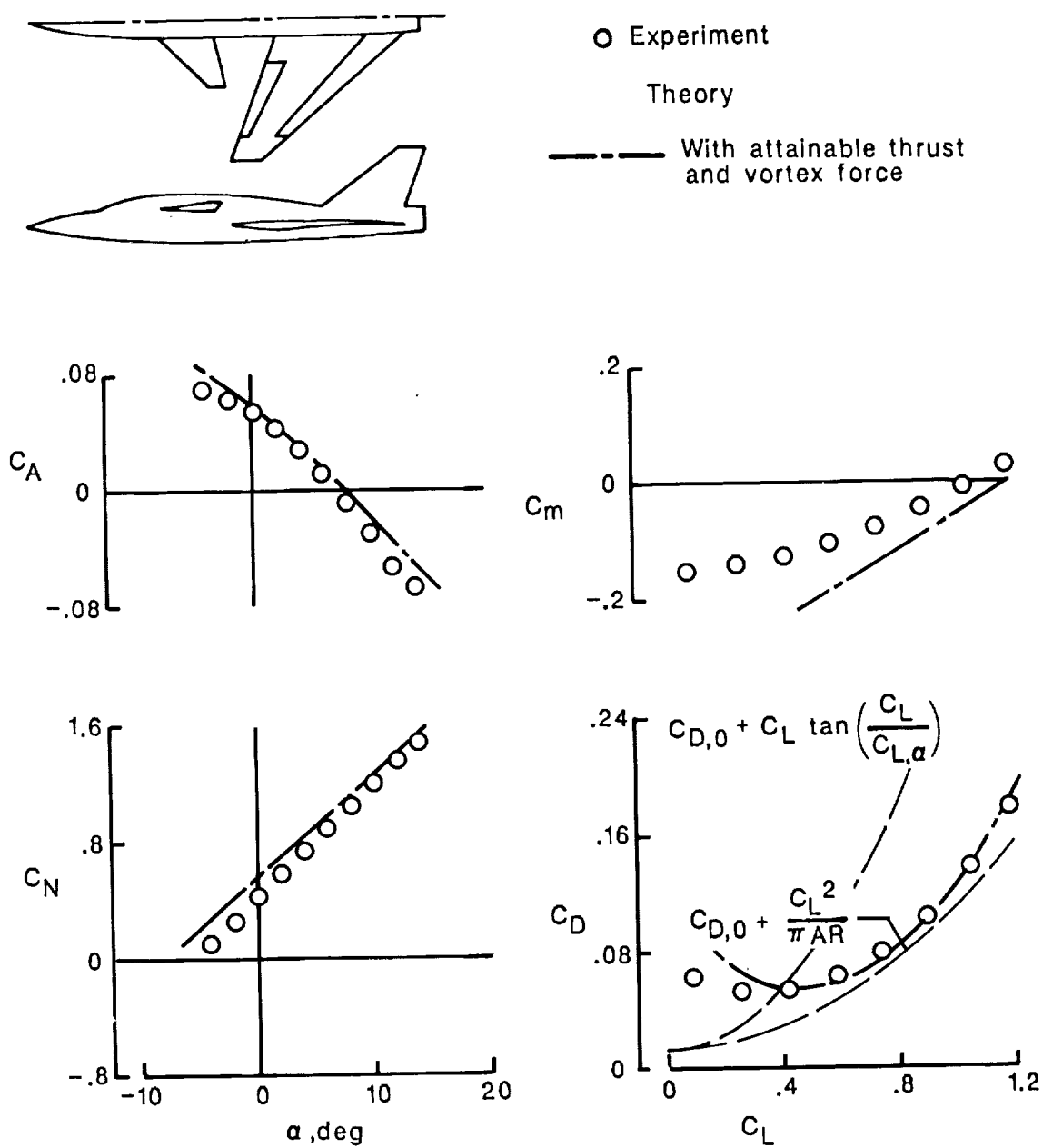
(f) $\delta_{L,s} = 10°$, $\delta_{T,s} = 10°$, $\delta_C = 0°$.

Figure 25. Concluded.
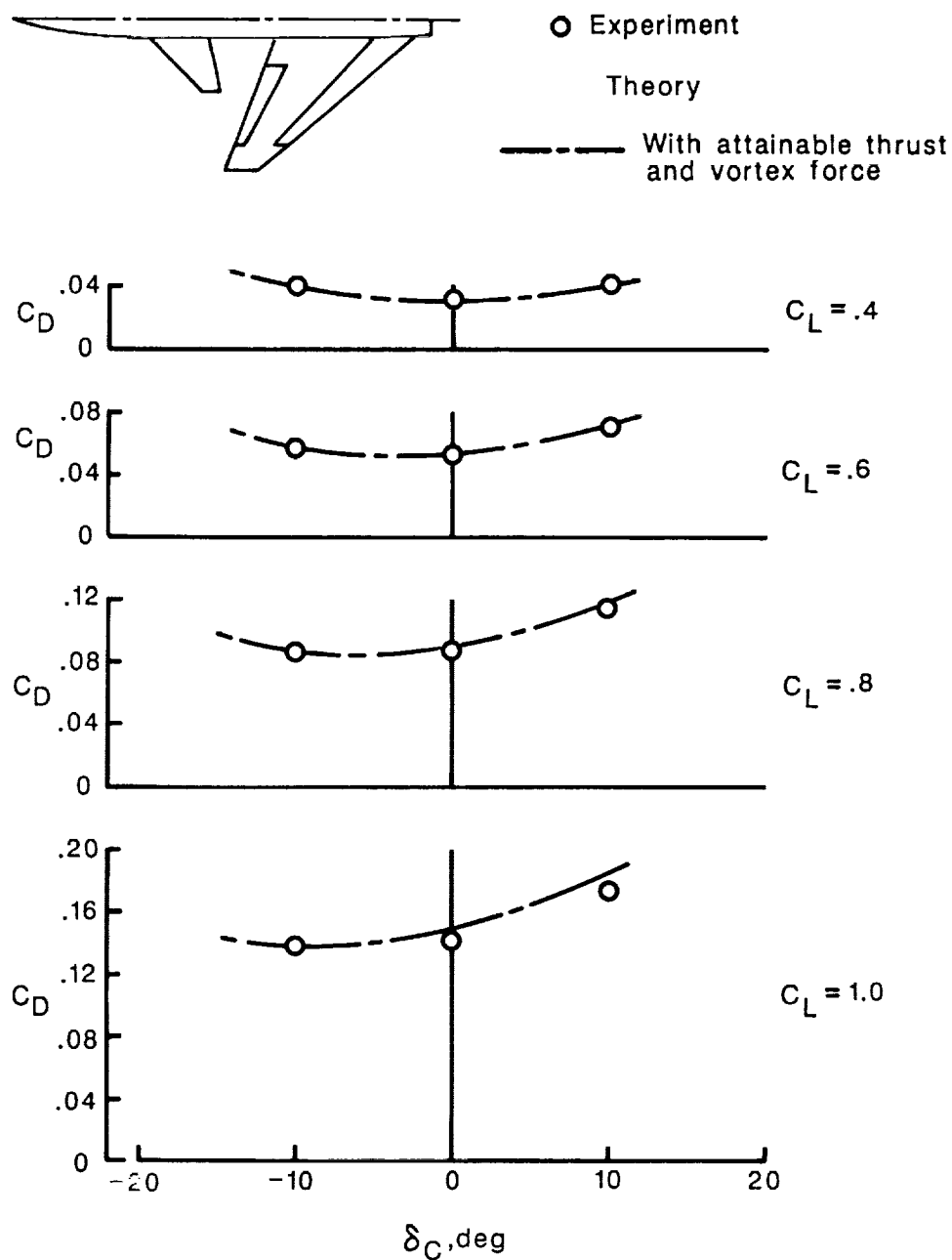
Figure 26. Variation of drag with canard incidence angle for selected lift coefficients for forward swept-wing fighter with canard. $\delta_{L,s} = 0°$; $\delta_{T,s} = 0°$; $M = 0.6$; $R = 2.5 \times 10^6$.
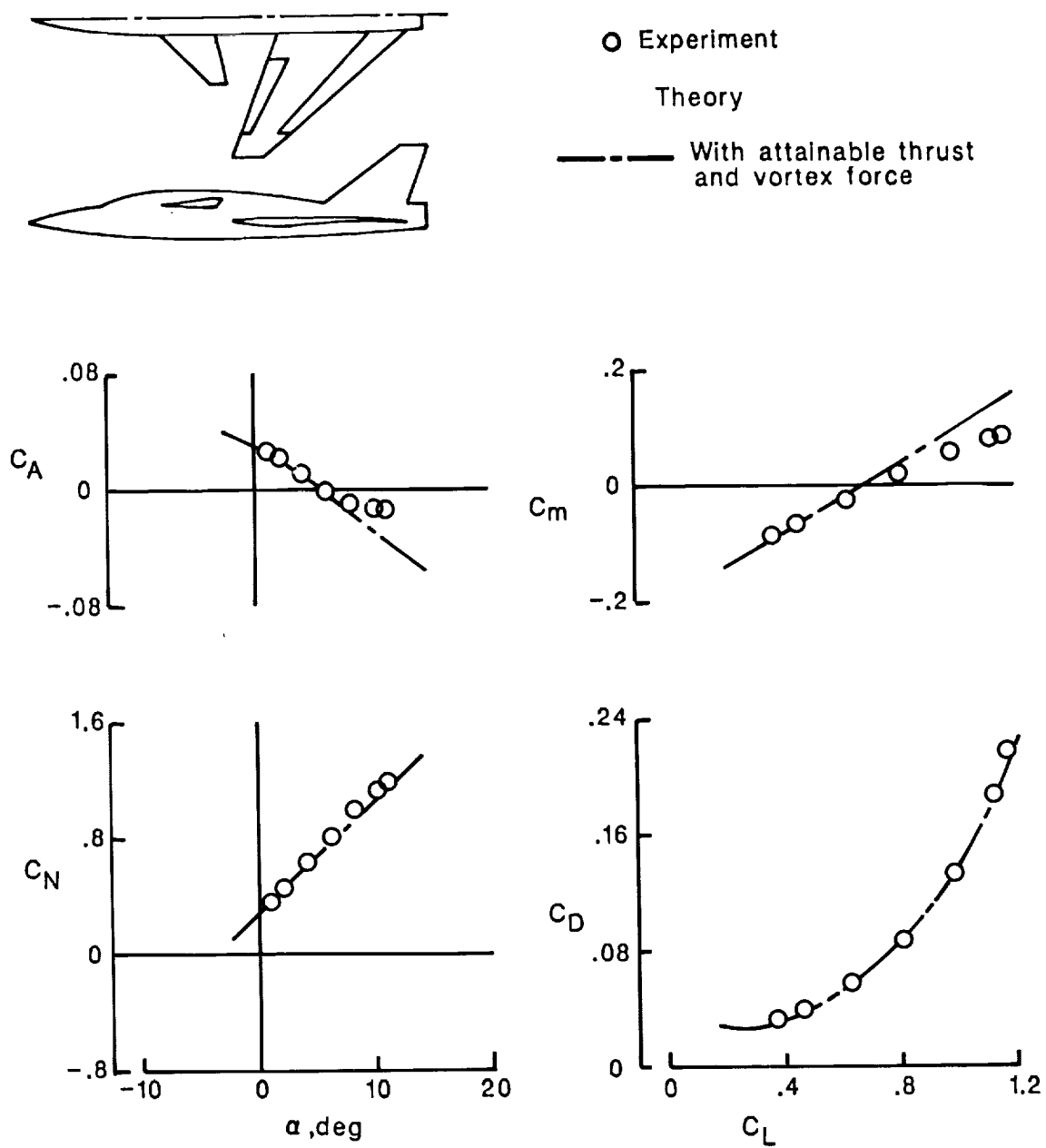
(a) $M = 0.8$.

Figure 27. Theoretical and experimental data for forward swept-wing fighter with canard at transonic Mach numbers. $\delta_{L,s} = 0°$; $\delta_{T,s} = 0°$; $\delta_c = 0°$.

O Experiment

Theory

With attainable thrust and vortex force
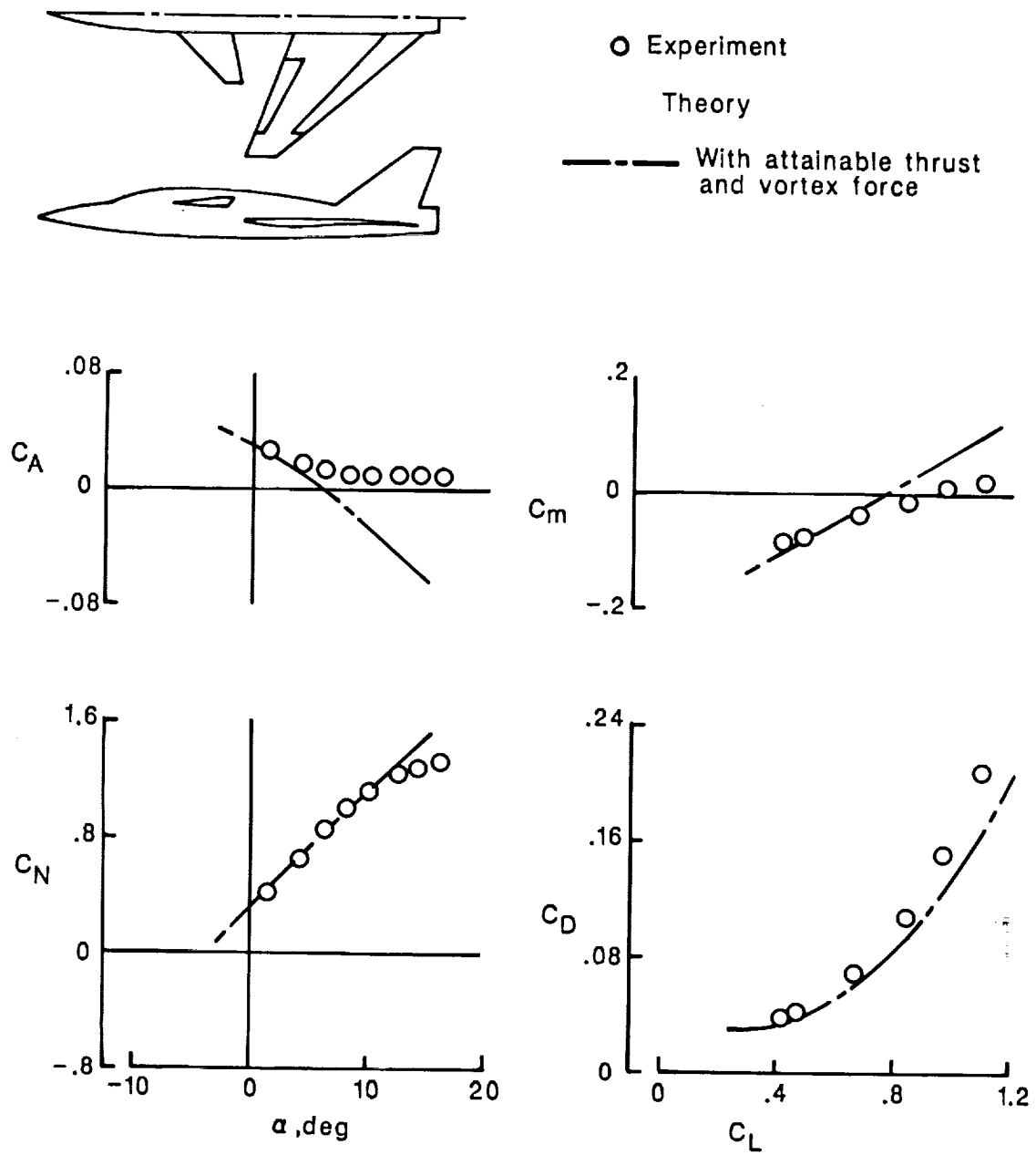
(b) $M = 0.9$.

Figure 27. Concluded.

O Experiment

Theory

— · — With attainable thrust and vortex force

— — — — Without thrust or vortex

(a) Wing-body configuration; $\delta_{L,n} = 0°$; $\delta_{T,n} = 0°$.
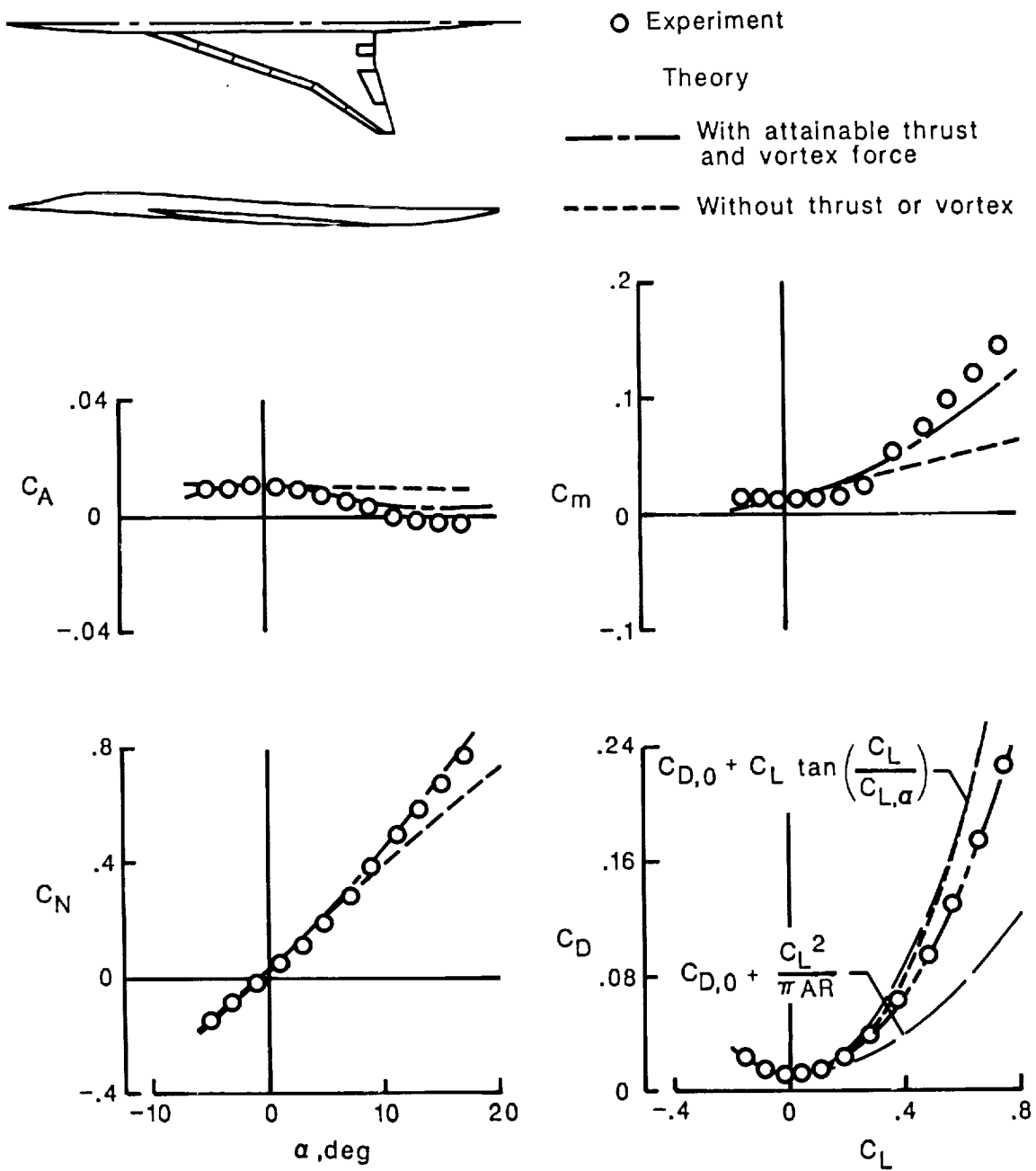
Figure 28. Theoretical and experimental data for arrow-wing supersonic transport. $M = 0.99$; $R = 4.19 \times 10^6$.
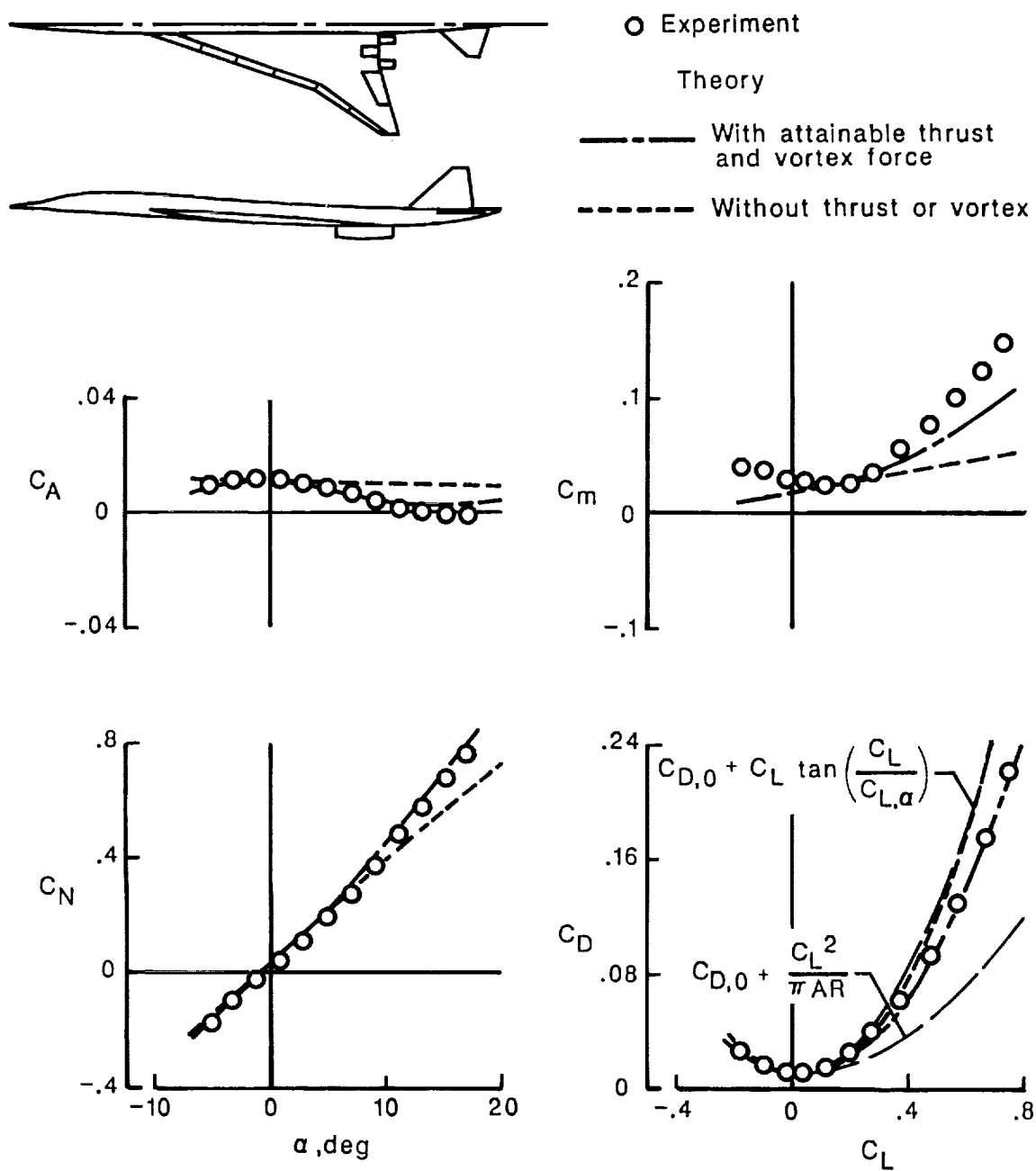
(b) Complete configuration; $\delta_{L,n} = 0°$; $\delta_{T,n} = 0°$; $\delta_H = 0°$.

Figure 28. Continued.

Legend:
- O Experiment
- Theory
- With attainable thrust and vortex force
- Without thrust or vortex

C_A vs α plot; C_m vs C_L plot; C_N vs α plot; C_D vs C_L plot.

$$C_{D,0} + C_L \tan\left(\frac{C_L}{C_{L,\alpha}}\right)$$

$$C_{D,0} + \frac{C_L^2}{\pi AR}$$

(c) Complete configuration; $\delta_{L,n} = 0°$; $\delta_{T,n} = 0°$; $\delta_H = -5°$.

Figure 28. Continued.

Legend:

○ Experiment

Theory

——— With attainable thrust and vortex force

- - - - Without thrust or vortex
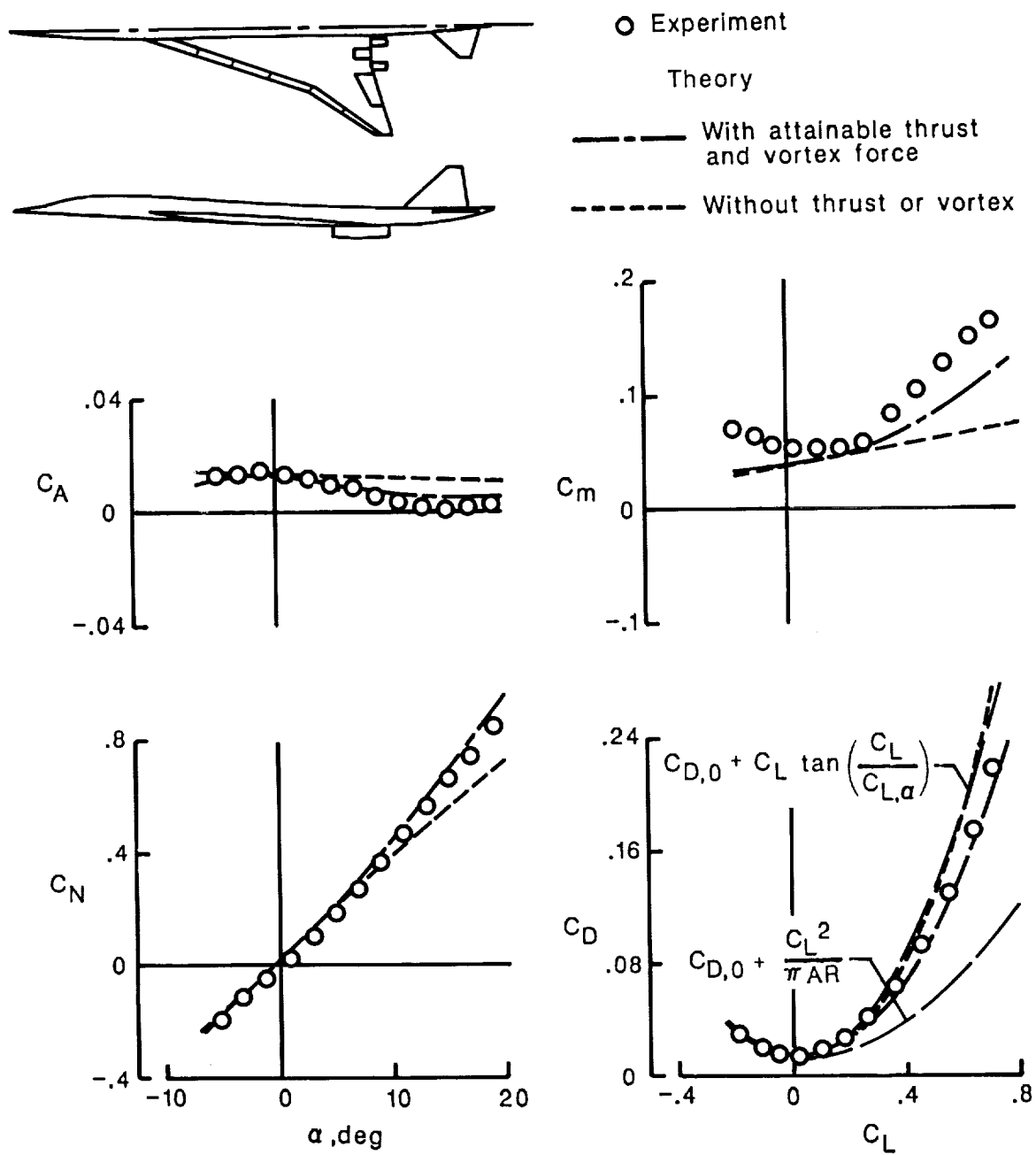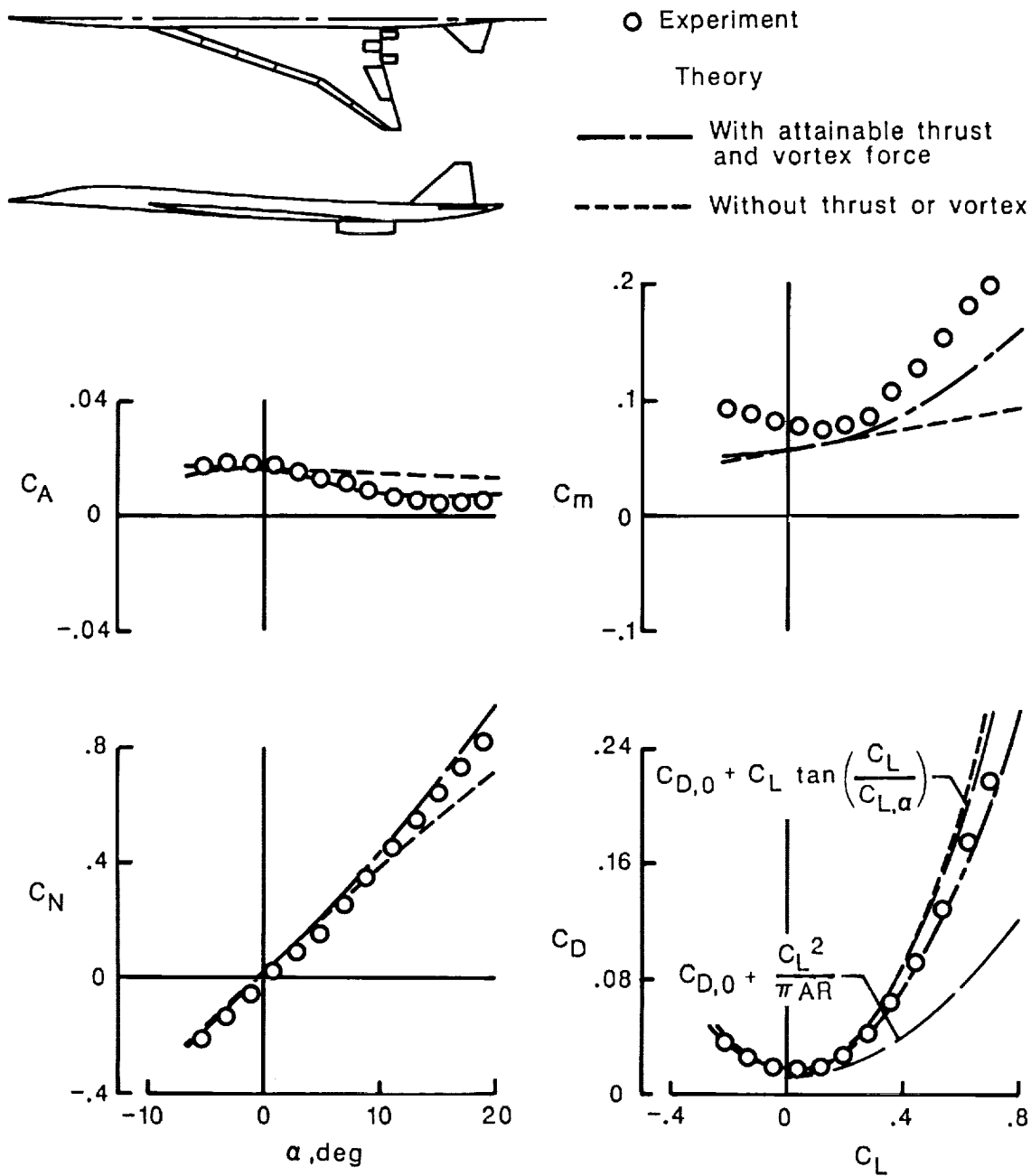
(d) Complete configuration; $\delta_{L,n} = 0°$; $\delta_{T,n} = 0°$; $\delta_H = -10°$.

Figure 28. Continued.
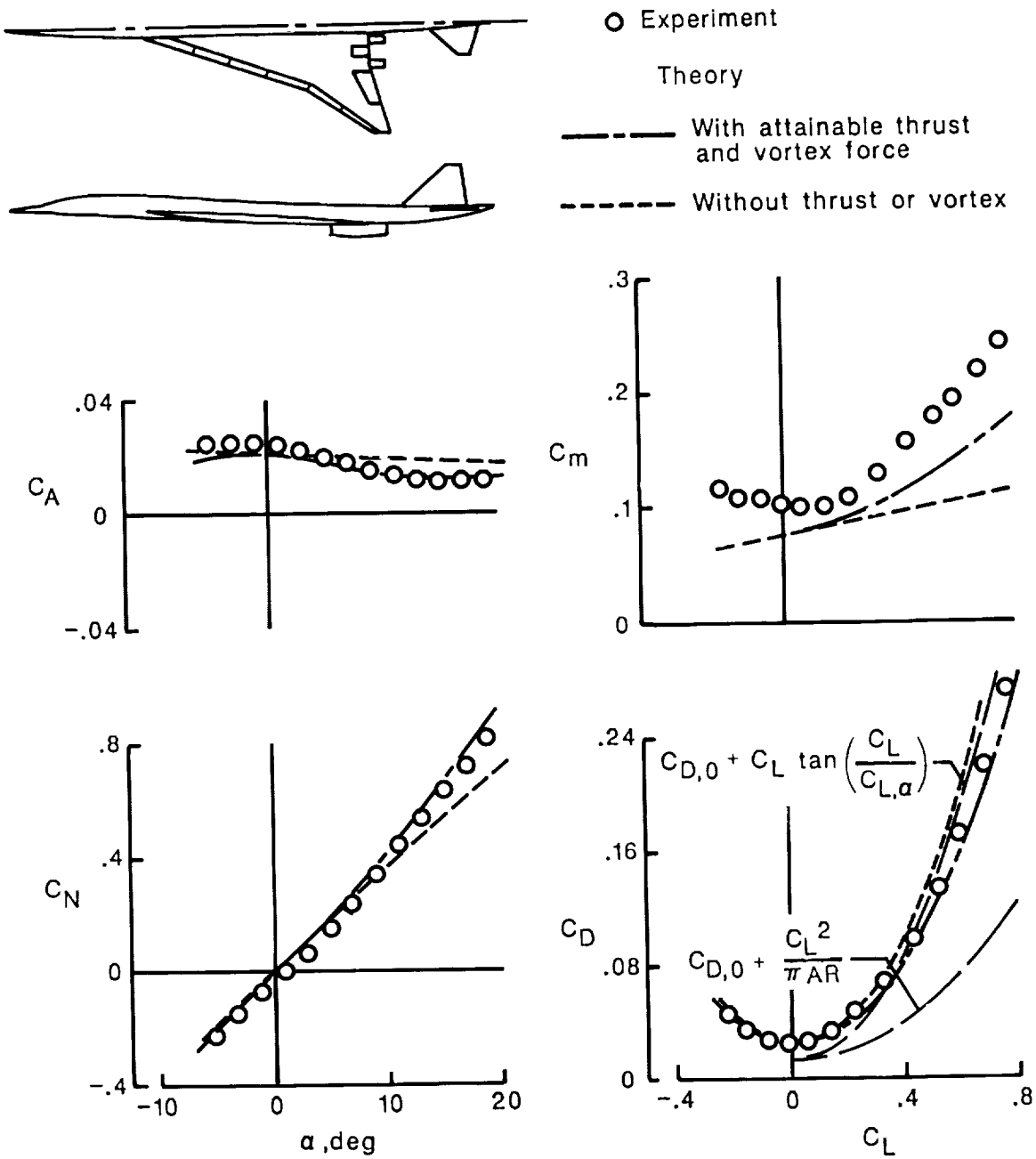
(e) Complete configuration; $\delta_{L,n} = 0°$; $\delta_{T,n} = 0°$; $\delta_H = -15°$.

Figure 28. Continued.

(f) Complete configuration; $\delta_{L,n} = 0°$; $\delta_{T,n} = 0°$; $\delta_H = 5°$.

Figure 28. Continued.

Legend:

○ Experiment

Theory

——— ⋅⋅ ——— With attainable thrust and vortex force

— — — — — Without thrust or vortex

$C_{D,0} + C_L \tan\left(\dfrac{C_L}{C_{L,\alpha}}\right)$

$C_{D,0} + \dfrac{C_L^2}{\pi\,AR}$
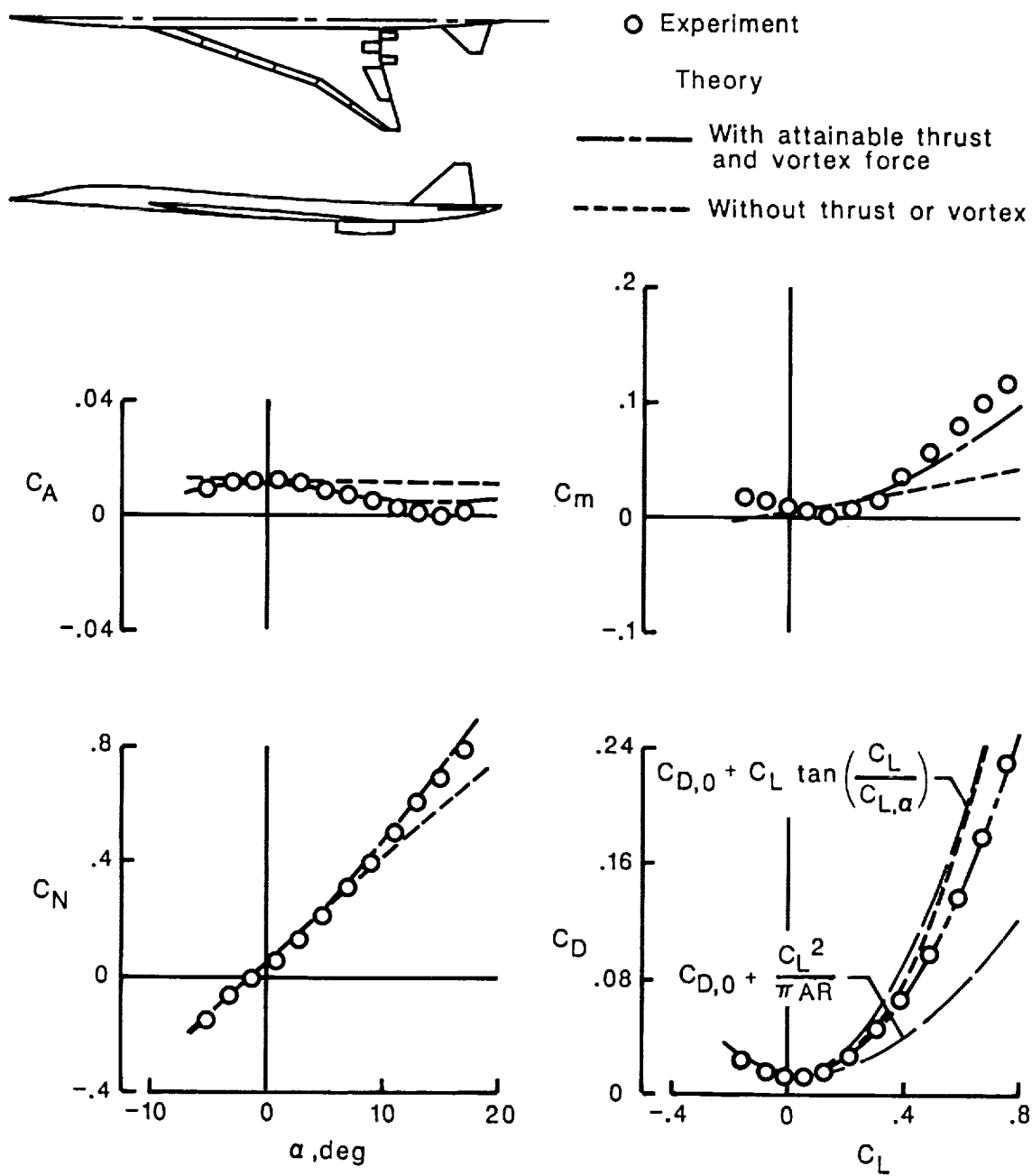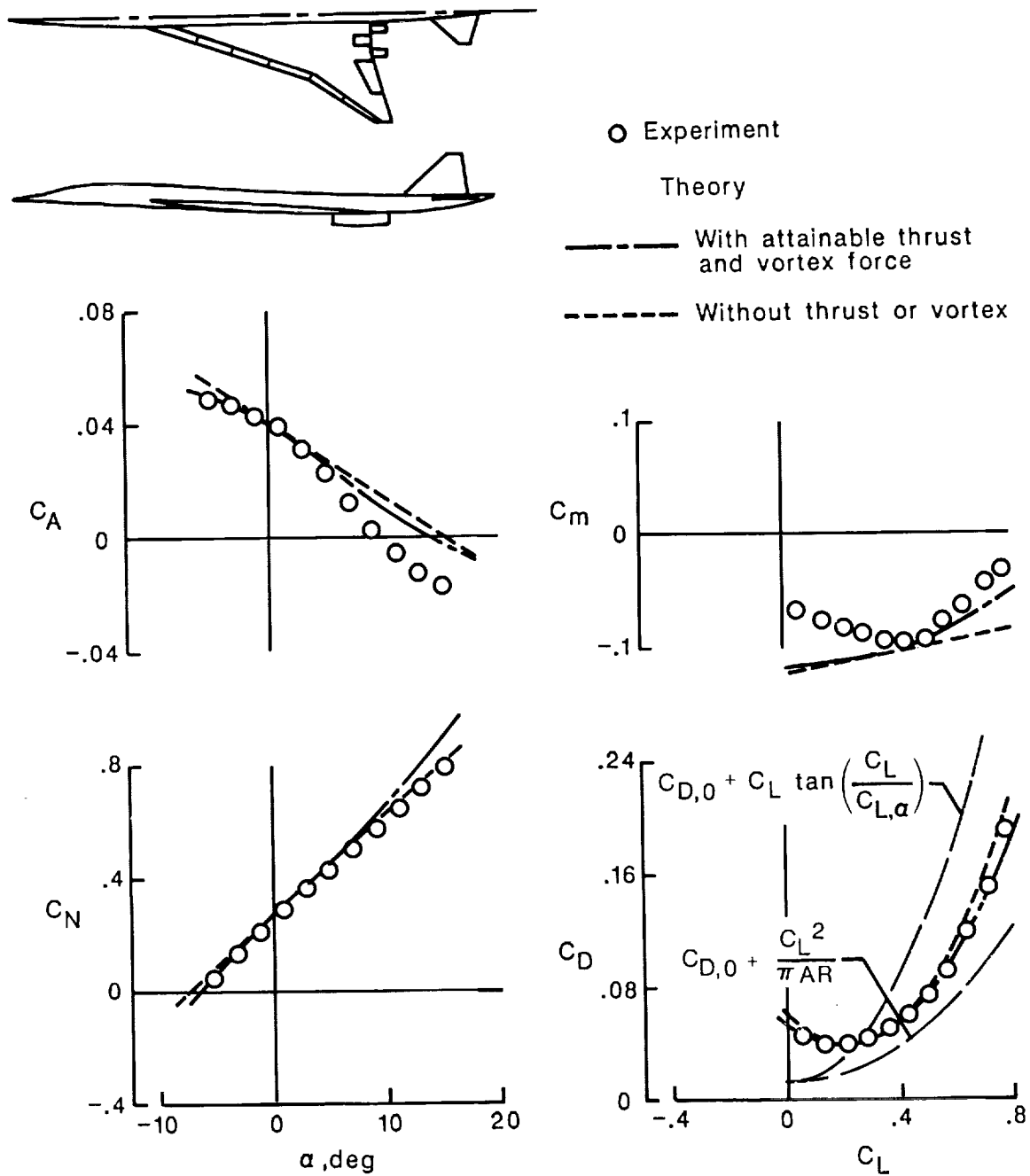
(g) Complete configuration; $\delta_{L,n} = 13°/34°/35°/35°/19°/29°$; $\delta_{T,s} = 30°$; $\delta_H = 0°$.

Figure 28. Continued.
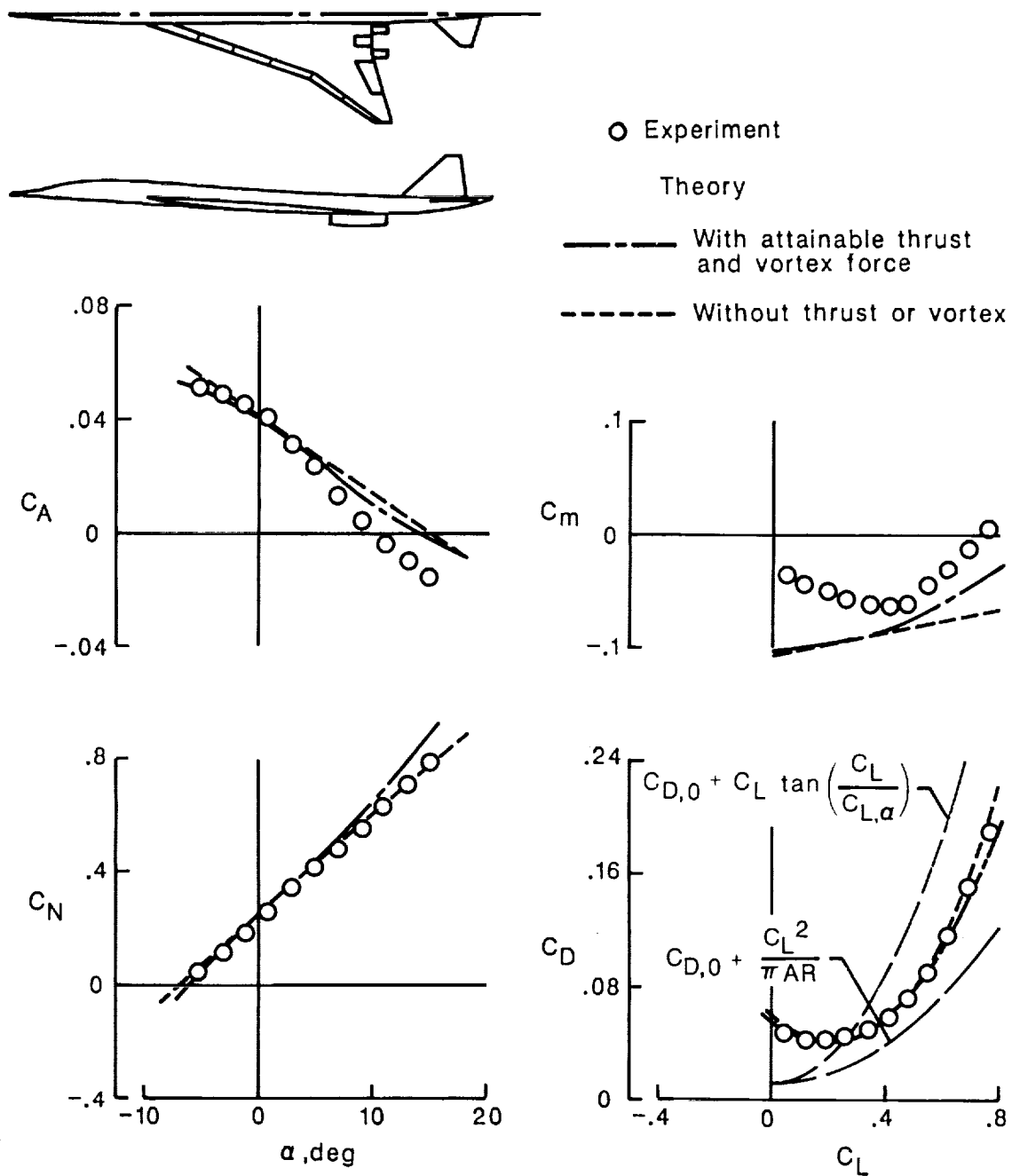
(h) Complete configuration; $\delta_{L,n} = 13°/34°/35°/35°/19°/29°$; $\delta_{T,s} = 30°$; $\delta_H = -5°$.

Figure 28. Continued.
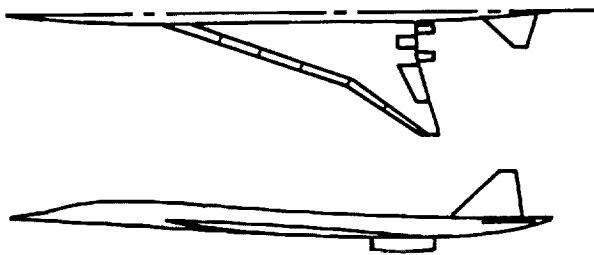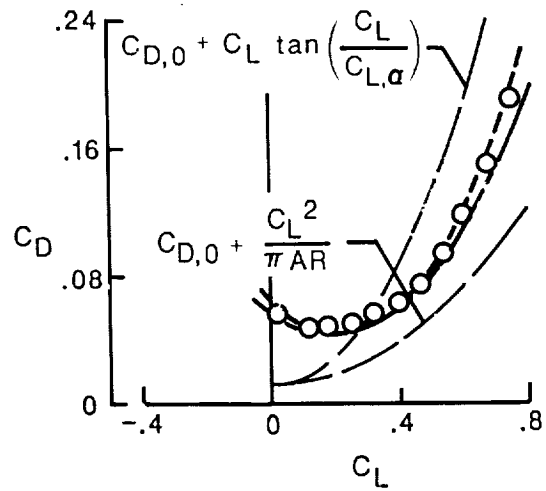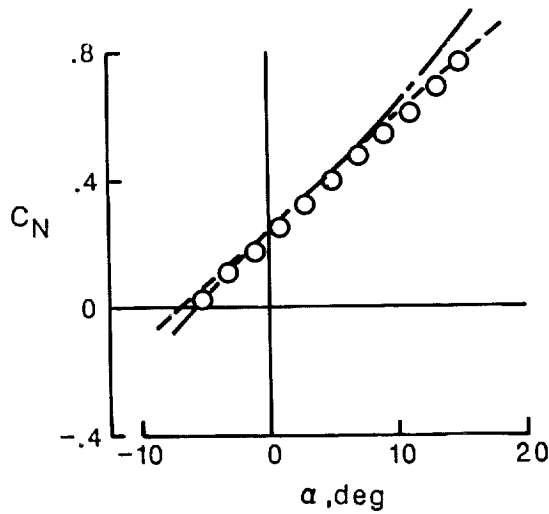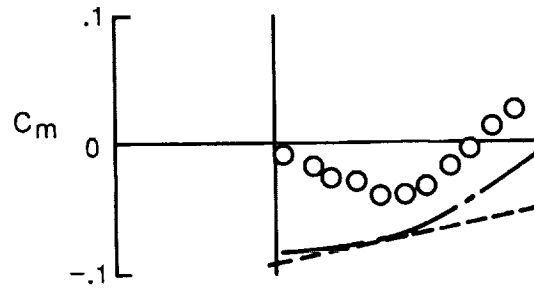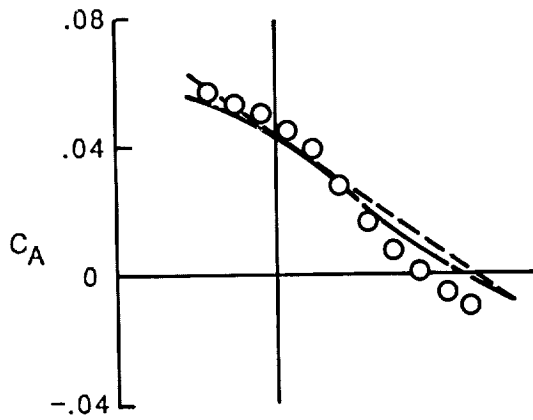
(i) Complete configuration; $\delta_{L,n} = 13°/34°/35°/35°/19°/29°$; $\delta_{T,s} = 30°$; $\delta_H = -10°$.

Figure 28. Concluded.
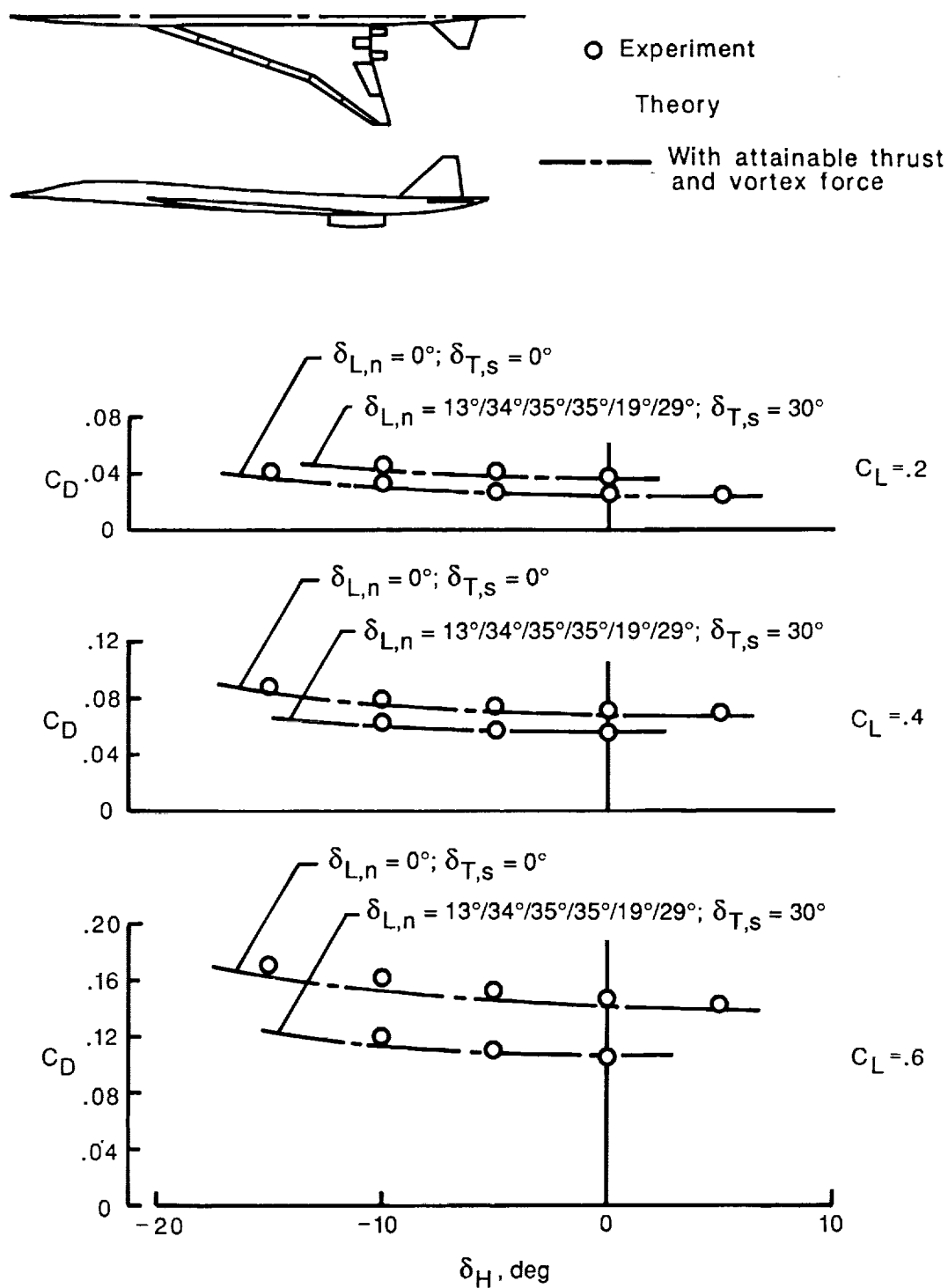
Figure 29. Variation of drag with horizontal-tail incidence angle for arrow-wing supersonic transport. $M = 0.09$; $R = 4.19 \times 10^6$.
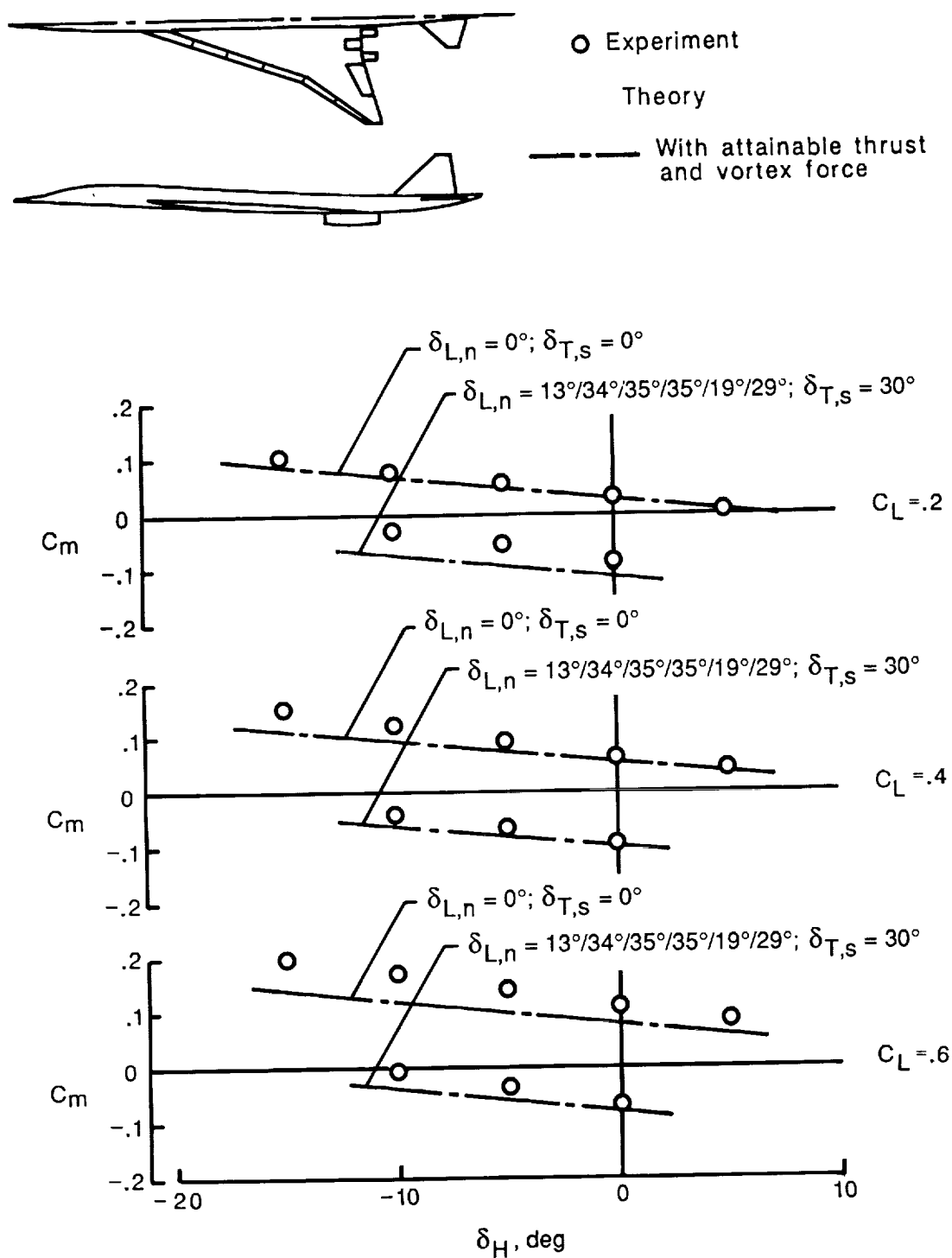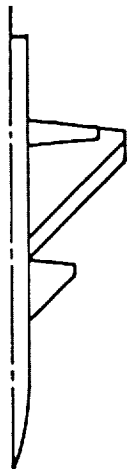
Figure 30. Variation of pitching moment with horizontal-tail incidence angle for arrow-wing supersonic transport. $M = 0.09$; $R = 4.19 \times 10^6$.
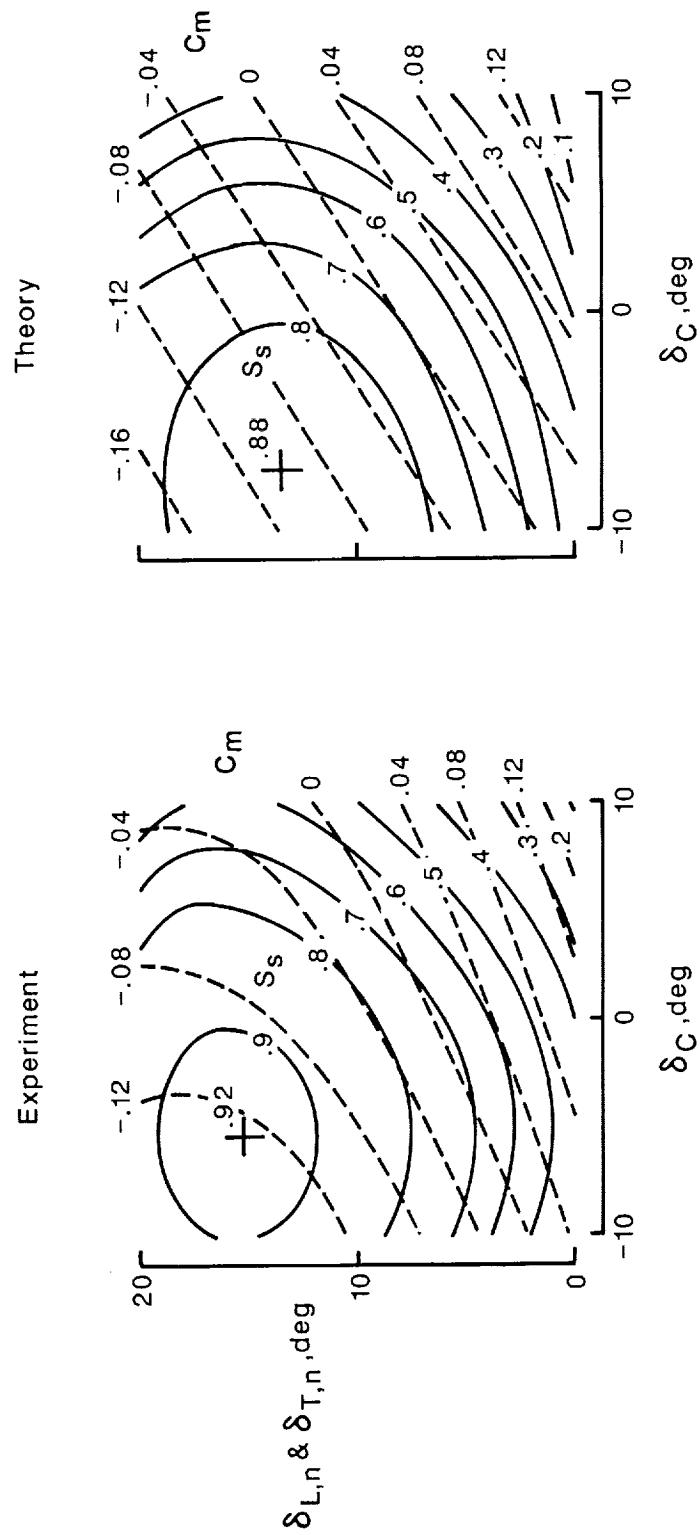
Figure 31. Suction-parameter contour map for 44°-swept trapezoidal-wing fighter with canard. $\delta_{L,n}$, $\delta_{T,n}$, and δ_C are independent variables; $M = 0.4$; $R = 1.9 \times 10^6$; $C_L = 0.6$.
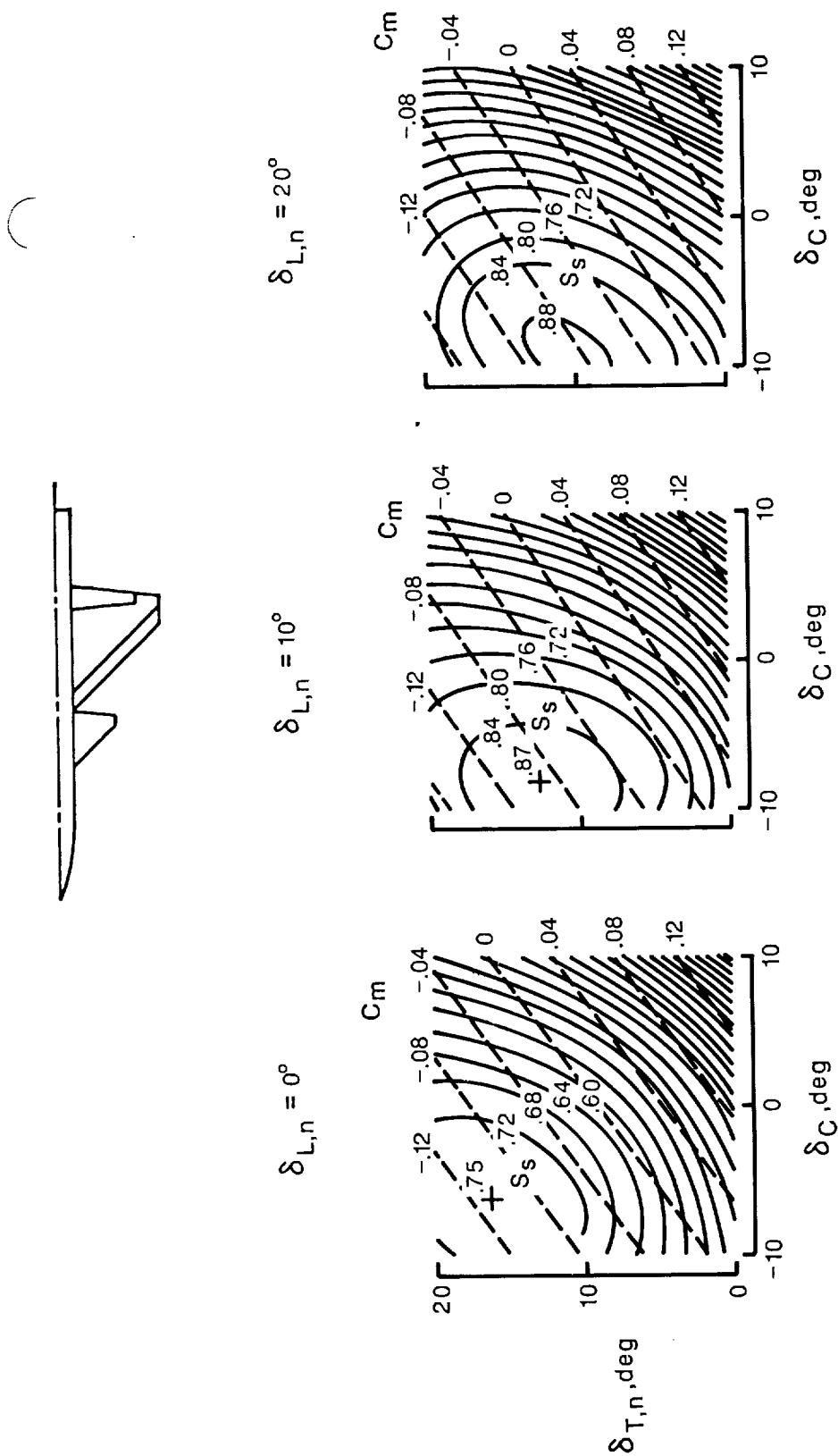
Figure 32. Theoretical suction-parameter contour maps for 44°-swept trapezoidal-wing fighter with canard. $\delta_{T,n}$ and δ_C are independent variables for selected leading-edge-flap deflection angles; $M = 0.4; R = 1.9 \times 10^6; C_L = 0.6.$
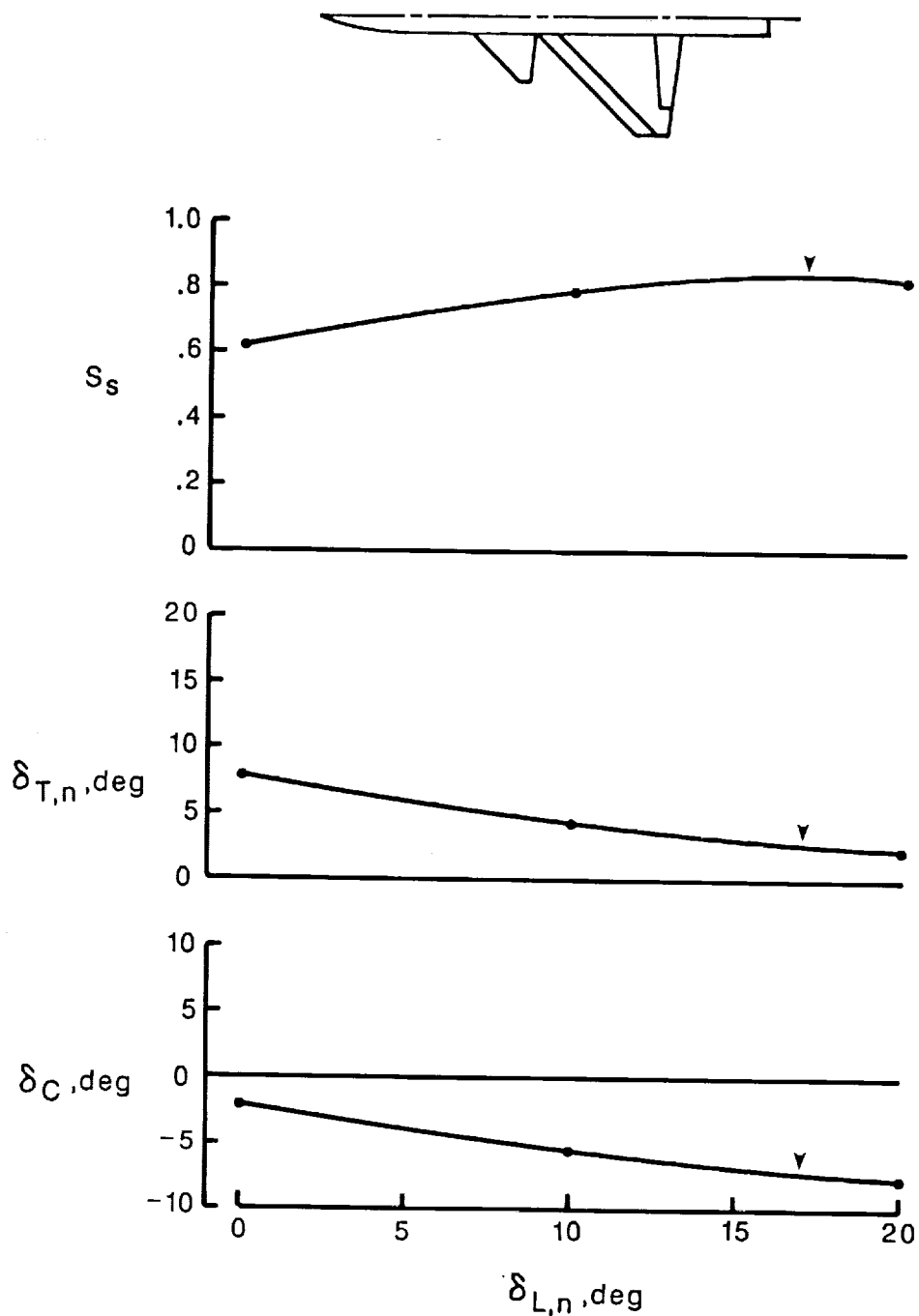
Figure 33. Theoretical maximum suction parameter for $C_m = 0$, required trailing-edge-flap deflection, and required canard incidence angle for 44°-swept trapezoidal-wing fighter with canard as a function of leading-edge-flap deflection. $M = 0.4$; $R = 1.9 \times 10^6$; $C_L = 0.6$. Arrows indicate maximum performance.
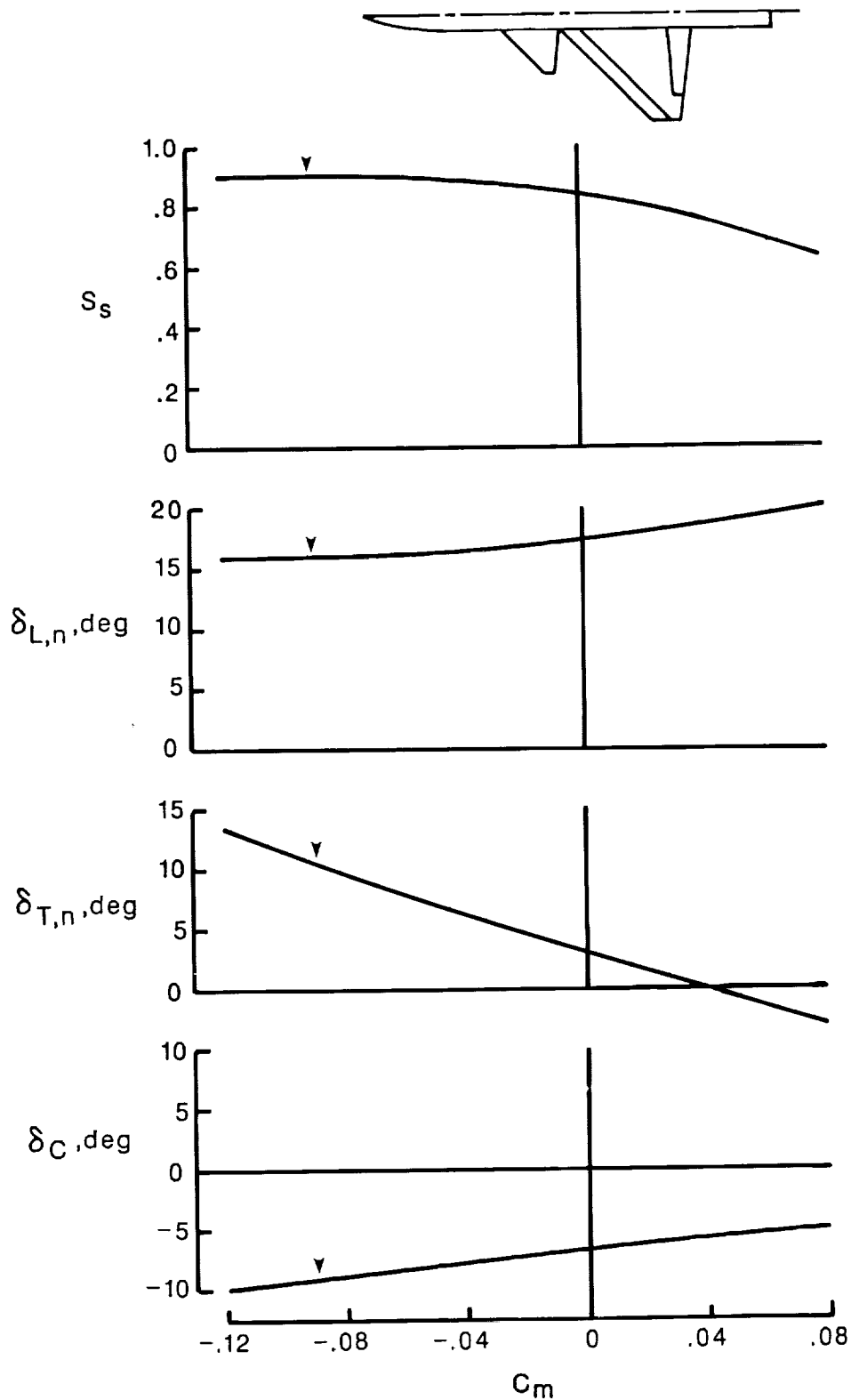
Figure 34. Theoretical maximum suction parameter, required trailing-edge-flap deflection, and required canard incidence angle for 44°-swept trapezoidal-wing fighter with canard as a function of moment restraint. $M = 0.4$; $R = 1.9 \times 10^6$; $C_L = 0.6$. Arrows indicate maximum performance.
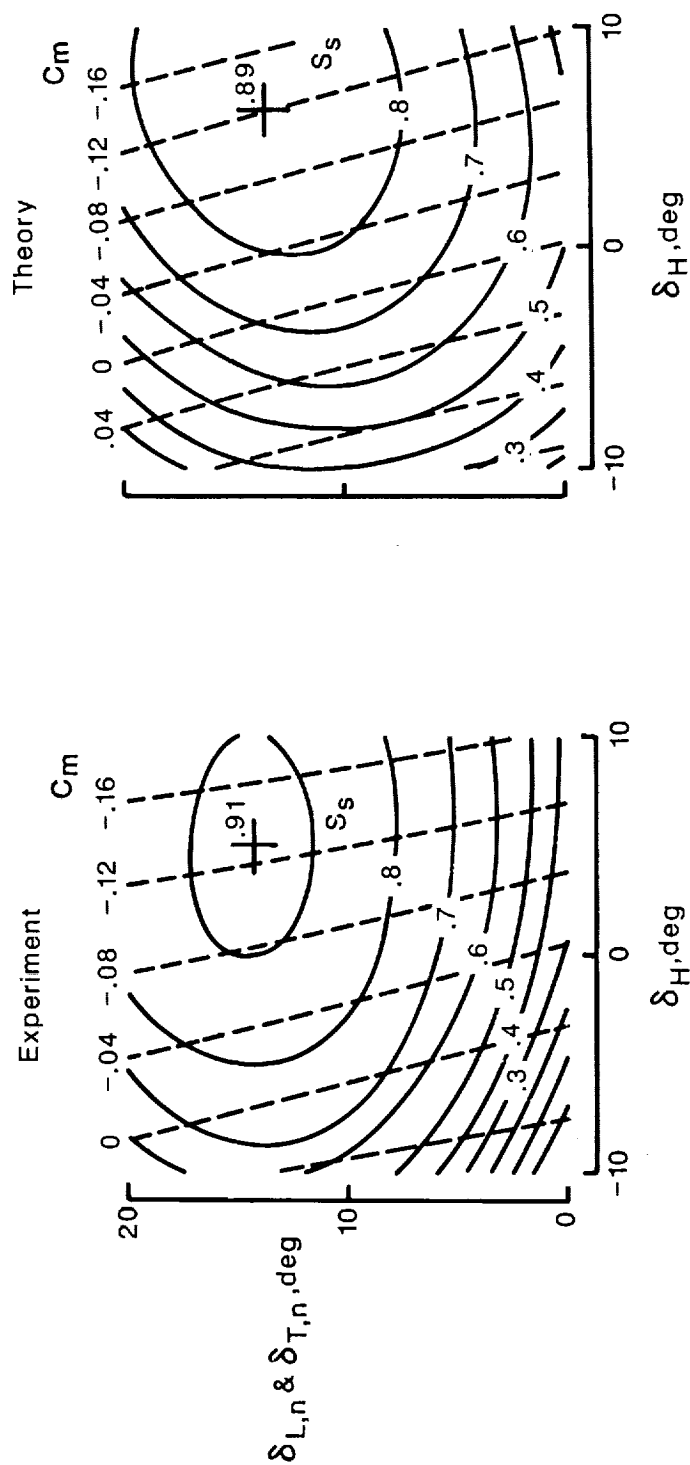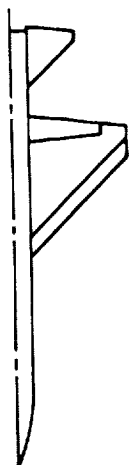
Figure 35. Suction-parameter contour maps for 44°-swept trapezoidal-wing fighter with horizontal tail. $\delta_{L,n}$, $\delta_{T,n}$, and δ_H are independent variables; $M = 0.4$; $R = 1.9 \times 10^6$; $C_L = 0.6$.
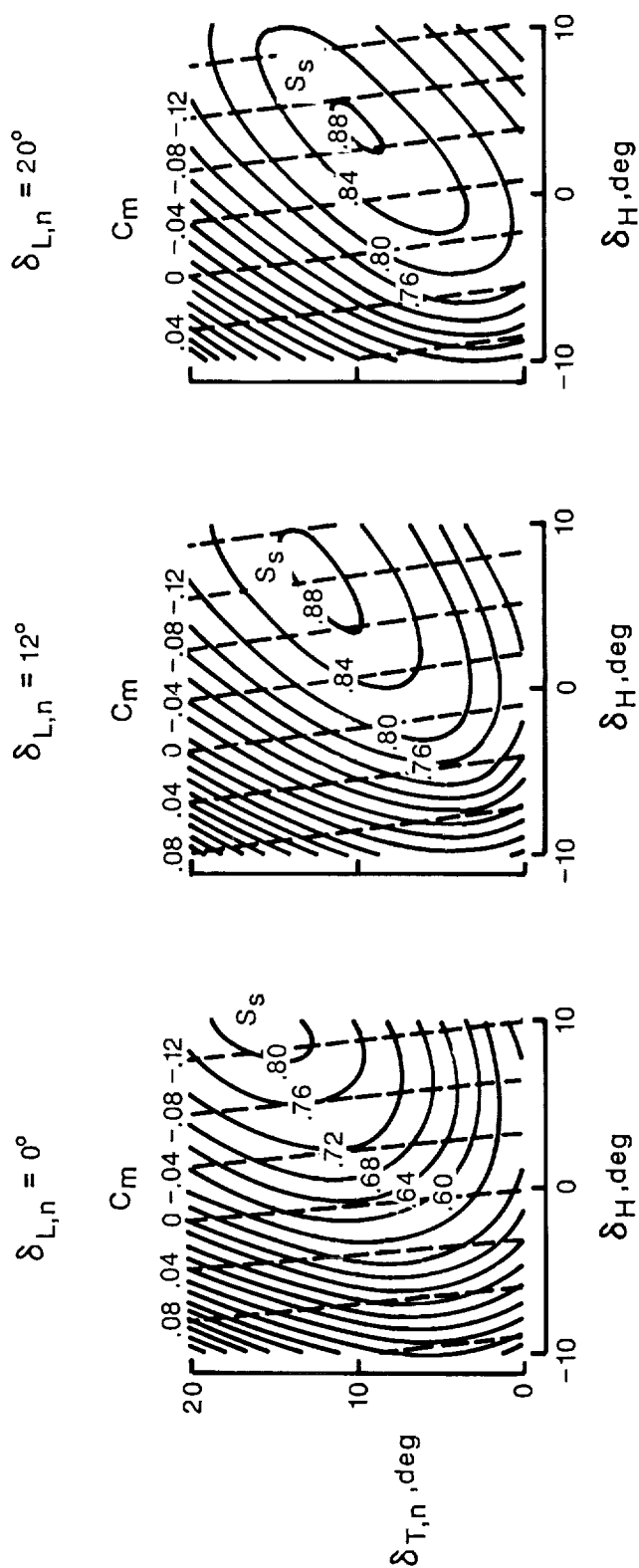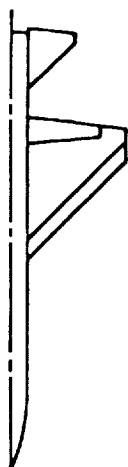
Figure 36. Theoretical suction-parameter contour maps for 44°-swept trapezoidal-wing fighter with horizontal tail. $\delta_{T,n}$ and δ_H are independent variables for selected leading-edge-flap deflection angles. $M = 0.4$; $R = 1.9 \times 10^6$; $C_L = 0.6$.
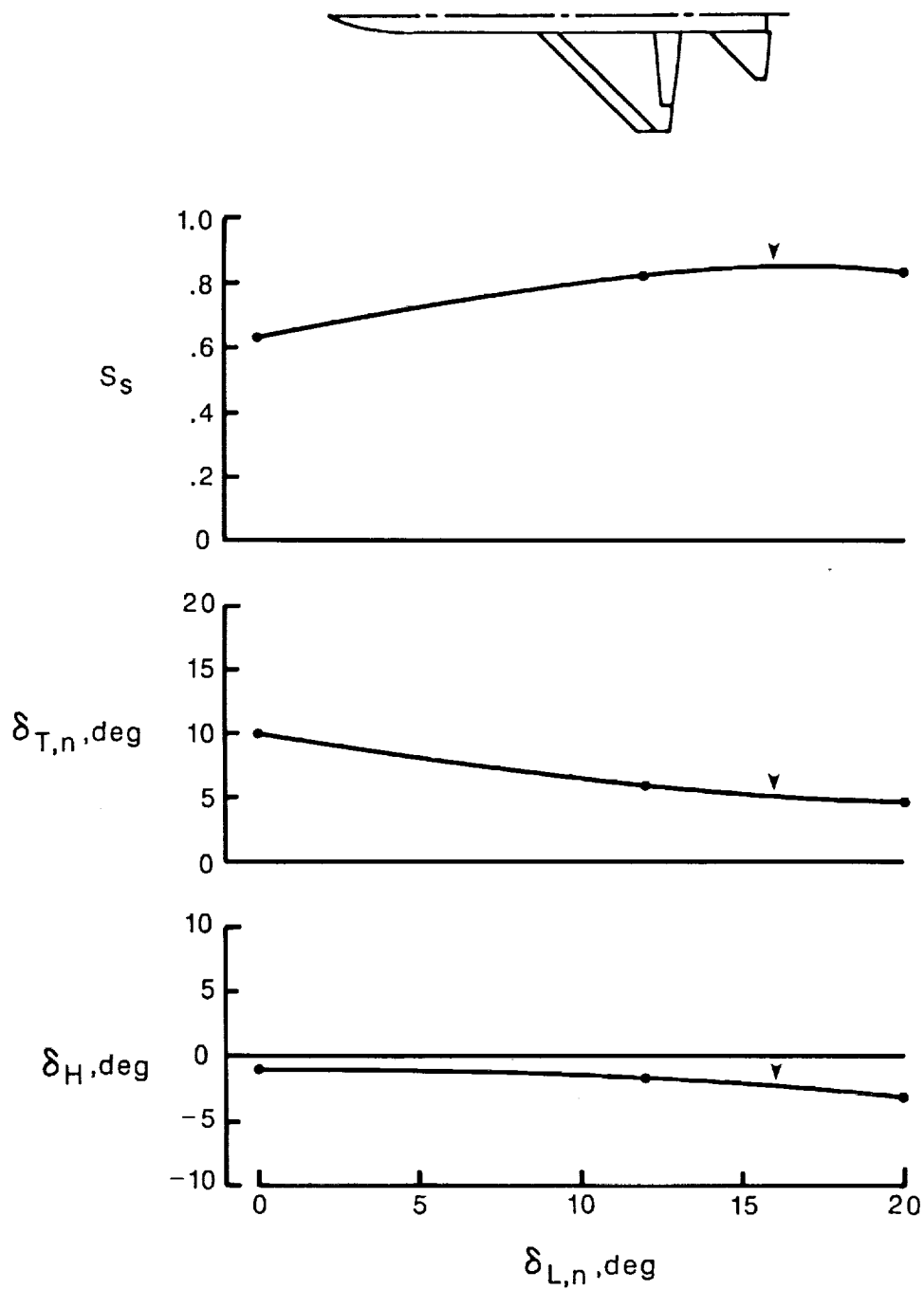
Figure 37. Theoretical maximum suction parameter for $C_m = 0$, required trailing-edge-flap deflection, and required horizontal incidence angle for 44°-swept trapezoidal-wing fighter with horizontal tail as a function of leading-edge flap deflection. $M = 0.4$; $R = 1.9 \times 10^6$; $C_L = 0.6$. Arrows indicate maximum performance.
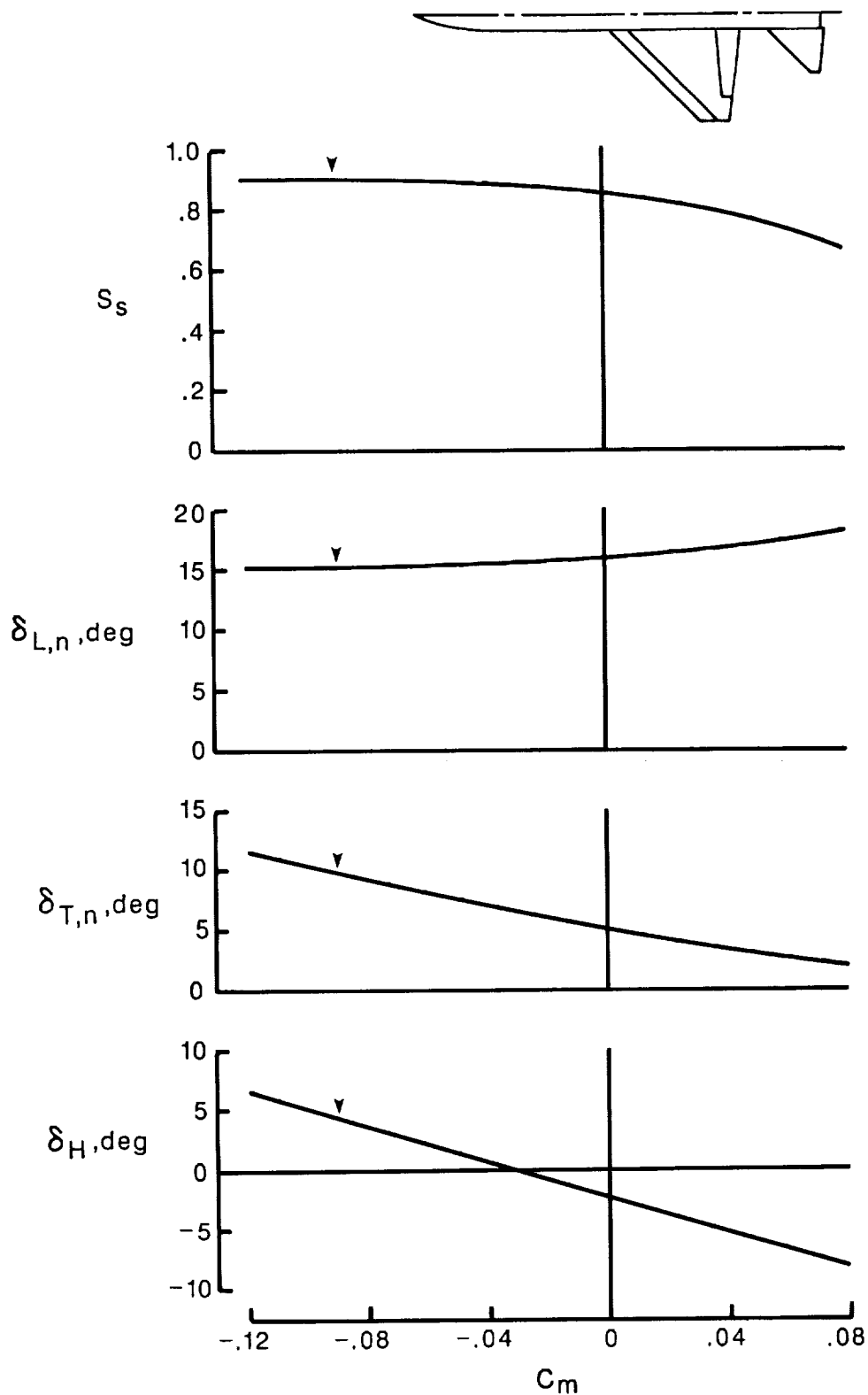
Figure 38. Theoretical maximum suction parameter, required flap deflection, and required horizontal-tail incidence angle for 44°-swept trapezoidal-wing fighter with horizontal tail as a function of moment restraint. $M = 0.4$; $R = 1.9 \times 10^6$; $C_L = 0.6$. Arrows indicate maximum performance.
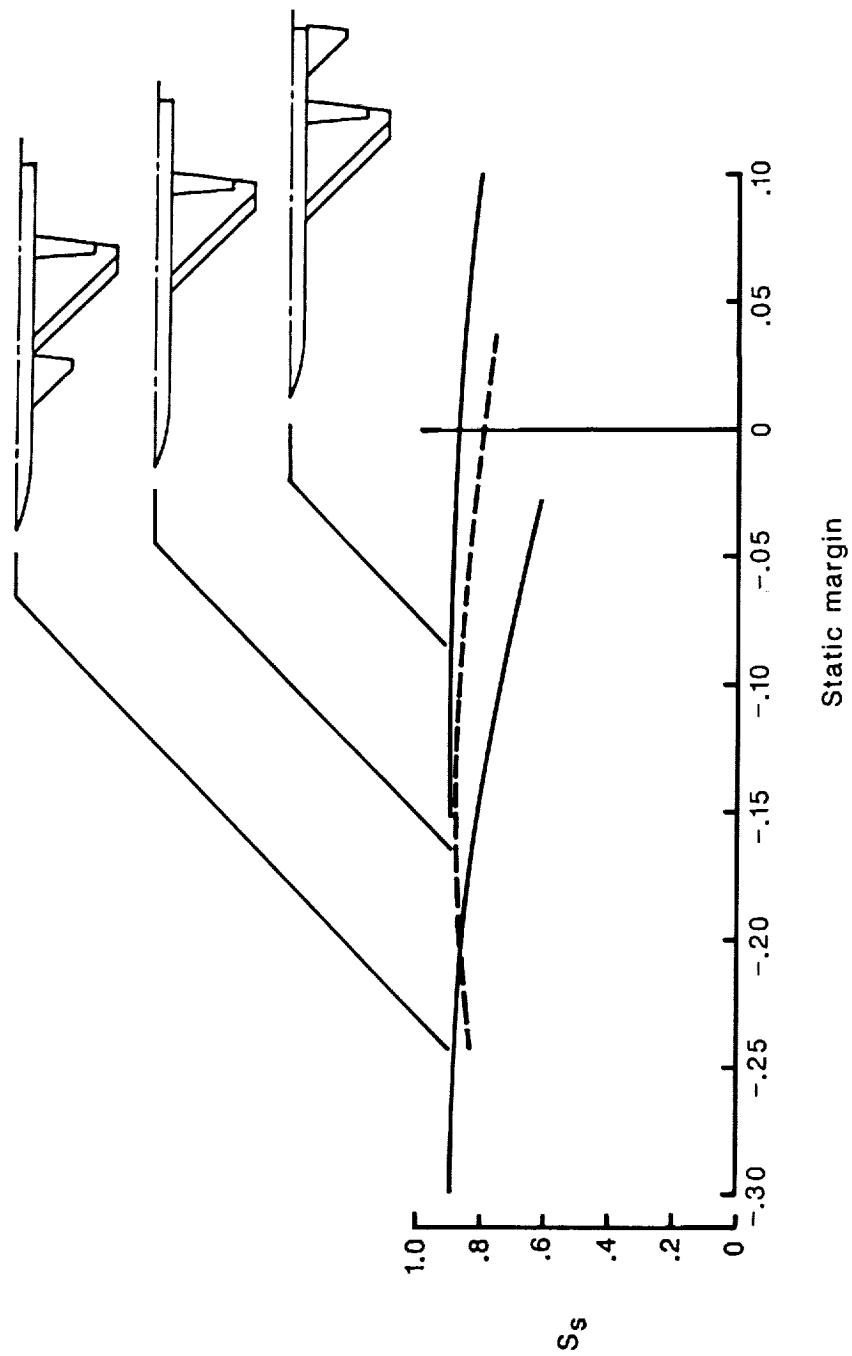
Figure 39. Theoretical maximum suction parameter as a function of stability level for 44°-swept trapezoidal-wing fighter with canard and with horizontal tail. $M = 0.4$; $R = 1.9 \times 10^6$; $C_L = 0.6$.

NASA National Aeronautics and Space Administration	Report Documentation Page		
1. Report No. NASA TP-2961	2. Government Accession No.	3. Recipient's Catalog No.	
4. Title and Subtitle Validation of a Computer Code for Analysis of Subsonic Aerodynamic Performance of Wings With Flaps in Combination With a Canard or Horizontal Tail and an Application to Optimization		5. Report Date January 1990	
		6. Performing Organization Code	
7. Author(s) Harry W. Carlson, Christine M. Darden, and Michael J. Mann		8. Performing Organization Report No. L-16611	
9. Performing Organization Name and Address NASA Langley Research Center Hampton, VA 23665-5225		10. Work Unit No. 505-68-91-02	
		11. Contract or Grant No.	
12. Sponsoring Agency Name and Address National Aeronautics and Space Administration Washington, DC 20546-0001		13. Type of Report and Period Covered Technical Paper	
		14. Sponsoring Agency Code	

15. Supplementary Notes

Harry W. Carlson: PRC Kentron, Inc., Aerospace Technologies Division, Hampton, Virginia.
Christine M. Darden and Michael J. Mann: Langley Research Center, Hampton, Virginia.

16. Abstract

Extensive correlations of computer-code results with experimental data are employed to illustrate the use of a linearized-theory, attached-flow method for the estimation and optimization of the longitudinal aerodynamic performance of wing-canard and wing–horizontal-tail configurations that may employ simple hinged-flap systems. Use of an attached-flow method is based on the premise that high levels of aerodynamic efficiency require a flow that is as nearly attached as circumstances permit. The results of this study indicate that linearized-theory, attached-flow, computer-code methods (modified to include estimated attainable leading-edge thrust and an approximate representation of vortex forces) provide a rational basis for the estimation and optimization of aerodynamic performance at subsonic speeds below the drag-rise Mach number. Generally, good prediction of aerodynamic performance, as measured by the suction parameter, can be expected for near-optimum combinations of canard or horizontal-tail incidence and leading- and trailing-edge-flap deflections at a given lift coefficient (conditions which tend to produce a predominantly attached flow).

17. Key Words (Suggested by Authors(s)) Aerodynamics Numerical methods Flap systems Canards Horizontal tails		18. Distribution Statement Unclassified—Unlimited Subject Category 02	
19. Security Classif. (of this report) Unclassified	20. Security Classif. (of this page) Unclassified	21. No. of Pages 123	22. Price A06

NASA FORM 1626 OCT 86

NASA-Langley, 1990

For sale by the National Technical Information Service, Springfield, Virginia 22161-2171